ABSTRACT

EPITAXIAL GROWTH OF III-NITRIDE NANOSTRUCTURES AND THEIR OPTOELECTRONIC APPLICATIONS

by
Moab Rajan Philip

Light-emitting diodes (LEDs) using III-nitride nanowire heterostructures have been intensively studied as promising candidates for future phosphor-free solid-state lighting and full-color displays. Compared to conventional GaN-based planar LEDs, III-nitride nanowire LEDs exhibit numerous advantages including greatly reduced dislocation densities, polarization fields, and quantum-confined Stark effect due to the effective lateral stress relaxation, promising high efficiency full-color LEDs. Beside these advantages, however, several factors have been identified as the limiting factors for further enhancing the nanowire LED quantum efficiency and light output power. Some of the most probable causes have been identified as due to the lack of carrier confinement in the active region, non-uniform carrier distribution, and electron overflow. Moreover, the presence of large surface states and defects contribute significantly to the carrier loss in nanowire LEDs.

In this dissertation, a unique core-shell nanowire heterostructure is reported, that could overcome some of the aforementioned-problems of nanowire LEDs. The device performance of such core-shell nanowire LEDs is significantly enhanced by employing several effective approaches. For instance, electron overflow and surface states/defects issues can be significantly improved by the usage of electron blocking layer and by passivating the nanowire surface with either dielectric material / large bandgap energy semiconductors, respectively. Such core-shell nanowire structures exhibit significantly increased carrier lifetime and massively enhanced photoluminescence intensity compared

to conventional InGaN/GaN nanowire LEDs.

Furthermore, AlGaN based ultraviolet LEDs are studied and demonstrated in this dissertation. The simulation studies using Finite-Difference Time-Domain method (FDTD) substantiate the design modifications such as flip-chip nanowire LED introduced in this work. High performance nanowire LEDs on metal substrates (copper) were fabricated *via* substrate-transfer process. These LEDs display higher output power in comparison to typical nanowire LEDs grown on Si substrates. By engineering the device active region, high brightness phosphor-free LEDs on Cu with highly stable white light emission and high color rendering index of > 95 are realized.

High performance nickel–zinc oxide (Ni-ZnO) and zinc oxide-graphene (ZnO-G) particles have been fabricated through a modified polyol route at 250°C. Such materials exhibit great potential for dye-sensitized solar cell (DSSC) applications on account of the enhanced short-circuit current density values and improved efficiency that stems from the enhanced absorption and large surface area of the composite. The enhanced absorption of Ni-ZnO composites can be explained by the reduction in grain boundaries of the composite structure as well as to scattering at the grain boundaries. The impregnation of graphene into ZnO structures results in a significant increase in photocurrent consequently due to graphene's unique attributes including high surface area and ultra-high electron mobility.

Future research directions will involve the development of such wide-bandgap devices such as solar cells, full color LEDs, phosphor free white-LEDs, UV LEDs and laser diodes for several applications including general lighting, wearable flexible electronics, water purification, as well as high speed LEDs for visible light communications.

EPITAXIAL GROWTH OF III-NITRIDE NANOSTRUCTURES AND THEIR OPTOELECTRONIC APPLICATIONS

by
Moab Rajan Philip

A Dissertation
Submitted to the Faculty of
New Jersey Institute of Technology
in Partial Fulfillment of the Requirements for the Degree of
Doctor of Philosophy in Electrical Engineering

Department of Electrical and Computer Engineering

May 2019

.

APPROVAL PAGE

EPITAXIAL GROWTH OF III-NITRIDE NANOSTRUCTURES AND THEIR OPTOELECTRONIC APPLICATIONS

Moab Rajan Philip

Dr. Hieu Pham Trung Nguyen, Dissertation Advisor — Date
Assistant Professor of Electrical and Computer Engineering, NJIT

Dr. Durgamadhab Misra, Committee Member — Date
Professor of Electrical and Computer Engineering, NJIT

Dr. Nirwan Ansari, Committee Member — Date
Distinguished Professor of Electrical and Computer Engineering, NJIT

Dr. Abdallah Khreishah, Committee Member — Date
Associate Professor of Electrical and Computer Engineering, NJIT

Dr. Siva P.V. Nadimpalli, Committee Member — Date
Associate Professor of Mechanical Engineering, NJIT

BIOGRAPHICAL SKETCH

Author: Moab Rajan Philip

Degree: Doctor of Philosophy

Date: May 2019

Undergraduate and Graduate Education:

- Doctor of Philosophy in Electrical Engineering,
  New Jersey Institute of Technology, Newark, NJ, 2019

- Master of Technology in Nanotechnology,
  National Institute of Technology Karnataka, Surathkal, India, 2014

- Bachelor of Technology in Mechanical Engineering,
  College of Engineering Trivandrum, Kerala, India, 2012

Major: Electrical Engineering

Presentations and Publications:

Peer Reviewed Papers:

M. Rajan Philip, H.P.T. Nguyen, R. Babu and V. Krishnakumar, "Enhanced efficiency of dye-sensitized solar cells based on polyol-synthesized nickel–zinc oxide composites," *J. Electron. Mater.*, vol. 48, no. 1, p. 252, 2019.

M. Rajan Philip, H.P.T. Nguyen, R. Babu, V. Krishnakumar and T.H.Q. Bui, "Polyol synthesis of zinc oxide-graphene composites: enhanced dye-sensitized solar cell efficiency," *Curr. Nanomat.*, vol. 3, no. 1, p. 52, 2018.

M. Rajan Philip, T.H.Q. Bui, M. Djavid, M.N. Bhuyian, P. Vu and H.P.T Nguyen, "Phosphor-free III-nitride nanowire white-light-emitting diodes for visible light communication," *Proc. SPIE.,* vol. 10595, p.105953I, 2018.

M. Rajan Philip, T.H.Q. Bui, D.D. Choudhary, M. Djavid, P. Vu, T.T. Pham, H.D. Nguyen and H.P.T Nguyen, "Molecular beam epitaxial growth and device characterization of AlGaN nanowire ultraviolet-B light-emitting diodes," *J. Adv. Opt. Photonics.*, vol. 1, no. 1, p. 003, 2018.

M. Djavid, D.D. Choudhary, **M. Rajan Philip**, T.H.Q. Bui, O. Akinnuoye, T.T. Pham and H.P.T. Nguyen, "Effects of optical absorption in deep ultraviolet nanowire light-emitting diodes," *Photon. Nanostruct.*, vol. 28, p. 106, 2018.

M. Djavid, M.H.T Dastjerdi, **M. Rajan Philip**, D.D. Choudhary, T.T. Pham, A. Khreishah and H.P.T. Nguyen, "Photonic crystal-based permutation switch for optical networks," *Photo. Net. Comm.*, vol. 35, no. 1, p. 90, 2018.

M. Rajan Philip, D.D. Choudhary, M. Djavid, M.N. Bhuyian, T.H.Q. Bui, D. Misra, A. Khreishah, James Piao, H.D. Nguyen, K.Q. Le and H.P.T Nguyen, "Fabrication of phosphor-free III-nitride nanowire light-emitting diodes on metal substrates for flexible photonics," *ACS. Omega.*, vol. 2, no. 9, p. 5708, 2017.

M. Rajan Philip, D.D. Choudhary, M. Djavid, K.Q. Le, J. Piao, H.P.T Nguyen, "High efficiency green/yellow and red InGaN/AlGaN nanowire light-emitting diodes grown by molecular beam epitaxy," *J. Sci. Adv. Mat.*, vol. 2, no. 2, p. 150, 2017.

Editor's Pick: **M. Rajan Philip**, D.D. Choudhary, M. Djavid, M.N. Bhuyian, J. Piao, T.T. Pham, D. Misra and H.P. T. Nguyen, "Controlling color emission of InGaN/AlGaN nanowire light-emitting diodes grown by molecular beam epitaxy," *J. Vac. Sci. Technol. B.*, vol. 35, p. 02B108, 2017.

M. Djavid, M.H.T. Dastjerdi, **M Rajan Philip**, D.D. Choudhary, A. Khreishah, H.P.T. Nguyen, "4-Port reciprocal optical circulators employing photonic crystals for integrated photonics circuits," *J. Light. Elec. Opt*., vol. 144, p. 586, 2017.

M. Rajan Philip, T.N. Narayanan, M. Praveen Kumar, S. Bhushan Arya, D.K. Pattanayak, "Self-protected nickel–graphene hybrid low density 3d scaffolds," *J. Mater. Chem. A.*, vol. 2, p. 19488, 2014.

Conferences:

M. Rajan Philip, T. H. Q Bui, M. Djavid, M.N. Bhuyian, P. Vu and H.P. T. Nguyen, "Phosphor-free III-nitride nanowire white-light-emitting diodes for visible light communication," *Active and Passive Smart Structures and Integrated Systems XII*, Denver, Colorado, USA, 2018.

M. Rajan Philip, H.P. T. Nguyen, D.D. Choudhary and M. Djavid, "AlGaN/GaN nanowire UV-B light-emitting diodes grown by molecular beam epitaxy," *33rd North American Conference on Molecular Beam Epitaxy*, Galveston, Texas, USA, 2017.

M. Rajan Philip, T.H.Q. Bui, M. Djavid and H.P.T. Nguyen, "Phosphor-free InGaN/AlGaN white-light- emitting diodes on flexible substrates," *Annual Meeting of the APS Mid-Atlantic Section*, Newark, New Jersey, USA, 2017.

T.H.Q. Bui, **M. Rajan Philip**, M. Djavid and H.P.T. Nguyen, "Full-color phosphor-free InGaN/AlGaN nanowire light-emitting diodes grown by molecular beam epitaxy," *Annual Meeting of the APS Mid-Atlantic Section*, NJIT, New Jersey, USA, 2017.

(Invited): H. P. T. Nguyen, **M. Rajan Philip**, D.D. Choudhary and M. Djavid, "III-nitride nanowire lighting emitting diodes on flexible platform," *EITA Conference on New Materials, Nanotechnology and New Energy*, University of Michigan, Ann Arbor, Michigan, USA, 2017.

M. Rajan Philip, H.P.T. Nguyen, D.D. Choudhary and M. Djavid, "Controlling color emission of InGaN/AlGaN nanowire light-emitting diodes grown by molecular beam epitaxy," *32nd North American Conference on Molecular Beam Epitaxy*, Saratoga Springs, New York, USA, 2016.

(Invited): H.P.T. Nguyen, S. Zhao, M. Djavid, **M. Rajan Philip** and Z. Mi, "III-nitride nanowire LEDS and LASERS: the next generation lighting technology," *13th China International Forum on Solid State Lighting,* Beijing, China, 2016.

(Invited): H.P.T. Nguyen, **M. Rajan Philip**, D.D. Choudhary, M. Djavid, and J. Piao, "Photoelectrochemical hydrogen generation using multi-band III-nitride nanowire arrays," *Water Energy Nexus, 252nd American Chemical Society National Meeting and Exposition*, Philadelphia, USA, 2016.

(Invited): H.P.T. Nguyen, M.N. Bhuyian, **M. Rajan Philip**, A. Diop, Y. Evo, R. Rocha, and J. Piao, "Self-organized InGaN/AlGaN superlattice core-shell heterostructures for high power phosphor-free nanowire white light-emitting diodes," *The 5th International Workshop on Nanotechnology and Application*, Vung Tau, Vietnam, 2015.

To my immediate family comprising of my wife (Sunu Mathew), father (Rajan John), mother (Mary Philips), brother (Meck Rajan John), parents-in-law (Gracy Mathew and Sunny Mathew).

I dedicate this dissertation in token of their earnest prayers, affection and gratitude, they have showered on me.

ACKNOWLEDGMENT

"Trust in the Lord with all your heart, and lean not on your own understanding, in all your ways acknowledge Him, and He shall direct your paths." Proverbs 3:5-6.

First and foremost, I would like to thank my loving Creator and Lord almighty for making me a curious being who loves to explore His creation and for giving me the opportunity to write this proposal defense report. Without Him, I can do nothing.

My most sincere thanks go to my advisor and mentor, Dr. Hieu P Nguyen, without whom the research so far would have been impossible. I appreciate him for familiarizing me to the wonders and frustrations of scientific research especially in III-nitride nanowire devices and fabrication, design phase of the latter. I thank him for his guidance, encouragement and support during the development of this work and teaching me virtues of patience and hard work during the time. He taught me to sharpen my skills in laboratory work and in written scientific communication.

I am indebted to my committee members: Dr. Durga Misra, Dr. Nirwan Ansari, Dr. Abdallah Khreishah, and Dr. Siva P.V. Nadimpalli, I appreciate their insight and suggestions during the experiments pertaining to my research, which were precious to me. Moreover, for agreeing to spend their valuable time to be my committee members.

I would like to thank the members in my research group, Dr. Mehrdad Djavid and Mr. Dipayan Datta Choudhary, Dr. Md Nasiruddin Bhuyian, Velpula Ravi Teja and Ha Quoc Thang Bui. Especially Dipayan and Mehrdad were my supports in the system who helped me in introducing me to some of the simulation software like Finite Difference Time

Domain (FDTD) Lumericals, Sketchup.

The department of Electrical and Computer Engineering at New Jersey Institute of Technology and its administration run by Ellen, Joan, Teri, Tanita, and Barbara, who help run it so smoothly were of great help, without them, students like me would never be able to do just our research; they keep so much off our plates. The Global Studies Office has been of immense help, especially to a foreign student such as me. They were always available to remind me of what I had to do to maintain the status of a student and provide great assistance to all foreign students.

I would like to thank the cleanroom personnel in Cornell Nanoscale Science and Technology Facility (CNF), Cornell University, Ithaca, New York, USA and Micro/Nano Fabrication Laboratory (MNFL), Princeton University, USA and James Piao of Epitaxial Laboratories, Princeton, USA for the equipment support and fruitful discussions during our research. I would like to thank also New Jersey of Technology Institute for their Teaching assistantship financial support of this research.

I would also like to give my thanks where they are due, mainly to my support system, which is comprised of teachers, friends, and family that has really helped me transition into the researcher I am today.

Finally, I would like to express my eternal gratitude to my wife, parents, brother and his wife for their everlasting love and support. Their love and helpful spirit have motivated me to achievements beyond my own expectations especially in this arduous journey.

TABLE OF CONTENTS

TABLE OF CONTENTS
(Continued)

TABLE OF CONTENTS
(Continued)

TABLE OF CONTENTS
(Continued)

TABLE OF CONTENTS
(Continued)

LIST OF TABLES

LIST OF FIGURES

LIST OF FIGURES
(Continued)

LIST OF FIGURES
(Continued)

LIST OF FIGURES
(Continued)

LIST OF FIGURES
(Continued)

LIST OF FIGURES
(Continued)

LIST OF FIGURES
(Continued)

LIST OF SYMBOLS

Am-MBE	Ammonia- Molecular Beam Epitaxy
CIE	1931 Commission International de L'eclairage Chromaticity Diagrams
DSSC	Dye Sensitized Solar Cell
DoS	Density of States
CVD	Chemical Vapor Deposition
EBL	Electron Blocking Layer
EL	Electroluminescence
FTIR	Fourier Transform Infrared Spectroscopy
HAADF	High Angle Annular Dark Field
ITO	Indium Tin Oxide
IR	Infra-Red
IQE	Internal Quantum Efficiency
LED	Light Emitting Diode
LD	Laser Diode
MBE	Molecular Beam Epitaxy
MOCVD	Metal Organic Chemical Vapor Deposition
MQW	Multi-Quantum Well
NW	Nanowire
Ni-ZnO	Nickel-Zinc Oxide
PAMBE	Plasma Assisted Molecular Beam Epitaxy
PL	Photoluminescence

QCSE	Quantum Confined Stark Effect
QD	Quantum Dots
QW	Quantum Well
RF	Radio Frequency
RGO	Reduced graphene oxide
RHEED	Reflection High Energy Electron Diffraction
SEM	Scanning Electron Microscopy
SRH	Shockley-Read Hall
SSL	Solid State Lighting
UV	Ultra-Violet
VLS	Vapor-Liquid-Solid
XRD	X-ray Diffraction
XRF	X-Ray fluorescence spectroscopy
ZnO	Zinc oxide
ZnO-G	Zinc Oxide-Graphene

CHAPTER 1

INTRODUCTION

1.1 Development of III-Nitride based Optoelectronics Application

AlN and InN were synthesized for the first time in 1907 and 1910 by Fichter et al. and Schröter et al., respectively [1, 2]. Later, Johnson et al. demonstrated the first GaN material by reaction of Ga with ammonia in 1932 [3]. In 1969, Maruska and Tietjen at RCA laboratories fabricated the first large-area epitaxial single crystalline GaN film on a sapphire substrate *via* hydride vapor phase epitaxy/chemical vapor deposition (HVPE) [4]. In 1971, Pankove et al. developed the first blue GaN light-emitting diode (LED) using the metal-insulator-semiconductor type structure [5]. In the same year, Dingle et al. showed optically pumped GaN needles that exhibited stimulated emission [6].

Maruska et al. fabricated the first violet electroluminescent diode in 1972. However, the poor quality of the grown epilayers hindered the progress of GaN devices as most of the optical and electrical results were not reproducible. In this regard, modern growth techniques such as metal-organic chemical vapor deposition (MOCVD) and molecular beam epitaxy (MBE) were made in earlier 1970's especially in 1971 and 1974 that lead to further development and progress of III-nitride growth [7, 8]. By instituting buffer layers, considerable efforts to optimize growth conditions were made, and thus in 1983 Yoshida et al. added an AlN layer grown at low temperature between the sapphire substrate and the GaN using MBE. This two-step method for growing GaN films on sapphire was later improved using MOVCD by Amano et al. in the late 1980's where they showed that an AlN layer grown at 500 °C, followed by GaN growth at 1050 °C produced smooth surfaces with low background carrier density and high room temperature

photoluminescence (PL) intensity [9, 10].

Preceding to 1986, the research on GaN based LEDs met with two major challenges, including obtaining the *p*-type GaN and materials of high quality. The early GaN films were unintentionally doped *n*-type and *p*-type doping was almost impossible to achieve. Doping of GaN with zinc, (the standard element which provides *p*-type doping in GaAsP and GaP), magnesium, cadmium, mercury, and germanium to realize *p*-type doping plagued researchers on account of the poor crystal quality and impurity contamination. However, Akasaki et al. successfully grew a high-quality GaN film on a sapphire substrate *via* a two-step growth approach in 1988, which have now been widely implemented across the industries. Later in 1989, Akasaki's same group realized *p*-type doping for the first time in GaN by doping with magnesium (Mg) during GaN growth and then activating the acceptors *via* low energy electron beam irradiation (LEEBI) [11, 12]. This understanding of *p*-type growth then quickly led to the world's first GaN based *p*-*n* junction LED in 1989. In 1992, Nakamura et al. developed a new technique of obtaining *p*-GaN using a very cost-effective approach, by annealing GaN film under N_2 ambient at a high temperature [13]. Nakamura et al. showed that acceptor activation can be also occurred after thermal annealing. These developments resulted in the realization of the mass production of GaN LEDs.

In the early 1990's, ternary alloys were finally realized. $In_xGa_{1-x}N$ films on sapphire with different values of x were grown by Matsuoka et al. in 1992 [14], and later Nakamura et al. reported InGaN/GaN heterostructures [15]. Khan et al. [16] and Itoh et al. [17] were the first to grow AlGaN on GaN. These developments lead to a boom in GaN research in the mid-to-late 1990's. The first electrically injected laser diode in the blue spectrum range was reported by Nakamura's group in 1996. Visible wavelength regime LEDs in the green

and blue electromagnetic spectra soon became commercially available from Nichia Laboratories. Research on GaN-based lasers also progressed rapidly with reports on surface mode emission, optical gain, optically pumped lasers, and injection lasers. Since 2000, ultra-violet (UV) LEDs in the UV spectrum range from 210 nm to 380 nm have also been reported by different groups [18-21]. Apart from LEDs, the InGaN/GaN based laser diodes started gaining interest. As the material quality and device structure were being improved, several laser diodes with higher performance are being reported.

1.2 Motivations of Using III-Nitride Semiconductor and III-Nitride Nanowires

Group III-nitride semiconductors including GaN, InN, AlN, and their alloys have been gaining attention as one of the most prominent semiconductors due to their direct and wide-bandgap nature. Additionally, the ability to tune bandgap energy of III-nitride semiconductors in a wide-range of the electromagnetic spectrum, ranging from the deep UV (AlN, E_g = 6.2 eV) through the visible and to the infrared range (InN, E_g = 0.7 eV) *via* bandgap engineering makes them vital for majority of the photonic devices such as laser diodes and LEDs.

III-nitride based electronic and photonic devices hold great potential in a variety of applications including solid-state lighting (SSL), medical equipment, high-density optical storage, water purification, and for the space and military industries also. To list a few of the devices, high power, high temperature and high frequency electronic devices based on GaN field effect transistors and hetero-bipolar transistors and high luminous efficiency and mechanical robustness of GaN LEDs are some of the major devices under severe exploration in the photonics industry. Figure 1.1 lists the bandgap energy and lattice

constants for some of the most common indirect and direct bandgap semiconductors used in the photonics industry.

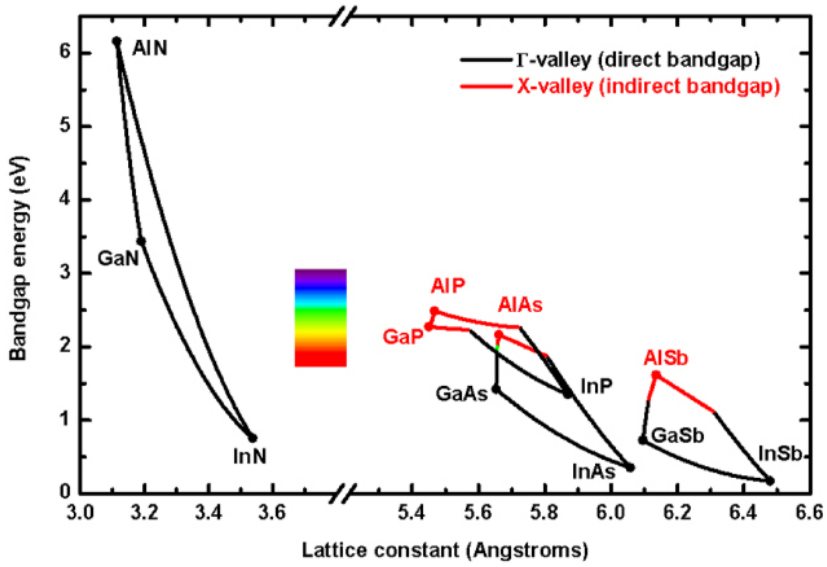

Figure 1.1 Bandgaps vs lattice constant for most common elemental and binary semiconductors at room temperature.
Source: [22].

Compared to their conventional planar counterparts, III-nitride nanowires exhibit significantly better performance including largely free of dislocations and piezoelectric polarization field, due to the effective lateral strain relaxation associated with the large surface-to-bulk-volume ratio [23]. Additionally, recent studies have shown that nearly defect-free III-nitride nanowires can be grown virtually on any substrates [24]. Moreover, due to their significantly reduced dimensions, III-nitride nanowires offer a new avenue to scale down the dimensions of future devices and systems. In the past decade, a broad range of III-nitride nanowire optoelectronic devices have been demonstrated, including LEDs, lasers, photodetectors and solar cells among many others. Strain relaxation through fabricating quantum wells (QWs) into a nanorod array structure is reported to reduce the

electron-longitudinal-optical phonon coupling strength, which is closely associated with the Indirect Auger recombination (IAR) process [25]. Thus, nanorod structure is often linked with potential minimization of the efficiency droop observed in III-nitride planar films.

Furthermore, the vertically aligned grown nanowires of small diameters, offer much improved lateral stress relaxation while being grown on a lattice mismatched substrate. Therefore, the stress in the epilayer is effectively accommodated in a nanowire structure. Because of this, nanowires offer a larger critical thickness to form dislocations and the crystal quality is superior in contrast to its planar counterpart [26].

1.3 III-Nitride Material Properties

III-nitride semiconductor materials can be either of three crystallographic structures including a cubic zinc-blende, hexagonal wurtzite or rock-salt structure. The formation of rock-salt structure is possible only under high pressure [27, 28]. Hexagonal wurtzite structure is the most stable crystalline structure under ambient conditions for the III-nitride semiconductors when compared to the cubic zinc-blende and rock-salt structure. Both zinc blende and wurtzite phase can coexist under the various parameters used for crystal growth. The cubic structure is thermodynamically metastable and wurtzite structure is thermodynamically stable. Figure 1.2 depicts a typical GaN hexagonal wurtzite structure.

The hexagonal wurtzite structure of III-nitrides consists of two interpenetrating hexagonal close-packed (HCP) sub-lattices, and each HCP sub-lattice is composed of six atoms of each type. For GaN, this requires each Ga atom to be surrounded by four N atoms and vice versa. The crystal lattice of the hexagonal wurtzite structure is defined by two

lattice constants, a in the basal plane and c in the perpendicular direction to the basal plane, and a microscopic dimensionless parameter u. The internal parameter u represents the interatomic distance within the basic unit cell of a hexagonal wurtzite phase structure, which is defined as the bond length between cation and anion divided by c lattice parameter.

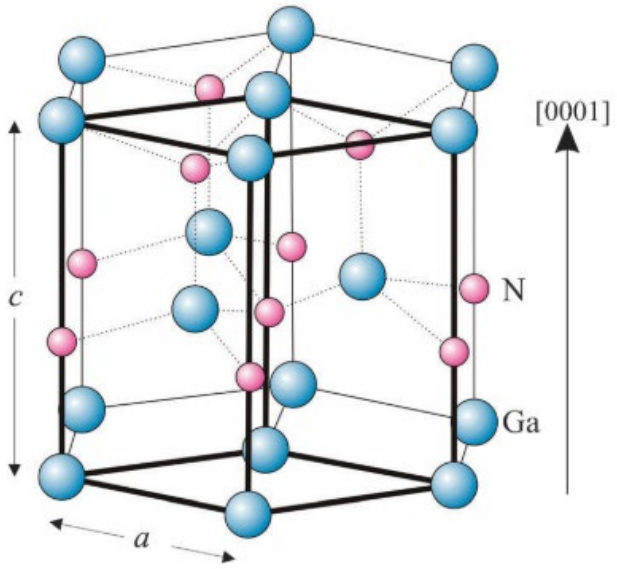

Figure 1.2 III-nitride hexagonal wurtzite crystal structured unit cell.
Source: [29].

Table 1.1 Lattice Parameter Values for III-Nitride Hexagonal Phase Semiconductors

Binary alloy	a (A^0)	c (A^0)	c/a ratio	u
InN	3.5170	5.6850	1.616	0.379
GaN	3.1894	5.1861	1.626	0.3789
AlN	3.1120	4.9808	1.600	0.3869

Table 1.1 lists the lattice parameter values for wurtzite III-nitrides. Internal parameter u is equal to 3/8=0.375, and the ratio of c/a is always 1.633 in an ideal wurtzite structure. But on account of the strong ionic bonding resulting from the large differences in the electronegativity of the Group III-metal atoms and nitrogen atoms, III-nitrides are not ideal wurtzite structures, which results in the parameter u always higher than 0.375 and the c/a value always lower than 1.633, as listed in Table 1.1. The unit cell distortion of III-nitrides from the ideal wurtzite structure results in polarization charge along the c-axis, which is referred to as spontaneous polarization. The value changes from 0.034 C/m^2 for GaN through 0.042 C/m^2 for InN to 0.090 C/m^2 for AlN along the opposite to the [0001] direction. Moreover, due to the lack of inversion symmetry in the unit cell of a wurtzite group III-nitride semiconductor, the polarity of a structure causes much more concern.

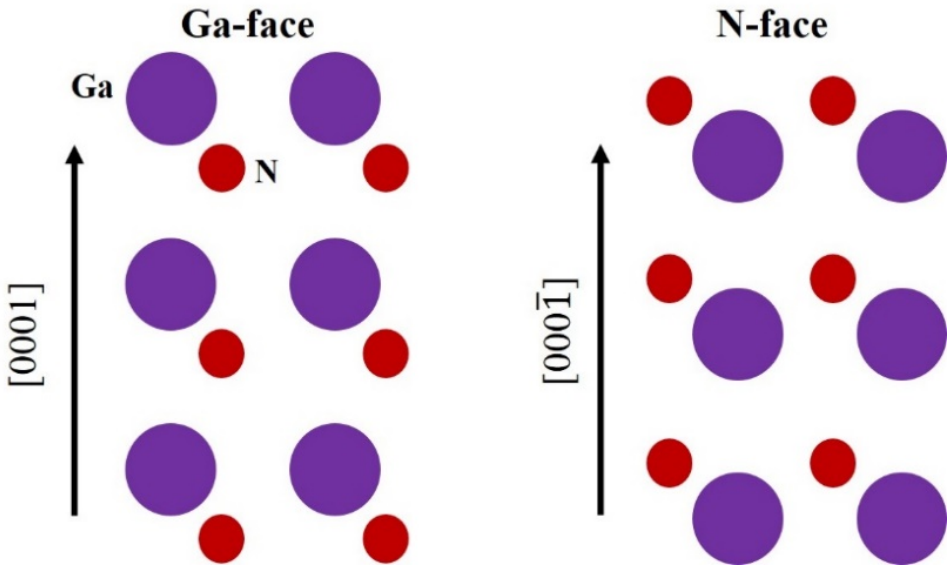

Figure 1.3 Different polarities (Ga and N-face) of wurtzite GaN.

Figure 1.3 represents the Ga and N polar surfaces grown for III-nitrides. The directions of spontaneous polarization in III-nitride semiconductors having different polarities, Ga-polar and N-polar, are illustrated in Figure 1.4 respective to the [0001] direction.

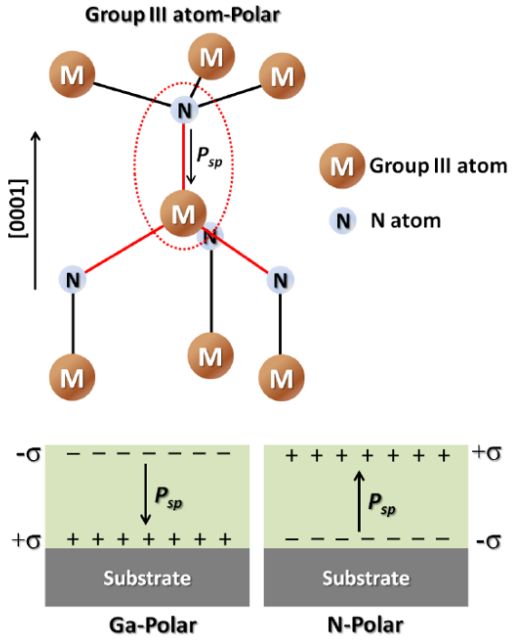

Figure 1.4 Spontaneous polarity direction in III-nitrides w.r.t polarity (Ga and N-polar) along the [0001] direction.
Source: [30].

The (0001) and (000$\bar{1}$) surfaces of the wurtzite structure are not equivalent which results in having distinctive chemical properties. Ga and N atoms are arranged in bilayer and the polarity of III-nitride material is typically defined by the top layer. If the top layer is metal/Ga it is metal/Ga polar and otherwise it is N-polar. The (0001) and (000$\bar{1}$) polarity depends on whether Ga atoms or N atoms lie at the top of bilayer as shown in Figure 1.3. Normally, high-quality epitaxial GaN films deposited by MOCVD on *c*-plane sapphire substrates grow in the (0001) direction with Ga-faced surfaces, while MBE growth

commonly occurs in the $(000\bar{1})$ direction, yielding an N-faced film [31, 32]. The Ga-faced GaN usually have a smooth and more chemically stable surface.

Large differences in the electronegativity between the group III-metal cations and nitrogen anions introduces a strong ionic bonding in the group III-nitride semiconductor. Moreover, the large variation in the bonding energies and ionic radii of the group III atoms (cations) lead to different lattice constants, bandgap energies, and electron affinities of the III-nitride semiconductors. The strong bond strength in III-nitrides leads up to superior thermal-and chemical stability for the wurtzite III-nitrides. These attributes lead to III-nitride being an excellent candidate for future high power and high-temperature environment devices especially in the photonic and electronic industry.

III-nitride wurtzite alloys are direct bandgap semiconductors having wide bandgap energy. The bandgaps of III-nitride binary alloys including InN, GaN and AlN are reported to be in the range of 0.7±0.05 eV, 3.52±0.1 eV, and 6.1±0.1 eV, respectively [33, 34]. By controlling the mole fraction of each binary component in the ternary or quaternary alloys, tunable bandgap alloys can be engineered.

$$E_g(A_xB_{1-X}N) = xE_g(A) + (1-x)E_g(B) - bx(1-x) \tag{1.1}$$

The effective bandgap of ternary combinations, such as $In_xGa_{1-x}N$, $Al_xGa_{1-x}N$, and $In_xAl_{1-x}N$, can be determined theoretically by Vegard's Law by making use of the mole fraction of the binary alloys and their fundamental bandgap energies, as reported in Equation (1.1). E_g (A) and E_g (B) represents the bandgap energies of binary alloy A and B, respectively, x is the alloy mole fraction in $A_xB_{1-x}N$ alloy, and b is the bandgap bowing parameter that is unique to each compound and determined experimentally. The notation E_g ($A_xB_{1-x}N$) refers to the bandgap energy of the engineered resulting ternary alloy.

The bandgap energies of each binary alloy and the bowing parameters for group III-nitride ternary alloys are shown in the Table 1.2.

Table 1.2 Vegard's Law Employed in the Calculation of Bandgap Energy of Group III-Nitrides

Alloy	E_g of A (eV)	E_g of B (eV)	Bowing Parameter "b"
$Al_xGa_{1-x}N$	6.1 ± 0.1	3.52 ± 0.1	0.7 ± 0.1
$In_xGa_{1-x}N$	0.7 ± 0.05	3.52 ± 0.1	1.6 ± 0.2
$In_xAl_{1-x}N$	0.7 ± 0.05	6.10 ± 0.1	3.4 ± 1.2

1.4 Current Research Trend of GaN based LEDs

In solid state LEDs, the electrons (from *n*-type semiconductor) and holes from the (*p*-type semiconductors), recombine radiatively emitting photons or visible light. LED essentially consists of a *p*-*n* junction on a chip of semiconductor material. Under a forward bias, light emission is realized by the electron–hole recombination at the active region/ junction between the *p*-*n* junctions in a semiconductor. The emitted photons thus have an energy approximately equal to the band gap of the active material. In homojunction semiconductors, light emission is obtained by electron-hole recombination between the *p*-*n* junctions. However, in a double heterostructure LED the photon emission is achieved effectively by the recombination of electrons and holes in the smaller bandgap active region as opposed to the *n*- and *p*-type cladding layers in homojunction LEDs.

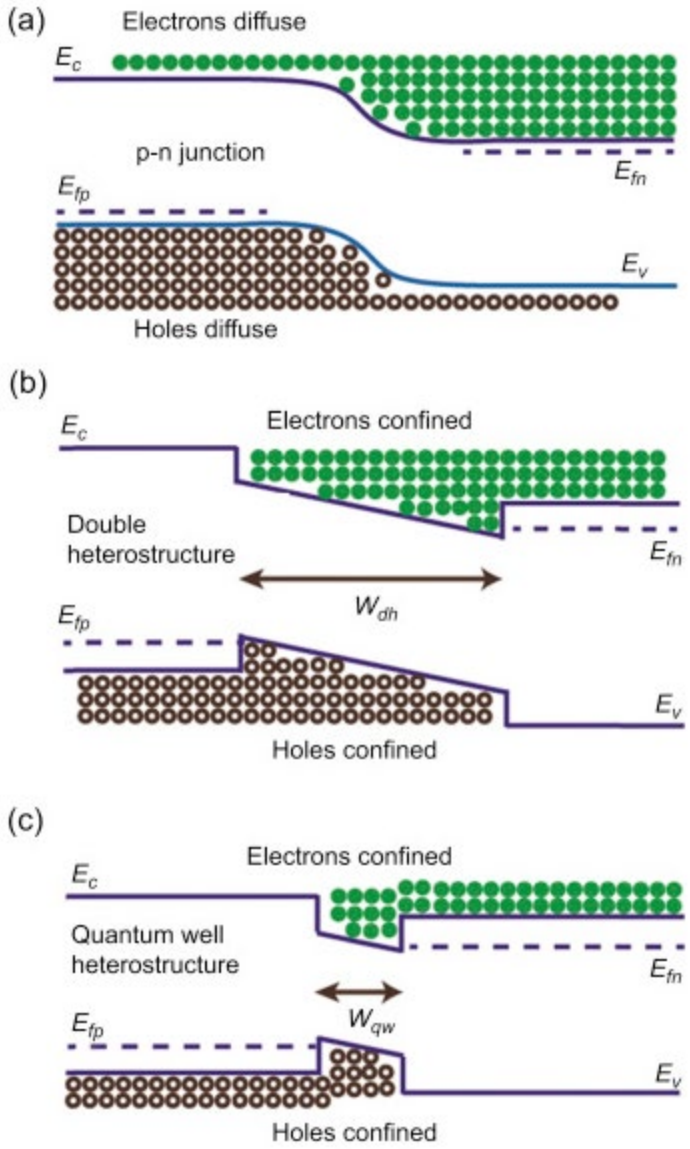

Figure 1.5 Conduction band diagrams illustrating confinement and carrier diffusion in (a) a typical *p-n* junction, (b) a double heterostructure (heterojunction), and (c) QW heterostructure. As $W_{qw} < W_{dh}$, the carrier confinement is pronounced in a QW as compared to that of a double heterostructure leading to a higher carrier concentration in QW.
Source: [35].

The active region of LED can be either of those including a depletion region as observed in a homojunction, QW or QD region incorporated in the barrier surrounded depletion region as in heterojunction or a small bandgap depletion region as seen in double

heterostructure p-n junction. As illustrated in Figure 1.5, in such a double heterostructure design with small bandgap sandwiched between *n* and *p* type materials, the electron and holes would be confined to the small band gap region as compared to being distributed along the whole diffusion length. Such device design leads to an enhanced carrier concentration and consequently a higher recombination efficiency. By embedding smaller bandgap single QW or multiple QWs in the active region, at small voltages, the quasi-Fermi levels can be pushed into the bands, thus resulting in a higher carrier injection for the same voltage.

The main adversity facing SSL technology is the development of LEDs, of ultrahigh efficiency, long term reliability, and tunable color emission featured monolithically integrated blue, green, and red devices. The GaN based semiconductor devices emitting light in visible and UV regime can be incorporated for multifunctional applications including liquid crystal displays (LCD) backlight [36-38], traffic lights [39], automotive lighting [40], biomedical diagnostics [41-43], disinfection [44-46], and water purification purposes [47, 48]. External quantum efficiency (EQE), which is the product of carrier injection efficiency, internal quantum efficiency (IQE) and light extraction efficiency (LEE) are the key criterion in estimating the performance of an LED device. LEDs employing conventional GaN based planar heterostructures are limited by their low IQE and low LEE. The low IQE in the GaN based LEDs has been explained by the presence of polarization fields, Auger recombination [49, 50], poor hole transport, defects/dislocations, and electron leakage and overflow [51-53].

Due to their low power consumption, long lifetime, and eco-friendly characteristics, III-nitride based visible LEDs are currently widely employed in display- and general-lighting applications. The enhancement in the IQE and EQE have played a

crucial role in phasing out the conventional lighting sources such as incandescent and fluorescent lamps with high brightness LEDs [54]. Best blue LEDs exhibit the IQE of above 80 % at a current density of ~35 A/cm^2 [55]. Even though the peak luminous efficiencies of LED-based lamps at relatively low currents far exceed those of incandescent and fluorescent lamps and have a better light quality, high efficiency and longer operating life [56-59], the efficiency of LED lamps at high currents decreases with increase in driving current, which is referred to as an *efficiency droop*, under high injection current densities. This efficiency droop is thus one of the most significant challenges faced by high power GaN LEDs. The origin of the efficiency droop is still controversial, and several possible mechanisms to correct this problem have been suggested. The most probable reasons are the presence of defects, polarization field, poor hole transport, Auger recombination, and electron overflow which are described in the following sections.

Nanowire LEDs were developed later as compared to thin-film structures. However, they are emerging as a viable and prospective candidates for high performance GaN based devices. In nanowire devices, mechanisms that may contribute to efficiency degradation of GaN devices, such as dislocations, polarization fields, as well as the associated QCSE, are greatly reduced. Nanowire LEDs can be grown spontaneously using MBE on low cost, large area Si substrates [24, 60, 61]. Kikuchi et al. reported such nanowire LEDs with the embedded InGaN/GaN multiple quantum disk in 2004 [62]. Selective area growth can be utilized for realizing nanowire LEDs with well-defined position and size [63, 64]. The emission characteristics of such selective area grown nanowire LEDs can be tuned by the position and size of holes arrays on pre-patterned substrates. Nanowire LEDs offer an efficient light emission across from deep UV to near IR spectral range [65-67]. Different color emissions can be achieved by varying the *In*

composition of the InGaN active region. White-light LEDs, therefore, can be envisioned by mixing multiple color emissions from a single nanowire. Such white-light LEDs have been reported by various groups [67].

The performance of a nanowire LED is limited by the surface state defects, which can reduce the carrier injection efficiency and consequently the EQE by capturing carriers from the active region [68]. With the use of self-organized InGaN/AlGaN dot-in-a-wire core-shell nanowire arrays we can significantly improve carrier injection efficiency. In this structure, an AlGaN shell can be spontaneously formed on the sidewall of the nanowire during growth of the AlGaN barrier of the quantum dot active region, which can lead to drastically reduced nonradiative surface recombination [69].

1.5 Green-Gap Problem and ABC Model for III-Nitride LEDs

1.5.1 Green-Gap

The famous 'green-gap' depicted in Figure 1.6 is the main limitation in III-nitride LEDs industry [57, 58]. InGaN LEDs exhibit high EQE in the blue and violet region, though a drop in EQE is observed in the green/ yellow region. With an increase in *In* content in the active region, the lattice mismatch between InGaN and GaN increases, thus resulting in an increasing dislocation density and enhanced polarization fields. In other words, the material quality and also, the polarization effects get more pronounced with increase in *In* content in the longer wavelength region limiting the device performance.

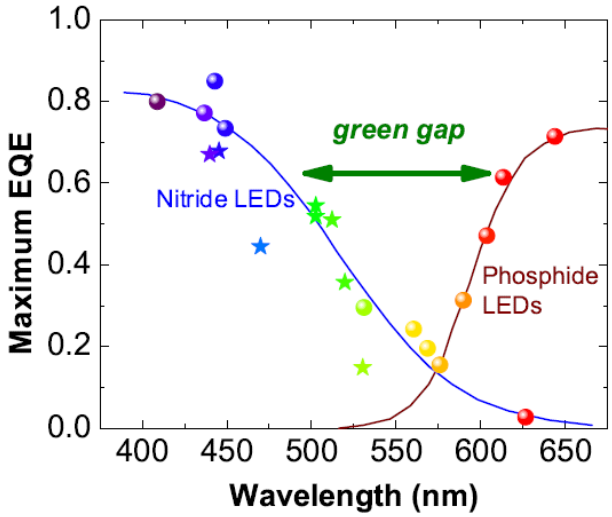

Figure 1.6 EQE vs wavelength plot for visible LEDs. EQE is very low in 500-600 nm referred to as the 'green-gap'.
Source: [70].

The direct bandgap available for AlGaInP material is from 1.9eV (650 nm) to 2.2eV (560 nm). Be that as it may, AlInGaP LEDs display high efficiency in longer wavelength region but performs poorly in short wavelength region due to having indirect bandgap in that region [57, 71, 72]. The other major problem of III-nitride LEDs is efficiency droop.

1.5.2 ABF Model for III-Nitride LEDs

Considering the several reasons that are responsible for efficiency droop, namely the presence of defects, polarization field, poor hole transport, Auger recombination, and electron overflow, the IQE can be typically described by the ABF model [73, 74] where A, B and C represents the SRH non-radiative coefficient, radiative coefficient, and Auger coefficient, respectively. The function f(n) represents the carrier overflow outside the active region. We use an ABF model to study the various carrier recombination processes and the IQE of GaN-based LEDs. The IQE of GaN-based LED is given by Equation (1.2)

$$\eta_{IQE} = \frac{Bn^2}{An + BN^2 + f(n)} \quad (1.2)$$

Where η_{IQE} is the internal quantum efficiency, n is the carrier density and A, and B are the Shockley-Read-Hall nonradiative recombination and radiative recombination coefficients. Auger recombination and any other high order carrier loss processes are described by f(N). f(N) also represents the carrier leakage outside the active region. Thus f(N) is generally used to describe any other higher-order carrier loss processes, such as Auger recombination and electron overflow. Mathematically, it can be written as $CN^3 + DN^4$ sometimes. In nanowire devices, due to the highly effective lateral stress relaxation associated with the large surface areas, it is expected that both the polarization fields and dislocation densities can be significantly reduced. However, because of the surface states and defects present and due to the large surface-to-volume ratios of nanowires it can lead to carrier loss in nanowire LEDs. Additionally, it has remained debatable whether Auger recombination plays an important role on the performance of GaN-based devices.

1.6 Current Problems of III-Nitride LEDs

Due to the lack of native substrates, conventional III-nitride planar heterostructures have very high dislocation densities that restraints the device performance and reliability. Moreover, the presence of large dislocation densities and strain-induced polarization field associated with large inter-layer lattice mismatch limits the traditional quantum well based LEDs performance. The efficiency droop in InGaN based LEDs which occurs at high injection currents thus limiting the realization of high brightness and high-power lighting when operating at high current levels also poses a challenge for the III-nitride lighting

industry. Extensive investigation is taking place to tackle this issue. Carrier delocalization, polarization field, Auger recombination, carrier leakage and poor hole transport are some of the reasons identified attributing to this efficiency droop.

The following sections will describe these phenomena which attributes to lack of efficiency, or in other words, efficiency droop, in III-nitride LEDs in detail.

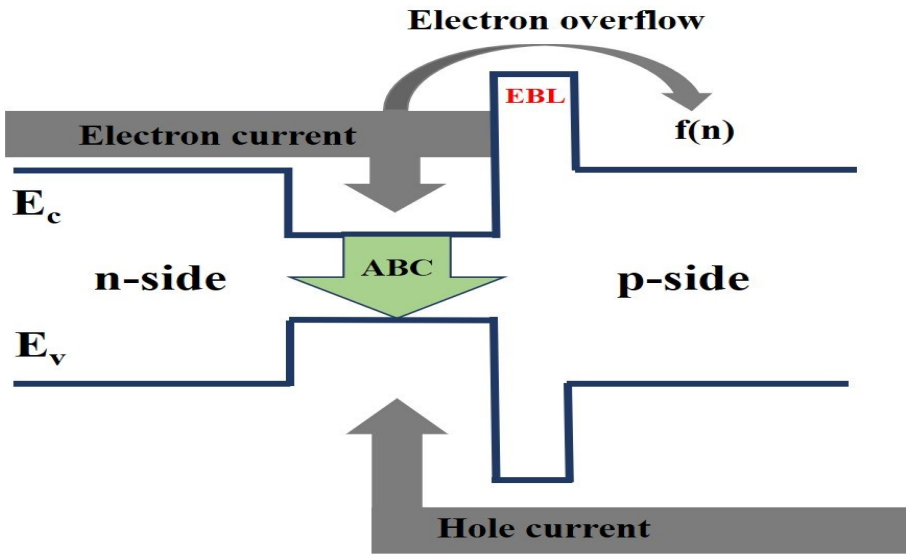

Figure 1.7 Schematic depiction of injected current components into the LED device.

Figure 1.7 shows how the carrier loss mechanism in LEDs under injection current. LED efficiency is ideally 100% when every electron-hole pair injected to the LED device can generate a photon that escapes from the LED. Yet this is a theoretical scenario, excluding the electrical to optical energy conversion which is normally accompanied as losses during the process. The real scenario can be represented by the Equation (1.3).

$$\eta_{EQE} = \eta_{INJ} \, X \, \eta_{IQE} \, X \, \eta_{EXE} \tag{1.3}$$

η_{EQE} is the external quantum efficiency referred to as the ratio of the number of photons emitted from the LED to the number of electrons passing through the device. η_{INJ} is the carrier injection efficiency that is the proportion of electrons passing through the device and injected to the device active region. η_{IQE} is the internal quantum efficiency/ radiative efficiency and is described as the ratio of the photons generated inside the quantum wells (QWs) to the total number of electrons injected into the LED. $\eta_{EXE}$is the optical or extraction efficiency and is defined as the ratio of photons emitted from the LED to the photons generated in the LED quantum wells active region, hence, it counts for the photons lost inside the LED.

1.6.1 Polarization

III-nitride semiconductors exhibit wurtzite crystal structure. These hexagonal structures are defined by the edge length a, height c, and u the anion-cation bond length along the (0001) axis in units of c as shown in Figure 1.2. The Ga-N bond shows large ionicity and hence, it possesses a large piezoelectric polarization component. In addition to the large piezoelectric polarization, the III- nitride semiconductors also exhibit strong spontaneous polarization in the wurtzite phase as shown in Figure 1.4. Piezoelectric polarization is also considered as strain induced polarization which is present due to the displacement of anion sub-lattice based on interface strain.

When compared to spontaneous polarization, piezoelectric polarization plays a more important role in GaN based LEDs. Spatial separation of electron and hole is caused due to the increase in polarization field leading to increase in lattice mismatch. Therefore, radiative carrier recombination efficiency is also reduced. An internal built-in electric field greatly impacts the attributes of the quantum well active regions. Since electron-hole

separation is more dominant in wider wells, as compared to more narrow ones, optical gain and spontaneous emission are smaller in wider wells. A red-shift or a blue-shift may occur as a result of this phenomena.

Polarization field, which plays a crucial role in degrading the performance of nitride-based LEDs arises because of the large lattice mismatch between the substrate and the epitaxial layer. The presence of polarization field, including the spontaneous and strained-induced piezoelectric polarization, spatially separates the electron and hole charge carriers within the quantum wells which is referred to as Quantum-confined Stark effect (QCSE) [75, 76]. The spatial separation of carriers arising from QCSE decreases the radiative recombination, thereby limiting the LED performance.

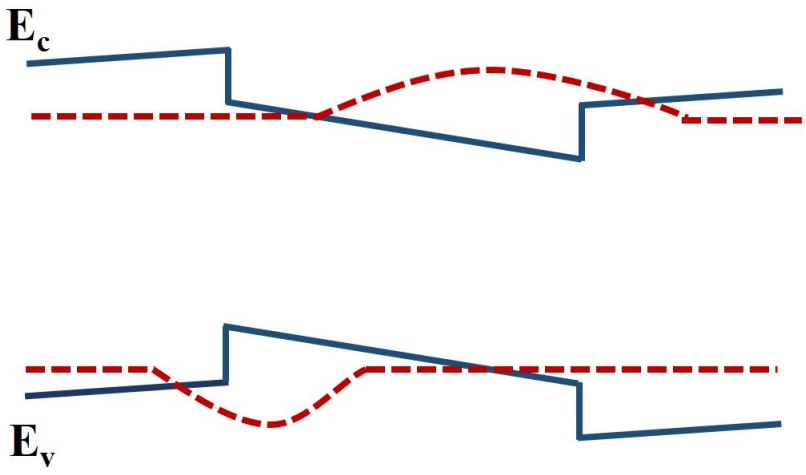

Figure 1.8 Polarization effects on the conduction and valence band edges of a single QW. The electron and hole wavefunction doesn't overlap completely as shown due to shifting.

Figure 1.8 depicts the conduction and valence band edges of a single quantum well when subjected to polarization. The electron and hole wave functions shown in the Figure 1.8 are shifted to the right and left, respectively because of the field. In comparison to the symmetric wave function seen without polarization field, the asymmetric wave function of electron and hole reduces the overlap of confined electrons and holes and subsequently results in a low radiative recombination rate / radiative efficiency [72].

1.6.2 Crystal Defects and Dislocations

InN and GaN have a large lattice mismatch of 11%. There are also a lack of suitable substrates for III-nitride semiconductors. Due to this, the developed LED heterostructures have very large crystalline defect densities. The dislocation density for GaN based heterostructures is typically in the range of 10^8 to 10^{10} cm^{-2} [77-79]. Buffer layers, growth conditions, carrier concentration and type of impurities are factors that determine the defect formation. These defects from intermediate energy levels, and the resultant nonradiative recombination that occur at these intermediary levels are called Shockley-Read-Hall nonradiative recombination. These nonradiative recombination can have an adverse effect on the device efficiency. In InGaN LEDs localized states such as clusters can be formed [80, 81] which are typically advantageous from carrier localization aspect. Nonetheless, these states gets saturated and can lead to efficiency droop at high injection currents [82].

As described by the ABF model, parameter A is related to crystal defects and has an influence to the maximum achievable efficiency. Yet, efficiency droop may also occur depending on the quantum well carrier density or the carrier localization related to the non-uniform indium distribution in the quantum well active regions. Hence, scientists have not been able to precisely determine the role of defects in the efficiency droop if GaN-based

LED, and this topic has been a subject of great interest.

Large lattice mismatches between the III-nitride based material and the substrates such as sapphire, SiC and Si can be accounted to the origin of defect states and dislocations. These defect states in the bandgap act as Shockley–Read–Hall (SRH) non-radiative recombination centers, limiting the performance of GaN LEDs. In effect, SRH non-radiative recombination is enhanced in the presence of surface states and results in the slow rising trend of EQE under electrical injection [83]. The thickness of the epitaxial growth of layers on substrate beyond the critical thickness can account for the dislocations generated in the epi-layers. The dislocations result in defect states in the bandgap and consequently severe degradation in the performance of the GaN LEDs. Therefore, it is crucial to reduce the lattice mismatch of LEDs and minimize the performance degradation in the optical and electrical performance of these devices. Defect density is much more severe in case of planar GaN LEDs due to the lattice mismatch between the epitaxial layer and substrate surface, as well as lattice mismatch between epitaxial layers

1.6.3 Spontaneous Emission

Equation (1.2) shows the relation between spontaneous emission rate and carrier density. It can be seen that the spontaneous emission rate depicted by η_{IQE} is proportional to n^2. This holds true for low injection currents. However, at high injection currents, it shows a non-linear dependency on n. Using this relation, the following graph in Figure 1.9 has been plotted to show this dependency. The resulting IQE values are compared to the cases with constant B parameters. This relationship does not directly affect efficiency droop but lowers the barrier for the non-radiative process to trigger the efficiency reduction.

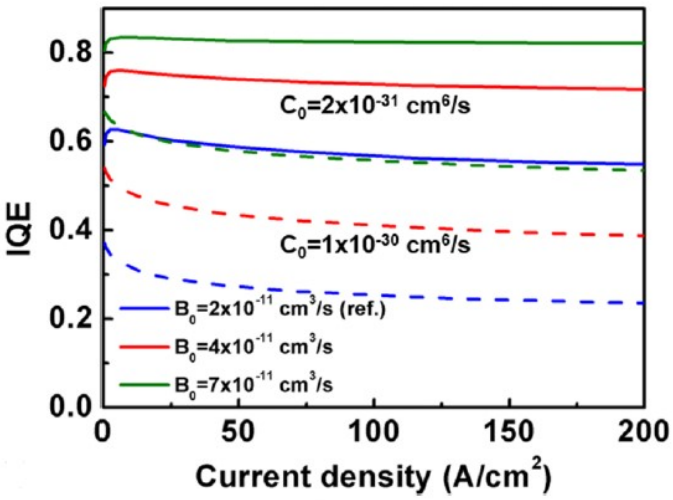

Figure 1.9 IQE curve with different radiative recombination coefficients (B_0) and auger recombination coefficients (C_0).
Source: [84].

1.6.4 Auger Recombination

During the non-radiative electron-hole recombination process, there is production of excess energy. This excess energy is utilized by electrons and holes in the same energy band and are then excited to higher bands themselves. This is referred to as the Auger recombination process. Auger coefficient C is used to describe the probability of the Auger recombination process. Wide bandgap semiconductors generally exhibit a smaller Auger recombination rate, when compared to semiconductors with a narrower bandgap [85]. For GaN (3.4 eV), the expected Auger coefficient C is $10^{-34}cm^6s^{-1}$. Nonetheless, much lower values (in the range of $10^{-30}cm^6s^{-1}$) have been reported for InGaN alloys. With these values, efficiency droop can be explained when assumed that the carrier leakage is nearly zero in the ABF model with A and B values being 10^7 s^{-1} and $2x10^{-11}cm^3s^{-1}$.

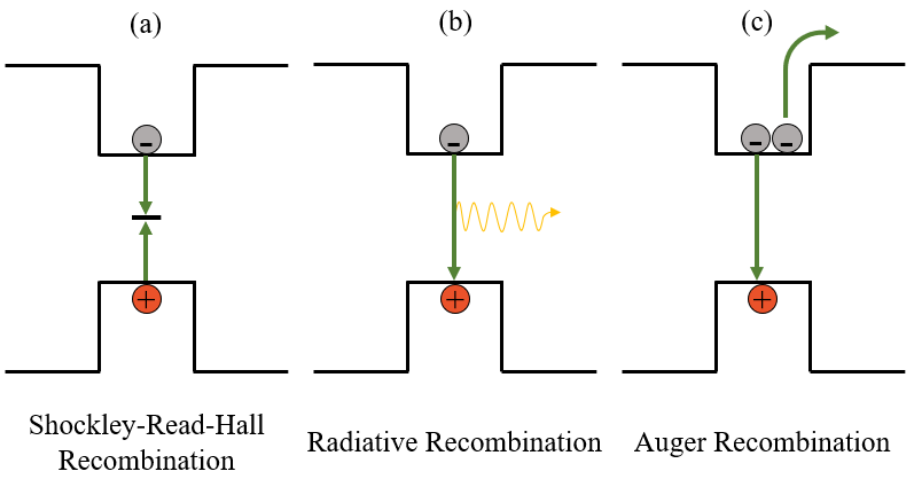

Figure 1.10 Different recombination processes in a semiconductor (a) SRH recombination (b) Radiative recombination and (c) Auger recombination.

Evidently, efficiency droop increases as the Auger coefficient C becomes larger. Auger recombination, illustrated in Figure 1.10 which can be characterized as three-carrier nonradiative recombination process, is primarily responsible for performance degradation of GaN based LEDs at high injection currents. The excess energy released by the recombination of an electron-hole pair is transferred to a third carrier, which can be either an electron or a hole with high kinetic energy, which is then excited to a higher energy state. This in turn contributes to a large efficiency droop observed in GaN LEDs. By thermally releasing the excess energy, third carrier then gradually relaxes to the band edge.

Auger recombination is more dominant at high current densities and highly doped materials [83, 86], since it involves three carriers and is proportional to the third power of carrier concentration. The Auger recombination rate is typically higher for narrow bandgap materials compared to wide bandgap materials such as GaN. Özgür et al. showed that in his works that wide bandgap materials like GaN, have ~50 times smaller Auger recombination rate rather than narrow bandgap materials such as GaAs. Shen et al.

characterized the Auger recombination coefficient for InGaN/GaN quantum well LEDs in the range of ~ 10^{-30} - 10^{-31} cm^6 s^{-1} [49].

In the Auger process as shown in Figure 1.10, an electron and a hole are recombined, and the excess energy released from this process is transferred to another electron. Auger recombination processes are reported to be either direct or indirect [87]. Indirect Auger recombination assisted by phonon and alloy scattering is the dominant factor that cause the large Auger coefficient, which affects the efficiency of nitride-based devices at high currents while direct Auger recombination is typically weak in the same nitride-based devices [87]. Iveland et al. reported that Auger recombination can be accounted for the observed efficiency droop in InGaN/GaN quantum well LEDs [88].

Guo et al. though reported a much smaller value of 10^{-33} cm^6 s^{-1} for the Auger recombination coefficient in InGaN nanowires [89]. Similar to that, a small Auger coefficient was also reported by Nguyen et al. w.r.t the temperature dependent emission characteristics of dot-in-wire white LEDs [83]. These studies strongly suggest that Auger recombination plays a negligible role only on the nanowire LED performance. However, scattering induced indirect Auger recombination is used to explain large efficiency droop rather than direct intraband Auger recombination [87]. Electron-phonon interaction [90], charge defects and alloy induced symmetry reduction are reported as some parameters that assist indirect Auger recombination. Auger recombination coefficient for InGaN alloys can be high as ~ 10^{-31} $cm^6 s^{-1}$ as regards to indirect auger recombination effects [50, 91, 92].

1.6.5 In-homogeneous Carrier Distribution

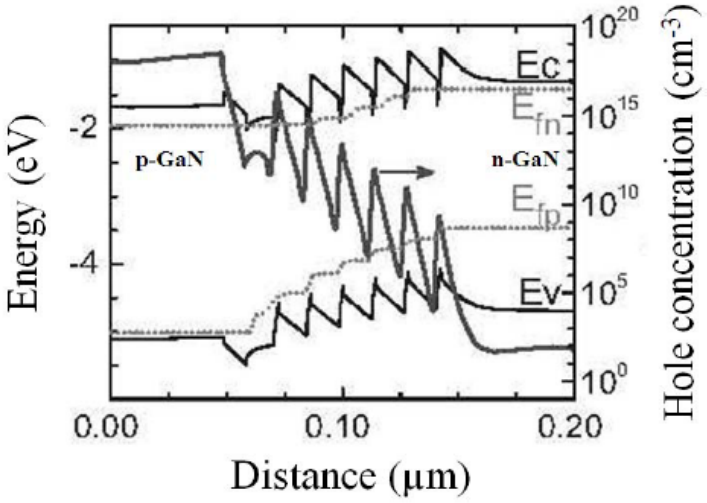

Figure 1.11 Simulated band diagrams and hole concentrations for LEDs with InGaN/GaN MQW LEDs under +6 V forward bias at 300 K .Hole distributions within the QWs are shown by thick solid lines while dashed lines represent quasi-fermi levels.
Source: [93].

Holes have high effective mass and hence low mobility. Due to this, the hole mobility in LED active regions may be inefficient. Therefore, injected holes are majorly located close to the *p*-doped GaN layer and this concentration tapers off as it approaches the *n*-type side. The simulated band diagrams and hole concentrations for InGaN/GaN based MQW LEDs are illustrated in Figure 1.11.

On the contrary, electrons have a more uniform carrier distribution throughout the device. This leads to highly inhomogeneous carrier distribution throughout the LED device active region. The hole density reduces steeply from *p*-GaN to *n*-GaN, resulting in non-uniform hole distribution in the MQWs. This issue can be addressed by reducing the barrier thickness. This would allow hole injection to occur more freely, therefore, reducing electron leakage. This would also lead to significantly augmented Auger recombination and increase in electron overflow, further limiting the optical emission efficiency at high

injection levels. *P*-doped active region, barrier thickness variation [93] and addition of a thin InGaN barrier next to p-GaN region [94] have been used as solutions to improve the performance of conventional InGaN/GaN QWs.

1.6.6 Electron Overflow

The aforementioned factors mentioned in the earlier sections include internal factors that affect efficiency. Electron overflow is however an external phenomenon and can result because of numerous possible situations. The band energy tilts because of the polarization fields, reducing carrier recombination. Nonuniform carrier concentration can also cause a polarization field to occur which leads to electron leakage out of the LED active region, which then can recombine with holes in the *p*-GaN region before they can reach the active region. Reduction in energy barrier due to the built-in polarization field is one of the main reasons for electron overflow. The presence of a polarization field causes the band gap to be tilted downward near the *p*-GaN region. This problem generally occurs in Ga-polar III-nitride LEDs. To tackle this issue, electron blocking layer (EBL) is utilized between last quantum well and the *p*-GaN region, often made up of AlGaN due to its high band gap, thus increasing the barrier height for electrons in active region [95]. Yet, an EBL cannot completely rectify electron overflow, and efficiency droop can still occur.

The GaN LED performance is limited by the poor hole injection caused by the heavy effective mass, and subsequent poor mobility of holes. While the electron distribution is rather uniform across the entire active region, the injected holes largely reside in the small region close to the *p*-GaN region. The highly non-uniform distribution of charge carriers leads to a significant enhancement in electron overflow, and subsequent efficiency droop at high injection levels. The presence of the polarization field could tilt

the band-edge and effectively reduce the barrier height for electrons, which results in electron overflow, and thus lowers the performance of the LED. These overflowed electrons can recombine with the holes in the *p*-GaN region, reduce the radiative recombination rate, and thus can degrade the LED performance. The non-uniform carrier distribution in the active region of the GaN LEDs is another significant mechanism which constraints the GaN LED performance. The poor hole mobility results in non-uniform carrier distribution in the active region of the GaN LEDs. The non-uniform carrier distribution in active region of the GaN LEDs reduces the radiative recombination rate and thus in overall promotes electron overflow.

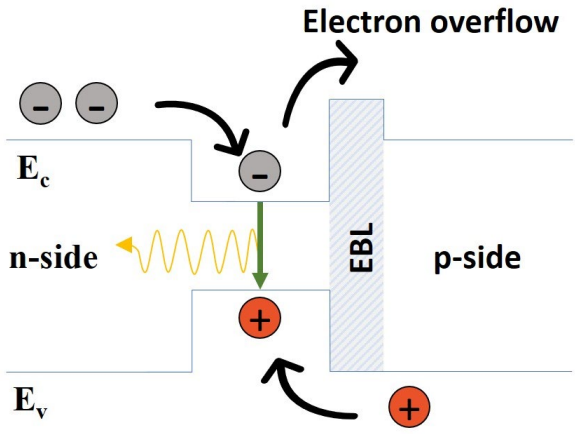

Figure 1.12 Electron overflow mechanism in the LED structure which depicts some overflowing electrons with enough energy out of the active region without recombining with holes.

Figure 1.12 depicts the electron overflow mechanism happening in the LED structure. The electrons and holes-charge carriers injected into the device can recombine in the active region. However, some electrons having sufficient energy can surmount the barrier and flow out of the active region without recombining with holes. The electron

overflow has been reduced by implementing an EBL in the *p*-side of the LED. A wide bandgap AlGaN layer can be typically inserted between the active region and the *p*-side in the GaN LEDs to prevent the electrons from overflowing out of the active region. Nonetheless, the EBL could reduce the hole injection efficiency depending on the band offset. Nguyen et al. reported that by employing a *p*-doped AlGaN electron blocking layer in nanowire structures, electron overflow could be largely suppressed [96].

1.7 Dissertation Overview

In this dissertation, the optical and electrical characteristics of nanowire-based light sources -especially in the visible and UV regime and the dye sensitized solar cell (DSSC) potential for Zinc oxide graphene (ZnO-G) and nickel-zinc oxide (Ni-ZnO) composites have been intensely studied. We have investigated several methods such as nanowire-based LEDs and approaches like flip chip nanowire-based LEDs to enhance the EQE of GaN based LEDs. Such claims have been supported by simulation and experimental results. We have further reported on the demonstration of full color tuning by controlling the *In* and *Ga* flux ratio in the quantum wells. Further, we reported phosphor-free white nanowire LEDs with improved LEE. Moreover, we have shown that the LEE of GaN LEDs can be significantly enhanced by integrating with nanowire arrays. The light extraction involves two successive steps, including the coupling from the light source to the tube and the subsequent emission from the tube to the air. We have enhanced the light extraction efficiency of deep UV LEDs using periodic array of nanowires. The emission of the guided modes could be inhibited and redirected into radiated modes utilizing nanowire structures. By polyol method we developed ZnO composites within our research.

Chapter 1 gives an overview about the advantages of GaN based structures, current problems of III-nitride structures and presents a compilation on the current status of the III-nitride based device structures.

Chapter 2 presents an overview of the MBE growth, device fabrication and characterization methods utilized for the GaN based LEDs. Finite difference time domain was employed to determine the LEE, specifically the software FDTD Lumericals. A nanowire structure can be utilized to inhibit the emission of the guided modes and redirect trapped light into radiated modes. We have investigated the LEE of LEDs using three-dimensional (3D) finite difference time domain method. We have studied the dependence of light extraction efficiency with nanowire structural parameters such as the nanowire size and density and the *p*-GaN thickness, which play an important role on the light extraction efficiency. We have further investigated the effect of device sizes, as well as the random variation in the nanowire diameter and spacing on the light extraction efficiency. It is observed that an unprecedentedly large light extraction efficiency can be achieved.

Chapter 3 presents the topic of controlling color emission of nanowire LEDs. This can be achieved by controlling the In/Ga flux ratio in active region or by altering nanowire packing density. This in turn results in a range of optoelectronic devices emitting light in a broad range spanning from deep UV to near IR. We have demonstrated highly stable, phosphor-free white light emission.

Chapter 4 presents the potential of GaN based nanowire LEDs when compared to thin film LEDs, on account of their reduced QCSE for visible light communication (VLC). The reduced strain resulting from nanowire relaxation results in a higher bandwidth for VLC when compared to the conventional thin film based III-nitride system.

In Chapter 5, nanowire LEDs on flexible metal substrates are introduced. The arrangement and optimization of the nanowire structure followed by fabrication and flip chip nanowire design on copper contributed to a higher LEE in comparison to a typical nanowire structure.

Chapter 6 introduces the MBE growth and simulation studies based on ultraviolet based AlGaN nanowire LEDs. Specifically, UV-B LEDs having immense potential in the biomedical industry have been demonstrated. Chapter 6 also illustrates the effect of optical absorption and the need for new alternate designs respective to AlGaN based UV LED.

Chapter 7 and 8 introduces polyol based ZnO-G and Ni-ZnO composites, respectively and their potential for dye sensitized solar cell. The highly porous ZnO based composites displayed a higher efficiency than the bare ZnO counterpart.

Chapter 9 lists the future work we plan to do. Micro LEDs for micro displays, ZnO nanowire LEDs by hydrothermal growth on silicon and transparent substrates including FTO, ITO and flexible substrate- paper and the potential of III-nitride based LEDs for VLC, are briefly mentioned.

CHAPTER 2

DESIGN, EPITAXIAL GROWTH, FABRICATION AND DEVICE CHARACTERIZATION

The research objective is to fabricate novel nanowire LEDs with high output power and reduced efficiency droop. To achieve these high performance nanowire LEDs, it requires careful design, epitaxial growth and device fabrication. In this chapter, the nanowire LED growth mechanism, fabrication process, and characterization principles are explained.

2.1 Finite Difference Time Domain Method (FDTD)

FDTD is a simple full-wave technique often employed to solve electromagnetics problems. FDTD which is thus a numerical analysis technique used for modeling computational electrodynamics (by calculating the approximate solutions to set of differential equations), is normally used as a time-domain method. This aids us in finding the solutions for EM wavelength scenario, that can cover a broad frequency range with a single simulation run and treat nonlinear material properties. *Via* a set of simulations in Finite Difference Time Domain (FDTD) Lumericals software, the device structure with the maximum LEE or optimum nanowire array arrangement decision can be made. This helps in attaining the best structure out of nanowires with minimum production cost. FDTD Lumerical software package, used in design aspect gives the user the flexibility to recreate a photonics environment that would closely resemble the fabricated LED performance. Device performance is often quantified in terms of externally emitted power, P_{out}. The other two parameters that's used to study device performance includes wall plug efficiency (WPE) *i.e.,* the ratio of electrical input power to optical output power, and the external quantum

efficiency (EQE or η_{extr}) which is the ratio of number of electrically injected carriers to externally observed photons.

The conventional ray tracing calculation method is the commonly used approach in designing phase of optics when the feature size is much higher than the simulated wavelength of optical rays. But, when simulated objects dimensions are in the range of micron or nanoscale, the optical components will interact with the light by lot of mechanisms such as scattering, absorption and polarization effects, where optical rays are to be considered as electromagnetic waves. This makes the traditional method of tracing of optical rays invalid at submicron scale and paving the way for FDTD. Besides FDTD [97], the other common methods used for optical device analysis includes Finite Element Method and Beam Propagation Method.

FDTD calculates the solutions for Maxwell's equations for specific boundary conditions inside the complex geometries. When compared to approximate solutions like traditional ray tracing method, Maxwell's differential equations are solved by the FDTD method to obtain accurate solutions for the propagation of EM waves. FDTD algorithms can compute Maxwell's equations in a time-domain, thus paving the way for the calculation to fully cover the frequency range by Fourier transformation. The Maxwell's curl equations in differential forms for a linear isotropic material in a source free region are mentioned as follows in Equations (2.1) and (2.2).

$$\frac{\partial \mathrm{H}}{\partial \mathrm{t}} = -\frac{1}{\mu(\mathrm{r})} \nabla \mathrm{X}\, \mathrm{E} \tag{2.1}$$

$$\frac{\partial \mathrm{E}}{\partial \mathrm{t}} = \frac{1}{\varepsilon(\mathrm{r})} \nabla \mathrm{X}\, \mathrm{H} \tag{2.2}$$

In aforesaid equations, ε(r) and μ(r) represents the position dependent parameters - permittivity and permeability of the material. In two-dimension scenario, the fields are resolved into two transversely polarized modes referred to as the TM and TE modes. In space and time domain, the preceding equations are discretized using Yee algorithm principles [98]. In these equations $\vec{E}$, $\vec{H}$, μ, ε and σ represents the electric field, magnetic fields. medium permeability, medium permittivity and medium conductivity, respectively.

By computing the ratio of total extracted light power to the total power emitted from active region of LEDs, the LEE can be calculated with the use of monitors. Extracted power from LED emission surface can be computed by integrating the Poynting vectors over far field projection surface. In the simulation, total power emitted from active region were calculated by surrounding the dipole with a box of power monitors to record the net outflowing power through integrating Poynting vectors in the near field of dipole source. In general, for the FDTD approach, we launch into the active region an adequately broadband and modulated Gaussian pulse or dipole source. The detectors placed around calculates the time varying electric and magnetic field. *Via* Fast Fourier Transform (FFT) of the fields computations in FDTD, the Poynting vector over the detectors is integrated and power transmission spectra are calculated. Thus, by making use of FDTD, nanowire LED structure can be optimized to have the maximum LEE. Within one simulation run, the FDTD approach could work out the resonance spectrum over a wide range of frequency.

2.2 III-Nitride Nanowire Growth Mechanisms

Most common techniques used in III-nitride nanowire fabrication are dry etching [99-101], direct reaction between Ga and NH_3 [102, 103], molecular beam epitaxy [104-106], chemical vapor deposition [107], hydride vapor phase epitaxy [108] and chemical beam

epitaxy [109] etc. These techniques are classified into two approaches including top-down and bottom-up. The fabrication of nanowires via top-down approach is related to the utilization of dry etching, wet chemical etching or reactive ion beam etching fabrication methods. However, the structural quality of such fabricated nanowires depends on etching method employed, induced defects while etching and dislocations present in the material bulk. By controlling the growth conditions, virtually dislocation free nanowires with atomic perfection in both lateral and growth directions can be grown *via* bottom-up approach methods. The epitaxial growth of nanowire structures include the following growth techniques: Vapour-liquid-solid (VLS) phase epitaxy, selective area growth (SAG) and spontaneous growth of nanowires under nitrogen rich conditions. The growth mechanisms of these processes are described below.

2.2.1 Vapour-Liquid-Solid Growth

Wagner and Ellis introduced the VLS mechanism of nanowire growth in 1964 [110]. In VLS growth mechanism, Au, Ni, or Fe -metal particle serves as catalyst and aids in nanowire formation [111]. The growth process comprises of three main steps: I) the deposition of metal alloys and matrices, followed by the formation of liquid droplets on the substrate surface, II) crystal nucleation, and III) axial growth of nanowires, where the vapor reaches supersaturation with respect to the solid phase.

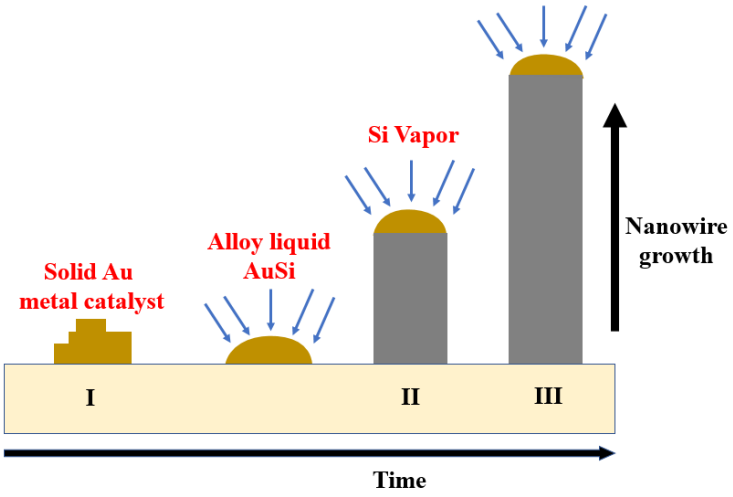

Figure 2.1 VLS growth process depiction: I) semiconductor in vapor phase is introduced into the system with metal catalyst on the substrate surface, II) the formation of liquid droplets on the substrate surface near or above the eutectic temperature, and III) supersaturation and the formation of nucleation sites and the nanowire axial growth.

The low solubility of metal particles in growing semiconductor structures leads to a low melting temperature (eutectic point) in the alloy phase diagram, thus resulting in a VLS growth at temperatures of around or higher than the eutectic melting temperature. The. position and size of the metal particles and other growth parameters such as temperature and pressure define the position and diameter of nanowires grown by the VLS method. Growth rate and time determines the nanowire length.

The growth rate relies on vapor supersaturation, which is impacted by the source concentration and substrate temperature. The growth kinetics influence the morphological configuration, nanowire orientation and other structural properties [112]. As commonly observed in the growth of III-V and group IV nanowires, growth along the <111> crystal orientation is generally preferred because of the reduction of the surface energy on the exposed sidewall facets [113]. Nanowires with catalyst size less than 10 nm along the

<001> direction have also been reported [114]. VLS technique grown III-nitride nanowires has been reported by techniques using a low pressure metal-organic vapour phase epitaxy [115], quartz tube furnace [116] and thermal chemical vapour deposition [117]. Highly uniform and vertically aligned GaN nanowires on c-Al_2O_3 substrates has been reported by Kang et al. by thermal CVD method using Ni catalysts [118]. Other substrates such as silicon, GaAs and GaP are often used for III-nitride nanowire growth [115].

In nanowire growth assisted by metal catalyst, the metal catalyst generally remains on the tip of nanowires after growth and can be subsequently removed. But metal catalyst atoms during the growth stage can diffuse into semiconductor nanowires and thus may introduce impurities in the nanowires [119, 120]. These latter impurities can cause deep level trap states in the nanowire semiconductors and can lead to a reduced minority carrier lifetime. Thus, in overall, the emission efficiency or carrier collection will be reduced, thus degrading nanowire device performance [121, 122]. Figure 2.2 illustrates the VLS growth mechanism.

2.2.2 Spontaneous Formation

Under nitrogen rich conditions, III-nitride nanowires can be formed spontaneously without the use of any foreign metal catalysts [123, 124]. Since foreign metal catalyst is not used in this technique, catalyst droplet at the top of nanowires is not observed [125]. Molecular beam epitaxy method is typically used for the spontaneous or self-organized growth of III-nitride nanowires. The mechanism of the self-organization or spontaneous formation of InN and GaN nanowire heterostructures is still under ambiguity. A self-catalytic growth process wherein Ga and In droplets can serve as catalysts to assist the nanowire formation, is suggested as the reason behind the spontaneous formation of InN or GaN nanowires

[104, 105, 126]. However, Ga (or In) droplets at the tip or sidewall of the nanowires is not found present during the experimental observation [123-125, 127]. Figure 2.2 shows the schematic of III-nitride nanowire growth by MBE.

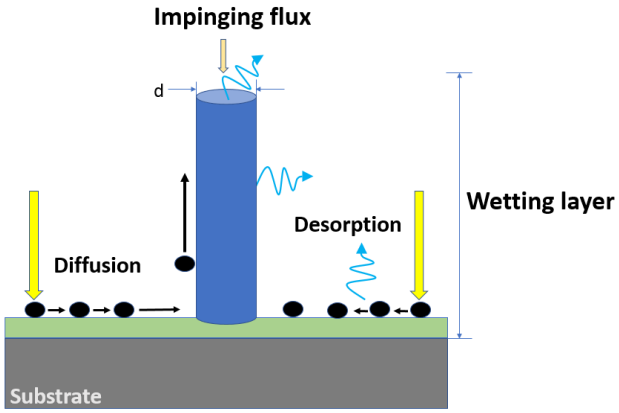

Figure 2.2 Schematic of spontaneous growth of III-nitride nanowires by MBE including adatom absorption, desorption, diffusion, and nucleation processes.

Thus, the diffusion-induced growth has been implied as the main driving factor behind the III-nitride spontaneous formation by MBE [106]. In this proposed model, the differences in sticking coefficients, surface energies and diffusion coefficients on various crystal planes is reported to be driving force / initiative behind the nanowire growth. Since the top surface has a lower chemical potential, adatoms diffuse from the nanowire sidewall to the top. Moreover, nanowire tip has a higher sticking coefficient than that on the nanowire sidewalls. These factors lead to Ga adatoms which are directly impinging on or within a surface diffusion length of the nanowire tip to be incorporated on the nanowire tip, thus leading to the axial nanowire growth.

Proposed diffusion-induced mechanism still holds steady, with the fact that nanowire axial growth rate increases rapidly with the increase in substrate temperature,

because of the considerable enlarged surface migration of adatoms [106, 123]. Such self-organized III-nitride nanowires typically display superior crystalline quality and uniformity, which makes them a prominent candidate for optoelectronic devices.

2.2.3 Selective Area Growth

This approach involves the nanowire growth on pre-patterned substrates. Selective area growth masks, such as SiO_2, Ti, Au and Al are typically used [63, 64, 128-130]. Nanowire position, size, and aspect ratio can be controlled precisely to an extent with selective area growth method. The SAE technique offers better control while growing materials with controlled emission wavelengths. In SAE method, nanowire growth is predominantly determined by adatom migration, adsorption, and desorption on the exposed substrate surface as well as the masked region, which can be regulated by changing growth parameters such as substrate temperature and III/V flux ratios.

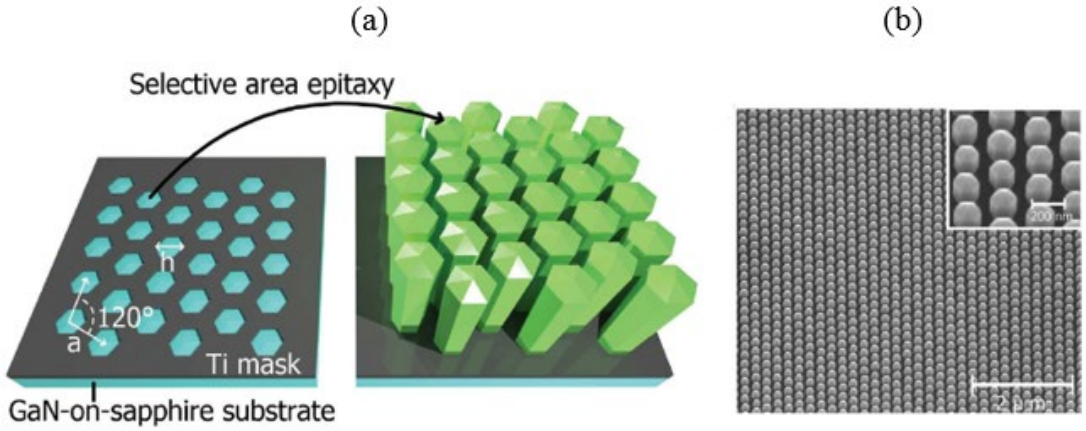

Figure 2.3 (a) Nanoscale arrays developed by e-beam lithography process on a Ti mask on planar GaN template on c -plane sapphire substrate. (b) SEM image showing GaN nanowire arrays selectively grown in the opening apertures.
Source: [131]

Desired nanowire structures can be obtained by designing masks of specific size and position of the patterns on the mask. Effects associated with the profile of the nanoscale masks, the anisotropic lateral overgrowth, and faceting should be considered though in SAE approach growth of nanowires. *Via* metal-organic chemical vapour deposition through a selective growth mask, high-quality and uniform GaN nanowires with precisely controlled positions and diameters can be grown [63]. By employing a set of nanohole arrays arranged in a triangular lattice, which was fabricated on a Ti (5 nm) film by focused-ion-beam etching, highly uniform GaN nanocolumns can be grown as well [64]. Figure 2.3 depicts the scanning electron microscopy images of highly uniform diameter GaN nanoarrays grown by SAE approach.

2.3 Plasma Assisted Molecular Beam Epitaxy (PAMBE) System

Currently, MBE and MOCVD are the two commonly used techniques for growing high quality III-Nitride optoelectronic materials. In general, due to the lack of efficient nitrogen sources in the MBE growth, MOCVD is typically used for large scale commercial production of LEDs and LDs. But MBE approach when compared to the MOCVD offers several unique advantages such as better interface control and suitability for exploring new material structures for realizing high quality crystalline materials. MBE can also provide the highest control for the nanostructure epitaxial growth.

In contrast to MOCVD, MBE offers several attributes including a slow deposition rate (typically less than 1000 nm/hr) and an ultra-high vacuum environment (~10^{-8} to 10^{-10} Pa), which will be extremely useful to minimize the epitaxial layer impurity incorporation. High indium content InGaN structures can be realized with MBE, due to the fact that much

lower growth temperature is possible in MBE w.r.t that of MOCVD, thus providing an enhanced indium incorporation. Composition and thickness of the grown epilayer can be precisely controlled to a mono-atomic layer level by MBE method. The supplementary in-situ monitoring capability adds further value to MBE thus aiding researchers to manage the growth quality and to develop novel materials. Figure 2.4 shows the Veeco Gen-II MBE system in New Jersey Institute of Technology (NJIT).

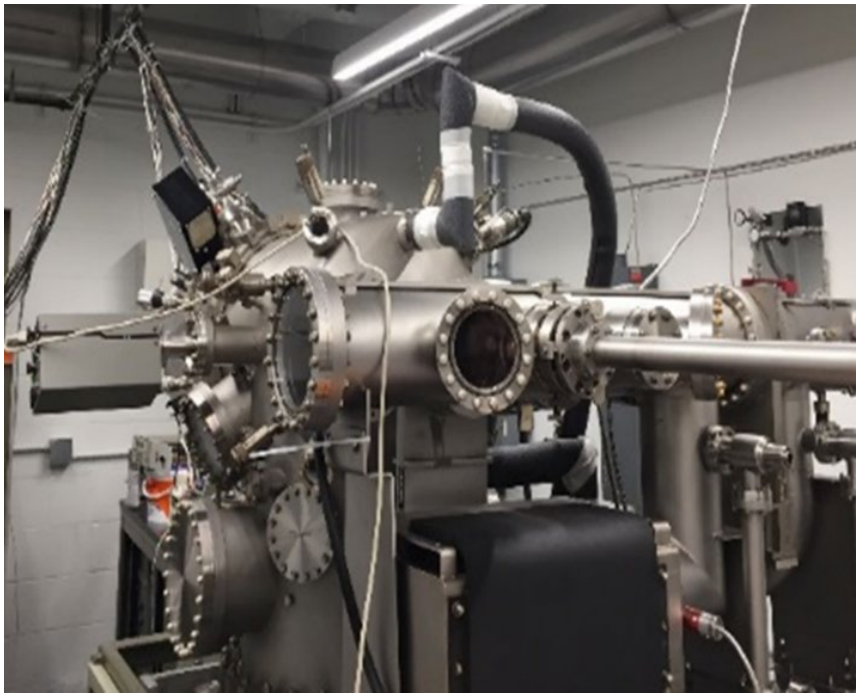

Figure 2.4 Veeco Gen-II MBE system with radio frequency plasma assisted nitrogen source in Nano Optoelectronic Materials & Devices Laboratory at NJIT.

The III-nitride MBE growth processes are mainly divided into two classes -either based on nitrogen sources such as ammonia-molecular beam epitaxy (Am-MBE) and plasma-assisted molecular beam epitaxy (PAMBE), respectively. In an Am-MBE system and PAMBE system, ammonia (NH_3) gas and high purity N_2 gas are used as group V

sources/elements, respectively. The high thermal stability of N_2 molecule makes us use a high energy source such as radio frequency (RF) plasma to often break the N_2 and create atomic N. Both MBE techniques use solid group III sources such as In, Ga, and Al. In an Am-MBE system, the NH_3 breaking efficiency is contingent upon the growth temperature. Since the efficiency values are considerably low in such Am-MBE systems, the growth requires a large amount of NH_3. Furthermore, there also exists the adverse aftereffect that the undecomposed remaining NH_3 during growth can react with the chamber and effusion cell materials at high temperature. This resulting corrosive problem and chamber cleaning created big issues with Am-MBE growth method.

A plasma source of high purity inert N_2 gas is used to supply the group V element in the case of PAMBE systems. The active nitrogen plasma generated includes a species of ionized molecules (N_2^+), atoms (N), and ionized atoms (N^+), which are then introduced into the growth chamber during In(Ga)N deposition. By tuning the nitrogen flow rate and the plasma power (the maximum power is typically of order of ~ 500 W), amount of active nitrogen plasma can be well adjusted in PAMBE. Hence RF-plasma assisted MBE growth technique is considered much more efficient and preferable compared to the Am-MBE systems.

In our lab, Veeco Gen II MBE system equipped with a RF plasma-assisted nitrogen source was used to grow the III-nitride nanowire heterostructures. MBE system typically consists of three main vacuum chambers referred to as an intro-chamber, a buffer chamber, and a growth chamber. The load-lock introduction chamber used to load samples into ultra-high vacuum environment ensures that the pressure in other chambers are not influenced.

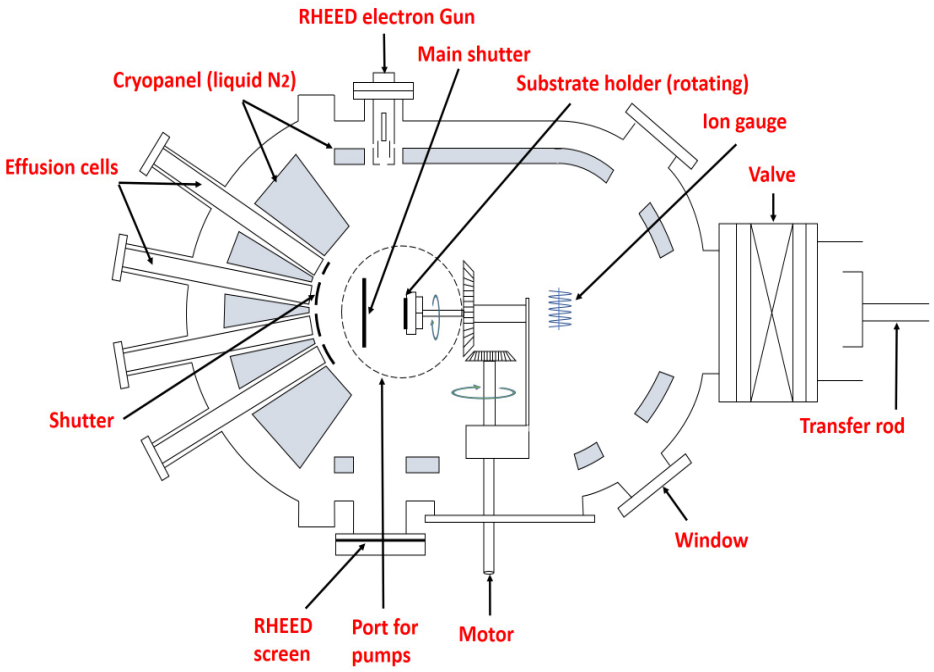

Figure 2.5 MBE growth chamber schematic.

Temperature of substrate is controlled by means of Eurotherm. Bakeout, which is referred to as heating the MBE system up to 170^0 C for at least one day, ensures water vapor that has accumulated at the chamber walls is desorbed. Generally, standard cleaning techniques like hydrogen fluoride (HF) acid treatment or RCA 25 technique is used for the initial cleaning of Si substrate wafer. Next stage involves the loading of latter substrates into the intro-chamber, followed by degassing at ~ 200 °C before finally being transferred to the buffer chamber. Preparation and storage of samples are mainly done in the buffer chamber of MBE. Before being transferred into the growth chamber which requires a very clean and high purity environment, a second degassing process of samples is performed in the buffer chamber. Knudsen / Effusion cells which houses the group III elements needed for deposition onto the substrate, can be thermally evaporated by heating the Knudsen cells. A purity of at least 99.9999% or 6N is used to charge the cells.

Eurotherm PID controllers regulate the cell temperature. The impinging of group III atoms onto the heated sample surface and reaction with the active nitrogen species ensures that In(Ga)N materials are formed. By varying the group III effusion cell temperature, group III fluxes can be controlled. In order to avoid cracks in the pyrolitic boron nitride (PBN) crucible due to frequent solidification of the materials arising from various thermal expansion coefficients, the standby temperatures have to be kept well above the melting points of the materials, 660.3^0 C for Al, 156.6^0 C for In and 29.76^0 C for Ga. Figure 2.5 shows the schematic of the parts housed inside the MBE growth chamber.

Parameters such as the control of the wire uniformity, diameter, height, shape, density and orientation / alignment of the nanowires as well as the elimination of stacking faults and other defects are some of the main challenges while nanowire growth mechanisms. To address the prior issues, growth parameters including substrate temperature, III/V fluxes, and growth rate can be carefully optimized and tuned accordingly. For example, by decreasing the growth temperature higher density nanowire arrays can be realized while a higher temperature growth can result in reduction of nanowire density. This is explained by the fact that adatom surface migration is enhanced at high temperatures [132]. Moreover, an increase in nanowire density can be obtained by increasing the growth rate. Nanowire size predominantly depends on the size of the metal catalyst used in the case of VLS growth method, or the size of the patterned area in the SAE approach. Nanowire alignment is strongly influenced by the substrate orientation. Because of the reduction of surface energy of the exposed sidewall facet during growth process, the <111> growth direction is commonly preferred over <001> direction during the III-N and group IV nanowires growth [113].

To ensure growth and high crystalline quality of material systems, MBE is generally equipped with a reflection high energy electron diffraction (RHEED) system. This in-situ monitoring within the ultra-high vacuum MBE system enables the user to study the surface properties and the quality of nanowire structures easily. In RHEED system, the generated beam of electrons from an electron gun, impinges in a very small angle on to the sample surface. Regular patterns on phosphorous detector screen can be observed because of the interaction between electrons and atoms on the sample surface. RHEED pattern reveals the sample surface properties. In addition, the in-situ oxide desorption of the substrate surface can be inferred from the RHEED pattern.

During the growth of nanowires, RHEED screen displays a spotty pattern (an array of dots). Meaningful information regarding nanowires such as size, shape, orientation and density can be obtained from the size, shape and density of the dots displayed on the RHEED screen. An array of tightly spaced small dots on the RHEED screen implies small diameters and high densities for the grown nanowires. A contradiction of the preceding is that an array of well-spaced, large dots on the RHEED screen refers to the growth formation of low density and thick nanowires. Generally, before any nitrogen species is introduced when the growth starts with a few monolayers of In or Ga seeding layer, the RHEED pattern shows a bright array of circular dots. The dot arrays are still bright during the beginning of nanowire growth. With the subsequent growth of nanowires, the dot arrays while maintaining the dot shape will turn significantly dimmer.

The dimmer RHEED patterns observed with nanowire growth continuation can be interpreted to the nonuniformity in nanowire heights, thus resulting in destructive interference as electrons are being deflected off the wire structures in alternate paths. The shape of the dots observed on RHEED pattern provides a measure of the nanowire

orientation. For example, circular dots refer to nanowires that are grown perpendicular to the substrate while elliptical dots present in the RHEED pattern suggests that nanowires are tilted and oriented in multiple directions.

2.3.1 Growth Modes in Molecular Beam Epitaxy

In MBE, III-nitride growth takes place either layer by layer (Frank-van der Merwe), in form of islands (Volmer-Weber) or a mixture of both (Stranski-Krastanov growth).

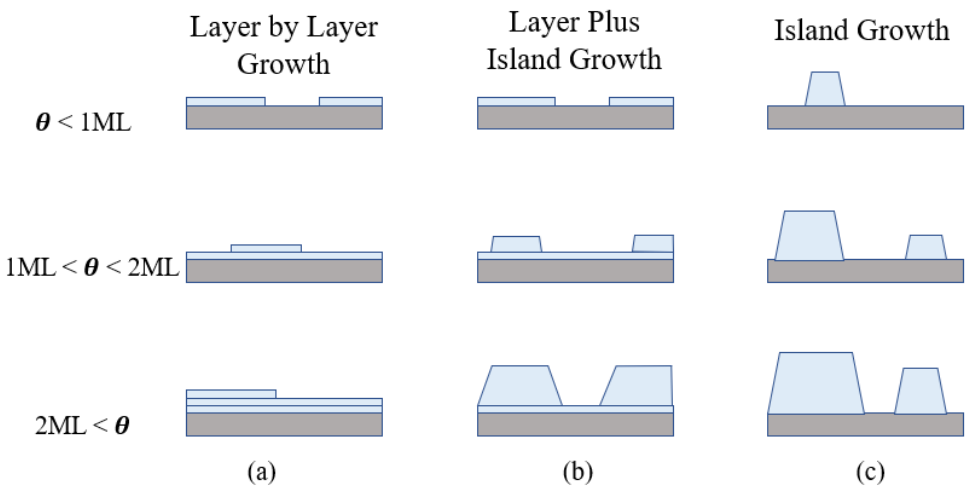

Figure 2.6 Schematic representation of different growth modes for film formation in MBE for multiple coverage (θ) regimes (ML refers to monolayer) (a) layer by layer or Frank-von der Merwe mode (b) Layer plus island growth or Stranski -Krastanov growth mode and (c) Island growth or Vollmer-Weber growth mode.

Figure 2.6 shows the schematic of different growth modes. Volmer–Weber (VW) growth mode refers to the formation of formation of three-dimensional adatom clusters or islands, where adatom–adatom interactions are stronger than those of the adatom with the surface. In such VW growth mode, the coarsening will cause rough multi-layer films to grow on the substrate surface. When the atoms are more attracted to each other than to the substrate, island growth is preferred from the start. The strain in thinner epilayer that results

due to the lattice mismatch between the substrate and the layer, can lead to islanding. The growth rate is also a significant parameter on the surface island formation. For high growth rates there is a higher probability for islands to be formed, due to the increased number of atoms diffusing about on the surface. An island diffuses a lot slower than a single atom or molecule and thus layer by layer growth is less likely.

In Frank–van der Merwe (FM) growth, atomically smooth layers are fully formed due to the fact that adatoms attach preferentially to surface sites. If the atoms or molecules are more strongly bound to substrate than to each other, the initial atoms form a complete monolayer. The subsequent layers are less tightly bound, but if the decrease in binding is monotonic towards the bulk value, layer by layer growth is obtained. This growth mode is two-dimensional, thus leading to complete films form prior to growth of subsequent layers.

Stranski–Krastanov growth is an intermediary process, which can be referred to as a combination of both 2D layer and 3D island growth. The layer-by-layer to island-based growth transition takes place at a critical layer thickness which is mainly dependent on the chemical and physical properties including surface energies and lattice parameters of the film and substrate.

Preference of these growth modes depends on parameters like substrate temperature, interaction strength between adatoms in the growing layer and the substrate surface, strain in the grown layer and growth rate. Increase in substrate temperature enhances the probability for an atom to cross the Schwobel-barrier, but at the same time inter-diffusion increases. Thus, growth parameter has to be carefully optimized.

2.3.2 Morphology and Growth Parameters in GaN Growth

GaN nanowire morphology is highly dependent on the combination of three growth parameters including gallium flux (Φ_{Ga}), nitrogen flux (Φ_N) and substrate temperature (T_{sub}). A lower III-V ratio results in preferentially nanowire growth. However, an increase in III-V ratio leads to coalescence of nanowires or a compact morphology. The increase in substrate temperature leads to a higher Ga desorption and a lower effective III-V ratio. As well as an increase in the growth rate due to the diffusion along the nanowire sidewalls. But no growth occurs due to Ga desorption at high Tsub.

Figure 2.7 represents the qualitative phase diagram for GaN growth by PAMBE [133]. N-rich samples display a rough morphology while in Ga-rich conditions the layer is compact although still exhibiting defects due to dislocations, that form at the interface. The increase in Φ_{Ga} can result in a reduction of these pits but an excess may cause formation of Ga droplets. III-V ratio surface morphology is explained by terms of surface diffusivity. In GaN grown on Si (111) by MBE which exhibits Ga polar surfaces, there is considerable difference in surface diffusivity of adatoms based on the surface termination [134]. Ga and N terminated surfaces have one and three dangling bonds per atom, respectively. This results in a higher mobility of adatoms for a Ga-terminated surface (or Ga-polar films). This also results in N-rich and Ga-rich grown condition samples to have a have a rough and smooth morphology, respectively. Ga which can act as an auto surfactant is reported to increase the surface mobility thus promoting 2D growth. This is supposed to be the reason behind improvement in smooth surface morphology with increasing Φ_{Ga}. The dependence of Ga flux and temperature of the substrate on morphology of the fabricated structures is illustrated in Figure 2.7.

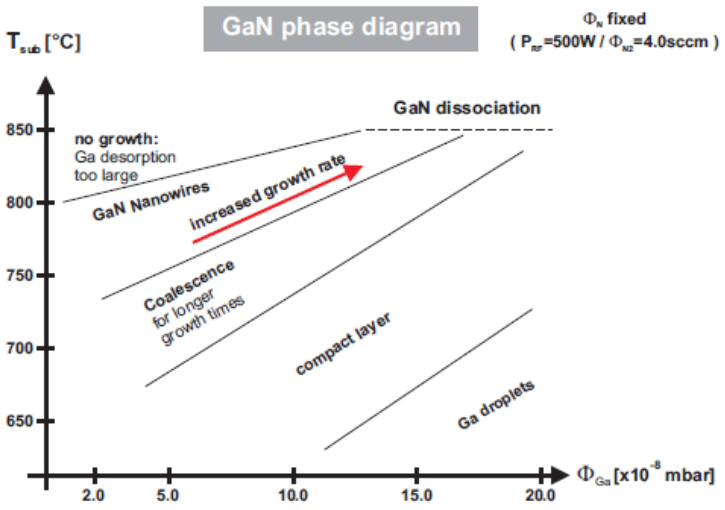

Figure 2.7 Qualitative phase diagram for GaN growth by PAMBE as functions of Φ_{Ga} and T_{sub} at fixed plasma conditions.
Source: [133].

Columnar structures with a small diameter in the nanometer range GaN layers are grown under highly nitrogen-rich conditions *i.e.,* with a low III/V ratio (Ga/N ≪ 1). Because of the high lattice mismatch between Si (111) and AlN, even though if we use a 100 nm buffer layer not all the strain can be relieved. This in turn results in straining of top GaN layer and can leads to the island growth. The reduced surface diffusivity resulting from N-rich growth conditions can prevent quick coalescence of the islands and columns. GaN samples grown directly on Si (111) has a high lattice mismatch of -16.9 % (tensile) and thus has a low critical thickness (value up to which GaN can grow pseudomorph on Si). thus, preferring Volmer-Weber growth or islands formation. Calleja et al. proposed a self-catalyzed VLS mechanism to explain the limited surface diffusivity and anisotropic axial growth under nitrogen-rich conditions, with small Ga droplets / clusters acting as catalyst [104].

2.4 Fabrication of Nanowire Light Emitting Diodes

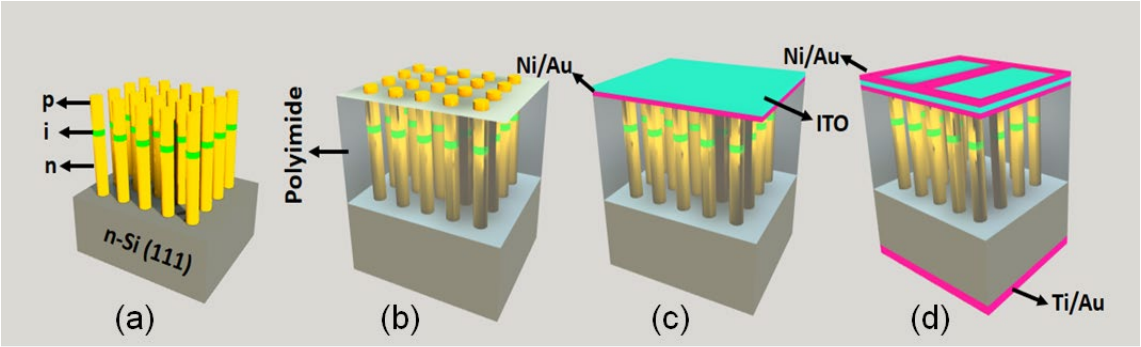

Figure 2.8 Schematic diagram of fabricated nanowire LED.

The nanowire LED structures are first grown on Si substrates by MBE, followed by standard device fabrication procedure. The nanowire LED samples are spin coated by polyimide for surface planarization and passivation. Subsequently, the nanowire top surface is revealed by performing reactive-ion etching using O_2 gas on the nanowires. This is then followed by the standard photolithography step used for patterning samples into various sizes. Top and bottom metal contacts are then deposited in the next stage by e-beam evaporator technique. In case of visible nanowire LEDs, top p-metal contact consists Ni (5 nm)/ Au (5 nm)/ indium tin oxide (ITO: 200 nm), whereas, bottom n-contact is composed of Ti (20 nm)/ Au (120 nm). ITO layer serves as current spreading layer. To facilitate hole transport, device surface is deposited with metallic contact grid patterns. Annealing at 500 °C in nitrogen ambient for 1 minute is performed on the fabricated devices with top and bottom contacts. This is then followed by a second annealing at 300° C in vacuum for one hour after ITO deposition. The schematic diagram of the fabricated devices are depicted in Figure 2.8.

AlN nanowire LED employs Ti (10 nm)/ Au (30 nm) as back metal contact and Ni (15 nm)/ Au (15 nm) as front metal contact. There are still issues pertaining to deep UV LEDs in the sense such as: there is an absence of deep UV transparent polymer for planarization and passivation and the Ni/Au layer used as the front p-metal contact is semi-transparent in the UV range. These reasons limit the EQE of the LED device, requiring much further research into the field. The processed LED is then diced and mounted on to a chip holder.

2.5 Characterization Methods

In this section, LED processed devices are studied regarding electro-luminescence, I-V measurements, two dimensional and three-dimensional FDTD simulation results etc. Analysis here refers to finding the output wavelength of emission, stability of emitted light and the device's diode characteristics. Some of the characterization techniques are described below.

2.5.1 Photoluminescence

In photoluminescence (PL) spectroscopy, direct light source impinges on the electronic structure of material. This contactless non-destructive optical characterization results from material absorbing a portion of incident energy and rest of the excess energy dissipating through the emission of light or luminescence. 405 and 266 nm lasers were used as the excitation sources here in this dissertation.

The energy band structure and quality of Group III-nitride semiconductors can be evaluated using PL. Typically a monochromatic excitation source like laser which gives large enough photon energy is used to excite the electrons in material from valence band

states to the conduction band states. Upon incident light on the material, photon is absorbed, and electrons are excited from the conduction band to the valence band and electron hole pairs (EHPs) are generated. These created EHPs recombine together to give off energy. Or in other words, electrons and holes relax to the respective band edges by means of phonon emission and ultimately recombine across the band gap. Photons are generated when radiative recombination occurs.

Recombination can be typically either radiative or non-radiative. Following the annihilation of EHP, a photon is emitted in a radiative recombination process. In direct bandgap semiconductors, radiative recombination is the more predominant one while in indirect bandgap semiconductors an additional assistance of a phonon is needed to conserve the momentum thus resulting in extremely low efficiency. Energy is dissipated as heat through the emission of phonon in a non-radiative recombination process. This makes indirect band gap materials not suitable for optoelectronic device applications. Band-to-band, free and bound excitons, donor bound electrons to free holes in the valence band, free electrons in the conduction band to acceptor bound holes and donor-acceptor pairs are the main recombination processes that results in radiative recombination. Detector collects the emitted photons resulting from radiative recombination.

PL can also provide details including the nature of energy states by observing the processes of absorption and carrier transfer. Equation (2.2) defines the electronic energy bandgap of the semiconductor material. Since defects such as impurities and dislocations are linked with non-radiative recombination rates, the PL measurement can qualitatively analyze the material quality and relative amount of radiative and non-radiative recombination rates.

$$E_g = \frac{(hc)}{\lambda} \tag{2.2}$$

Here E_g, h, c and λ represents the electronic energy bandgap of the semiconductor material, Planck constant, speed of light and wavelength of the emitted photons, respectively. As shown in Figure 2.10, various transition mechanisms across the bandgap can result in radiative recombination process. These are listed as below.

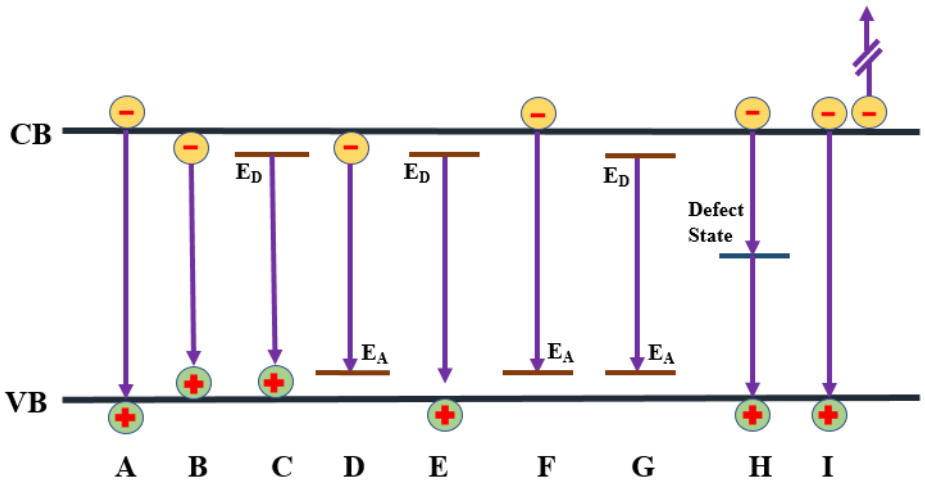

Figure 2.9 Radiative and non-radiative optical transitions. radiative transitions include A (band to band), B (free exciton), C and D (bound excitons), E (donor to valence band), F (conduction band to acceptor band), G (donor to acceptor pair) while non-radiative transitions include H (defect state related) and I (auger recombination).

Process A (Band-Band Transition): Radiative recombination that results between a conduction band electron and a valence band hole is referred to as Band-Band transition. Such processes occur in very pure crystals at relatively high temperatures. The intentional or unintentional introducing of impurity in the material results in creation of states in energy band. In these states, electrons and holes are trapped and can lead to a recombination with each other - either radiatively or non-radiatively. These transitions are illustrated in

the Figure 2.9 by processes E, F, and G. Moreover, the band-to-band transition transfers to excitonic transition that occur at low temperatures are also defined by processes B, C, and D.

Processes B, C, and D (Excitonic Transition): At low temperature in a very pure crystal, both free and bound excitonic transitions are observed. Free exciton consists of a conduction band electron and valence band hole bound together by Coulomb interaction. The recombination of electron and hole results in the emission of a photon having energy ($h\upsilon = E_g - E_x$). Since the exciton levels are well defined, there is a sharp emission spectrum. Bound excitonic transitions are found in intentionally doped high purity material. The exciton can be bound with either a donor or acceptor impurity atom. Bound exciton has a lower energy ($h\upsilon = E_g - E_x - E_b$) than the free exciton energy by the binding energy of the exciton to impurity.

Excitonic transitions are generally found at low temperatures, where the thermal energy is lower than exciton binding energy. With increase in temperature since the thermal energy becomes larger than the binding energy, the excitons become unstable and band-to-band transitions can be seen in PL spectra.

Processes E and F (Band-Edge to Donor/Acceptor Transition): This commonly observed process refers to the transition of a free carrier to a bound carrier. The transition involves recombination of neutral donor to a valence band hole or the recombination of an electron in the conduction band to the neutral acceptor ($h\upsilon = E_g - E_A$ or $h\upsilon = E_g - E_D$)

Process G (Donor-Acceptor Pair Transition): In Donor -Acceptor Pair (DAP) transition, the recombination accompanies when an electron moves from the neutral donor to the neutral acceptor. Such a transition results in the ionizing of both donor and acceptor. Due to the coulombic attractive force developed between them, the energy of the emitted photon

is defined by ($h\upsilon = E_g - E_A - E_D + \frac{q^2}{\varepsilon r}$, where q, ε and r refers to the elementary charge, dielectric constant and donor-acceptor distance, respectively. DAP transition can result in a broad emission spectrum, since the photon energy depends on parameter r and r and can vary in a wide range.

Processes H and I (Non-Radiative Recombination): Non-radiative recombination arises mainly due to the crystal defects such as dislocations, vacancies, interstitials, and foreign atoms present. The transition between the electron / hole carriers to the defect associated energy levels developed within the bandgap, results in phonon emission which is eventually dissipated as heat. In Auger recombination which is another dominant non-radiative recombination mechanism, the energy resulting because of EHP recombination excites another carrier, which transits to a higher energy level in the same band. By means of multiple phonon emission (by losing energy) the latter excited carrier relaxes back to the respective band-edge. Energy and momentum are conserved in an Auger recombination process. Though auger recombination becomes negligible at lower carrier concentration, at high carrier injection currents and very high excitation intensity the mechanism cannot be neglected anymore.

2.5.2 Electroluminescence

In Electroluminescence (EL), photon emission results from the radiative recombination of excess carriers *i.e.,* injected electrons and holes is measured. EL optical characterization technique ensures that whether the device is emitting the specific wavelength spectrum in accordance with the design parameters and fabrication. Spectra Suite software couples the LED light through the ocean optics cable, thus providing the EL spectra. In particular, EL spectra images shows the stability of the LED light source - whether there is any blue or

red shift with injection current bias. In nanowire LEDs, an electrical potential is applied to excite the electrons in the MQW region and the radiative recombination of the injected excess carriers occurs in the active region. Such emitted photons give an idea about the electronic energy bandgap of the active region.

The mechanism behind EL is explained in this section. The electrons (holes) from the *n- (p-)* region diffuse to the *p- (n-)* region when a *p-n* junction is setup in the semiconductor. This results in a positive (negative) space charge in the *n- (p-)* region. The generated electric field localized in a narrow region near the junction (from n to p region) at the interface vicinity, prevents further carrier diffusion to the opposite end and thus creates an equilibrium condition. Thus, the Fermi levels are equalized, and a potential barrier develops from *n-* to *p-* region. This narrow depletion region is depleted of any free charge carriers. With forward bias being applied to the p-n junction, there is decrease in both the internal potential barrier and depletion width while the excess electrons (holes) are injected from the *n- (p-)* region to the *p- (n-)* region. This radiative combination of high concentration of minority and majority carriers results in electroluminescence.

2.5.3 Importance of PL and EL Spectroscopy

Photoluminescence (PL) and Electroluminescence (EL) spectra provide insight into lot of meaningful information w.r.t the LED fabricated structures. Some of them are listed as follows.

Band gap: The semiconductor band gap can be analyzed using the PL spectra. The peak wavelength position in the PL spectra corresponds to the effective semiconductor bandgap. Using Vegard's law, the alloy composition in ternary bandgap engineered structures can be calculated. However, band gap might get affected w.r.t band tailing effect [135], which

can be associated with high doping concentrations. The random distribution of impurities in a semiconductor host lattice generates energy levels within the forbidden energy gap, thus introducing potential fluctuations. At high doping concentrations thus, the unperturbed density of states of the pure semiconductor is altered and substantial band tails might be observed. Another issue found with heavily doped semiconductors is the Moss-Burstein effect which can be referred to as the increase in apparent band gap of a semiconductor as the absorption edge is pushed to higher energies. This phenomenon of PL peak in a heavily doped semiconductor showing higher energy than the bandgap can be accounted to the fact that some states close to the conduction band are being populated at high doping levels / degenerate semiconductor. Thus, doping level of the material is an important parameter while determining the bandgap.

Stress: Since III-nitride materials are grown on lattice mismatched substrates, stress is an important issue. Due to the lattice mismatch and difference in thermal expansion coefficients between the epilayer and substrate, the epitaxial layer experiences strain. If lattice constant of the epilayer is larger (smaller) than the substrate, it experiences biaxial compressive (tensile) stress. This stress can be resolved into two components referred to as hydrostatic component and a uniaxial component. The hydrostatic component of the stress alters the lattice constant thus bringing about a change in the band gap and ultimately introducing a peak shift in the position of PL spectra. Valence band degeneracy at zone-center (Γ=0) is disrupted due to the uniaxial component. This results in the splitting of the valence bands into light hole and heavy hole sub-bands. Since carrier excitation and recombination involves these bands any considerable change in their order is seen in the PL spectrum typically as either by a peak position shift or the splitting of single PL peak into multiple peaks. PL can thus provide an idea about the strain present within the material

as well as can be used as a tool to quantitatively measure the magnitude and direction of the strain [136].

Crystal Quality: PL signal's intensity and full-width-at-half-maxima (FWHM) are indicators of the material quality. A strong intensity and narrow FWHM and absence of defect related peaks in the PL spectra implies excellent material quality.

IQE and EQE: As explained in the previous sections, EQE (which is defined as the ratio of number of photons emitted into free space per unit time to the number of electrons injected to the device per unit time) and IQE are important parameters w.r.t LED performance. For LEDs, EQE is given as the product of IQE (η_{IQE}), injection efficiency (η_{inj}) and light extraction efficiency (η_{ext}). IQE or η_{inj} is the ratio of the injected electrons to the active region to the total number of injected electrons to the device. For planar structures, η_{inj} is considered unity. But due to the presence of surface recombination in nanowire structures that takes place η_{inj} is very low. η_{IQE} is referred to as the ratio of the number of active region emitted photons emitted per second to the number of active region injected electrons per second. Only some photons recombine radiatively thus limiting the efficiency. As reported in earlier sections the LEE is limited by the total internal reflection. In planar structures the LEE values are of the order of ~ 4%, thus limiting device performance [137].

Temperature dependent PL/EL measurement can be used to deduce IQE. In such a scenario, defect related recombination is assumed to be nearly zero at cryogenic temperature due to thermal freeze-out effect. This makes the PL/EL intensity maximum value at low temperatures. η_{IQE} is defined here as the ratio of room temperature integrated PL/EL intensity to the low temperature integrated PL/EL intensity. But this assumption

might not be true for all material systems. For example, PL intensity of InGaN LED is not always saturated at low temperature [138]. Also, IQE calculation using this method depends on parameters such as excitation level and doping density of the material [139, 140].

Power dependent PL/EL measurement can be used to calculate EQE. EQE can be estimated *via* the rate of increase of the integrated intensity with increasing power. η_{EQE} droop is considerable at higher injection currents for III-nitrides. The common efficiency droop mechanisms including electron overflow, Auger recombination, inhomogeneous carrier distribution, etc. have been discussed in Chapter 1. By observing the shift in the peak position with increasing power, QCSE can be estimated. This shows the stability of the device under high current bias.

Color Rendering Index (CRI): CRI refers to color rendering index. This important functional property of white light sources defines it's color rendering ability. CRI is dependent on the light source spectral power distribution derived from EL spectrum. Planck's black body radiator is considered to have a CRI value of 100. CRI of the fabricated light source is computed by comparing the color rendering of the light source to that of a reference source. Eight standard color samples are illuminated by the test light source and the reference source. The standard color samples are presented in Figure 2.10. The CRI of the i-th sample is defined by the expression $CRI_i = 100-\Delta C_i$, where ΔC_i refers to the quantitative color change of the sample when illuminated by the reference and the test light source. $CRI = \frac{1}{8}\sum_{i=1}^{i=8} CRI_i$ which is the average of these special eight CRI's represents the general CRI. This implies that a higher CRI values is observed for a light source with smaller color deviation (ΔC) between the two sources. Or in other words, when the spectral

power distribution of light source closely resembles the black body radiation spectrum, CRI value is very high.

Figure 2.10 Eight color samples employed for calculation of CRI.
Source: [141].

2.5.4 Current-Voltage Characterization

The diode properties of the fabricated device can be evaluated using current versus voltage (I-V) characteristics. Turn on voltage, series resistance, shunt resistance and power from the integration of I-V graph can be acquired with the use of I-V characteristics.

CHAPTER 3

VISIBLE InGaN/AlGaN NANOWIRE LIGHT-EMITTING DIODES GROWN BY MOLECULAR BEAM EPITAXY

This chapter reports the realization of full-color nanowire LEDs, with the incorporation of InGaN/AlGaN nanowire heterostructures grown directly on the Si (111) substrates by MBE [24, 142]. Multiple color emission along the entire visible wavelength range can be made possible by varying the *In* and *Ga* composition in the InGaN quantum dot active region. Furthermore, spontaneous formation of multiple AlGaN shell layers during the growth of InGaN/AlGaN quantum dots, leads to the drastically reduced nonradiative surface recombination, and an enhanced carrier injection efficiency. Such core-shell nanowire structures can exhibit significantly increased carrier lifetime and massively enhanced photoluminescence intensity when compared to conventional InGaN/GaN nanowire LEDs. A high color rendering index of ~98 was recorded for white-light emitted from such phosphor-free core-shell nanowire LEDs.

High efficiency green, yellow, and red InGaN/AlGaN dot-in-a-wire nanowire light-emitting diodes grown on Si (111) by molecular beam epitaxy are also reported in the chapter. The devices demonstrated relatively high (> 40%) internal quantum efficiency at room temperature, relative to that measured at 5 K. Moreover, negligible blue-shift in peak emission spectrum associated with no efficiency droop was measured when injection current was driven up to 556 A/cm^2 [24, 142].

3.1 Research Motivation for Developing InGaN/AlGaN Core-Shell LEDs

Phosphor-free white light-emitting diodes (LEDs) have been intensively studied and identified as an emerging platform for future solid-state lighting and displays. To realize high performance, low cost phosphor-free white LEDs, it is critically important to develop high efficiency LEDs with emission wavelengths in the deep green to red spectral range [57, 143]. The achievement of such devices using conventional InGaN/GaN quantum well heterostructures has been difficult, due to the presence of large densities of dislocations and polarization fields [51]. Moreover, they suffer from efficiency droop, which has been explained by the Auger recombination [49], poor hole transport [144, 145], and carrier delocalization [82] in InGaN/GaN heterostructures. In this regard, InGaN-based nanowire heterostructures have been intensively investigated, which provides a relatively defect strain- and polarization-free platform for realizing high performance LEDs and other nanoscale devices [105, 108, 146, 147]. Tunable emission has been demonstrated using InGaN/GaN nanowire heterostructures [65, 148, 149]. In spite of the progress, however, the achievement of high efficiency nanowire LEDs has remained elusive.

Phosphor-free white-LEDs have been recently reported using bottom-up nanowire heterostructures which are generally formed along the axial or radial dimensions, leading to the dot [65]/disk [62]/well-in-a-wire [148] or core-shell nanoscale heterostructures [60, 150, 151]. The device performance, however, suffers severely from nonradiative surface recombination [83]. The large surface recombination is directly reflected in the commonly reported very short carrier lifetime (~ 0.3 ns) of conventional nanowire structures [60, 152]. The use of AlGaN shell in InGaN/(Al)GaN core-shell LEDs can further enhance the carrier confinement, reduce nonradiative surface recombination and enhance carrier injection into the device active region [60, 69].

Due to the large surface-to-volume ratios, the surface plays a key role in the operation and electrical and optical properties of III-nitride nanowire LEDs [60, 153]. Depending on the energy levels of the surface states, as well as the surface stoichiometry, Fermi-level pinning has been theoretically predicted and experimentally observed on the (11-00) plane [154, 155], *i.e.,* the lateral surfaces of commonly reported GaN nanowire LEDs. The resulting lateral electric field, as well as the associated surface nonradiative recombination is highly detrimental to the performance of GaN-based nanowire LEDs. In this context, InGaN/AlGaN dot-in-a-wire nanoscale heterostructures are fabricated, which can provide enhanced carrier confinement and carrier injection, thereby leading to high emission efficiency [24]. Furthermore, by engineering color emission of such InGaN/AlGaN nanowire heterostructures, full-color emission across the visible spectrum has been realized and reported in this chapter, leading to achievement of phosphor-free white LEDs [24]. Emission wavelengths can be tuned from green to red spectral range by varying the sizes and/or compositions of the dots. In addition, relatively high (> 40%) internal quantum efficiencies were measured for GaN-based nanowire yellow LEDs. No efficiency droop was observed for injection current as high as 556 A/cm^2 at room temperature.

In this context, a unique core-shell nanowire LED heterostructure has been developed by employing axial self-organized InGaN/AlGaN heterostructure which has demonstrated significantly improved carrier injection efficiency and output power, compared to conventional nanowire LEDs. These core-shell nanowire LED arrays were grown by MBE, where the device light emission properties, including the correlated color temperature (CCT) and color rendering index (CRI) can be readily engineered by varying the size and composition of the InGaN dots in a single epitaxial growth step. The

electroluminescence (EL) spectra show a very broad spectral linewidth and fully covers the entire visible spectrum. Additionally, the InGaN/AlGaN LEDs exhibit good current-voltage characteristic. Phosphor-free InGaN/AlGaN nanowire white-LEDs hold high CRI up to ~98, which is more efficient compared to the current phosphor-based white-LED technologies.

3.2 Experimental and Fabrication Details

Veeco GEN II MBE system was employed to grow vertically aligned InGaN/AlGaN dot-in-a-wire core-shell LEDs on Si substrates. Figure 3.1(a) depicts the schematic structure of an InGaN/AlGaN core-shell nanowire LED structure on Si substrate. The inset presents detailed LED structure. First, 0.4μm GaN:Si nanowire was grown at ~ 770ºC, followed by ten coupled InGaN/AlGaN dots grown at relatively low temperatures of 640ºC - 680ºC to enhance *In* incorporation in the InGaN dots. Emission wavelength of LEDs can be precisely controlled by varying the *In* composition in the InGaN/AlGaN active region. AlGaN barriers have been grown in the active region instead of GaN barriers, thus dramatically reducing the surface recombination. During the growth process of AlGaN barrier, an AlGaN downward-bending shell layer was also formed around the InGaN dot due to the diffusion-controlled growth process [69]. The barrier of each quantum dot was also modulation doped *p*-type using Mg to enhance hole transport. Finally, 0.2μm GaN:Mg section was grown on top of the LED structure.

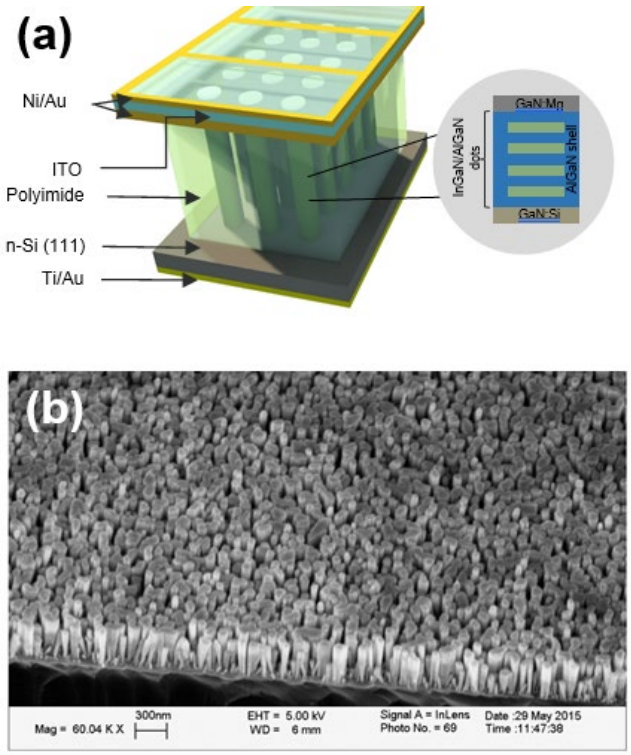

Figure 3.1 (a) Schematic illustration of an InGaN/AlGaN dot-in a- wire core–shell led heterostructure on Si substrate. Inset depicts the layer by layer structure. (b) A 45^0 tilted SEM image of a typical InGaN/AlGaN core–shell nanowire LED sample.

The nanowire diameter and density can be controlled by the substrate temperature and/or In/Ga flux ratios, while the nanowire length can be adjusted by the growth duration [156, 157]. Using such nanowire structures, by varying the growth conditions, high brightness green, yellow and red emissions from the InGaN/AlGaN dot-in-a-wire heterostructures were achieved as well.

Figure 3.1(b) is a 45 degree-tilted scanning electron microscopy (SEM) image for a typical InGaN/AlGaN core-shell sample. Highly uniform nanowires on Si substrate were achieved. The variation of *In* concentration in the InGaN dots ranges from 8% to more than 50%. For the ideal performance scenario of InGaN/AlGaN core-shell LEDs, the best *Al* composition in the AlGaN barrier is predicted to be in range of 15% to 20%.

The device fabrication route of InGaN/AlGaN dot-in-a-wire core-shell devices comprises of the steps as explained in Figure 3.2. First, nanowire arrays were spin-coated with polyimide resist for planarization and passivation, which is followed by O_2 dry etching to expose the top region of the nanowires. The exposed GaN:Mg surface were then deposited with layers including Ni (5nm)/Au(5nm)/indium tin oxide (ITO) to form top metal contacts. Afterwards to form the backside and topside contacts, respectively, Ti/Au (10nm/100nm) and Ni/Au (10nm/100nm) layers were evaporated on the backside of the Si substrate and top of ITO, respectively.

3.3 Results and Discussion

Optical properties of InGaN/AlGaN dot-in-a-wire LED heterostructures were investigated by using PL spectroscopy with a 405nm laser as an excitation source at room temperature. Full-color emission with wavelengths can be readily tuned across nearly the entire visible wavelength range. Performance characteristics of the dot-in-a-wire LEDs were measured under pulsed bias conditions with 1% duty cycle to minimize junction heating effect.

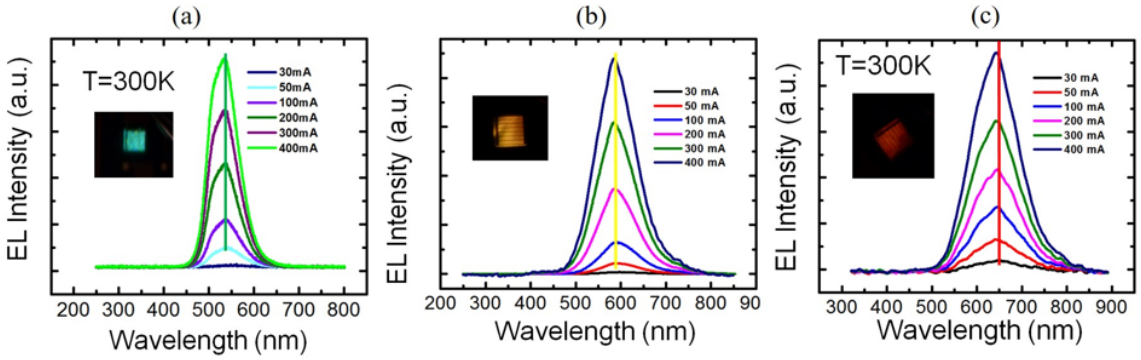

Figure 3.2 Room temperature electroluminescence spectra under different injection currents for (a) green, (b) yellow, (c) red nanowire LEDs. The inset of each figure shows the corresponding light emissions from green, yellow and red nanowire LEDs.

Strong green, yellow, and red emissions were measured from the InGaN/AlGaN dot-in-a-wire LEDs at room temperature, shown in Figure 3.2. The EL spectra of the green, yellow, and red nanowire LEDs under different injection current varied from 30 mA to 400mA were shown in Figures 3.2(a), 3.2(b) and 3.2(c), respectively. At injection current of 400 mA, the peak emission wavelengths at ~ 535, 585, and 645nm for green, yellow, and red LED devices, respectively. It may also be noticed that the spectral linewidths increase progressively with emission wavelengths, varying from 75, 105, to 125 nm for the green, yellow, amber, and red-emitting devices, respectively. This is a direct consequence of the enhanced *In* phase separation with increasing *In* compositions, that leads to the formation of *In*-rich nanoclusters in the dots as well as in the barrier layers. The emission properties of LEDs are depended on the compositions, the sizes of the dots, and the diameter of the nanowires as well. These parameters can be controlled by adjusting substrate temperature, growth duration, and In/Ga flux ratio. The achievement of strong emission in long wavelength from green to red region attributed to the successful usage of core-shell nanowire heterostructure associated with the embedded quantum dots.

Shown in Figure 3.3(a), the peak emission wavelength of InGaN/AlGaN core-shell nanowire LEDs varies from 460nm to 660nm. Effective variation in the *In* composition in the InGaN quantum dots can be achieved either by using different growth temperatures and/or In/Ga flux ratios. A longer wavelength as in red light is typically associated with a lower bandgap material. This gives us an impression about the composition of *In* in the nanostructure to achieve the desired color of light from the active region. The latter suggests that in the room temperature PL spectra, *In* composition increases from a lower value to a higher value for switching from blue to red color emission in the visible spectrum. The latter engineered structures can be used to envision various color emissions

as expected.

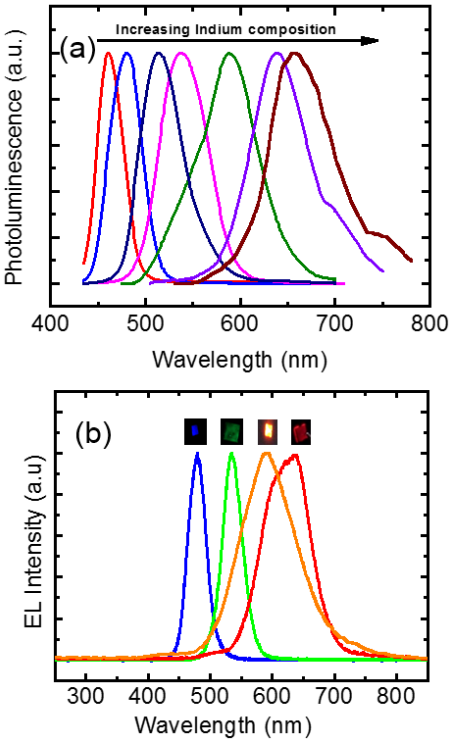

Figure 3.3 (a) Normalized room temperature photoluminescence spectra of multiple emission colors from multiple InGaN/AlGaN nanowire LEDs. (b) electroluminescence spectra of various InGaN/AlGaN LEDs with distinct emission colors, along with their optical image.

Figure 3.3(b) shows the EL spectra of different InGaN/AlGaN LEDs with various emission colors ranging from 475 nm to 650 nm, which agrees with their PL results presented in Figure 3.3(a). The optical images of full-color emission from these LEDs are also presented in the inset of the figure 3.4. Strong white emission has been realized by mixing multiple colors within InGaN quantum dots in AlGaN nanowires. The core-shell LED sample exhibits significantly improved optical intensity (a factor of > 8 times higher) when compared to a conventional InGaN/ GaN structure. It is suggested that radiative

recombination is more dominant due to the carrier confinement in the active region of InGaN/AlGaN LEDs which is much more efficient compared to that of InGaN/GaN LED without using AlGaN core-shell structure. Such enhancement is attributed to the drastically reduced nonradiative surface recombination as well as strong carrier confinement, due to the effective lateral confinement offered by the large bandgap AlGaN barrier that also serves as a shell layer. Moreover, the InGaN/AlGaN LEDs with core-shell structure have significantly increased carrier lifetime which is more than 15 times higher compared to the InGaN/GaN LEDs without the shell covering the nanowires. Such greatly enhanced carrier lifetime attributed to the reduced non-radiative surface recombination was due to the effective lateral confinement offered by the large bandgap AlGaN shell [69].

The emission spectra of phosphor-free InGaN/AlGaN core-shell white-LEDs are presented in Figure 3.4(a). In order to minimize junction heating effect, the devices were measured under pulsed biasing conditions (~1% duty cycle). It is seen that the emission spectra have very broad spectral linewidth with the full-width-at-half-maximum more than 150nm and fully covers the entire visible spectrum. Also, the spectra are highly stable and nearly independent of injection currents [61, 69]. Illustrated in Figures 3.2(a) and 3.2(b), peak wavelengths of the green and yellow-emitting LEDs are also virtually invariant with increasing current, suggesting the presence of a negligible quantum-confined Stark effect. A very small blue shift (~ 3 – 5 nm), on the other hand, was observed for the red-emitting devices, illustrated in Figure 3.2(c).

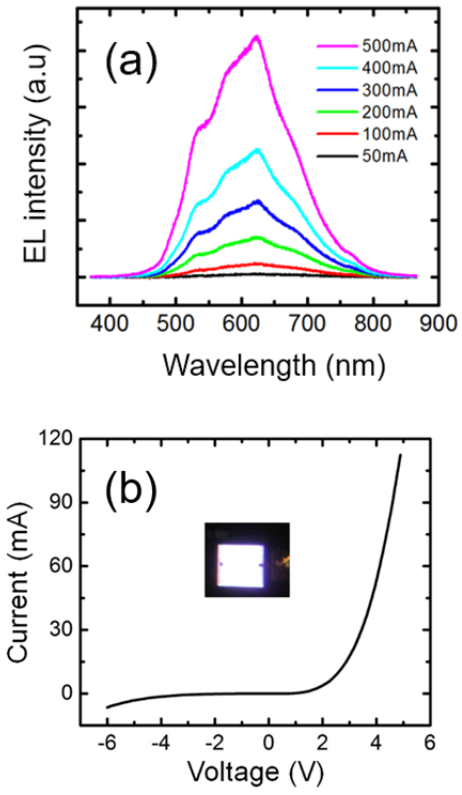

Figure 3.4 (a) Room temperature electroluminescence spectra of an InGaN/AlGaN core-shell LED under different injection current levels (b) current-voltage characteristics of the core-shell nanowire LED along with the optical image of the white LED.

The current-voltage (I-V) characteristics of the InGaN/AlGaN core-shell nanowire LED is shown in Figure 3.4(b). The sharp increase of current in the forward bias confirms excellent characteristics with low resistance value. Optical image of a white LED is also shown in the inset of Figure 3.4(b).

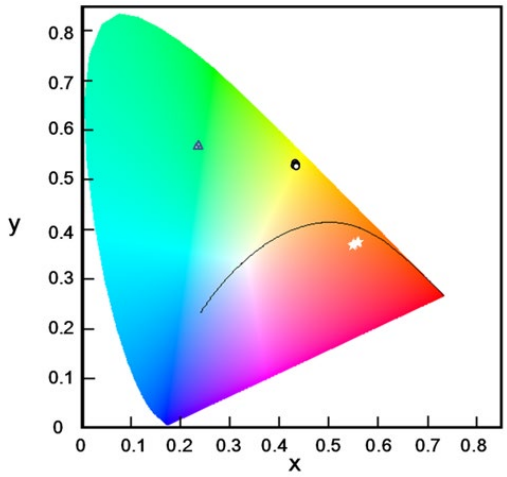

Figure 3.5 1931 Commission International de l'Eclairage (CIE) chromaticity diagrams of the light emission of green (triangles), yellow (circles), and red (stars) LEDs.

The highly stable emission characteristics are further illustrated in Figure 3.5, which shows locations of the light emission from the various LEDs on the 1931 Commission International de l'Eclairage (CIE) chromaticity diagram under injection currents from 100 to 400 mA. As expected, the green (triangles) and yellow (circles) LEDs exhibit nearly invariant CIE chromaticity coordinates of (x=0.22, y=0.55) and (x=0.44, y=0.50) with increasing current, respectively. The red (stars) devices show very small variations, with the derived CIE chromaticity coordinates being ($x \approx$ 0.54-0.55, $y \approx$ 0.36-0.37). To engineer the CRI of phosphor-free InGaN/AlGaN core-shell nanowire white-LEDs, several core-shell LED heterostructures in which the *In* composition in the InGaN active region is adjusted to generate different emission spectra as well as various spectral power distribution (SPD) characteristics. Most importantly, compared to conventional planar LEDs, InGaN/AlGaN core-shell nanowire LEDs hold flexibility in tuning the emission wavelengths and spectral linewidths, which are the two most important parameters for CCT and CRI.

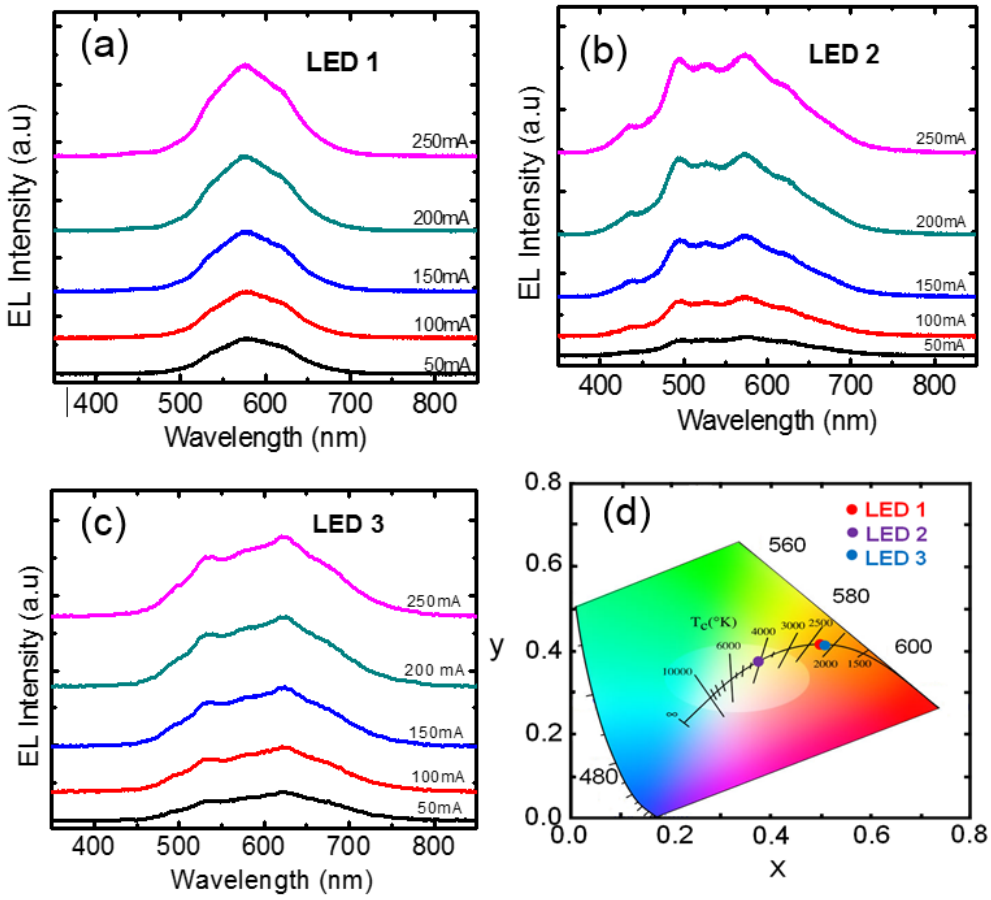

Figure 3.6 EL Spectra of three distinct LEDs (a) LED 1 (b) LED 2 (c) LED 3. (d) CIE 1931 chromaticity diagram illustrating the emission characteristics of three different InGaN/AlGaN nanowire LEDs.

Figure 3.6(a), 3.6(b) and 3.6(c) shows the EL spectra of three LEDs with different characteristics grown by distinctive conditions. The measurements were performed at distinctive injection currents, varying from 50mA to 250mA. The CIE coordinates for these LED devices are illustrated in Figure 3.7(d). At an injection current of 150mA, LED1 has a narrow spectrum compared to that of other LEDs. The full-width at half-maximum (FWHM) of emission spectrum of LED1 is ~ 110 nm while LED2 and LED3 both have broad spectra with FWHM of 176 nm and 171 nm, respectively. As a result, LED1 has a lower CRI value (66.5) compared to LED2 and LED3. LED2 and LED3 have SPD in the

range of 380 - 780 nm, and 410 - 800 nm, respectively. However, LED3 has more contribution from red emission resulting in higher CRI values. The measured CRI values for LED3 and LED2 are 97.5 and 92.2, respectively. LED1 has a CCT of 2387 K (warm white) and the CIE coordinates of (0.50, 0.43). The SPD of LED2 incorporates short wavelength components, thus emitting cool white light (CCT ~ 4428 K). It also demonstrates a high CRI value of 92.2, and the CIE 1931 coordinates of (0.38, 0.38).

In the injection current range of 50mA to 250mA, these InGaN/AlGaN nanowire LEDs do not show a significant change in CRI, CCT, and CRI values attributed to the stable operation under current injections. For instance, LED3 shows stable CRI values (96.8 - 97.8), CCT varies from 2259 K to 2429 K, and nearly stable chromaticity coordinates ($x \approx 0.48 – 0.49$ and $y \approx 0.42$ - 0.43). LED2 has lower CRI values compared to LED3 which is in the range of ~ 91.8 - 92.6, CCT varies from 3883 K to 4534 K and nearly stable chromaticity coordinates ($x \approx 0.38$ - 0.40 and $y \approx 0.38$ - 0.39). Due to narrow spectral linewidth and having mostly the short wavelength components in the SPD, LED1 shows the lowest CRI values which is in the range of ~ 62.1 - 67.5, CCT varies from 2887 K to 3359 K and chromaticity coordinates are nearly stable ($x \approx 0.46$ - 0.48 and $y \approx 0.47$ - 0.50). Moreover, negligible blue-shift in the peak positions of the EL spectra of these nanowire LEDs are attributed to the greatly reduced QCSE in the nanowire heterostructures due to effective strain relaxation.

The current-voltage and light-current characteristics of the yellow LEDs are presented in Figure 3.7. The defect density, polarization field, and internal electric field induces quantum confined Stark effect were minimized also results in perfect diode performances with very low leakage current of ~0.5 mA at -6 V, as presented in Figure 3.7(a). We have further confirmed that the dot-in-a-wire yellow LEDs exhibit virtually no

efficiency droop at room temperature.

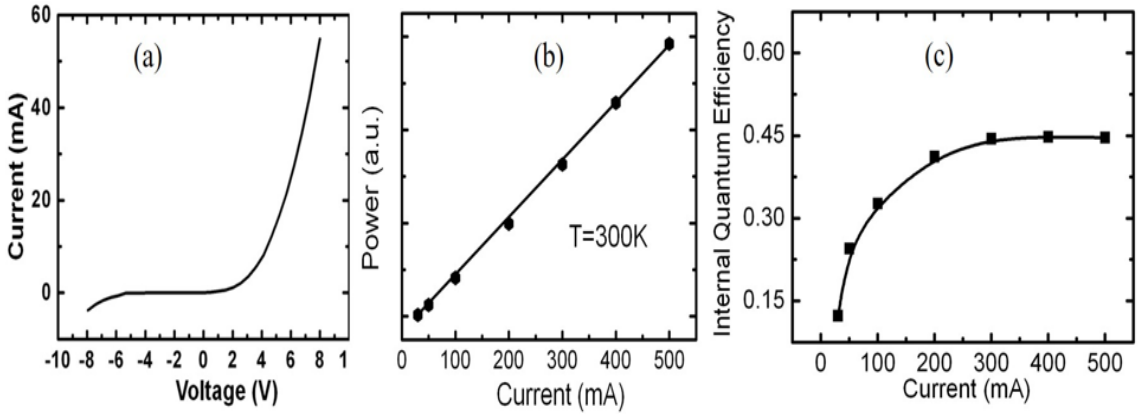

Figure 3.7 (a) Room temperature current-voltage characteristic of the yellow nanowire LED. (b) light-current characteristic of yellow nanowire LED under different injection currents. (c) room temperature internal quantum efficiencies of typical yellow LED versus various current levels.

Illustrated in Figure 3.7(b), the output power increases linearly with current for the entire measurement range (up to ~ 556 A/cm^2). This observation is consistent with recent studies that Auger recombination is significantly reduced in InGaN/GaN nanowire heterostructures, due to the reduced defect densities [153]. Additionally, hole transport problem may also be minimized with the use of *p*-type modulation doping in the device active region [65] and the use of self-distributed AlGaN multi-shell electron blocking layer [69, 96].

Finally, we have investigated the internal quantum efficiencies (IQEs) of the dot-in-a-wire LEDs by comparing the integrated electroluminescence intensity measured at 300 K to that measured at 5 K under the same injection current. Shown in Figure 3.7(c), the IQEs increase with injection currents and reach maximum values of 44.7% for injection currents at ~ 300mA (~333 A/cm^2) for the yellow-emitting LEDs, suggesting a small, or negligible efficiency droop under relatively high current injection conditions. The peak

IQE was measured at high injection current (~ 333 A/cm^2) which is significantly higher than that of conventional InGaN/GaN thin-film LEDs which is normally at 10-20 A/cm^2 [65, 158]. The very slow rising trend of the IQE has been commonly reported in nanowire LEDs and is attributed to the presence of large surface states and defects on nanowire surfaces [61, 65, 89].

The negligible efficiency droop is attributed to the strong carrier confinement provided by the quantum dot heterostructures, the enhanced carrier injection, the reduced electron overflow and other higher order effects on the device quantum efficiency [73, 159]. Compared to previously reported InGaN/GaN nanowires [160] or well/disk-in-a-wire LED heterostructures [161, 162] in the same wavelength range, the unique dot-in-a-wire heterostructures exhibit significantly higher IQE which can be explained due to the higher effective carrier confinement along the wire radial direction, thereby minimizing the nonradiative carrier recombination on the lateral surfaces. Moreover, the significantly improved IQEs measured in the dot-in-a-wire LEDs is attributed to the significantly enhanced carrier confinement and reduced nonradiative carrier recombination associated with the presence of surface states, as well as the enhanced carrier injection to the device active region.

3.4 Summary and Conclusion

In conclusion, high performance InGaN/AlGaN core-shell nanowire LED heterostructures on Si substrates have been developed. By controlling the indium composition in the InGaN/AlGaN quantum dot active region, full-color emission has been accomplished. Furthermore, core-shell nanowire heterostructures offer the benefit of enhanced carrier

injection efficiency to the LED active region as well as a drastically reduced nonradiative recombination on nanowire surface. We demonstrated superior performance phosphor-free nanowire white-LEDs, holding highly stable emission with CRI of ~98 under injection current range of 50mA to 250mA. This work addresses the major roadblock in regard to the practical applications of nanowire-based LEDs and has provided a novel perspective of having high efficiency phosphor-free white LEDs as well as full-color LEDs with tunable emission for advanced solid state lighting applications in the near future.

In summary, we have demonstrated that, with the use of self-organized InGaN/AlGaN dot-in-a wire heterostructures, GaN-based nanowire LEDs can exhibit relatively high internal quantum efficiency in the deep green to red wavelength range under electrical injection. Moreover, the devices show highly stable emission characteristics with increasing current and virtually no efficiency droop at relatively high injection conditions (up to 556 A/cm^2). These results provide a significant progress for future solid-state lighting applications wherein the usage of low cost, high efficiency, smart LEDs are realized. Such nanowire LEDs are perfectly suited for wearable flexible electronics as well as high speed LEDs for visible light communications.

CHAPTER 4

PHOSPHOR-FREE III-NITRIDE NANOWIRE WHITE-LIGHT-EMITTING DIODES FOR VISIBLE LIGHT COMMUNICATION

This chapter emphasizes on the self-organized phosphor-free III-nitride nanowire LEDs grown by MBE and their application in visible light communication (VLC) [163]. The electroluminescence spectra of these nanowire LEDs show a very broad spectral linewidth and fully covers the entire visible spectrum. The InGaN/AlGaN core-shell nanowire LEDs exhibit relatively high output power of >5mW which is more than two orders of magnitude higher than that of conventional LEDs without using core-shell technique. Additionally, high-brightness phosphor-free LEDs with highly stable white-light emission and high color-rendering index (CRI) of >98 were obtained by controlling the Indium composition in the device active region. Moreover, the III-nitride nanowire phosphor-free white-LEDs exhibit relatively high 3-dB frequency bandwidth of ~ 1.4 MHz which is higher compared to that of phosphor-based white LEDs at the same measurement condition. Such high-performance phosphor-free nanowire LEDs are being further improved and are ideally suited for future smart lighting applications and communications.

4.1 Research Motivation of III-Nitrides for Visible Light Communication

III-nitride nanowire heterostructures are one of the most promising materials in semiconductor industry due to their excellent optical and electrical transport properties. Those nanowire devices exhibit high electric breakdown field, high electron mobility, large saturation velocity and extreme chemical stability thus offering promising scope for applications in solid state lighting. Compared to conventional thin-film light-emitting

diodes (LEDs), nanowire LED structures have exceptional features, including drastically reduced dislocation densities and polarization fields as well as a lower quantum confined Stark effect (QCSE) because of the effective stress relaxation. Gallium nitride (GaN) based optoelectronic devices are being explored as hybrid visible LEDs by means of an overcoating or by incorporating light emitting nanocomposites and nanospheres [164]. These are sought out for applications including solid state lighting [165], bioinstrumentation [166] etc. LED light sources have been explored for visible light communication (VLC) which has been recently gaining extreme popularity due to its immense potential in fast data transmission and superior processing ability. The current white light generation using the means of phosphor has been constrained in terms of modulation speed due to lower intrinsic bandwidth and slower relaxation time of phosphors. These conventional low bandwidth transmitters have been met with improvements and replacements including multiple novel modulation and demodulation techniques ranging from GaN based micron-size LEDs [167], optical wireless multiple-in multiple-output (MIMO) systems [168], orthogonal frequency division multiplexing [169].

In comparison to conventional lighting technologies like incandescent bulbs, white LED offers longer lifetime, cooler operation, reduced power consumption, lower voltage and small size, high luminous efficiency and ease in color rendering. The dual ability of LED to serve as a lighting source along with being a communication device arises because of the capability of fast switching of LEDs and modulation of visible electromagnetic light waves for communications. As reported by Komine et al. LEDs for VLC also offers advantages like minimum shadowing, easy installation, absence of electromagnetic or RF interference and avoids the need for widening angle at the receiver end in contrast to infrared wireless communication [170]. In addition, VLC using LEDs can boast higher

privacy/security for optical communication, license free spectrum and ecofriendly (no health regulation) benefits which makes it an intriguing choice. The optical VLC system can be easily utilized with the modulation of parameters including intensity, polarization or phase/frequency for the optical signal. The LED brightness can be adapted fast and at speeds faster than conventional light sources [171]. By controlling the LED light source intensity, data transfer can be made feasible through visible spectrum to a photo detector. The VLC system thus in total offers a lot of benefits including low power consumption, high bandwidth, and freedom from electromagnetic interference, no harm to the human body, and high security and privacy.

Current LEDs use the approach of generating white light by having a blue emitter in unison with a phosphor and mixing generates white light. The challenges/limited bandwidth of the phosphor-based emitters for VLC arises on account of the slow time constant of the phosphor utilized for generating white light. Enhancing the bandwidth of these phosphor-based sources involves complex techniques like equalization of driving circuitry [172] and filtering out slow yellow component at the receiver end using a blue filter [173]. Du et al. has reported the effect of strain compensation for high speed VLC by tuning the carrier lifetime in InGaN/GaN LEDs, thus providing a detailed overview on the effect of internal strain inside the quantum well along the growth direction and the impact it has on modulation bandwidth [174]. Monolithic integration of nitride-based LEDs and photodetectors for bi-directional VLCs has been reported by Jiang et al. [175]. In contrast, nanowire LED structures hold several distinct advantages, including reduced dislocation densities and polarization fields and associated QCSE due to the effective stress relaxation whereas planar counterparts are constrained by efficiency droop and low efficiency in the green to red spectral regime [57], mainly because of the presence of strong polarization

fields [51], poor hole transport [144], defects and dislocations, Auger recombination [49], carrier delocalization [82], electron overflow and leakage. Moreover, in terms of VLC applications, the bandwidth of conventional III-nitride systems is currently limited to the MHz level, which can be utilized for the needs of broadband Wi-Fi systems. This can be accounted to the long carrier recombination lifetime and piezoelectric fields in current III-nitride planar based LEDs.

The strong internal electric fields subsequently cause a reduced overlap between the electron and hole wave functions in the active regions of the LEDs, which in-turn suffer from long radiative recombination lifetimes (10-100 ns) as well as low internal quantum efficiency. The conventional phosphors used to convert the emission to white light are also reported to have even longer decay times and thus further causes severe concern regarding the available bandwidth. The nanowire-based LEDs offers ability to reduce the internal electric fields and are thus expected to fabricate faster and ultra-energy efficient LEDs with ultrafast modulation speeds for next generation III-nitride based white lighting and VLC applications. The nanostructures employed in LEDs also reports the reduction in the radiative recombination lifetime and increase in the optical efficiency. Such high-performance phosphor-free nanowire LEDs are being further improved and are ideally suited for future smart lighting applications and communications.

Furthermore, the transmission rate in VLC systems is dependent on the modulation bandwidth, which is estimated by the minority-carrier lifetime in III-nitride semiconductors. In this regard, we have developed InGaN/AlGaN core-shell nanowire white LEDs with drastically reduced surface non-radiative recombination, leading to an enhanced carrier lifetime and output power compared to conventional LEDs without using core-shell structures. Minority carrier lifetime in semiconductor further affects the response

frequency and consequently limits the LED modulation bandwidth. Hence currently LED bandwidth is limited below the theoretical bandwidth limit of 2 GHz. White LED modulation bandwidth and modulation characteristics along with the effect of spatial light intensity on amplitude frequency characteristics has been reported elsewhere [176].

VLC which thus encompasses short-range optical wireless communication using visible electromagnetic spectrum from 380 to 780 nm can thus utilize fast nanosecond switching of LEDs (faster than the persistence of the human eye) and can effectively provide an inexpensive alternate with just simple LEDs and photodetectors, to the already running out spectrum bandwidth for traditional radiofrequency (RF) communication below 6 GHz. LEDs [177] are thus being considered as an optimal stage for VLC due to its ability to emit and receive light at the same time (with multiplexing). In this context, we have fabricated III-nitride nanowire white-LEDs that exhibit high color rendering value (CRI) up to ~98, which is more efficient when compared to the current phosphor-based white-LED technologies. Moreover, we have explored the practical applications of nanowire-based LEDs for VLC and will thus provide a novel perspective for utilizing high efficiency phosphor-free white nanowire LEDs in indoor wireless and commercial broadband communication networks.

The III-nitride LEDs exhibit relatively high 3-dB frequency bandwidth of ~ 1.4 MHz. To this end, we found III-nitride LEDs can be utilized as light sources and can be easily modulated with injection current making it a viable candidate for the indoor VLC setups and increase in bandwidth would enhance the traffic data rate for VLC transmission. Such high-performance phosphor-free nanowire LEDs are being further improved and are ideally suited for future smart lighting applications and communications.

4.2 Experimental Details

Veeco Gen-II MBE system with RF plasma assisted nitrogen source was employed to grow the InGaN/AlGaN nanowire LED heterostructures. The *n*- and *p*-type doping of GaN was accomplished by using Si and Mg, respectively. The device active region consisted of 10 vertically aligned InGaN dots sandwiched by 3nm AlGaN shell layers. Additional information regarding MBE growth and device fabrication of nanowire structures can be found in Chapter 3 and our works [24, 142, 178].

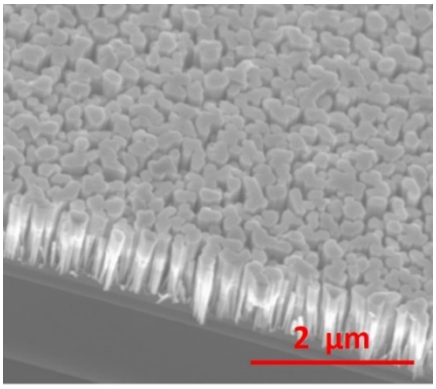

Figure 4.1 45^0 tilted scanning electron microscopy image illustrating the surface morphology of the molecular beam epitaxy grown InGaN/AlGaN dot-in-a-wire heterostructures grown on a n- type Si (111) substrate.

Surface morphology of the self-organized InGaN/AlGaN nanowire LED heterostructure on n-type Si (111) substrate acquired *via* SEM is depicted in Figure 4.1. The 45 degree-tilted cross-sectional SEM image shows that the nanowires grown on silicon substrate were highly uniform in nature. Variation of *In* concentration in InGaN dots resulted in the generation of multiple colors from the active region of the nanowire device. Wire areal density is ~1 x 10^{10} cm^{-2}. During the growth of AlGaN barrier layer, an AlGaN shell layer fully covering the InGaN dot active region is spontaneously grown due to the

diffusion-controlled growth process [60, 69]. These core-shell heterostructures offers exceptional reduced nonradiative surface recombination and enhanced carrier injection efficiency [96]. Detailed information for the MBE growth and structural properties of this InGaN/AlGaN core-shell nanowire structures can be found in our journals [69, 142].

4.3 Results and Discussion

Figure 4.2 represents the photoluminescence (PL) spectra of the InGaN/AlGaN LED structure acquired using a 405 nm laser excitation source at room temperature. The inside of Figure 4.2 represents the normalized PL intensity spectra for multiple colors obtained from nanowire devices.

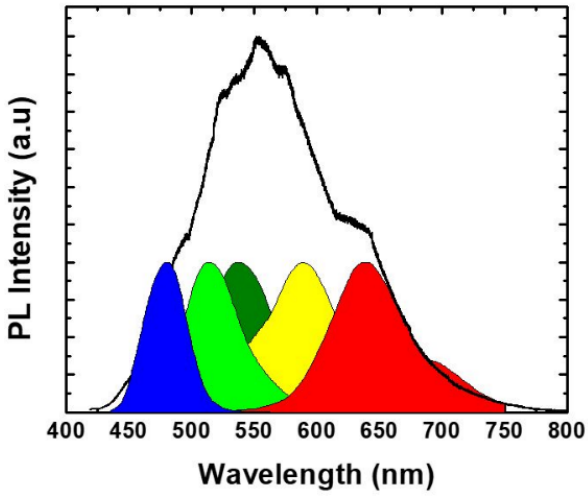

Figure 4.2 Photoluminescence spectra depicting phosphor free white LED with GaN/InGaN nanowire system with normalized individual color spectra shown inside.

Full color emission with wavelengths tuned from near infrared to deep ultraviolet can be realized by the tuning the band gap *viz.* by controlling growth temperatures and In/Ga flux ratio. The PL spectra, evident from Figure 4.2 shows that a broad PL spectrum which covers the entire visible wavelength range can be utilized to have phosphor-free

nanowire white LEDs. An increase in the concentration of *In* in the active region corresponds to a lower band gap material/ higher wavelength like red color emitting from the fabricated device. This color mixing approach has thus been reported to envision high quality (CRI values~98) for LEDs [24].

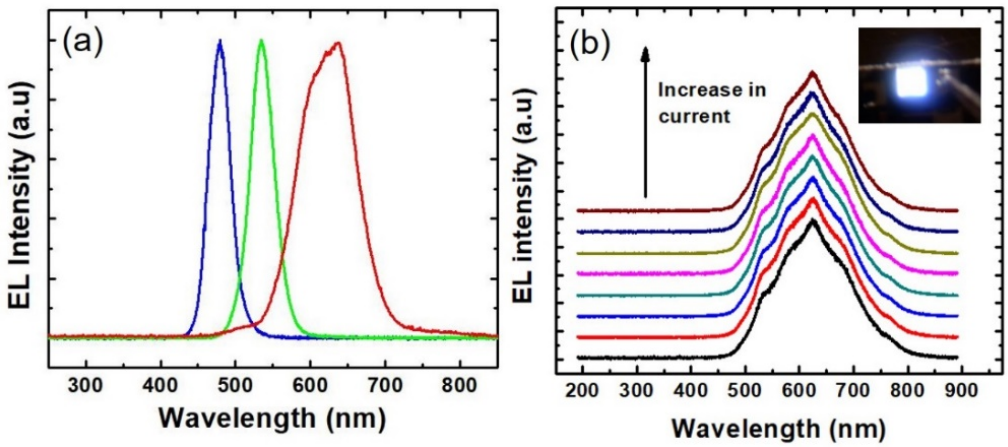

Figure 4.3 (a) Electroluminescence spectra illustrating color tuning and (b) electroluminescence spectra of phosphor free white nanowire LEDs along with optical micrograph.

Figure 4.3 shows the EL spectra from different InGaN/AlGaN LEDs. Figure 4.3(a) which is the normalized EL spectra shows the ability of the bandgap engineering approach to generate LEDs with peak wavelengths ranging from 475 nm to 650 nm, in accordance with the PL results. Strong white light emission was accomplished within a single nanowire device by mixing multiple colors within the active region of the InGaN quantum dots. The InGaN/AlGaN core-shell structure in contrast to the conventional InGaN/GaN structure exhibits an enhanced optical intensity of >8 times because of the reduced non-radiative surface recombination. The AlGaN barrier grown diffusively leads to effective carrier confinement due to its large band gap shell and consequently leads to a dominant radiative carrier recombination.

Figure 4.3(b) depicts the emission spectra of the InGaN/AlGaN core-shell phosphor-free white nanowire LED devices. Inset of Figure 4.3(b) represents the optical micrograph image acquired for the same white LEDs. To minimize junction heating effect, EL spectra was measured under pulsed duty cycles. The broad emission spectra cover the entire visible spectrum regime. The EL spectrum upon increasing injection current shows that the device emission was highly stable and is almost independent of injection currents. The negligible shift in the peak wavelength of EL spectra pointed out to reduced quantum confinement stark effect (QCSE) in the fabricated device [65].

The strain generated during the MBE nanowire growth has been relaxed through the higher surface area of the nanowire devices, especially through the top and side walls of the nanowires. This in turn leads to a reduced strain/ polarization within the device. The lower built in electric field is reported to result in improved radiative recombination rate in the quantum well and subsequently resulting in high speed bandwidth VLC. The negligible efficiency droop arising due to the strong carrier confinement provided by the quantum dot heterostructures further leads to a reduced electron overflow, enhanced carrier injection, and other higher order effects on the device quantum efficiency. Such novel and unique dot-in-a-wire heterostructures is shown to have significantly higher internal quantum efficiency (IQE) which has been linked to the higher effective carrier confinement along the wire radial direction, thus reducing the nonradiative carrier recombination on the nanowire lateral surfaces.

Figure 4.4 presents the current-voltage (I-V) characteristics of the InGaN/AlGaN nanowire LED. The reduced QCSE, defect density and internal electric field/ polarization which were minimized results in excellent diode performance. Sharp increase of forward bias current in I-V characteristics graph corresponded to the lower series resistance for the

device.

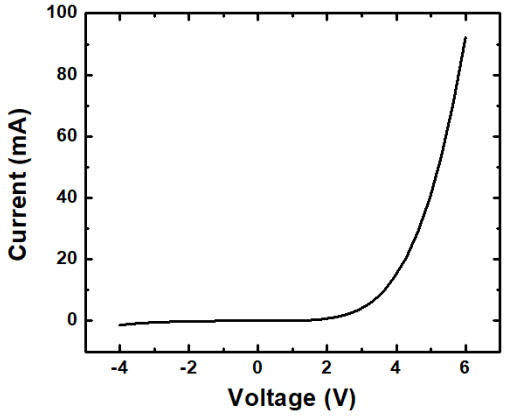

Figure 4.4 Room temperature current-voltage characteristic of the phosphor-free white nanowire LED.

Leakage current was found to be of the order of few milliamperes at higher voltages because of the excellent attributes for the nanowire structure. LED modulation speed, which is often constrained by the series high resistance of the device [179] can thus be significantly improved through the approach of having nanowire photonic LEDs because of its lower series resistance values.

The phosphor-free nanowire white LEDs were then characterized for application communication. Figure 4.5 represents the schematic of VLC experimental platform used. The LED was operated within the permissible DC current limit for avoiding reduction in electrooptical efficiency arising from temperature instability as required. The optical source was phosphor-free nanowire white LED with Lambertian emission. The electrical sinusoidal signal input was superimposed with the DC bias *via* a bias-T. The signal input was generated with the help of RIGOL DG 2041 A, 40 MHz Function/Arbitrary waveform generator. The VLC transmitter is composed of the nanowire phosphor-free white LED.

The receiver end is composed of focusing (concentration) lens from Edmund Optics and then coupled to a PIN photodetector (Thorlabs 200-1100 nm PDA10A Si amplified detector).

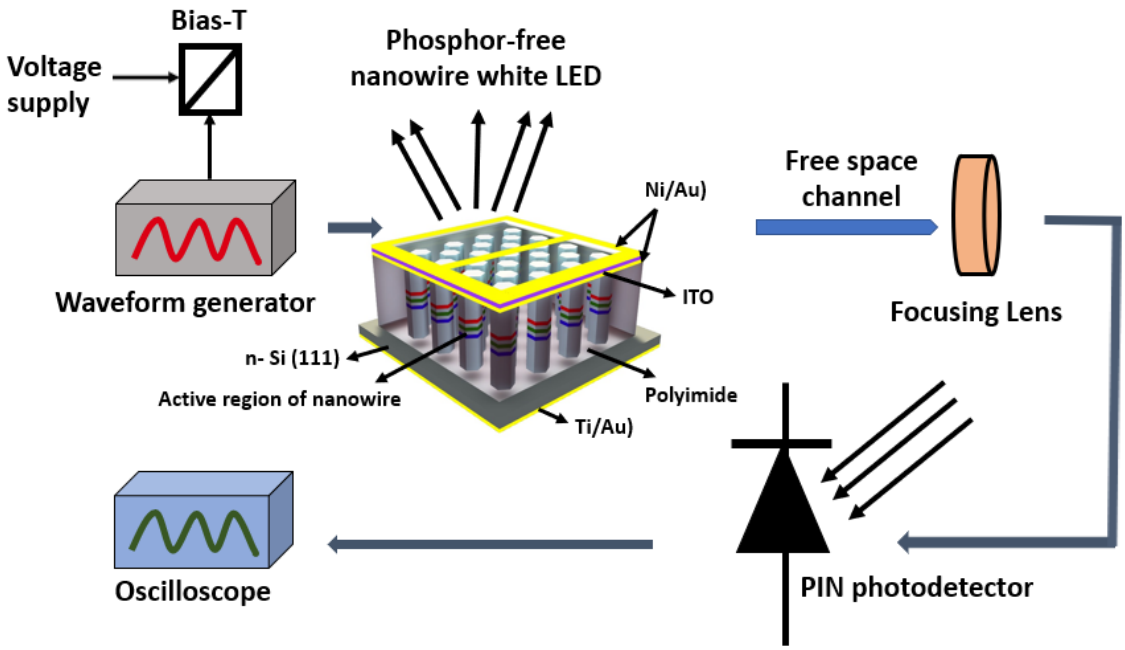

Figure 4.5 Schematic of the Experimental Setup for VLC.

Direct line of transmission between the receiver and transmitter was achieved by proper aligning and placing of receiver in front of the LED. The output signal from positive intrinsic negative (PIN) module was sampled and then saved by means of an oscilloscope for offline demodulation. The electrical signal output from the PIN photodetector can then be amplified using the amplifier or hooked up as it is to the oscilloscope (Tetronix 3 GHz MDO4034-3 Mixed Domain Oscilloscope). The 3-dB bandwidth is referred to as the frequency at which the peak-peak value of the applied signal drops to 0.707 times its initial peak-peak signal value.

Figure 4.6 shows the frequency response curves obtained for white LEDs. A DC bias current and peak-peak modulation current were tuned accordingly to optimize the signal to noise (SNR) of transmission [180]. A DC bias is applied so that the LED is in its linear region of operation and that it also generates adequate average light power for illumination.

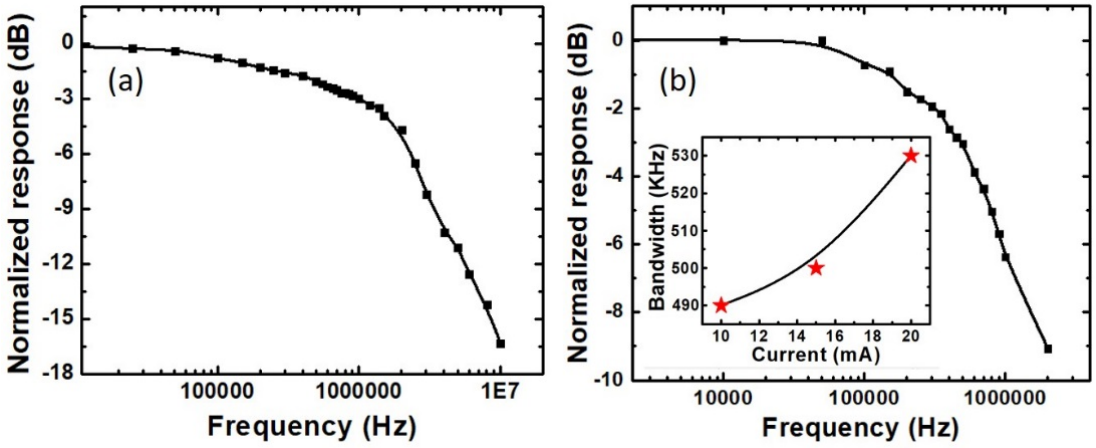

Figure 4.6 Comparisons of frequency responses between (a) commercially available planar thin film white LED and (b) III-nitride thin film white LEDs.

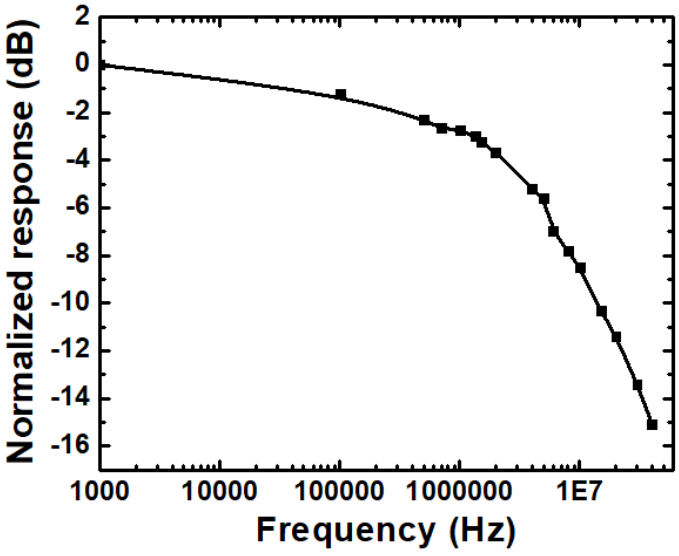

Figure 4.7 Frequency response of phosphor-free nanowire white LED.

Figure 4.6(a) and 4.6(b) shows the frequency response and the bandwidth achieved using the commercially available planar thin film white LED and III-nitride thin film white LEDs, respectively while Figure 4.7 shows the same for III-nitride nanowire white phosphor-free light emitting diodes.

The frequency characteristics of the electro-optical-electro channel measured shows that the three LEDs behave similarly. Bandwidths around 3-dB for III-nitride thin film LEDs and commercial planar thin film white LEDs was found to be around ~500 KHz, 1.4 MHz and ~1MHz further substantiating the claim of stress relaxation/ reduced polarization and QCSE in nanowire LEDs. The response frequency of LED is reported to play a crucial role in directly impacting the available bandwidth of the VLC system. Inset of Figure 4.6(b) shows that there is a linear relationship between the injection current density and bandwidth of VLC light sources. The measured 3 dB bandwidths of the LEDs improve with increase in current density, which has been attributed to the fact that enhances carrier injection density into the active volume leads to higher carrier bimolecular recombination of electrons and holes. This obtained trend of increasing current injection is being employed in high power LEDs for high speed VLC applications. The reduction in internal electric fields originated from stress relaxation through the top and sidewalls of nanowire surface consequently further leads to better overlap between the electron and hole wavefunctions in the active regions of the LEDs. This in turn improves the recombination lifetimes (10-100 ns) and enhances internal quantum efficiency.

4.4 Conclusion

This work has presented a simple approach using phosphor-free nanowire white LEDs and low-cost photodetectors in developing VLC systems with significant bandwidth. The experimental results show improvement of direct modulation speed in phosphor-free nanowire white LEDs and validate the claim that optical VLC using the latter is indeed feasible and can generate to a higher bandwidth than the conventional thin-film and existing LED sources, due to its reduced QCSE and enhanced stress relaxation. The modulation characteristics study of LEDs reveals linear relationship between operation current density and 3 dB bandwidth of LEDs which makes high power LEDs an excellent candidate for bi-directional high-speed VLC. With better optimizing of design structures to achieve LEDs, lasers, the system performance can be improved significantly to envision high speed broadband VLC. The ability of VLC using phosphor-free nanowire white LEDs will pave the way for next generation indoor communication on account of its high data rate possibly. Further exploration on stress relaxation of nanowires can contribute to innovating high bandwidth VLC.

CHAPTER 5

PHOSPHOR-FREE III-NITRIDE NANOWIRE LIGHT-EMITTING DIODES ON METAL SUBSTRATES FOR FLEXIBLE PHOTONICS

In this chapter, high performance III-nitride nanowire LEDs on copper (Cu) substrates were demonstrated *via* substrate-transfer process. Nanowire LED structures were first grown on silicon-on-insulator (SOI) substrate by molecular beam epitaxy. Subsequently, the SOI substrate was removed by combining dry and wet etching processes. Compared to conventional nanowire LEDs on Si, nanowire LEDs on Cu exhibit several advantages, including more efficient thermal management and enhanced light extraction efficiency due to the usage of metal-reflector and highly thermally conductive metal substrates. The LED on Cu, therefore, has stronger photoluminescence, electroluminescence intensities and better current-voltage characteristics compared to the conventional nanowire LED on Si.

Our simulation results further confirm the improved device performance of LED on copper, compared to LED on Si. The light extraction efficiency of the nanowire LED on Cu shows 9 times higher than that of LED on Si at the same nanowire radius of 60 nm and spacing of 130 nm. Moreover, by engineering the device active region, we achieved high brightness phosphor-free LEDs on Cu with highly stable white light emission and high color rendering index of ~ 95, showing their promising applications in general lighting, flexible displays and wearable applications.

5.1 Research Motivation

III-nitride semiconductors have been intensively studied for optoelectronic devices, due to the superb advantages offered by this materials system [33, 181]. The direct energy bandgap III-nitride semiconductors can absorb or emit light efficiently over a broad spectrum, ranging from ~ 0.65 eV (InN) to 6.4 eV (AlN), which encompasses from deep ultraviolet to near infrared spectrum [33, 182]. However, due to the lack of native substrates, conventional III-nitride planar heterostructures generally exhibit very high dislocation densities that severely limit the device performance and reliability. On the other hand, nanowire heterostructures can be grown on lattice mismatched substrates with drastically reduced dislocation densities, due to highly effective lateral stress relaxation [23, 183]. The growth of nearly defect-free III-nitride nanowire heterostructures has been reported on various substrates, including Si and sapphire [148, 184, 185]. Moreover, nanowires have emerged as a powerful platform to effectively scale down the dimensions of devices and systems, ideally suited for future nanophotonic and nanoelectronic devices [186-189].

Nanowire LEDs with emission in the ultraviolet to visible wavelength range have been intensively studied for applications in solid-state lighting, flat-panel displays, and solar-blind detectors [24, 142, 190-192]. Nevertheless, currently reported nanowire LEDs generally exhibit very low external quantum efficiency, which may be attributed to the presence of defects on nanowire surfaces [83] and/or low light extraction efficiency (LEE) [193]. Moreover, III-nitride nanowire LEDs are normally grown on Si substrates, which may largely absorb photon emitted from the LED active region, severely limiting the light output power. Additionally, Si semiconductor exhibits low electrical conductivity and thermal expansion coefficients compared to metal substrate [194]. High power LED

applications, nonetheless, require large-area chips and can operate at high injection current which mostly will heat up the devices. Generally, quantum efficiencies, output power and lifetime reduce rapidly when the junction temperature increases [195]. Therefore, managing heat dissipation is seriously considered. Besides the applications in solid-state lighting illumination, the use of LEDs in telecommunications, and decoration displays for flexible electronics devices has also been intensively developed due to the feasible integration of such LEDs in these electronic devices [196-200]. Organic LEDs have been first studied because of their ease to grow on plastic substrates. However, for these types of LEDs, high electrical performance, low resistance, long-term reliability and controlled doping concentrations still remain challenging issues [201, 202]. These issues can be addressed in inorganic semiconductor using III-V and related materials. In this regard, the replacement of Si substrate by a suitable metal, therefore, promises the improved device performance, including high output power and less heating effect [203].

In this work, we have systematically developed high brightness InGaN/AlGaN nanowire full-color LEDs on Cu substrate from both simulation and experiment. The simulation results show that LEDs on Cu has significantly enhanced LEE compared to other LED structures; which is ~ 9 and 7 times higher than that of LED on Si and flip-chip LED on Si substrates, respectively. The experimental results further confirm that the LED on Cu substrate shows significantly enhanced light output intensity, and better current-voltage characteristics over the conventional LEDs on Si substrates. Moreover, highly stable white light emission with color rendering index of ~95 was recorded for the flip-chip nanowire LED on Cu substrate due to the properly controlled Indium composition in the device active region.

5.2 Simulation and Device Structure

Illustrated in Figure 5.1, three InGaN/AlGaN nanowire LED structures were comprehensively studied utilizing the finite difference time domain (FDTD) method. These LED structures include conventional *p*-side up nanowire LED on Si substrate (LED 1), *n*-side up LED on Si substrate (LED 2), and *n*-side up LED on metal substrate (LED 3), shown in Figures 5.1 (a), (b) and (c), respectively. *N*-side up LEDs are also called as flip-chip LEDs throughout this work.

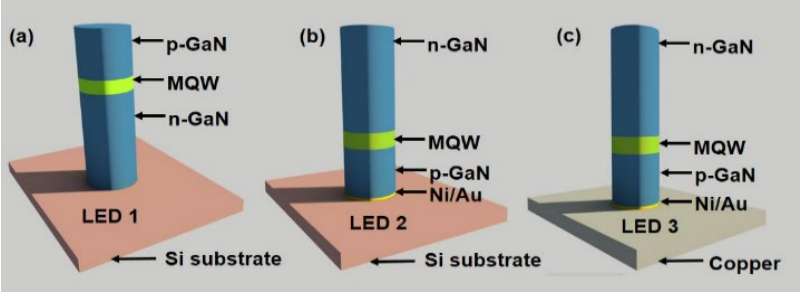

Figure 5.1 Schematic structures of (a) LED 1, (b) LED 2, and (c) LED 3 with peak emission wavelength at 550 nm.

The device structure is composed of an *n*-GaN layer, InGaN/AlGaN multiple quantum well active region and a *p*-GaN layer. The active region is composed of ten InGaN wells (3 nm thick layer) sandwiched by 3 nm AlGaN barrier layers. The thickness of *n*- and *p*- type GaN regions are 350 nm and 150 nm, respectively. The underlying substrate is assumed to be Si and metal for the typical and flip-chip InGaN/AlGaN nanowire LEDs, respectively. The refractive indices of the AlGaN and *n*-GaN/*p*-GaN regions considered in all simulations are 2.6 and 2.5, respectively. Flip-chip LEDs exhibit lower forward voltage and series resistance, which can be accounted to the enhanced current spreading in the *p*-

GaN layer. This can be attributed to the reason that the whole *p*-GaN layer is in contact with the Cu layer here, thereby improving the innate high resistivity of *p*-GaN; as reported in similar work [204]. Hence, during the design phase of the nanowires, we have further optimized the *p*-GaN thickness to study the effect of *p*-GaN thickness on the LEE of nanowire LEDs.

Lumerical FDTD solution [205] is employed to numerically investigate and compare the LEE of nanowire LEDs versus spacing and radius of nanowires. The measuring monitors placed above and around the LEDs to collect all optical power emitted from the designed nanowire device structures. The LEE is defined as the ratio of the power emerging from the structure to the total power generated within the active region by the dipole. Generally, III-nitride nanowire LEDs grown by molecular beam epitaxy (MBE) have radius in the range of 20-80 nm [96, 148, 206, 207]. In our simulation, therefore, we first considered the nanowire array with hexagonal arrangement of 50 nm radius and the nanowire centre-to-centre spacing of 130 nm for all LED devices. The geometry of the nanowires has a dominant effect in the emission of generated photons from active region into air. The radius and spacing of nanowires are among the parameters which can be used to maximize the LEE of nanowire LEDs. With proper design of nanowire spacing and radius, the light can be coupled through nanowires and scattered out of the device.

Figures 5.2(a) and 5.2(b) depict the LEE vs radius at a constant spacing of 130nm, and LEE vs. spacing at a constant nanowire radius of 50nm, respectively. Shown in Figure 5.2(a), LED 2 demonstrated an enhancement in the LEE compared to LED 1 because of the shorter distance between the active region and the Si substrate, consequently stronger reflection from substrate. When compared to the light absorptive properties of silicon material, flip-chip LEDs with light reflective mirrors has been reported to have an

enhanced LEE [204, 208, 209]. The aforementioned argument has been used to support the fact that LED 3 has a higher LEE compared to LED 2, attributed to the presence of a stronger reflection of light from metal/Cu substrate, and also due to the reduced absorption in Cu as compared to Si substrate [210, 211].

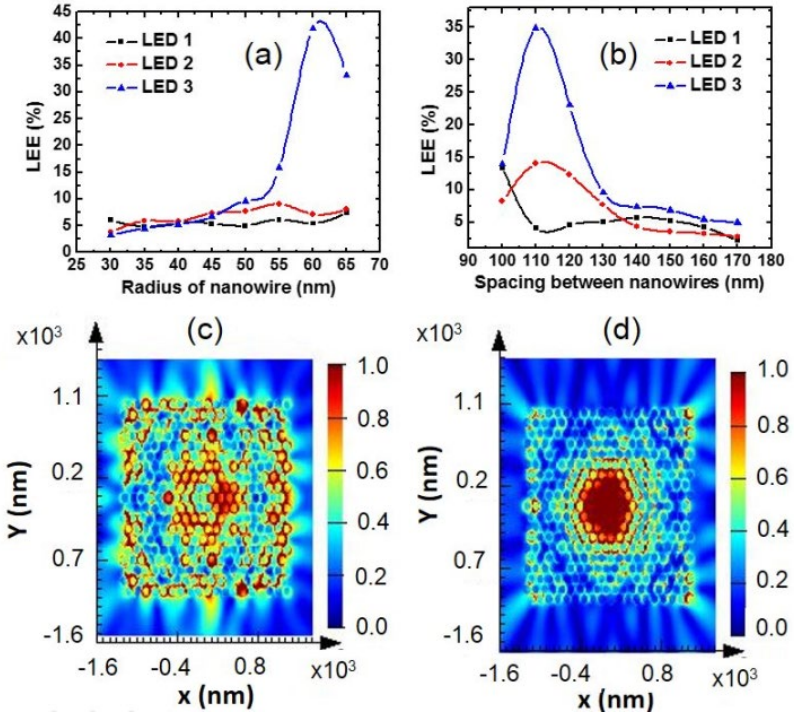

Figure 5.2 (a) Variation of LEE with change in spacing (for a constant radius of 50 nm) and (b) change in radius (constant spacing of 130 nm. (c) electric field distribution plot from top monitor for a flip-chip on metal. (d) electric field plot from top monitor for a normal p-i-n LED structure on Si substrate.

The stronger reflection ensures a higher probability of light generated from the active region to be reflected back from the substrate, which is eventually extracted after multiple total internal reflections inside the LED structure. Moreover, the presence of a metal layer in flip-chip LEDs ensures the formation of a good ohmic contact at the *p*-type region [208, 209] and serves as optical reflector and current spreading layer [212] to

facilitate the current injection to LED active regions.

Variation of critical parameters such as radius and spacing between nanowires play an important role on LEE. Shown in Figure 5.2, there is an optimum radius and spacing to avoid photonic bandgap (PBG) and have high LEE. The electric field plots depicted in Figures 5.2(c) and 5.2(d) show the electric field distribution for both the flip-chip LED structures on Cu and typical LED structure on Si substrate, respectively. Both flip-chip structures refer to regular periodic structures with a radius of 50 nm and centre-to-centre spacing of 130 nm. Illustrated in Figure 5.2(c), in the flip-chip structure, the light is not locally stagnant, rather much better propagated within the structure. In other words, as compared to a conventional LED device composed of multiple nanowires, there is a contribution from majority of nanowires within the device towards light extraction, as opposed to a normal *p*-side up structure on Si substrate (shown in Figure 5.2(d)), where light extraction is typically concentrated towards the centre and only a minority of nanowires (placed in the middle of the device) contributes to the light extraction.

We have further considered a variation in nanowire radius and wire spacing for nanowire LEDs in which nanowires are randomly arranged since self-organized III-nitride nanowires are not naturally periodically arranged on the substrate. Figure 5.3(a) represents the LEEs of 16 typical random flip-chip LED structures with different nanowire radius and spacing. The radius from 47.5 nm – 52.5 nm and centre-to-centre spacing in the range of 125 nm – 135 nm were considered. The LEE of the random LED structure has an average LEE of 26.79% while the nanowire LEDs with nanowire radius of 50 nm and a spacing 130 nm is 9.61%. For periodic structures, the LED devices may operate in the PBG mode, while for the same amount of randomness in a random structure, there is the probability of device working outside the scope of PBG modes. Figure 5.3(b) depicts the effect the *p*-

GaN thickness on LEE of a flip-chip device structure. Modification in *p*-GaN thickness of nanowire has a sizable contribution to the LEE. *P*-GaN shows a strong variation in trend of LEE with *p*-type thickness. The latter behavior is explained by the superimposition/interference effect between the forward and backward travelling photons [213]. The latter reaffirms the necessary constraints for constructive reflection occurring within the active region of the nanowire. This in turn stresses the need for optimizing the *p*-type layer thickness for the best LEE. Compared to previously mentioned parameters, the *p*-GaN shows a strong variation in LEE. It is even worse for smaller thickness because of the high reflection from reflective layer on the top of substrate.

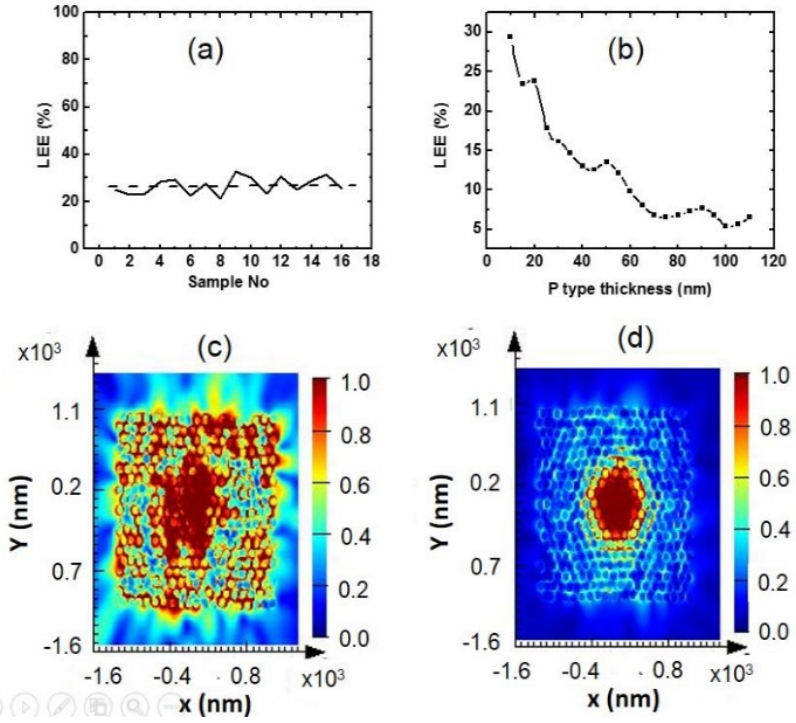

Figure 5.3 (a) LEE for 16 different random structures with multiple nanowire diameter and nanowire spacing and between them. (b) variation of p-type height with LEE of a flip chip (n-i-p) structure on metal. (c) and (d) electric field contour plots for a typical random flip chip structure on metal and a random normal (p-i-n) structure on Si Substrate.

Figures 5.3(c) and 5.3(d) represent the electric field contour plots of a random flip-chip on metal and random normal *p-i-n* structure on Si substrate, respectively. As in the case depicted in Figures 5.2(c) and 5.2(d) periodic nanowire structures, the distribution of contribution towards light extraction remains the same in random flip-chip and regular random *p-i-n* structures, illustrated in Figures 5.3(c) and 5.3(d).

5.3 Experiment and Results

Highly uniform nanowire LEDs with radius of ~60 nm was grown on the SOI substrate, shown in Figure 5.4. The device-active region consists of 10 vertically aligned InGaN/AlGaN quantum dots, which can provide white light emission, because of the *In* compositional variations (∼10−50%) of the InGaN-active region [61, 65]. Each InGaN quantum well has a thickness of ~ 3 nm and is capped by ~ 3nm AlGaN layer. Detailed growth conditions for such nanowire LED heterostructures were described in other publications [60, 65, 69, 184].

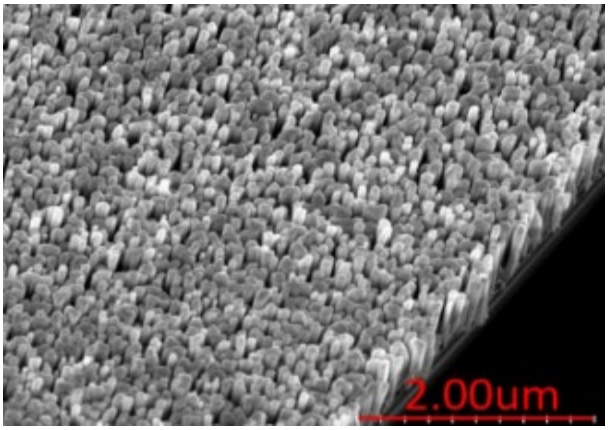

Figure 5.4 45^{o} tilted SEM image of nanowire LEDs on SOI substrate.

The surface morphology and orientation of nanowire LEDs grown directly on SOI substrate are much more uniform compared to those of nanowire LEDs grown on SiO_2-on-Si substrate reported in our previous study due to the local surface roughness of amorphous SiO_2 on Si [214, 215]. Such properties may lead to higher optical and structural performances of the LEDs on SOI compared with LEDs on SiO_2-on-Si wafers.

The fabrication process of LEDs on Cu substrate is described in Figure 5.5. Nanowire LEDs were first grown on SOI substrate by MBE. Polyimide resist was then spin-coated to fully cover the nanowire, followed by oxygen plasma etching to reveal the nanowire top portions (Figure 5.5(a)). Subsequently, polyimide was hard-baked at 350^{o} C for 45 minutes. Metal contact with Ni (10 nm)/Au (150 nm) was then deposited on top of nanowires to serve as *p*-type contact and also the metal reflector, followed by electroplating of 150μm Cu. Deep reactive-ion etching was then applied to remove Si substrate with the etching rate of 12 μm/min, illustrated in Figure 5.5(b). The etch-stop SiO_2 layer was then removed by buffered oxide etching solution while the remaining Si top layer was removed by Tetra methyl ammonium hydroxide (TMAH). Finally, Ti (5 nm)/Au (5 nm)/ITO(200 nm) and Ti(10 nm)/Au(100 nm) were deposited to serve as the top metal contacts, shown in Figure 5.5(c). The LEDs on Si substrate were also fabricated for comparison. Devices with areal size of 1×1 mm^2 were used for characterization. For a fair comparison, all measurements were performed on LEDs at similar locations on the wafers for both LEDs on Cu and LEDs on Si substrates.

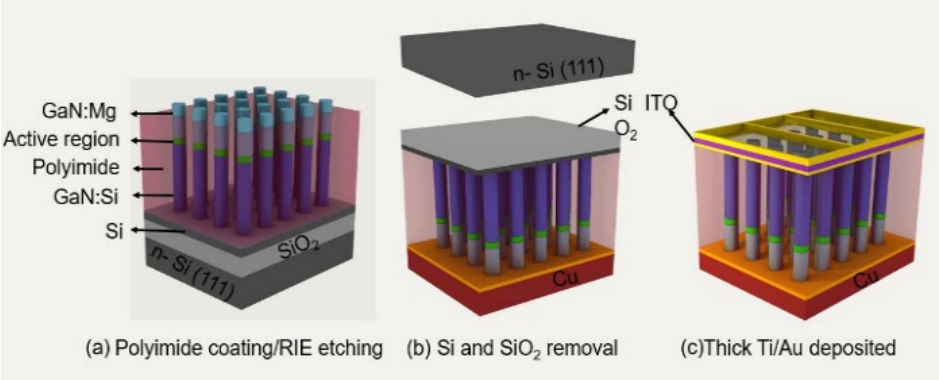

Figure 5.5 Fabrication procedure of nanowire LEDs on copper substrate.

Detailed optical and electrical characterizations of nanowire LEDs on Cu substrate were performed. PL study was performed by using a 405 nm laser as the excitation source with a microscope objective, high-resolution spectrometer, and photomultiplier tube to collect and detect the emissions from the LED samples. The current-voltage of the nanowire LEDs were measured using a power supply (Keithley 2402). EL emission of the LED devices was collected by an optical fiber directly connected to an Ocean Optics spectrometer. All measurements were conducted at room temperature.

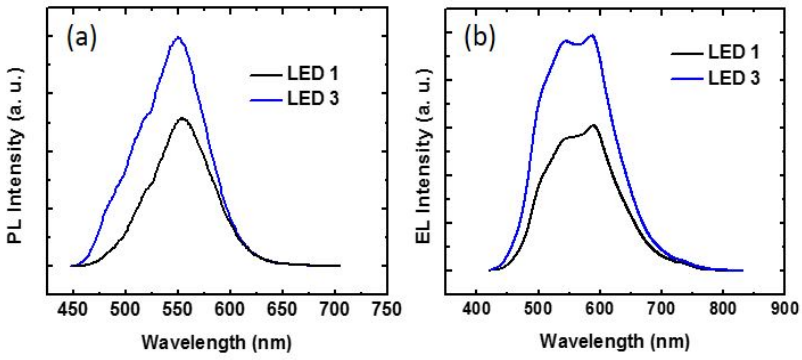

Figure 5.6 Room Temperature (a) photoluminescence spectra of flip-chip nanowire LED on Cu (blue curves) and conventional nanowire LED on SOI substrates (black curves). (b) electroluminescence spectra of flip-chip nanowire LED on Cu (blue curves) and conventional nanowire LED on Si substrates (black curves).

Shown in Figure 5. 6(a), after being transferred to Cu substrate, the PL intensity of nanowire LED on Cu (LED 3) is enhanced by a factor of 1.5 compared to that of as-grown nanowire LEDs on SOI substrate. Such enhancement is mainly attributed to the improved light extraction efficiencies due to the significantly reduced light absorption after removing the Si substrate. Moreover, the Ni/Au bi-layer may work efficiently as a reflector to further enhance the LEE [194]. This further confirms that the nanowire damage during the transferring process is almost negligible. A small blue-shift of ~1.5 nm was recorded for nanowire LED on Cu compared to that of nanowire on SOI which is attributed to the fact that the strain has been relaxed due to the release of nanowires from the SOI substrate [216]. The EL intensity of the LED 3 was measured of nearly twice higher than that of the regular nanowire LED on Si (LED 1), shown in Figure 5.6(b). Such enhanced PL and EL intensities agree well with the simulation results presented in Figures 5.2 and 5.3.

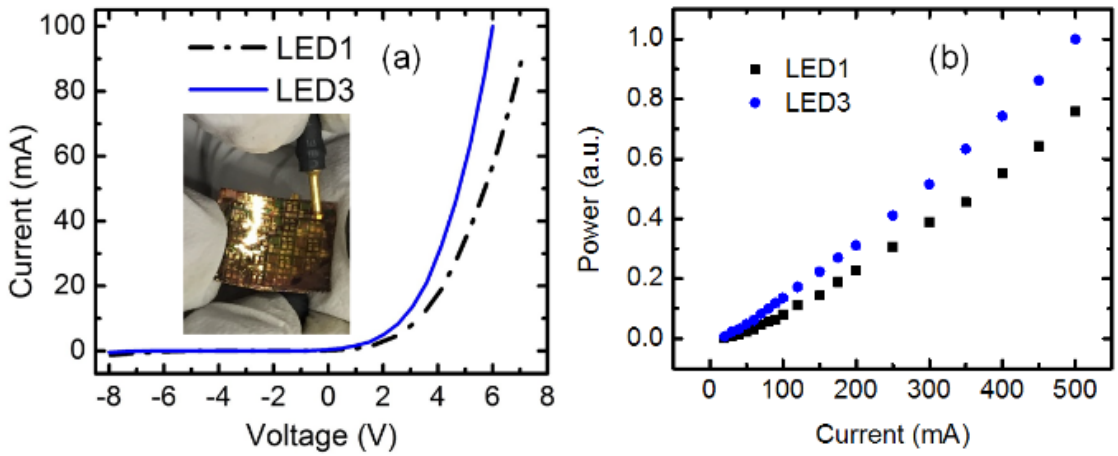

Figure 5.7 (a) Current-voltage, and (b) light output power versus injection current characteristics of conventional nanowire LED on Si Substrate (LED 1) and nanowire LED on Cu (LED 3).

Figure 5.7(a) shows the current-voltage characteristics of a nanowire LED on Cu compared to a similar growth condition nanowire LED on Si substrates. The LEDs on Cu substrate (LED 3) exhibit excellent current-voltage characteristics and show lower leakage current and slightly higher current in forward bias, compared to the LED device on Si substrate (LED 1) at the same voltage. At 20 mA injection current, the operating voltages for LED 3 and LED 1 are 3.2 V and 4.1 V, respectively. At -8V reversed bias, the corresponding currents for LED 3 and LED 1 are -0.5 mA and -1.5mA, respectively. The lower voltage of LED 3 may be attributed to the better heat dissipation and substrate conductivity of the nanowire LED on Cu substrate which is consistent with other reports [195, 217, 218]. Shown in the inset of Figure 5.7(a), the optical image of light emission from the LED device on Cu substrate, demonstrating the successful fabrication of such nanowire of on metal substrates. Figure 5.7(b) shows the relative light output power of both LED 1 and LED 3 for comparison. It is shown that LED 3 exhibits stronger output power compared to that of LED 1. Such output power enhancement is attributed to the enhanced LEE in LED 3 which was explained previously. To further increase the output power of LED 3, several limiting factors should be considered and addressed, for instance, improving the transparency of the top Ti/Au/ITO top metal contact and optimizing the nanowire geometry including wire density, diameter, and height.

We have further developed phosphor-free white LEDs on Cu substrate by engineering the *In* composition in the InGaN active region, thereby, white light emission with full visible spectrum was achieved. This method was reported earlier in chapter 5.

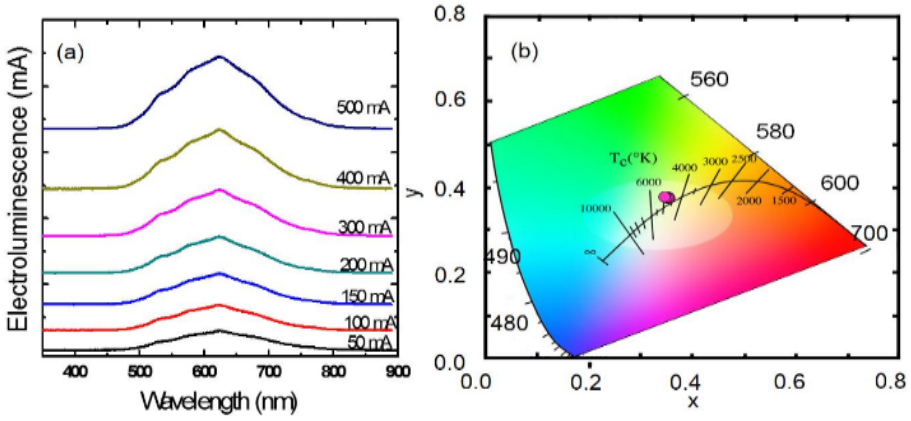

Figure 5.8 (a) EL spectrum and (b) CIE Diagram of phosphor free white LEDs on Cu substrate.

Figure 5.8(a) shows the EL spectra of phosphor-free white-LEDs on Cu substrate under different injection currents. The experiment was conducted under pulse bias condition with duty cycle of 1% to minimize junction heating effect. The peak wavelength is almost stable when current increases from 50 mA to 500 mA attributed to the low quantum confined Stark effect [219]. Moreover, the LED device achieves stable white light emission on CIE diagram, shown in Figure 5.8(b). The device achieves high CRI of ~95 showing promise as a candidate for solid-state lighting and display.

5.4 Summary and Conclusion

In summary, we have demonstrated high performance InGaN/AlGaN nanowire white LEDs on Cu substrate without using any phosphor converter. The improved performance including stronger photoluminescence, electroluminescence intensities, and current-voltage behavior were recorded for the transferred nanowire LED on Cu substrate, compared to conventional LED on Si. Such enhancements are attributed to the reduced light absorption by the substrate, the enhanced LEE and reduced heating effect. Moreover,

the substrate transfer approach presented in this work can be applicable for fabricating LED devices on metal substrate, plastic or many other platforms where the epitaxial growth of LED structures cannot be directly grown on, due to high growth temperature. This work also provides promising approach for the integration of III-nitride nanowire LEDs in future solid-state lighting, visible light communication, and decoration displays as flexible electronics devices.

CHAPTER 6

MOLECULAR BEAM EPITAXIAL GROWTH AND DEVICE CHARACTERIZATION OF AlGaN BASED NANOWIRE ULTRAVIOLET-LIGHT-EMITTING DIODES

This chapter reports on the design and fabrication of high performance $Al_xGa_{1-x}N$ nanowire ultraviolet (UV) LEDs on silicon substrate by MBE. The emission wavelength and surface morphology of nanowires can be controlled by varying the growth parameters that include substrate temperatures and/or Aluminum/Gallium flux ratios. The devices exhibit excellent current-voltage characteristics with relatively low resistance. Such nanowire LEDs generate strong emission in the UV-B band tuning from 290 nm to 330 nm. The electroluminescence spectra show virtually invariant blue-shift under injection current from 50 mA to 400 mA, suggesting the presence of a negligible quantum-confined Stark effect. Moreover, we have shown that, the AlGaN nanowire LEDs using periodic structures, can achieve high light extraction efficiency of ~ 89% and 92% for emissions at 290nm and 320nm, respectively. The randomly arranged nanowire 290 nm UV LEDs exhibit light extraction efficiency of ~ 56% which is higher compared to current AlGaN based thin-film UV LEDs.

We also report in this chapter our study on the effect of optical absorption in nanowire UV LEDs using three-dimensional finite difference time domain simulation. Utilizing nanowire structures can avoid the emission of guided modes inside LED structure and redirect the trapped light into radiated modes. The optical loss due to material absorption can be decreased by reducing light propagation path inside the LED structure, and consequently enhance the light extraction efficiency (LEE). Nanowire form factors including size, and density play important roles on the LEE of UV nanowire LEDs. In this

chapter, the nanowire spacing and diameter are considered in simulation to reach maximum LEE. Our results show an unprecedentedly high LEE of ~34% can be achieved for deep UV emission at 240 nm. Moreover, UV nanowire LEDs with random structure can exhibit LEE of ~19% which is comparable or higher than that of high efficiency UV thin-film LEDs.

6.1 Current Problems with AlN and AlGaN based UV LEDs

Al(In)GaN-based semiconductor has the potential for optoelectronic devices, including LEDs and laser diodes (LDs),because of their ability to have emission wavelengths in the UV spectral region (200-365 nm). Such UV devices holds immense importance for broad range of applications in display, lighting, disinfection, chemical and biochemical sensors, air-water purification, and white-light generation *via* phosphor excitation. Earlier, the bulkier mercury and Xenon lamps were employed to visualize a UV emission source. But on account of their severe drawbacks such as being expensive, hazards it poses to environment due to presence of mercury, short lifetime, needing high voltage operation and more importantly since the emission wavelength cannot be tuned limited the practical operations of UV based lamps.

In contrast to mercury-based UV lamps AlGaN-based UV LEDs has many advantages, including cost-effective, mercury-free, long-life, low-to-moderate voltage operations, etc. But, the performance of such devices degrades significantly with decreasing operation wavelength, *i.e.,* increasing Al content. This is because of the increasing density of defects and dislocations during epitaxial growth with an increase in Al content or lower emission wavelength. For instance, the currently reported maximum

light output powers for AlGaN MQW deep UV LEDs for peak emission wavelengths of 241 nm, 256 nm and 284 nm are 1.1 mW, 4.0 mW and 10.6 mW, respectively. Highest EQE reported for 279 nm emission is as low as 7%.

IQE drops drastically from ~50% to less than 1% for the LEDs operating in the UV wavelength regime of 250-300nm [220-222] to 210 nm [221], respectively. For as AlN devices emitting in UV-C range, EQE values are of the order of ~0.1% and the output power is of a few tens of nW thus limiting practical applications. Thus the large densities of defects and dislocations and resultant low IQE of <10%, large device turn on voltage that stems from inefficient *p*-doping, strong polarization fields and unique transverse magnetic (TM) polarization of the light emission makes light extraction from conventional c-plane AlN LEDs real challenging [21, 221, 223-226].

6.1.1 Large Densities of Defects and Dislocations

III-nitride semiconductors can be grown on a variety of substrates including SiC, sapphire, Si, GaN etc. with different lattice constants and thermal expansion coefficients [227-229]. This lattice mismatch can lead to structural defects and threading dislocations (TD) and cracks during epilayer growth process [230]. Dislocation densities of the order of 10^8 cm^{-2}, or higher are typically observed in AlGaN and/or InGaN heterostructures grown on sapphire, SiC and other foreign substrates. Approaches to reduce dislocation densities include insertion of a low temperature AlGaN/AlN layer [231, 232], pulsed atomic layer deposition technique to grow high quality AlGaN [233-235], and epitaxial lateral overgrowth (ELO) [236-238]. By ELO method, significant reduction in dislocation densities (~10^6 cm^{-2}) can be achieved in GaN and AlN film structures [233, 239]. However, with the latter approach, dislocation reduction mainly occurs primarily over the mask

regions instead of the entire film.

6.1.2 Different Growth Kinetics of Al Adatoms

AlGaN material system is different from GaN material system in terms of growth kinetics [230]. The sticking coefficient of Al is higher than that of Ga adatoms. Thus, during the epilayer growth process Al adatoms prefers to cause islands to nucleate, rather than forming steps by the incorporation of energetically favorable lattice sites. This in turn leads to dislocations and grain boundaries disrupting the epitaxial growth.

6.1.3 Inefficient *p*-doping

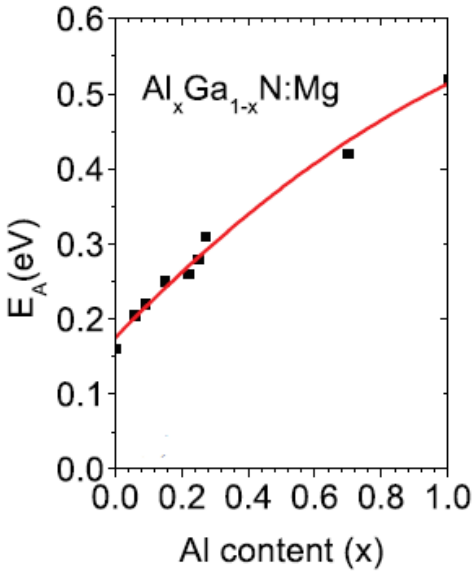

Figure 6.1 Mg acceptor activation energy level in AlGaN as a Function of Al composition for $Al_xGa_{1-x}N$ alloys [240].

Magnesium (Mg) is typically used as *p*-type dopant with III-nitride semiconductors. Also, with the increasing bandgap energies from InN (~0.65eV), GaN (~3.4eV) and AlN(~6.2eV), activation energies for Mg dopant also increase as well, *i.e.,* ~61 meV for InN, ~166 meV for GaN, ~550 meV for AlN [241]. Inefficient *p*-doping issue becomes

more pronounced in case of deep UV LEDs. Activation energy of a Mg acceptor in $Al_xGa_{1-x}N$ with x mole fraction from 0 to 1 increase from ~160 meV to ~500 meV, thus making realization of deep UV LEDs difficult [241]. The measured hole concentration in Mg-doped AlN epilayer is as low as ~10^{10} cm^{-3} because of this high acceptor ionization energy. Moreover, realizing *p*-type conduction in narrow bandgap $In_yGa_{1-y}N$ is severely limited by the commonly measured surface electron accumulation. Nevertheless, approaches like tunnel junction [242, 243], polarization induced hole doping [244, 245] and Mg-delta doping [246] has been proposed to increase the efficiency of *p*-type doping. Figure 6.1 depicts the activation energy of Mg acceptor as a function of Al composition [240].

6.1.4 Strong Polarization Fields and Unique TM polarization of the Light Emission

One of the major issues with realizing high performance deep UV and deep visible LEDs and lasers is the large polarization fields associated with the conventional c-plane of wurtzite III-nitrides. Optical emission is strongly polarized in the $Al_xGa_{1-x}N$ epilayers grown along c-axis. In other words, the electric field of photoluminescence of GaN is perpendicular to c-axis ($\boldsymbol{E}\perp\boldsymbol{c}$), which is referred to as transverse electric (TE) and that of AlN is parallel to c-axis ($\boldsymbol{E}\parallel\boldsymbol{c}$), known as transverse magnetic (TM) polarization. Furthermore, relative light emission intensity of the dominant TM polarization of the emitted light in $Al_xGa_{1-x}N$ compounds changes significantly with the varied Al composition. The TE and TM polarization crossover occurs at an Al molar fraction, *i.e.,* x value of 0.25 [247]. The polarization and subsequently the crossover thus depend on the internal electric field and strain present in the structure [248-252]. This unique light TM polarization property of $Al_xGa_{1-x}N$ prevents top surface light extraction from conventional c-plane Al-rich AlGaN UV LEDs, thus drastically degrading LED performance.

6.2 Research Motivation Behind UV Based III-Nitride Nanowire LEDs

GaN based LEDs are among the most promising next generation of solid state light sources which exhibit several advantages such as long lifetime, energy saving, compact size and environment friendly [36, 57, 253-260]. GaN based LEDs are applicable for various photonic applications with respect to their wavelength emission from deep UV to near infrared by tuning the compositions of their device active regions, consequently, altering the material band gap energy [15, 24, 261-263]. Recently, UV LEDs represents a potentially large market/customer base on water/air/surface purification and disinfections, and many other areas. The primary markets for these devices include bio-medical and analytical instrumentation, fluorescence sensing, curing, phototherapy and water/air/surface purification and disinfection [264-267].

The realization of efficient nanowire LEDs has been limited in the UV ranges because of the performance degradation with increasing Al composition due to the extremely low EQE, which is directly related to the UV light absorption in the Ga(Al)N p-contact layer [267] and, the unique transverse magnetic(TM) polarization properties of high Al composition AlGaN quantum wells (QWs) [251, 268]. Although the LEE of current UV LEDs is limited at <10% [193, 269], using nanowire structures could overcome the poor performance of such UV emitting devices. Moreover, due to the large surface to volume ratio, the LEE is expected to be tremendously improved in nanowire LED devices. We have recently reported the enhanced LEE of AlGaN UV LEDs by using nanowire structures [270] in which emission wavelength at 280 nm was considered.

Though, the LEE of UV LEDs have been enhanced by nanowire structures, the strong material absorption are not negligible especially at the short wavelength range such as deep UV (<280 nm). The performances of GaN based LEDs falls short of what is

expected due to material absorption. The material absorption is determined by the imaginary part of the dielectric constant which leads to the lower LEE due to the light being absorbed inside the UV LEDs. Photons emitted from active region may be either trapped or absorbed inside the UV LEDs. This shows that improving LEE and diminishing light absorption of UV LEDs have thus become the recent focus of researches [224, 271, 272]. The nanowire structures, which have large surface to volume ratio, can reduce the material absorption and enhance the LEE in III-nitride UV LEDs due to increased light escape probability and decreased light propagation path inside nanowires. In this chapter, we focus our study on the material absorption and LEE enhancement in III-nitride deep UV LEDs. Finite-difference time-domain (FDTD) analysis [205, 273, 274] is thoroughly conducted inorder to elucidate the role of material absorption and how this reduces the LEE of GaN based UV LEDs for various parameters such as the radius and spacing of the nanowires. The FDTD calculations predicted the UV LED design with the specific nanowire radius and spacing can be utilized to develop the high efficiency III-nitride UVLEDs.

A compact, highly efficient, and high-power UV light-source with emission wavelengths below 350 nm has attracted great attention due to its wide range of applications. The primary applications of such UV emitters include remote detection of biological and chemical compound, cancer detection and fluorescence sensing or Raman [253]. The possibility of generating light sources using GaN based LEDs for photonic applications, with emission ranging from deep UV to near infrared by tuning the material bandgap makes them the versatile materials in the photonic industries [24, 142, 178]. Optoelectronic devices working in the deep UV spectral region are being sought out because of their potential applications in disinfection [45, 46], water purification [47, 48], medical/biomedical instruments, and high-density optical LASER for recording [275].

In contrast to the existing bulky and hazardous mercury UV lamp sources, UV LEDs offer high efficiency [20, 276] and specific features like wavelength selectivity, compactness [256, 257] and environmental-friendly light sources which make them a better choice to replace the future era devices. UV-B (290 - 320 nm) range of wavelength has been sought out for its capability of generating vitamin D in our body through exposure [277, 278]. Moreover, UV-B emission is widely used for phototherapy which involves treatment of the skin, by exposing it to a UV-B source of light [279, 280]. The latter procedure is extremely useful to treat various diseases ranging from skin cancer, psoriasis, stimulating wound healing, stimulating the immune system and DNA analysis [277, 278]. This particular spectrum has also found its use almost exclusively in the skin tanning industry. The UV-B lights, when incident to the skin, activates a pigment called melanin in epidermal skin, which aids or accelerates the process of tanning [281]. Devices used traditionally for producing UV spectra of light are large and bulky, like UV lamps consisting of mercury. These devices exhibit low efficiency and lack of flexibility as well. The alternative approach for UV sources using highly efficient AlGaN nanowire heterojunction structures seems to be far superior [242, 244, 282].

To improve the performance of LEDs, their external quantum efficiency (EQE), which is directly proportional to the product of internal quantum efficiency (IQE) and light extraction efficiency (LEE), must be enhanced. Approaches that include patterned substrates [267], rolled up nanotubes [283], surface roughing [284] and photonic crystal patterns [271] have been used in the past to enhance the LEE of UV LEDs. In this regard, the III-nitrides targeted to reach the latter goal of UV LEDs has been limited by performance constraints on account of their extremely inefficient p-type doping [285, 286] due to only small fraction of Mg being activated at room temperatures, large dislocation

density [287], which lead to low efficient, low output power LEDs. On account of this, III-nitride nanowire based UV LEDs exhibit exceptional performance compared to AlGaN based thin-film UV LED structures resulted from the significantly improved light output power due to drastically reduced dislocations and polarization fields, and better effectiveness in p-type doping. Such great advantages pave the way for a candidate in boosting the IQE of UV LEDs [21, 288]. In this context, we have fabricated high performance LEDs with emission wavelength can be tunable from 290 nm to 330 nm grown by molecular beam epitaxy (MBE). The devices exhibit relatively low resistance with excellent current-voltage characteristics. The electroluminescence (EL) spectra show negligible blue-shift under injection current from 50mA to 400mA, proving that the nanowire UV LEDs exhibit strong and stable emission with significantly reduced polarization fields and negligible quantum-confined Stark effect [67, 148]. Moreover, using periodic nanowire structures, we have shown that, the UV LEDs can achieve high LEE of ~ 89% and 92% for emissions at 290nm and 320nm, respectively. The randomly arranged nanowire UV LEDs exhibit high LEE of ~ 56% which is higher compared to current AlGaN based thin-film UV LEDs at similar wavelength emission.

6.3 Structural Optimization and Simulation for UV-B Nanowire LEDs

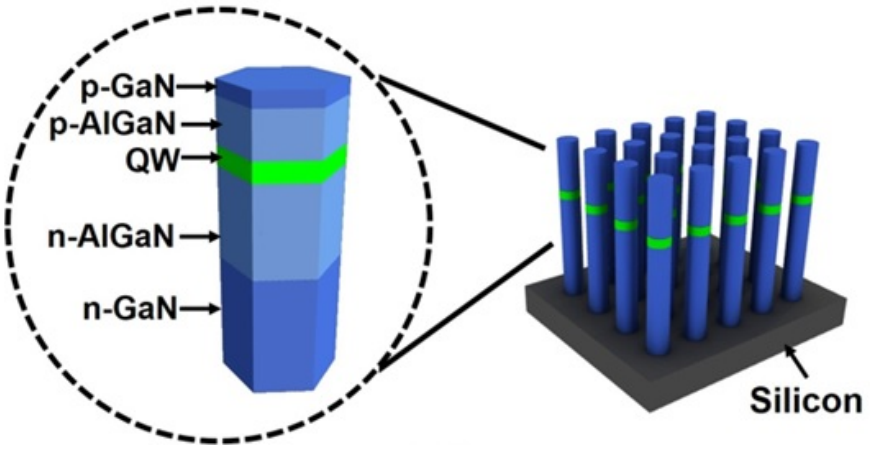

Figure 6.2 Schematic illustration of GaN based nanowire UV-B LED structure with inset image presenting the detailed structure of n-AlGaN layer, a quantum well active region, a p-AlGaN layer, and p-GaN layers.

Three-dimensional Finite-Difference Time Domain (FDTD) simulation is employed to analyze and calculate the LEE of the UV LEDs. The nanowire LED heterostructures are designed with emission wavelength in the UV-B band. The nanowire UV LED structure is schematically shown in Figure 6.2. The array is abab (hexagonal) form. Each nanowire consists of 250 nm n-GaN, 100 nm n-AlGaN, 60 nm quantum well (QW), 100 nm p-AlGaN and 10 nm p-GaN. The underlying substrate is Si (111). The device spans 2.5 μm × 2.5 μm, enclosed in 12 perfectly matched layers (PML) to absorb outgoing waves without causing any unwanted reflection of boundaries [289, 290].

The parameters of PML (attenuation factor (sigma)) and (auxiliary attenuation coefficient (kappa)) are set to 0.25 and 2, respectively. *Via* Lumerical adaptive meshing [291], the minimum mesh step size was set to 0.25 nm. The source to replicate the excitation was a single dipole source with Gaussian shape spectrum, and TM mode (electric field parallel to nanowire axial direction) is placed in the nanowire in the middle of the

nanowire array, in the middle of the active region. In AlGaN LEDs, the electric field direction parallel to the c axis which accounts for TE polarization which is the prominent emission in UV-B LEDs [251, 270] is taken into perspective. The simulation wavelengths are chosen to be 290 nm and 320 nm to cover the UV-B. The ratio of the power emitted from the side surfaces of the LED to the total emitted power of the device active region is considered as the LEE.

To understand the dependency of LEE on the nanowire parameters including radius and spacing, a contour plot relating these three parameters can be seen in Figures 6.3(a) and 6.3(b). A relatively high LEE (92%) is acquired at a center to center spacing of ~170 nm and radius of 65 nm for emission at wavelength equal to 320 nm. Similarly, LEE of ~89% was calculated for nanowire UV LEDs with emission at 290 nm when the radius and spacing value are ~62 nm and 186 nm, respectively. The enhanced LEE values especially from lateral sides of the nanowire structure arises due to the mode coupling within the nanowires. During the generation of coupled modes, light propagates horizontally through the nanowires and thus can be extracted.

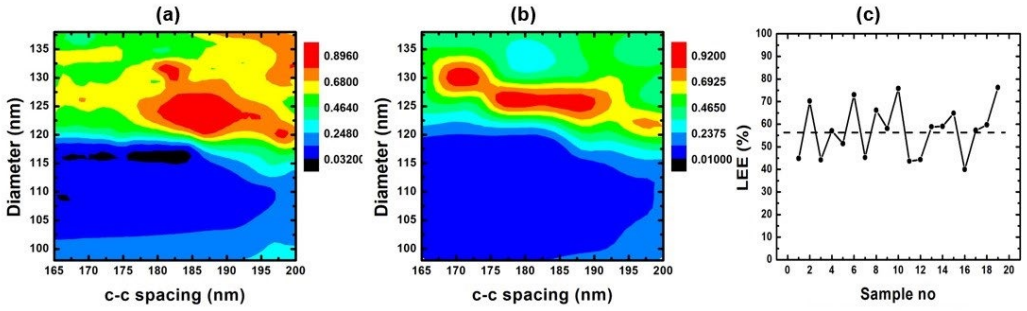

Figure 6.3 The contour plots for AlGaN based nanowire UV-B emitters depicting LEEs with the radius ranges of 49–69 nm, and center to center (c-c) spacing ranges of 165–200 nm with light sources of (a) 290 nm (b) 320 nm and (c) LEE for 19 different random structures with different nanowire diameter and nanowire spacing between them for a light source of 290 nm.

To replicate identical scenario to the fabricated nanowire structures *via* MBE spontaneous growth in which the nanowire diameter is varied in a range of 5%, we introduced a randomness of around 5% thus generating non-periodic structures with different nanowire radius and spacing and computed the LEE, as plotted in Figure 6.3 (c). The LEE of the random UV-B LED structure with a tolerance of 10% from the optimized conditions for LEE has an average LEE of ~56 %. This LEE value is lower than the periodic structures, however, it is still a high value in comparison to the existing UV-B LEDs at the same emission wavelength. This variation in LEE can be explained by the LED device switching within and outside the photonic band gap modes. The nanowire LED periodic arrays can be considered as active photonic crystal structures. Yet, photonic crystals themselves are utilized in photonic bandgap regions whereas the nanowire LED periodic array is utilized in the non-bandgap regions.

Photonic bandgap regions are sets of wavelengths prohibited from propagating throughout the structure. Since the nanowire LED arrays prefer non-bandgap regions, light propagates through the structure into surrounding air. Depending on the need of application, the nanowire photonic crystal structures have multiple operating regimes, namely, light confinement regime, which is used for lasers, and light transmission regime, used in LEDs [270]. Nanowires with varying diameter and spacing result in the formation of different wave vectors, and hence distinctive degrees of transmission at corresponding wavelengths. The low side LEE (blue area) represents the photonic bandgap region of periodic nanowire arrays or the inhibition of light propagation through the structure.

The FDTD simulation utilized to acquire information about LEE of diverse nanowire array diameter and spacing used Particle Swarm Optimization (PSO). Therefore, careful

control over spacing and radius is to be exercised to endure least possible total internal reflection at the semiconductor-air interface, which would aid the light to escape the device leading to a higher LEE and reduced material absorption in the deep UV LEDs [292]. The effect of variation in spacing and radius can be seen by examining the contour plot. The LEE varies from 1% to 90%. The reason for this can be accounted to the formation of coupled modes, leading to a jump in LEE.

6.4 AlGaN Periodic Nanowire UV LEDs

Figure. 6.4 shows the schematic of AlGaN based UV LED structure which is considered during the FDTD analysis for understanding the effect of optical absorption in deep UV nanowire LEDs. The LED structure includes an n-AlGaN layer, a multiple quantum well (MQW) active region, a p-AlGaN layer, and a p-GaN contact layer. Such nanowire arrays can be grown using the methods described in other works [293-295].

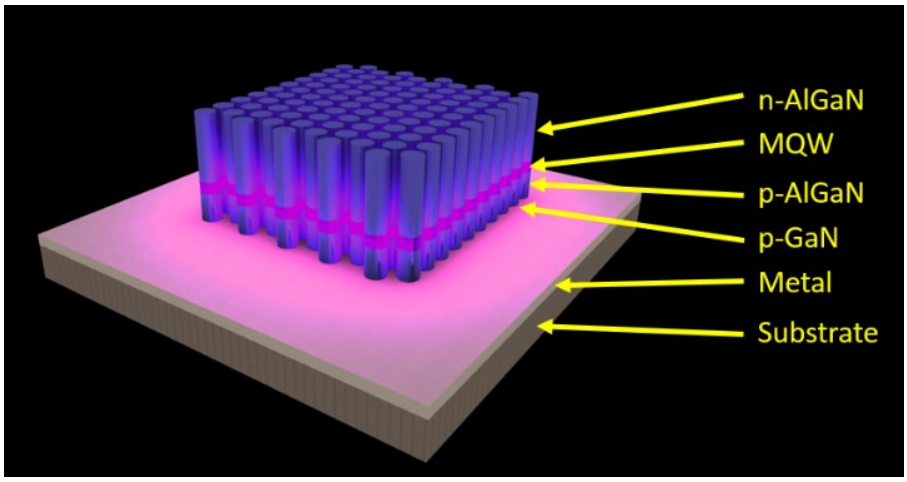

Figure 6.4 The 3D schematic of GaN based UV LED structure including an n-AlGaN layer, a multiple quantum well (MQW) active region, a p-AlGaN layer, and a p-GaN layer.

Additionally, selective area growth is considered as a matured technique for achieving highly uniform periodic nanowire arrays with precisely controlled radius and spacing [296, 297]. The nanowires geometry play an important role in directing the generated photons from active region to the air. In our simulation, the spatial grid sizes in the FDTD simulation were automatically assigned by Lumerical adaptive meshing [291, 298]. Compared to experiment results, some inconsistencies in the simulations can be induced considering the smaller device size which is adopted in the simulations due to limitations in computational resources. The simulated nanowire UV LED domain is 2.5 μm × 2.5 μm.

The perfect matched layers (PMLs) were employed as the absorbing boundaries all around the structures to avoid the undesired reflection of boundaries [289, 290, 299]. Although, the AlGaN MQW emit light in both transverse electric (TE) and transverse magnetic (TM) polarizations, the TM emission is dominant in AlGaN UV LEDs and increases significantly with increasing Al composition [251, 268].

The electric field directions are perpendicular and parallel to the c-axis for TE and TM polarizations, respectively. At short wavelengths ~240 nm, the optical emission of AlGaN LEDs is largely TM polarized. Therefore, the high LEE in deep UV nanowire LEDs is made possible by exploiting the lateral side emission properties of nanowires at the TM polarization. The significantly enhanced LEE from lateral sides of the nanowire structure is attributed to the mode coupling through the nanowires. When the coupled modes are formed, light propagates horizontally through the nanowires and can be readily extracted. The lateral side LEE is defined as the ratio of the output power observed around the side surfaces of the LEDs to the total power generated by the QW active region. When the material absorption is considered in AlGaN UV LEDs utilizing imaginary part of refractive

index, the LEE is estimated to be 34%, which is 30% lower than that of structure without considering material absorption. Such phenomena is a direct reflection of material absorption in this simulation.

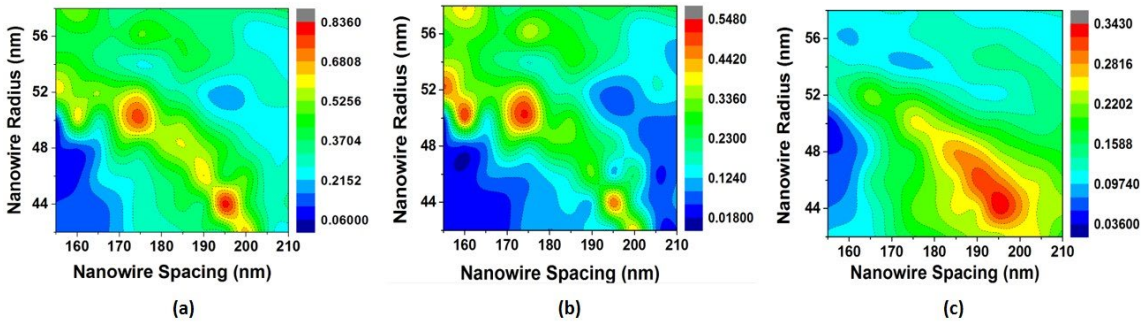

Figure 6.5 The contour plots show light extraction efficiencies with the radius ranges of 42 – 58 nm, and spacing ranges of 155 – 210 nm for (a) the structure without material absorption, (b) light power loss due to material absorption, (c) the structure with material absorption.

To provide a comprehensive understanding of LEE from nanowire UV LEDs, the contour plots constructed by LEEs with and without material absorption, and light loss due to material absorption were derived and presented in Figure. 6.5. In this regard, the variation in both nanowire radius and spacing between nanowires was introduced. The radius ranges of 42–58 nm, and spacing ranges of 155–210 nm were considered in this simulation. Shown in Figure. 6.5(a), the maximum LEE of 34%, which was calculated for the spacing of ~195 nm and nanowire radius of ~44 nm at wavelength of 240 nm. This is confirmed by the particle swarm optimization (PSO) process which is a population of random solutions [300]. It searches for the best solution by updating generations. In our study, a swarm includes 5 particles which represent a potential solution to LEE. The solution converged in 10 iterations, which means we perform the total number of 50 simulations.

The low side LEE (blue area) can be described by photonic bandgap of periodic nanowire arrays which inhibit the light propagation through the structure. For some maximum LEEs such as the spacing ~173 nm and radius of the nanowires ~50 nm, very high light absorption can be seen in Figure. 6.5(b) due to longer pathlengths of light propagation which leads the light stays more time inside the semiconductor and increase the light absorption. Consequently, it is highly required to shorten the light propagation path inside the nanowires which is applicable by smaller radius nanowires. Moreover, the observed light extraction enhancement can be from the large nanowires surface which reduce the total internal reflection and decrease the absorption of the material by the shorter propagation distance. Comparing Figure. 6.5(c) and 6.5(a), it reveals that the diminished LEE is attributed to light absorbed by absorptive material in nanowires. The simulation results approved that the material absorption is one of important factors which deteriorate the nanowire LEDs output power evidently.

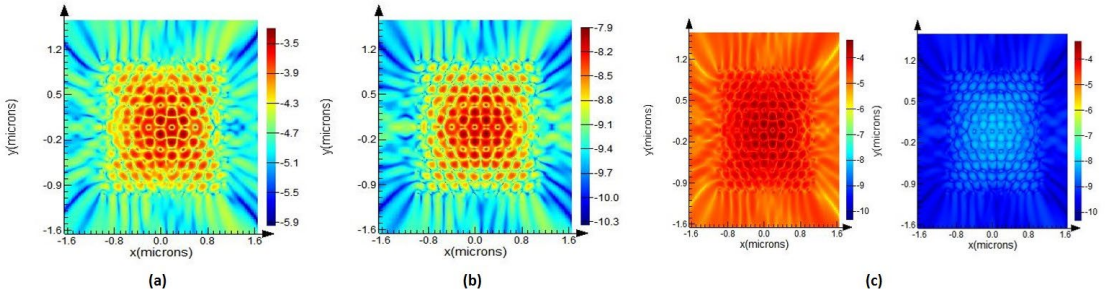

Figure 6.6 The simulated mode profiles with the optimized nanowire parameters for the spacing ~195 nm and radius of the nanowires ~44 nm for the UV LED (a) without and (b) with material absorption, (c) the simulated mode profiles with same intensity scale.

Figure. 6.6 shows the simulated mode profiles with the optimized nanowire spacing and diameter. It is seen that light can be mostly extracted from sides of device and it is nearly half for the LED with absorptive material compared to lossless LED.

The evanescent fields can be extended and produce a strong light propagation through the nanowires; thus, the LEE of the nanowire UV LEDs is significantly increased. Figure. 6.6(b) presents the simulated mode profiles for the UV LED with material absorption which has lower intensity compared to that of UV LED without material absorption, illustrated in Figure. 6.6(a). To clearly distinguish the difference between Figure. 6.6(a) and 6.6(b), the simulated mode profiles with same intensity scale are provided in Figure. 6.6(c). The light intensity for the structure with absorption is less than half compared to the lossless structure.

6.5 Dependence of LEE on the Position of Nanowires and Size of LED Devices

The LEE also depends on the device size. In order to gain further understanding of the relation between LEE and device size, we have performed simulation on devices with areal sizes in the ranges of Figure. 6.7. The simulated mode profiles with the optimized nanowire parameters for the spacing ~195 nm and radius of the nanowires ~44 nm for the UV LED (a) without and(b) with material absorption, (c) the simulated mode profiles with same intensity scale.2.5×2.5 μm^2–10 × 10 μm^2.

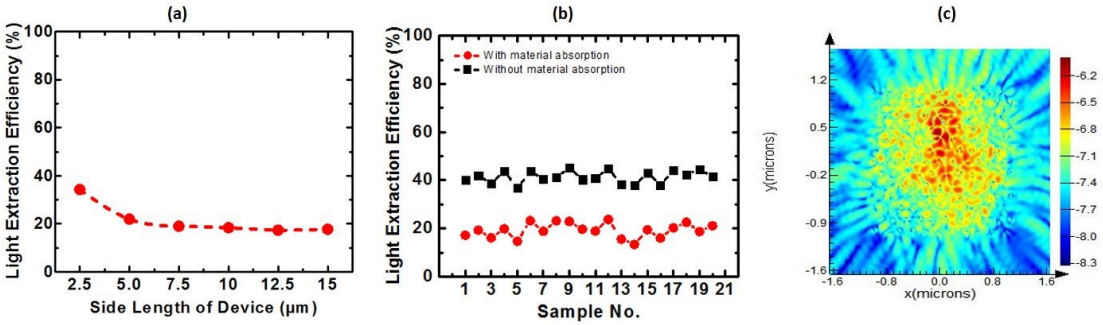

Figure 6.7 (a) Dependence of the light extraction efficiency on the various device sizes, (b) the light extraction efficiency for 20 different structures with random nanowire spacing and random nanowire radius, (c) the simulated mode profiles with the random nanowire spacing and radius.

Illustrated in Figure. 6.7(a), it is found that LEE is slightly decreased by increasing the device size, and the maximum LEE for device different device sizes decreases from ~34% to~18%. It is obvious that the LEE is less sensitive to the device size than other parameters such as nanowire radius and spacing. For practical applications, it is necessary to understand the dependence of the LEE on small variations of nanowire proper-ties due to the fabrication tolerances. The LEE is calculated for twenty distinct random structures as shown in Figure. 6.7(b). First, the spacing and radius of the nanowires are fixed at 195 nm and 44 nm, respectively. Then we introduced a ±10% random variation in the nanowire radius and spacing between nanowires. With such a random distribution, we observed that the average LEE for the nanowire devices with and without absorption are 19% and 41%, respectively. Figure 6.7(c) shows the simulated mode profiles with the random nanowire spacing and radius. It is seen that some local cavities are formed which confine and localize light inside the UV LED structure. It should be noted that the LEE of 19% is still nearly two times higher than deep UV LEDs which is previously reported with maximum external quantum efficiencies of <10%. With well-controlled growth and fabrication process, it is

expected that the LEE of deep UV LEDs can become comparable to that of high efficiency visible LEDs.

6.6 Experimental Details

The AlGaN nanowire UV-B LED heterostructure, illustrated in Figure 6.2, was spontaneously formed on Si (111) substrates under nitrogen rich conditions by a Veeco Gen-II MBE system equipped with a radio-frequency plasma-assisted nitrogen source. The nanowire diameter and density can be controlled by controlling the substrate temperature and/or Al/Ga flux ratios, while the nanowire length was varied mostly by the growth duration. The nanowire size was selected according to the results obtained from the simulation/design task.

Figure 6.2 depicts the schematic structure of GaN/AlGaN UV-B nanowire LED structure on Si substrate. The inset of Figure 6.2 presents the detailed structure of LED. The device fabrication route of AlGaN nanowire UV LEDs involves the following steps. Initially, for planarization and passivation, the nanowire arrays were spin-coated with polyimide resist solution, illustrated in Figure 6.8(a). This was followed by O_2 dry etching to expose the top region of the nanowires, shown in Figure 6.8(b). Metal contact layer including Ni (5 nm)/Au (5 nm)/indium tin oxide (ITO) was then deposited to the exposed GaN:Mg surface to form top metal contacts. Shown in Figure 6.8(c), Ti/Au (10 nm/100 nm) and metal-grid Ni/Au (10 nm/100 nm) layers were then evaporated on the backside of the Si substrate and top of ITO to form the backside and topside contacts, respectively.

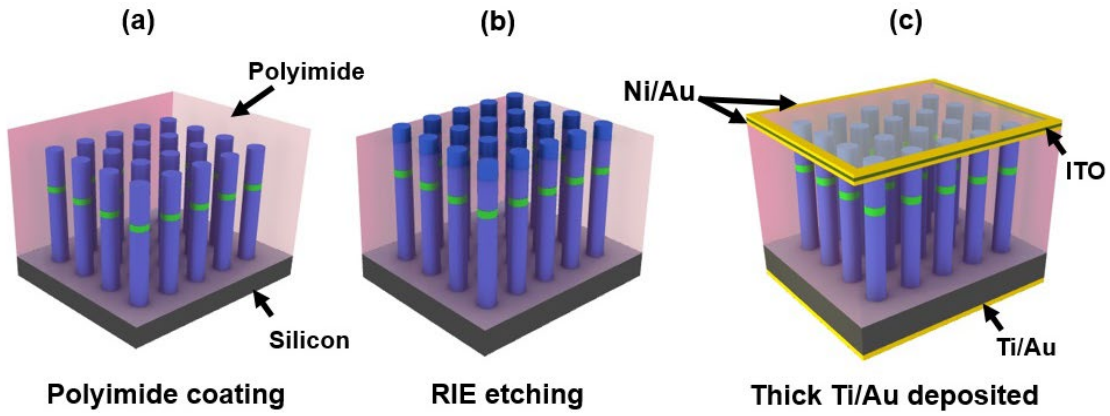

Figure 6.8 Fabrication Procedure of UV-B Nanowire LEDs on Si Substrate.

Additional information regarding the MBE growth and device fabrication of such nanowire LEDs can be found in similar works [24, 178]. Surface morphology of the UV nanowire LED heterostructures was studied by scanning electron microscopy (SEM). The nanowire UV-B LEDs exhibit quite uniform surface morphology and high density, as illustrated in Figure 6.9.

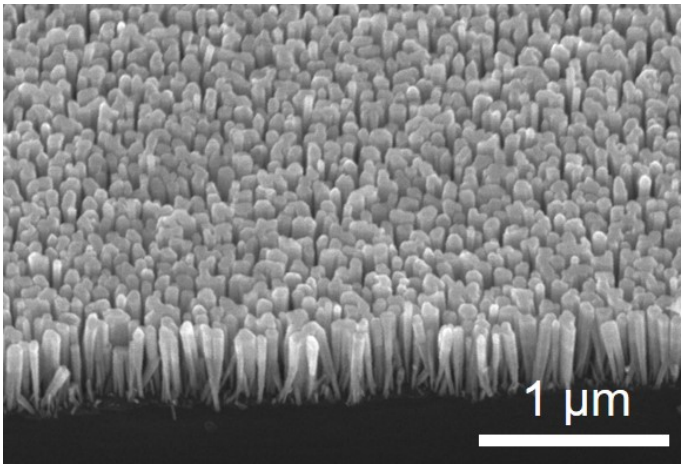

Figure 6.9 45^0 Cross-sectional SEM image of nanowires grown on silicon wafer.

6.7 Results and Discussion

Optical properties of AlGaN nanowire UV LEDs were examined using a 266 nm diode-pumped solid-state (DPSS) Q-switched laser as the excitation source. The duration, maximum energy, and repetition rate of the laser pulse are 7ns, 4uJ and 7.5 kHz, respectively. To eliminate the emission from the excitation laser source, a long pass filter (> 270nm) was placed in front of the spectrometer.

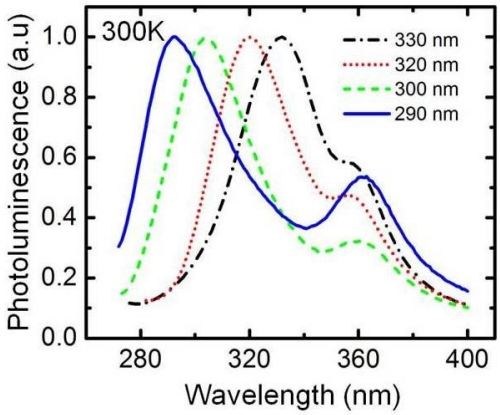

Figure 6.10 Normalized room temperature photoluminescence spectra of UV-B lights at 290 nm, 300 nm, 320 nm and 330 nm from multiple AlGaN nanowire LEDs.

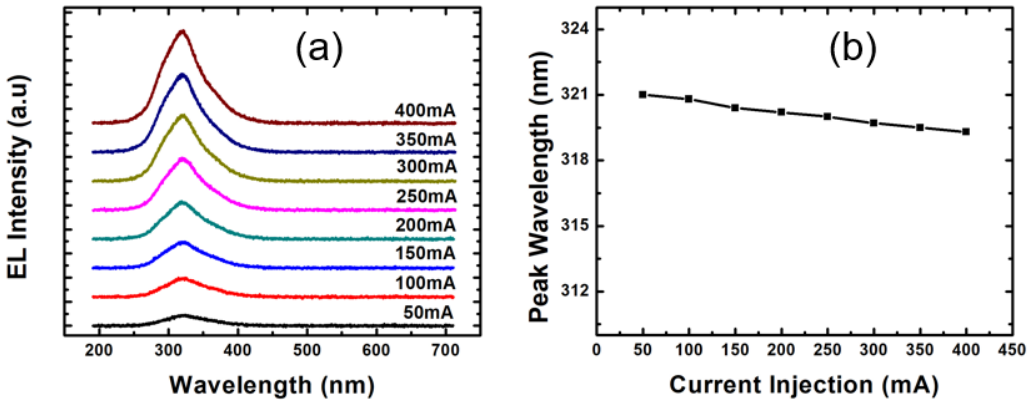

Figure 6.11 (a) Electroluminescence Spectra of GaN/AlGaN Based UV-B Nanowire LED from 50 mA to 450 mA (b) Variation of Peak Wavelength with Current Injection.

Figure 6.10 presents the room temperature PL spectra of nanowire LEDs with the peak wavelengths were measured at 290 nm, 300 nm, 320 nm, 330 nm, respectively. As seen from the corresponding plots, the peaks match the designed wavelength of the light excited from the nanowire LEDs. Alteration of Al composition in the AlGaN quantum dots can be achieved either by using different growth temperatures and/or Al/Ga flux ratios. In the room temperature PL spectra, Al composition increases for a lower wavelength (or higher bandgap material) emission in the electromagnetic spectrum. Thus, for tuning the emission from 290 nm to 330 nm UV-B regime, Al composition is increased in the active regions. The emission peak at ~ 365 nm is corresponded to the emission from GaN segment.

Figure 6.11 shows the EL spectra of the AlGaN nanowire UV-B LED with emission wavelength at 320 nm. The EL spectra were measured at room temperature using the Ocean Optics spectrometer (USB 2000) at injection currents from 50 mA to 400 mA for device area of 500μm × 500μm. The devices were measured under pulsed biasing conditions (~1% duty cycle) to minimize junction heating effect. The EL spectra exhibits a singular peak at around 320 nm which corresponds to the emission from the AlGaN quantum well, shown in Figure 6.11(a). Additionally, illustrated in Figure 6.11(b), the emission peak position shows very small shifts (1.5 nm) with increasing injection current, emphasizing the presence of a negligible polarization field due to the effective strain relaxation. It can be observed that the device shows a stable and strong emission at 320 nm independent of injection currents even with the absence of emission on the visible wavelength range; which was observed in AlGaN QW based UV LEDs, due to the deep level defects in AlGaN [301, 302]. This clean EL spectrum is crucial in the improvement of the signal-noise ratio.

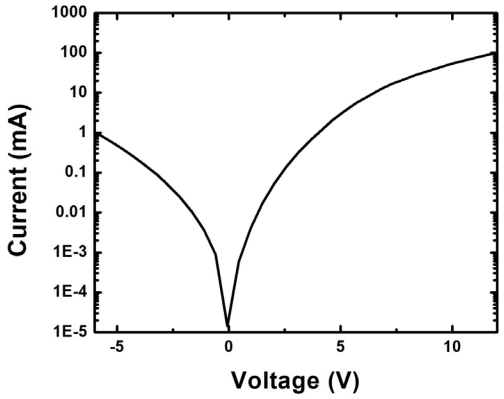

Figure 6.12 Current–Voltage Characteristics of the AlGaN Nanowire LED.

Current-voltage characteristics of the UV LEDs are depicted in Figure 6.12. The defect density, internal electric field induced quantum confined Stark effect and polarization field, are minimized in nanowires in contrast to thin films, resulting in perfect diode performances with very low leakage current which is <1mA at reverse voltage of ~ -6V. The sharp increase of current in the forward bias confirms excellent current-voltage characteristics with low resistance. The leakage current can be attributed to the leakage paths arising due to the inadequate insulation between the nanowires and the polyimide resist as well as due to carrier recombination happening in active region of LED near the nanowire sidewalls due to surface states present [303].

6.8 Summary and Conclusions

In summary, we have demonstrated high performance UV-B LEDs using novel AlGaN nanowire LEDs with high crystal quality on a large silicon substrate. The LEE of such nanowire UV-B LEDs has been significantly improved. The UV LEDs hold strong EL intensity with negligible blue shift. This study addresses some of the major issues with

reference to the practical applications of nanowire LEDs and provides a novel perspective of having high efficiency UV-B LEDs with tunable emission for medical applications.

We have presented the design of periodic nanowire deep UVLEDs and investigated the role of material absorption using 3D FDTD simulation. While the emission of the guided modes can be avoided and redirected into radiated modes utilizing nanowire structures, the light extraction can be decreased by light absorption due to absorptive materials. Through a comprehensive investigation of different parameters including the nanowire size, density as well as the LED device size, we have shown that an unprecedentedly high LEE of ~34% can be achieved. Although we have considered periodic nanowire UV LEDs with high LEE, UV LEDs with random structure can exhibit ~19% which is comparable to that of high efficiency planar UV LEDs. With properly designed nanowire structures, the UV light absorption can be reduced, resulted in the enhanced LEE in III-nitride deep UV LEDs. This study provides important information for the design of high performance opto-electronic devices operating in the deep UV wavelength regime.

CHAPTER 7

POLYOL SYNTHESIS OF ZINC OXIDE-GRAPHENE COMPOSITES: ENHANCED DYE-SENSITIZED SOLAR CELL EFFICIENCY

This chapter reports on the fabrication and characterization of Zinc Oxide (ZnO) and Zinc Oxide- Graphene (ZnO-G) composites *via* a simple chemical route-polyol process, using zinc nitrate hexahydrate, ethylene glycol and reduced graphene oxide (RGO) as the precursors [304]. The ZnO-G composites exhibit significantly enhanced photoluminescence, which is ~ 8 times stronger than that of ZnO samples. Such improved optical property is attributed to the contribution of plasmonic effect of graphene in ZnO-G. Moreover, the high crystalline quality ZnO-G composites hold great potential for dye-sensitized solar cell (DSSC) applications. The short-circuit current density was increased in the ZnO-G solar cell compared to that of bare ZnO device, which is around 1.930 mA/cm^2 and 0.308 mA/cm^2, respectively. The conversion efficiency of the ZnO-G DSSC was measured as 0.438%, which is ~ 7 times higher than that of ZnO DSSC. The enhanced conversion efficiency achieved in ZnO-G DSSC resulted from the enhanced absorption and large surface area of the composite compared to ZnO. The synthesized flakes like ZnO and ZnO-G composites offer promising materials for DSSC applications.

7.1 Research Motivation behind Zinc Oxide-Graphene Composites

Metal oxides have been found to be an emerging area of interest for the past few decades because of its superior properties including high thermal resistance, electronic, catalytic and optical properties. Metal oxides, therefore, are inevitable for most of the semiconductor, gas sensor, thin-film technology, biomedical as well as in heterogeneous

catalysis applications. Among metal oxides, ZnO is the most prominent multifunctional semiconductor material that can be fabricated at low temperatures [305]. The wide energy bandgap, high excitation binding energy, radiation resistance and high chemical stability makes it an interesting material for sensors [306, 307], light-emitting diodes (LEDs), short wave-length lasers, solar cells [308], piezoelectric devices [309, 310] and transistors [310, 311].

Different synthesis routes have been reported for the fabrication of ZnO nanostructures. Bitenc et al. developed hexagonal bipod like crystalline ZnO structures through a combination of polyol process and homogeneous precipitation by employing zinc nitrate hexahydrate and urea as starting materials [312]. Through ultrasonic reaction of zinc nitrate hexahydrate and hexamethylenetetramine, Pholnak et al. developed octahedral ZnO structures with excellent optical properties [313]. Morphologies of ZnO can be controlled by adjusting the temperature of the reaction as well as the concentration and type of process employed. ZnO particles in the form of wires [309, 314], sheets, needles, flowers, cups, multipods [312], octahedrons, pyramids and disks [315] have been developed through various methods like polyol method [316], sonication, chemical reduction and sol gel method [317].

ZnO materials have been made into composite/hybrid materials along with other metallic as well as graphitic structures to enhance their mechanical and piezoelectric properties. Li et al. improved the field emission of graphene by depositing ZnO nanorods on graphene surface by means of chemical vapor deposition [318]. These ZnO nanorod hybrid structures were shown to have efficient field emission with low threshold field, high field enhancement factor and excellent emitting stability. Recent studies have shown that the introduction of ZnO nanorods on graphene surface can enhance tunneling probability

as well as the number of emitters, thereby improving the field emission. ZnO has superior optical and electrical properties that include high electron mobility in the order of 1500 $cm^2V^{-1}s^{-1}$ at room temperature, wide band gap energy of 3.3 eV and a high exciton (electron-hole) binding energy of 60 meV. However, to overcome the drawback of poor catalytic activity in ZnO due to its photoelectron recombination [319], we are incorporating graphene into ZnO matrix thereby improving its photodegradation efficiency [320] and reducing photoelectron recombination. The latter reasons along with ZnO-G composite's photosensitivity, electron transport capability, chemical stability and better light adsorption make it an interesting material we can even employ in the textile industry to remove dyes and other pollutants from sewage water, making the water reusable again. Graphene also exhibits superior properties like ultra-high electron mobility, large surface area, high chemical and thermal stability, excellent electrical and optical properties. Hence, it is incorporated into ZnO matrix making ZnO-G composites to improve its capacitance, field emission and photocatalysis properties as reported in other studies [321]. In a similar study,

Le et al. reported the enhanced optical property of ZnO due to plasmon resonance effect of the metal nanoparticles by implanting plasmonic copper nanoparticle in ZnO and post annealing treatment [322]. Moreover, intercalating lithium into two dimensional materials like molybdenum disulfide (MoS_2) showed plasmon resonances in the near ultraviolet and visible regimes [323]. MoS_2 materials have also been intensively studied as prominent candidates for electronic and photonic devices due to their unique electronic and optical properties [323-325].

In this work, we have fabricated hexagonal wurtzite structure ZnO and ZnO-G foams, using zinc nitrate hexahydrate, ethylene glycol and reduced graphene oxide (RGO) as the precursors. The ZnO-G composites exhibit significantly enhanced

photoluminescence and absorption compared to bare ZnO. The dye-sensitized solar cells (DSSCs) fabricated from ZnO and ZnO-G composites are characterized. The conversion efficiency of ZnO-G DSSC is greatly increased compared to the bare ZnO devices, which are 0.438% and 0.067%, respectively. The prepared materials were characterized by X-ray diffraction (XRD), Fourier transform infrared spectroscopy (FT-IR), laser raman spectroscopy, scanning electron microscopy (SEM), energy dispersive X-ray analysis (EDX), photoluminescence spectroscopy (PL) and DSSC device performance studies.

7.2 Materials and Method

7.2.1 Reagents and Materials

The starting materials zinc nitrate hexahydrate and ethylene glycol needed for the synthesis of zinc oxide foam were purchased from Sigma Aldrich. Graphite powder, Hydrogen peroxide (H_2O_2), HCl, and Hydrazine hydrate needed for the synthesis of RGO were also purchased from Sigma Aldrich. All the chemicals used throughout the study were of reagent grade purity. Distilled water was used throughout the experiment for the synthesis of RGO using Improved Hummers method.

7.2.2 Preparation of Zinc Oxide (ZnO) and Zinc-Oxide Graphene (ZnO-G) Foam

Figure. 7.1 depicts the schematic route for the synthesis of ZnO-G foams. Fluffy porous ZnO-G composite samples were fabricated using polyol process. Zinc nitrate hexahydrate, RGO and ethylene glycol reactants are initially sonicated for 15 minutes followed by introducing into a preheated 250^0 C cylindrical glass dish. The NO_2 gas evolution upon heating the sample resulted in the formation of highly porous ZnO-G foam. ZnO foams were synthesized in the same manner with the exception that RGO was not required.

Ethylene glycol in the sample reduces Zn^{2+} to Zn foam, thereby acting as a reducing agent as well as a pore-forming agent. The reaction in air and the high reactive nature of zinc ensure that it is further oxidized to ZnO foam.

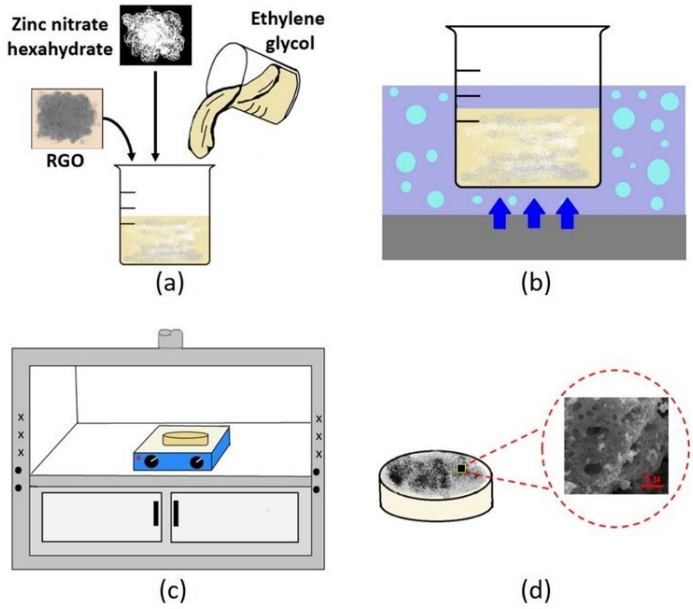

Figure 7.1 Schematic of polyol fabrication route of ZnO structure with (a) mixing of precursors including zinc nitrate hexahydrate, ethylene glycol and RGO (b) sonication of the reagent mixture for 15 minutes (c) burning of the reagent mixture at 250^0C on a hot plate kept in fume hood and (d) formation of highly porous ZnO-G composite with inset depicting SEM of same.

7.2.3 Fabrication of Graphite Oxide (GO) and Reduced Graphene Oxide (RGO)

Graphite oxide was synthesized using modified hummers method. 2 g of graphite powder was added to a mixture of phosphoric acid (40mL) and con.H_2SO_4 (98%, 360mL). The volume ratio of sulphuric acid to phosphoric acid was 9:1. Magnetic stirring was then carried out at room temperature for 10 minutes. It was followed by the gradual addition of powdered KMnO4. Stirring was continued for another 24 hours with temperature being maintained at 90^0 C. The solution mixture was then cooled in an ice bath to room temperature. 14mL of H_2O_2 was added to the latter solution while keeping the beaker in an

ice bath since the preceding reaction is a highly exothermic one and stirring was continued for another 3 hours. Graphite oxide (GO) solution becomes yellowish brown in color because of the loss in electronic conjugation of graphite powder brought by oxidation. Metallic manganese ions were removed from the latter GO solution by washing with dilute HCl (5%). During the following stages, the latter reaction mixture was washed with deionized water and ethanol until the pH of the product reaches neutral condition. The neutral pH brown GO residue, which was collected after the centrifuging process, was filtered through a 0.24μm filter paper by means of a vacuum pump. The latter GO residue films were then subjected to vacuum drying at 450^0 C for 24 hours, followed by grinding in an agate mortar.

The intercalated GO with covalently bonded oxygen and non-covalently bonded water molecules acts as a hydrophilic material because of its functionalities at the edges. RGO was then synthesized from GO by using hydrazine hydrate as a reducing agent. In the hydrothermal synthesis route, which we followed 0.2 g GO powder was treated with a mixture of 93mL of deionized water and 7mL of hydrazine, hydrate. The colloidal solution mixture formed by the 30-minute sonication of latter solution was then transferred to an autoclave, followed by heating to a temperature of 180^0 C for 12 hours. The thus obtained solution was washed with deionized water until neutral pH was attained for the fabricated RGO. The hydrophobic nature of RGO accelerates the later vacuum filtration and drying steps. Finely grounded RGO particles were obtained upon crushing of the latter dried RGO in agate mortar. The epoxide, hydroxyl, carbonyl etc. groups located apparently at the edges of the basal plane of GO layered structure were thus reduced using hydrazine hydrate, ensuring the formation of RGO.

7.2.4 Preparation of Electrodes for DSSC Studies

The synthesized ZnO and ZnO-G powders were made into a slurry/paste for DSSC cell fabrication by mixing 7 mL of ethyl cellulose aqueous solution with 3 mL of poly (ethylene glycol) in an agate mortar. The ZnO and ZnO-G slurries were then applied as thin films onto a FTO glass substrate using doctor blade technique. The working area of ZnO and ZnO-G films were 0.25 cm^2. Then the prepared films were air dried for 30 minutes, followed by annealing at 400^0C with an increment of 2^0C/minute and maintaining the latter temperature for 1 hour. The sintered active ZnO and ZnO-G electrodes were then immersed in an N-719 ethanolic dye solution for a duration of 4 hours at room temperature. The immersed electrode was then rinsed with ethanol, followed by drying at room temperature. The counter platinum electrode was prepared by the thermal reduction of hexachloroplatinic acid in isopropyl alcohol solution at 400^0C for 1 hour. By using a spacer, the separation was achieved between ZnO/ZnO-G photoelectrode and counter Pt electrode, sealing was performed by keeping the latter fabricated structure in a hot air oven at a temperature of 70^0C for a few seconds. Through the drilled hole in the counter Pt electrode electrolyte solution composed of 0.3 M lithium iodine and 0.03 M iodine in acetonitrile was introduced. At the end of the aforesaid-mentioned steps, the efficiency of the fabricated materials was calculated using a solar simulator under xenon light illumination with an intensity of 1 sun or 1000 W/m^2.

7.3 Experimental Section and Material Characterization

The fabricated ZnO and ZnO-G foams were subjected to various characterization and spectroscopic studies. The XRD analysis was done using a Bruker X-ray powder

diffractometer with Cu-Kα radiation (λ=0.154 nm) in the 2θ range of 10-70 degree. The diffractograms were then analyzed and compared with the standard JCPDS files. The FTIR spectra were recorded using Bruker Optic Gmbh, Tensor 27 Model in the range of 4000 cm^{-1} to 400 cm^{-1}. Here in this FTIR, we employed a Ge based coating on KBr as the beam splitter while source setting employed was middle infrared. The laser Raman spectra for the samples were investigated using Renishaw U.K, Invia Raman microscope. The source employed was He-Ne laser having an excitation wavelength of 633 nm and energy setting of 18 mW. The Raman spectra were collected using a back-scattering geometry within an acquisition time of 40 seconds. The morphology of the foam was examined with a scanning electron microscope (SEM, JEOL HITACHI Model S-3000H instrument), after having taken the foam from the dish. Resolutions of the order of nm were possible under high vacuum with an accelerating voltage of around 25KV using the equipment. Energy dispersive analysis (EDX) was carried out for the samples with the help of a separate EDS detector mounted as an attachment for the SEM equipment. Absorption measurements of the fabricated ZnO and ZnO-G samples were performed using Fischer scientific UV–visible spectrophotometer. PL measurements were carried out on a UV-VIS NIR double beam spectrophotometer (Model: Cary 5000 scan, PbS detector) under 275 nm excitation wavelength. The OCP (open circuit potential) variation of the fabricated ZnO and ZnO-G samples upon irradiation of UV light (wavelength 365 nm) over a span of 1 hour was measured through a 3-electrode system (employing fabricated ZnO-G as working electrode, platinum as a reference electrode and saturated Ag/AgCl as counter electrodes). DSSC current-voltage measurements were carried out using SS80 AAA Model solar simulator, with a light illumination intensity of 1 sun.

7.4 Results and Discussion

Figure. 7.2 which is composed of XRD spectra conducted across the fabricated samples clearly depicts the formation of ZnO and ZnO-G foams. The fluffy ZnO and ZnO-G composite foams are found out to be of good crystalline nature from Figure. 7.2. The relatively higher and sharper diffraction peaks can be attributed to the good crystallinity of ZnO and ZnO-G within the network structure.

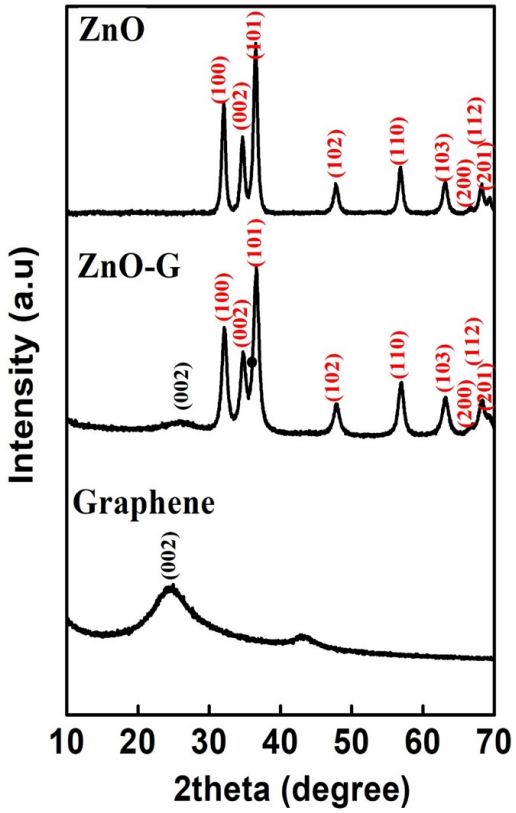

Figure 7.2 XRD spectra of fabricated ZnO, ZnO-G and RGO samples.

The strong diffraction peaks for ZnO are indexed such that 2θ peaks belong to (100), (002), (101), and (102) planes perfectly (JCPDS No: 361451) implying that hexagonal wurtzite phase ZnO foam is formed. The diffraction peak at $2\theta=23.9^0$

corresponds to the presence of (002) plane of π stacked hexagonal graphitic carbon/graphene in the foamy structure. The latter was having an interlayer spacing of 3.34A^0 corresponding to the van der Waal's distance for sp^2 hybrid carbon atoms [326].

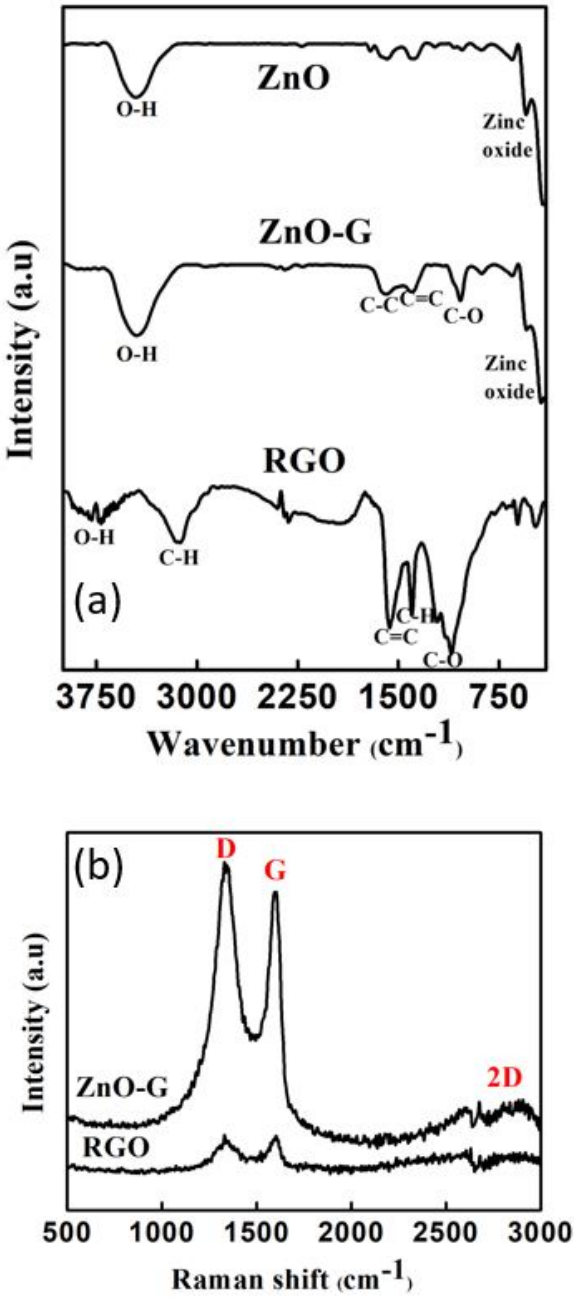

Figure 7.3 (a) FTIR and (b) Raman spectra of RGO and ZnO-G Samples.

Figure. 7.3 represents the FTIR and laser Raman spectra acquired for the samples. A small shift of around 4cm^{-1} is observed in the Figure. 7.3(a) laser Raman spectra of ZnO-G, datum being Raman spectra of RGO reaffirmed the chemical interaction between Zinc Oxide and reduced graphene oxide. The laser Raman spectra of 3-dimensional ZnO and ZnO-G foams as seen from Figure. 7.3(a) reveals that the porous fluffy ZnO-G material developed possess high quality graphene.

The laser Raman spectrum comprises mainly of G band and D band at 1334 cm^{-1} and 1598 cm^{-1}, respectively. The G band is associated to E_{2g} mode which refers to a measure of the vibration of sp^2 bonded carbon atoms in the hexagonal lattice, D band is attributed to the defects and disorder in the hexagonal honeycomb lattice of graphite.

Raman spectra gave an understanding of the degree of disorder within the graphitic lattice [327-329]. The shift in the Raman spectra for G band of ZnO-G in comparison to pristine graphene (1581cm^{-1}) can be associated to the structural distortion of graphene associated with different bonds of C-C, C=O, C-H etc. present in graphene. The appearance of a relatively lower 2D band suggested that the fabricated ZnO-G composite comprises of few layers of graphene. As shown in Figure. 7.3(b), the formation of ZnO and ZnO-G foams was confirmed by FTIR spectroscopy. The characteristic peaks around 545 cm^{-1} and 430 cm^{-1} observed in Figure. 7.3(b) corresponded to hexagonal wurtzite Zn-O. Typical stretching bands between 400 cm^{-1} – 600 cm^{-1} are reported to exist for pure wurtzite ZnO structure [312, 313]. Even though GO synthesized by modified Hummers method has been reduced into RGO by employing agents like hydrazine hydrate, still there will be some residual oxygen containing functional groups like O-H, C-OH in addition to the characteristic C=C bonds of graphene.

The FTIR spectra of RGO exhibited several distinct peaks at 1106 cm^{-1} (C-OH stretching vibrations), 1400 cm^{-1} (C-C stretch), 1569 cm^{-1} (C=C aromatic bending), 3158 cm^{-1} (C-H stretch). In addition, the band at 3460 cm^{-1} is associated with the stretching of hydroxyl (OH) group and the band at around 1608 cm^{-1} is related to C=C stretching within the graphitic domain. In ZnO-G composite, graphene incorporation into the ZnO matrix structure was clearly evident from the FTIR spectra. The high intensity of O-H might have been attributed to the presence of ethylene glycol acting as a protective agent on the surface of zinc oxide foams. There also arises a slight chance that one of the O-H groups of ethylene glycol interacts with ZnO surface getting adsorbed, enhancing the intensity of O-H bond in FTIR spectra [312, 313, 330].

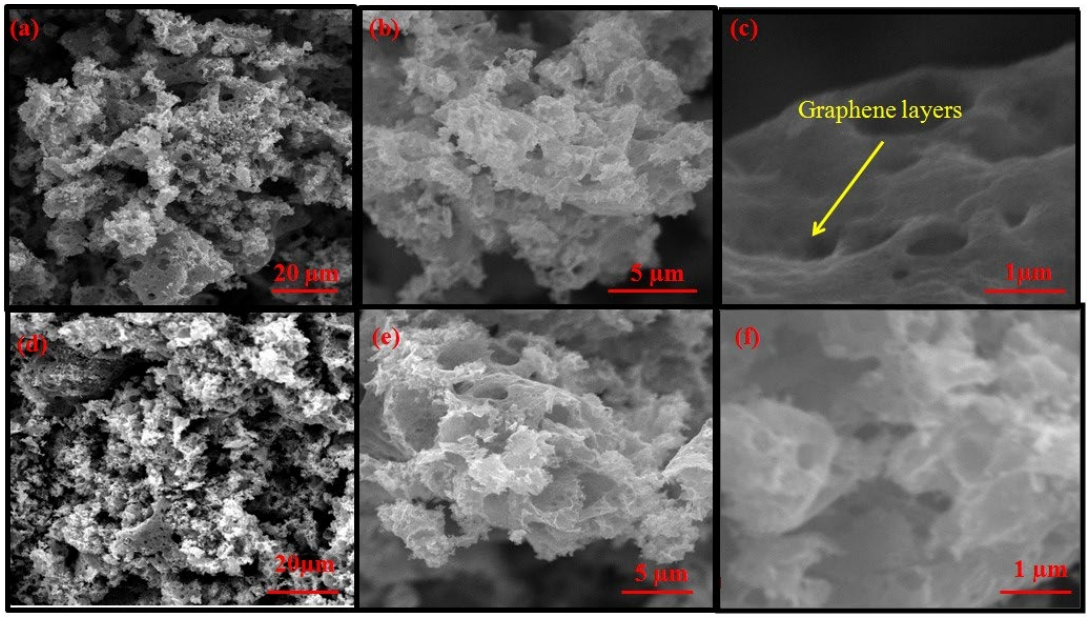

Figure 7.4 SEM micrograph of (A-C) ZnO-G composite and (D-F) undoped ZnO samples.

Figure. 7.4 depicts SEM images of ZnO and ZnO-G foams. SEM image revealed that the fabricated foam is a continuous porous structure with the appearance of flake/leaf like structure with pores at the surface and extended towards the interior. The SEM images

confirmed that spherical open pores of the order of nanometer and micrometer size are present in the sample, reaffirming our claim that the fabricated ZnO and ZnO-G foams are highly porous. In the presence of reducing agents like ethylene glycol the nuclei generation and growth are not controlled that much when compared to using powerful reducing agents like sodium borohydride and hydrazine hydrate. The latter reason results in the agglomeration of ZnO particles to acquire three-dimensional foam like structure as shown in the SEM images. High surface tension and high surface energy of zinc growth nuclei and nanoparticles also might have played a prominent role during the agglomeration of ZnO. Upon high magnification of the SEM micrographic of sample ZnO-G, we were able to visualize that fluffy graphene foam is composed of few graphene layers as witnessed earlier from Raman spectra. The ripples and wrinkles on the graphene film surface arise mainly because of the difference in thermal expansion coefficients between zinc oxide and graphene.

The chemical treatments like strong oxidizing by $KMnO_4$ and H_2SO_4 during modified Hummers method subjected on the graphite sample during the formation of GO also plays a significant role on the morphology of graphene films within ZnO-G. The nano sized pores might also improve BET surface as well as play a mighty role during electrochemical performance. Majority of ZnO foams appear to have been uniformly coated with graphene although only a comparative quantity of RGO was mixed with the precursor solution as starting material. Only few graphene nanosheets appeared on the surface morphology of ZnO-G composites. The aforesaid-mentioned phenomenon suggests that majority of reduced graphene sheets might have been embedded into the structure as a scaffold for ZnO structure as shown in the corresponding SEM image. Moreover, we cannot hinder the stacking tendency of graphene sheets to a complete extent.

The latter reason resulted in the generation of few-layer graphene films as reported in the literature. This drawback has been avoided by an extent by careful and controlled incorporation of graphene sheets. The pH of the reactant solution will have a major contributing effect to the morphology-shape and size of the particles.

The chemical compositions of ZnO-G foams which were conducted using EDX spectroscopy are depicted in Figure. 7.5. From EDX and laser Raman results, it clearly shows that graphene is incorporated into the ZnO matrix. ZnO foam is the source for the strong presence of zinc and oxygen. Hydroxyl groups produced during the reduction of GO and incomplete combustion of ethylene glycol served the purpose of capping around ZnO and graphene structures. Thus the generated OH groups might also have contributed to the oxygen presence.

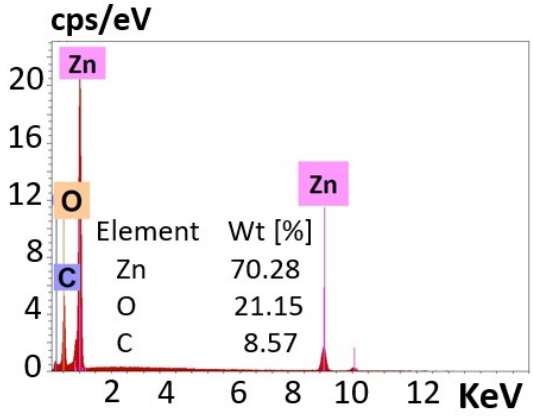

Figure 7.5 Elemental EDS analysis for ZnO-G sample.

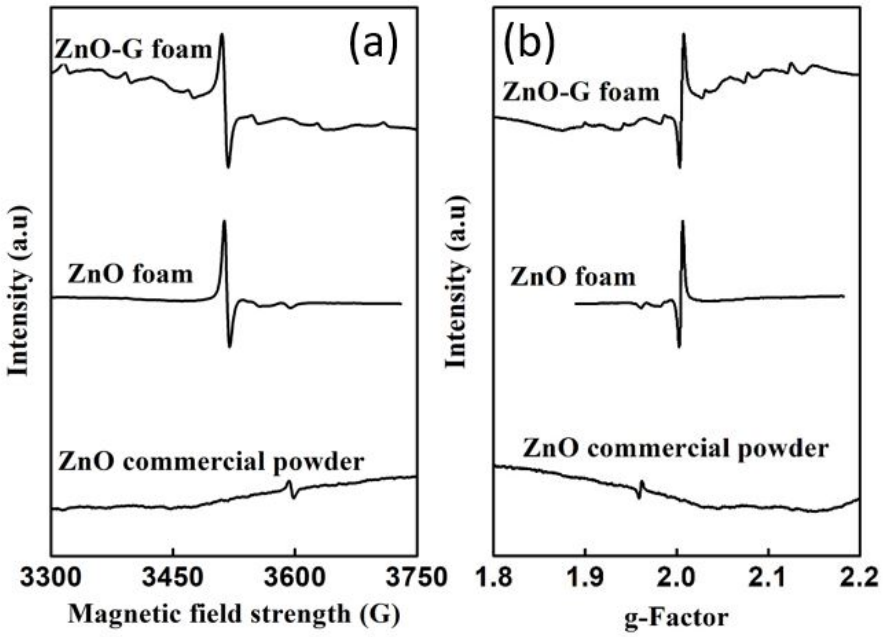

Figure 7.6 Comparison of the EPR Spectra for fabricated ZnO and ZnO-G samples w.r.t commercial ZnO powder.

EPR measurement shown in Figure 7.6 is a sensitive and direct technique by which we were able to able detect paramagnetic impurity atoms along with studying their change in magnetic states upon excitation by optical light. The prominent g=1.96 line observed in commercial zinc oxide samples might be arising from positively charged oxygen vacancy as well as due to the conducting electrons situated within the surface centers and donor centers existing in bulk ZnO particles. The g=1.96 line is photosensitive and hence we can employ it for monitoring the photoexcitation of electron arising from deep level centers in the ZnO gap. EPR thus helps us to characterize the magnetic properties of defect centers even on an atomic scale within the ZnO structure [331].

Possible defect centers in ZnO can be mainly classified as zinc vacancies, oxygen or interstitial sites, zinc on interstitial sites and oxygen vacancies. The commercial ZnO sample intrinsic defect g factor line at 1.96 has been given various explanations with respect to single ionized oxygen vacancies, assignments to shallow donors, zinc vacancies

or oxygen interstitials [332]. So, the controversy has been resolved partially by assigning the signal at 1.960 to a core signal within the core-shell framework model by researchers. The line shape of core signal has been reported to change with fabricating time suggesting strong size effect because of the phenomenon of confinement of electrons within the core. A single ionized zinc vacancy can be assigned to the EPR signal at g=2.00 as in the case of bulk ZnO we have fabricated here through polyol process. The latter mentioned g factor peak at 2.00 can also be accounted to an unpaired trapped electron on an oxygen vacancy site. It has been suggested based on Density functional theory (DFT) calculations reported by various researchers that the oxygen vacancies at the ZnO surfaces are stable and could trap electrons to generate paramagnetic (F^+ centers). The latter reasoning can thus account for the EPR g=2.00 signal peak. EPR yields information on the defect surroundings [333].

Based on the EPR results obtained, we can assume a core shell of ZnO as reported by many, in which the hexagonal core is composed of negatively charged zinc vacancies and the shell medium contains a high amount of defect complexes predominantly oxygen vacancies which are positively charged. The results in a discriminatory behavior of defect centers towards various excitation energies. The preceding reasons allow ZnO material to act like a p-type semiconductor [334] where by which we can utilize ZnO in the multidisciplinary fields of biomedicine and electronics.

Figure. 7.7 shows the variation in open circuit potential (OCP) arising because of applied rectangular UV pulse. As observed, the UV irradiation results in negligible OCP drop indicating the stability of the device. The drop absence can be attributed to the better effective propagation of electrons within the structure in contrast to the accumulation of electrons found in OCP drop structures. Relaxation of OCP to normal value is observed upon removal of UV irradiation.

Figure. 7.7 clearly depicts the generation of electron-hole pairs within the synthesized ZnO and ZnO-G structures. Upon the impinging of UV light with energy 3.4 eV (greater than the band gap of ZnO-3.3 eV) on ZnO samples, fluctuations in open circuit potential (OCP) was observed, suggesting the generation of electron- hole pairs [320, 335-337]. The photo generated electrons migrate to RGO sheets. The holes generated in the valence band of ZnO generate (OH) radicals while the electrons captured on RGO react with oxygen forming transient superoxide radicals. The recombination of superoxide free radicals with electrons in RGO can make it an effective photocatalyst.

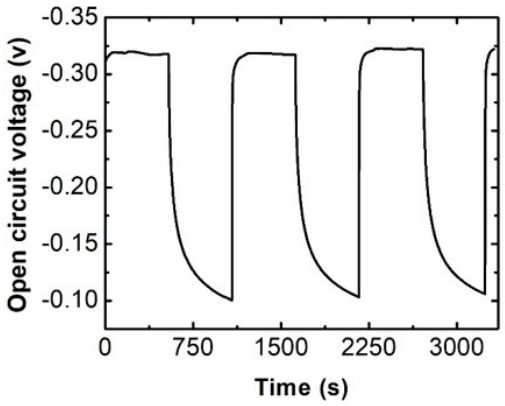

Figure 7.7 Transient open circuit potential vs. time curves for ZnO-G composites.

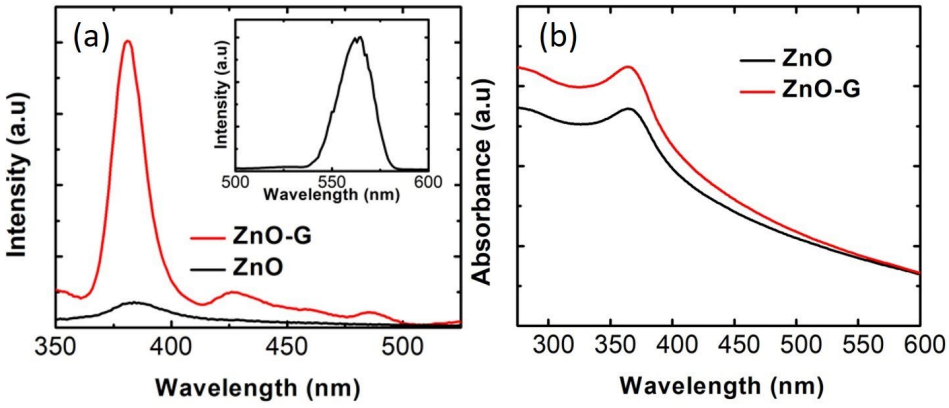

Figure 7.8 Comparison of (a) room- temperature pl spectrum with inset showing defect peak and (b) UV-Vis spectra for ZnO and ZnO-G samples.

Figure7.8(a) shows the room temperature PL characteristics of ZnO and ZnO-G samples. Strong PL peak intensity implies excellent optical characteristics. ZnO boasts about a UV centered emission of around 380 nm and a broad visible emission spectrum between 400 nm- 600 nm [338-340]. The peak at 380 nm can be accounted primarily due to the free exciton emission arising from ZnO structures [341]. The broad spectrum between 400 nm- 600 nm has been explained in relation to the presence of oxygen interstitials [342], single ionized oxygen vacancy in ZnO [343] and surface defects like oxygen vacancies [344] *via* multiple theories. Shown in the inset of (Figure. 7.8(a)), yellow defect emission is typically presented in samples fabricated from zinc nitrate hydrate aqueous solutions and arises on account of the oxygen interstitial [345, 346] and surface defect [347]. Because of the change in radiative transition rates / emission rates which consequently results in an enhanced specific narrow band PL spectrum. ZnO compounds shows enhanced absorption when mixed with RGO [348]. PL intensity of the ZnO-G composites was measured of around 8 times stronger than that of ZnO samples which is attributed to the plasmon resonance enhanced optical property in ZnO-G in accordance with previous reports [322, 323, 349]. Recent studies also suggest that the plasmonic effect of graphene do contribute in the enhancement of the photo response current in the ZnO–G DSSC [350].

Figure 7.8(b) depicts the UV–Vis absorption spectra of ZnO and ZnO-G composites. The absorption band at around 362 nm observed for ZnO can be attributed to the presence of highly crystalline ZnO [351], while an enhanced absorption was observed for ZnO-G composite. The latter ZnO-G presented with a red shift in the absorption edge towards 365 nm thus reinforcing claim of the incorporation of graphene in ZnO-G composite [352, 353]. Chemical interaction arising between the ZnO and graphene within

the hybrid structure resulted in a reduction of bandgap energy for ZnO-G composite, which in-turn researchers employ to tune the optical properties of ZnO [354, 355].

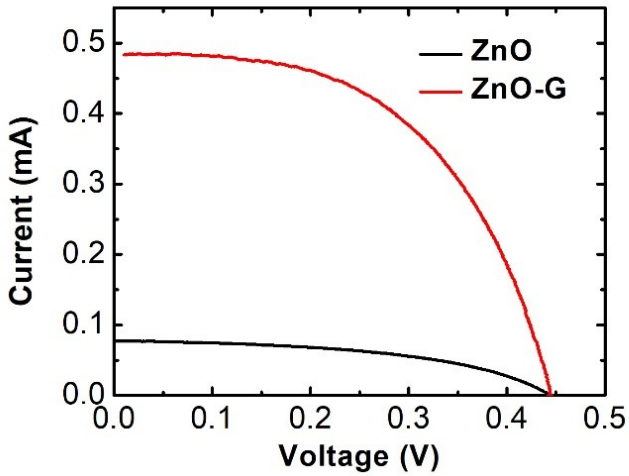

Figure 7.9 I-V-Characteristics of ZnO coated DSSCs and DSSC with ZnO-G electrode.

Figure 7.9 shows the I-V characteristics for flake like morphology of ZnO and ZnO-G DSSCs. From the I-V characteristics curves, the fill factor (FF) and the power conversion efficiency (η) can be calculated using the following equations.

$$FF = \frac{Vmax * Jmax}{Jsc * Voc} \tag{7.1}$$

$$\eta = \frac{Jsc * Voc * FF}{Pin} \tag{7.2}$$

In the previous Equations named (7.1) and (7.2), V_{max} and J_{max} are the maximum cell voltage and current density respectively corresponding to the maximum power point. The short circuit photo current density, open-circuit voltage and input power density are represented by the symbols J_{sc}, V_{oc} and P_{in}, respectively.

The solar cell efficiency along with other parameters are shown in Table 7.1. The enhancement in photocurrent generation efficiency of ZnO-G (η=.438%) electrode when

compared to ZnO electrode (η=.067%) presented in Figure. 7.9. By impregnating graphene into ZnO structures we were able to observe a significant increase in photocurrent (J_{sc}) because of graphene's unique attributes like ultra-high electron mobility and high surface area. ZnO nanocrystallites impart high surface area and large current density, high photon to current conversion efficiency thereby making ZnO a future material for employing in DSSCs [356].

Table 7.1 Characteristics of ZnO and ZnO-Graphene Dye-Sensitized Solar cells

Materials	**J_{SC} (mA/cm^2)**	**V_{OC} (V)**	**FF**	**Power Conversion Efficiency (η) (%)**
ZnO	0.308	0.444	0.121	0.067
ZnO-G	1.93	0.433	0.130	0.438

The high surface area of ZnO thus can maximize the uptake of dye molecules within ZnO nanocrystallite along with providing a better adherence between ZnO and FTO surface. Proper tuning of the physical parameters like morphology, surface area can be achieved by altering the processing temperature, composition and pH of reactants. The aforementioned parameters are reported to have a profound effect in increasing the phototovoltaic efficiency.

DSSC which is a low-cost solar cell is based on a semiconductor technology developed between an electrolyte and a photosensitized anode. Light energy which is stored in the form of photons is converted into electron-hole pairs in solar cells. Sunlight passes through the cathode and the conductor, finally reaching onto the metal oxide

nanoparticle coated anode. The generated electrons thus travel from anode to the cathode resulting in an electrical current [357]. In DSSC charge separation occurs at surfaces between dye, semiconductor and electrolyte. The dye molecules has to be thicker than the molecules so as to capture a large amount of incoming sunlight [358]. Here we have synthesized ZnO and ZnO-G composites having flower like morphology with satisfactory photovoltaic conversion efficiency. By proper tuning of various parameters like morphology, size distribution, fabrication temperature we can employ it in the future for making DSSCs with relatively high efficiency.

7.5 Summary and Conclusion

In summary, we report a new facile and reliable route for the formation of flower-like clusters of ZnO nano-materials based on polyol method. The fabricated ZnO-G composites and its properties were examined *via* multiple characterization techniques. Hexagonal wurtzite ZnO and ZnO-G foams were fabricated under ambient pressure in air through an inexpensive and straightforward modified polyol route. The environmentally friendly polyol route we have employed here is having the advantage that it can be extended for a large-scale synthesis as in industrial production without much difficulty. Enhanced photoluminescence intensity was achieved for the ZnO-G compared to ZnO. The high surface area ZnO particles thus fabricated can be used as a suitable anode material in DSSC as well as an excellent catalyst/adsorbent.

CHAPTER 8

ENHANCED EFFICIENCY OF DYE-SENSITIZED SOLAR CELLS BASED ON POLYOL SYNTHESIZED NICKEL-ZINC OXIDE

In the present work, nickel-zinc oxide (Ni-ZnO) particles have been fabricated through modified polyol route at 250^0 C [359]. The highly porous Ni-ZnO samples developed were of high crystalline quality and exhibited great potential for dye sensitized solar cell (DSSC) applications on account of the quadrupled intensity values of short circuit current density of around 1.42 mA/cm^2, in contrast to 0.31 mA/cm^2 for a bare zinc oxide (ZnO) device. The conversion efficiency of the Ni-ZnO DSSC was measured to be 0.416% which is ~ 6 times higher than that of ZnO solar cell. Detailed characterization techniques including X-ray diffractometry (XRD), photoluminescence (PL), scanning electron microscopy (SEM) and energy dispersive X-ray spectroscopy (EDX) were performed on the samples. The Ni-ZnO samples were crystalline with hexagonal wurtzite lattice structure. The improved efficiency of Ni-ZnO stems from the enhanced absorption and large surface area of the composite.

8.1 Research Motivation behind Ni-ZnO Composites for DSSC

Zinc oxide (ZnO) is the closest wide bandgap semiconductor for light-emitters and photovoltaics due to its direct bandgap and strong excitonic binding energy of 60 meV [360-362]. Diverse micro/nano-structures morphologies of ZnO including nanoribbons, needles [363], nanotubes, nanowires [314], nanowhiskers, pyramids [312], nanodots and flakes [364] have been fabricated using conventional ball milling, aqueous thermal decomposition, chemical precipitation [365, 366], hydrothermal reaction[367], catalyst

assisted vapor phase transport, thermal evaporation [368], sol-gel method [369], metal organic vapor-phase epitaxy [370] etc have been reported by multiple groups. For wide bandgap semiconductors, ZnO reported the first evidence for irreversible electron injection from organic molecules to the conduction band [371]. The diverse morphologies that can be attained for ZnO compared to existing metal oxides, and the unique anisotropic growth for crystalline ZnO material system provides key prospects for designing photoanodes of dye sensitized solar cells (DSSC). By incorporating metallic as well as carbonaceous/graphitic structures to ZnO [372], composite/hybrid materials with enhanced mechanical, optical and piezoelectric properties can be developed [373, 374]. Nanocrystalline ZnO has been doped with Mn^{2+}, Ni^{2+}, Co^{2+} and Cr^{3+} ions through solvothermal synthesis and sol-gel methods. The improved catalytic properties of ZnO upon doping with Ni^{2+} has been reported by Yang et al. [375].

The power conversion efficiencies of solid state ZnO based DSSCs are much lower in comparison to their counterparts with quasi-solid state and liquid electrolytes. This lower efficiency of ZnO based systems has been explained by researchers on account of the dissolution of ZnO to Zn^{2+} ions by the adsorbed acidic dyes. This in turn is reported to be followed by the formation of an isolating layer/agglomerates of dye molecules like N719 and Zn^{2+}, resulting in blocking injection of electrons from dye to the semiconductor. The isoelectric point of ZnO is ~9 which implies ZnO is basic and prone to be attacked by acidic dyes. But on account of the evolution of new dye systems, ZnO-composite material systems based DSSCs are expected to replace the traditional silicon solar cell based technology. Furthermore, when compared to the more expensive cleanroom technology and processing resources needed for silicon (Si) based solar cell, the ZnO attributes include *n*-type semiconducting material, high stability, abundance in nature, simple composition and the

ability to be fabricated at lower temperatures at low costs which makes ZnO a better choice for current generation DSSCs. The heterojunction DSSCs of tunable composition metal oxide solar cells holds immense potential for further cost reduction and simplification of manufacturing of DSSC than the comparable efficient conventional Si solar cells. Moreover, the controlled tuning in the composition of ZnO composites, can lead to change in lattice parameters and crystallite sizes thus altering the energy bandgap to be utilized for multifunctional applications. Thus, the composite has the potential to be utilized in many of the electronic devices such as optoelectronic devices.

The transition metal doped nanostructures are substantiated to be an effective method to adjust the energy bands and surface states of ZnO, introducing changes in the optical and physical properties of ZnO. These reasons along with the enhancement of photo conversion efficiency reported for NiO/ZnO cells, on account of decrease in charge recombination in photo electrode and increase of active surface area in counter electrode, makes Ni-ZnO composite DSSCs a unique candidate for future energy applications. Individual nickel and ZnO nanofiber yarn have been fabricated by electrospinning where a high voltage is applied over the precursor solution to overcome the surface tension of the solution, resulting in the generation of jet through the needle/nozzle [376]. Optical studies conducted across Ni-ZnO samples suggested that bandgap reduces with increase in nickel/doping agent, datum being bandgap (E_g) of ZnO-3.3 eV.

In this context, we have synthesized metal oxide/transition metal (Ni-ZnO) hybrid structures with potential tunable electronic and optical properties which might provide an efficient charge transfer within the fabricated structure itself. The preceding attributes including the superior piezoelectric and pyroelectric properties of ZnO promise the use of Ni-ZnO composite material in the fields of piezoelectric transducers, field effect

transistors, electrodes for solar cells, thin film printing and transparent conductors. The Ni-ZnO composites were fabricated by using nickel nitrate hexahydrate, zinc nitrate hexahydrate and ethylene glycol as starting materials. The polyol fabrication route at 250^0 C has other advantages including lower production cost, lower synthesis time and needs only moderate temperature for processing. The co-precipitation fabrication route with constant pH employed for the synthesis of metal-metal oxides have benefits that include high crystallinity, good textural properties and homogeneity [377].

The sol-gel technique implemented for the synthesis of nanoporous oxides, and metal-metal oxides has been gaining wide recognition by researchers due to their high chemical homogeneity, lower fabrication temperature and ability to control the size and shape of particles [378]. Polyol acts as a reaction medium, functions as a stabilizing agent and reduces the particle growth as well [379]. The moisture content present in the sample, pH, composition and fabrication temperature of the polyol process can be varied to yield different morphologies for Ni-ZnO composites. The porous, crystalline Ni-ZnO composites developed, showed excellent potential for DSSC applications on account of their enhanced current density values of around 1.42 mA/cm^2 which was 4 times higher than the value of a bare ZnO electrode, further improving the efficiency of the Ni-ZnO solar cell.

8.2 Experimental Section

Nickel nitrate hexahydrate, and ethylene glycol for the fabrication of Ni-ZnO hybrid structures were supplied by Sigma-Aldrich. Zinc nitrate hexahydrate starting material was provided by Merck. In our experiment, Ni-ZnO composites were fabricated *via* the

following procedure. Initially, the polyol process reactants- nickel nitrate hexahydrate and zinc nitrate hexahydrate were weighed and transferred into a small beaker. Ethylene glycol was added to the mixture of foregoing starting materials during the next step. Nickel nitrate and zinc nitrate hexahydrate materials must be transferred as fast as possible into the small beaker, because of their hygroscopic nature. The reactant solution mixture turned into a green color upon addition of ethylene glycol solvent. The latter solution mixture was then transferred into a cylindrical glass dish which was preheated to a temperature of 250^0 C, higher than the boiling point of the polyol process reactants. The evolution of the brown NO_2 gas from the sample ensures the fabrication of porous Ni-ZnO composite structures. By varying the ratio of starting reactants, we could obtain Ni-ZnO crystallites with different concentrations of Ni in ZnO.

The synthesized Ni-ZnO powder was then made into a slurry/paste for DSSC cell fabrication by mixing with ethyl cellulose aqueous and poly (ethylene glycol) in an agate mortar. The Ni-ZnO paste was further applied as a thin film onto a FTO glass substrate. The prepared films were then air-dried for 30 minutes, followed by annealing at 400^0 C for 1 hour. The sintered electrodes were then immersed in dye solution for 4 hours so that the active surfaces met the N-719 ethanolic dye. The latter processed electrode was then rinsed with ethanol, followed by drying at room temperature. The immersed electrode was then rinsed with ethanol, and then dried at room temperature. Thermal reduction of hexachloroplatinic acid in isopropyl alcohol solution at 400^0 C resulted in the generation of counter platinum (Pt) electrode. Separation was attained between the photoelectrode and counter Pt electrode *via* a spacer. Sealing of the aforementioned setup was performed by exposing the fabricated structure in a hot air oven at a temperature of 700 C for around 10 seconds. Through the drilled hole in the counter Pt electrode, electrolyte solution composed

of lithium iodine and iodine in acetonitrile was introduced. Through the drilled hole in the counter Pt electrode, electrolyte solution composed of lithium iodine and iodine in acetonitrile was introduced. The Current (I) - Voltage (V) measurements were carried out at the end of the previous steps.

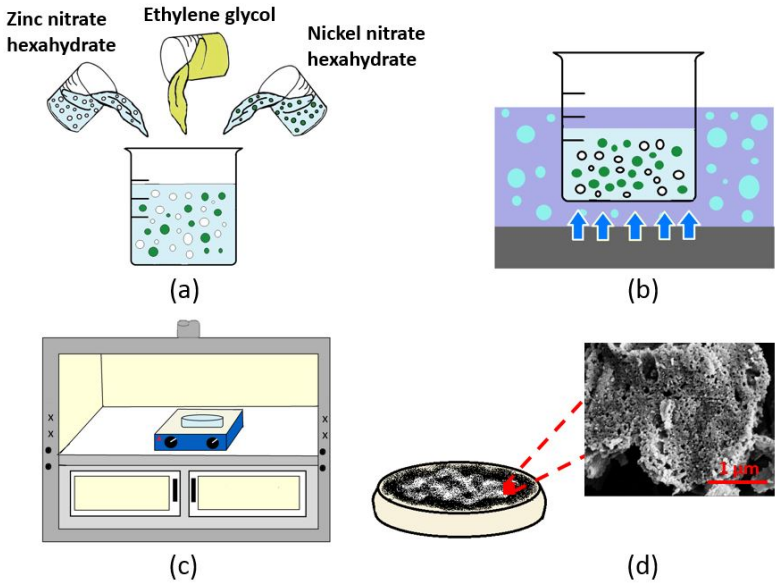

Figure 8.1 Schematic of Polyol Fabrication Route of Ni-ZnO Structure with (a) Mixing of Precursors Including Zinc Nitrate Hexahydrate, Nickel Nitrate Hexahydrate and Ethylene Glycol. (b) Sonication of the Reagent Mixture for 15 minutes. (c) Burning of the reagent Mixture at 250^0 C on a Hot Plate kept in Fume Hood and (d) Formation of Highly Porous Ni-ZnO Composite with Inset Depicting SEM of same.

Figure 8.1 represents the schematic route for the synthesis of Ni-ZnO composites. The modified polyol route is highly dependent on the concentration of precursors, moisture content present in the sample and other parameters such as temperature employed for processing and synthesis. The 3.5 pH of the reactant solution mixture played a crucial role in the morphology of synthesized Ni-ZnO. A higher temperature which must be more than the boiling point of the reactants will ensure complete burning of the precursors and generates crystalline Ni- ZnO structures.

The crystalline nature and the phase purity of fabricated Ni-ZnO structures were examined by Bruker X-ray powder diffractometer with Cu- Kα radiation (λ=0.154 nm) in the 2θ range 10-100 degree. The microstructure of the samples was acquired through field-emission scanning electron microscope (FESEM) in a JEOL HITACHI Model S-3000H instrument. Infrared spectra from 400 cm-1 to 4000 cm-1 of the powdered samples were obtained by KBr pellet method in a fourier transform Infra-Red spectrometer (Bruker Optic Gmbh, Tensor 27 Model). The optical absorption spectra of the fabricated Ni-ZnO samples were inspected using Fischer Scientific ultraviolet-visible (UV-Vis) spectrophotometer. The structural measurements of the samples were carried out at room temperature conditions. Electron paramagnetic resonance (EPR) measurements were performed at room temperature on Bruker EMX Plus model with a microwave frequency of 9.86 GHz and sweep width of 6000 G. Photo luminescence (PL) properties were acquired using a UV-Vis NIR Double beam spectrophotometer (Model: Cary 5000 scan, PbS detector) under an excitation wavelength of 275 nm. The open circuit potential (OCP) variation of the synthesized Ni-ZnO samples upon impinging of UV light (wavelength 365 nm) was recorded by employing a 3-electrode system (employing saturated Ag/AgCl and platinum as reference and counter electrodes, respectively).

8.3 Results and Discussion

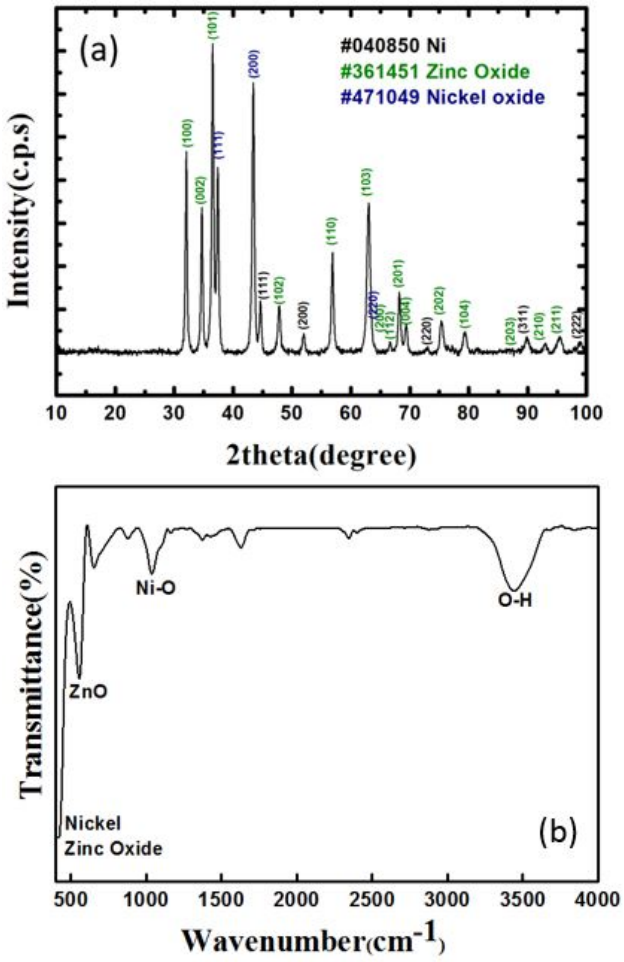

Figure 8.2 (a) XRD pattern (b) FTIR spectrum plotted for Ni-ZnO structure.

Figure 8.2 shows the X ray diffraction pattern and FTIR spectra of Ni-ZnO particles synthesized. Figure 8.2(a) which is the XRD image, clearly affirmed the formation of Ni-ZnO. The XRD patterns of Ni-ZnO samples fabricated at 250^0 C shows the reflection planes indexed to hexagonal wurtzite structure of ZnO material. However, the presence of additional diffraction peaks corresponding to the NiO pattern suggests that the phase segregation might have happened in the samples. Moreover, the increase in nickel concentration shifts the NiO peak to a lower angle with an increase in sharpness of the peak

which was previously reported by other studies [317]. The blue shift of NiO peak is attributed to the oxidization of nickel, resulting in the distortion of NiO to a larger spacing with the incorporation of Ni into ZnO matrix structure. The XRD pattern recorded for Ni-ZnO composite affirms the incorporation of both Ni and Zn from precursors. The identified sharp spectral diffraction peaks at 2θ = 37.250, 43.270, 62.870, 75.410, 79.410, 95.060 can be assigned to (111), (200), (220), (311), (222), and (400) NiO cubic phase planes (JCPDS No: 471049). The relatively higher and sharper diffraction peaks can be attributed to the good crystallinity of Ni, NiO and ZnO within the porous Ni-ZnO structures. The strong diffraction peaks positioned at around 2θ=44.870, 52.20, 76.60, 93.160 belong to (111), (200), (220) and (311) planes of face centered cubic (fcc) Ni perfectly (JCPDS No: 040850) implying that a nickel-nickel oxide (Ni-NiO) structure was formed instead of a nickel core. The diffraction peak at 2θ = 31.770, 34.420, 36.250, 47.530, 56.600, 62.860, 66.380, 67.960 corresponds to (100), (002), (101), (102), (110), (103), (200), (112) planes of the hexagonal wurtzite ZnO structure (JCPDS No: 36-1451). The crystalline Ni-ZnO surfaces developed, may contain lot of active sites. The phase segregation of NiO within the Ni-ZnO matrix and larger amount of nickel present in the sample results in strain relaxation [380].

Figure 8.2(b) illustrates the FTIR analysis performed for Ni-ZnO samples. Vibration modes above 600 cm^{-1} are weak when compared to the hexagonal wurtzite ZnO phase vibration positioned at around 550 cm^{-1}, clearly reassuring our claim that the samples are good crystalline structures devoid of impurities. The Fourier transform infrared spectroscopic technique is based upon the concept that the material shows a selective absorption in the infrared region. The FTIR spectrum also was comprised of a prominent O-H functional group peak at 3450 cm^{-1}, which might have arised by the adsorption of

water molecules present in air [321]. The absorption peak at around 1090 cm^{-1} can also be associated with the lattice vibrations of bulk sized and nanosized NiO. The characteristic band at around 457 cm^{-1} for Ni-ZnO as reported by Devadathan et al. is observed here as well [381], which reaffirms our claim about developing Ni-ZnO. The peaks at around 540 cm^{-1} correspond to ZnO vibrations [382]. The characteristic band at lower wavelength also corresponds to the metal-oxygen (Zn-O) E_2 (LO) mode lattice vibration of the wurtzite structure [383].

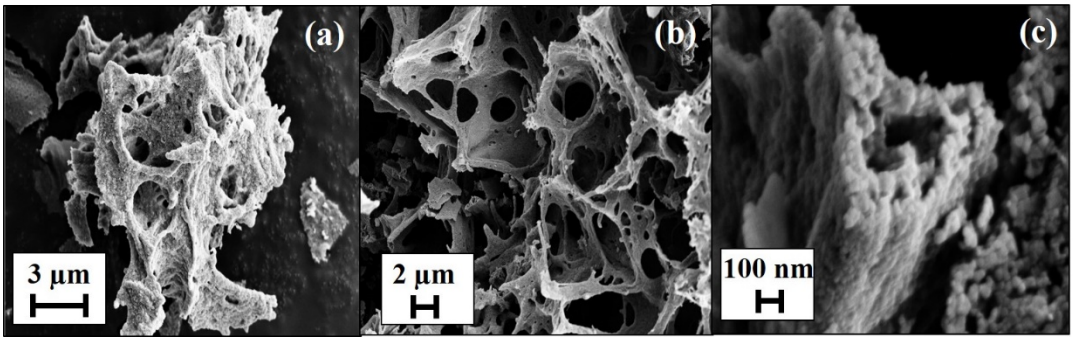

Figure 8.3 FESEM images of Ni-ZnO structures at different magnifications with scale of (a) 3 micron (b) 2 micron and (c) 100 nanometer.

Shown in Figure 8.3, FESEM image revealed the continuous interconnected 3D network within Ni-ZnO composite. Nickel metal provides a scaffold/template on which the ZnO structure is formed. The 3D frame network provided by nickel foam thus reinforces the Ni-ZnO structure. The agglomeration of the nanoparticles and growth nuclei, which resulted in the generation of foam like Ni-ZnO hybrid composites, are depicted in Figure 8.3. The 3D framework of nickel metal comprised mainly of macro and nanopores. The surface roughness of the Ni-ZnO composite due to the porosity and difference in thermal coefficient between nickel and zinc, resulted in an effective template for the growth of ZnO structures. The improved Ni frame support for ZnO and short diffusion paths between ZnO

and Ni could lead to an enhanced activity. Ni-ZnO was thus synthesized through polyol route *via* template free method, when compared to existing pulsed laser deposition techniques [380]. The large driving force of Ni-O bond compared to Zn-O bond results in the phase segregation of NiO within the Ni-ZnO system which makes the latter an ideal component for future diluted magnetic semiconductor (DMS) applications.

The FESEM image of Ni-ZnO composite suggests that the frame network of Ni-ZnO foam has a large distribution of pores at the surface and is extending towards the interior. A detailed inspection of the FESEM image presented in Figures 8.3(a) – 8.3(c) of the synthesized Ni-ZnO mesocrystals shows that the crystals were of few micrometers in size. The nanometer sized pores present in the sample might provide more adsorption sites for gas molecules. The particles are interlinking 3D templates/scaffolds of nickel with ZnO coating developed on and within the surfaces of Ni. Nickel atom preferably tends to occupy the grain boundary regions. The difference in atomic radius between Zn^{2+} (0.074nm) and Ni^{2+} (0.069nm) inhibit grain growth to an extent.

However, the presence of a weak reducing agent like ethylene glycol (when compared to sodium borohydride and hydrazine hydrate), the generation and growth of nuclei are somewhat less controlled, resulting in the generation of Ni-ZnO agglomerated foam. High surface tension and high surface energy of zinc growth nuclei and nanoparticles generated over the course of synthesis also might be a major reason for the agglomerated 3D Ni-ZnO structure. The surface energy of nanoparticles is reported to be significantly higher as compared to that of the bulk and is found to be vital in coalescence, growth of nanoparticles resulting in three dimensional structures.

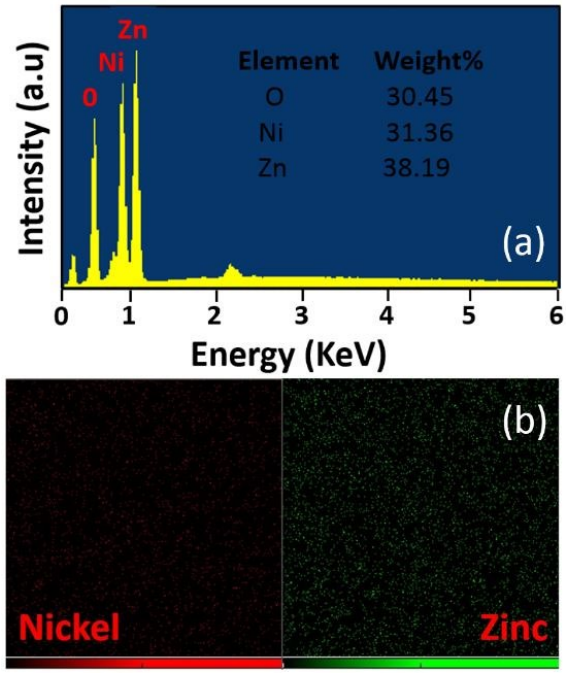

Figure 8.4 (a) EDX profile conducted across the bulk of Ni-ZnO Region (b) XRF spectra of Ni-ZnO structures along with elemental mapping profile of the composite structures.

The EDX profile conducted across the Ni-ZnO samples as observed in Figure 8.4(a) reaffirms the presence of Ni-ZnO hybrid composite. The oxygen presence revealed from the EDX spectra conducted across the profile of Ni-ZnO sample, might be arising due to the formation of ZnO and NiO phases present within the sample. The atomic percentages of oxygen, nickel and zinc were around 62.98%, 17.68% and 19.34%, respectively while the weight percentages were 30.45%, 31.36% and 38.19%, respectively. There also arises a slight chance where water molecules can adsorb to the Ni-ZnO material. XRF studies were performed on the samples and the elemental mapping profile images are illustrated in Figure 8.4(b).

Illustrated in Figure 8.5, the EPR spectra of Ni-ZnO composite, the structural defects and purity of fabricated Ni-ZnO samples can be analyzed. Ferromagnetism nature is accounted to the oxygen and zinc vacancies of the transition metal oxide composite [384,

385]. Ni-ZnO samples yielded a symmetrical resonance signal for EPR when compared to the resolved hyperfine structure observed in ZnO. This might be due to the strong- spin interactions between Ni^{2+} ions present in the sample [386].

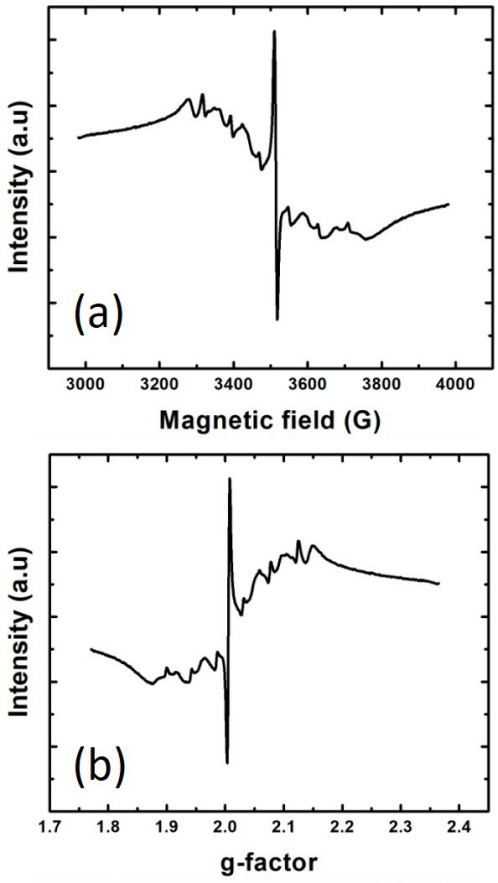

Figure 8.5 EPR Spectra for fabricated Ni-ZnO samples with (a) magnetic field and (b) g factor.

The lower solubility of NiO in ZnO might have resulted in the incorporation of Ni ions into the lattice along with phase segregation at the surface. We were able to observe a shift in the value of g factor, datum being the free electron position. The resonant field value decreases with increase in nickel concentration in the sample with reference to ZnO spectra reported. The hexagonal wurtzite structure ZnO composite samples fabricated

through polyol process is found to have resonant field located at around 3480 G, slightly different from the commercial ZnO samples with a resonant field value of around 3600 G. The latter phenomenon can be attributed to the following reason. The increase in nickel concentration reduces the distance between Ni^{2+}-Ni^{2+} ions thus bringing the nickel atoms within the Ni-ZnO structure close together. Thus, the increase in nickel concentration brings about super–exchange interactions between the closely arranged Ni^{2+} atoms, resulting in an increase in the internal field which then decreases the resonant field.

The broad peak observed for the Ni-ZnO composite structure suggests that the latter may also comprise of a constituent, which is not ferromagnetic like NiO. The presence of Ni is reported to result in enhanced magnetic d-d exchange interaction between the magnetic moment of Ni^{2+} leading to composite's ferromagnetism [387]. From EPR spectra, it's inferred that the free radical generation is happening within the structure. The Zn^{2+} ions having ionic radius 0.074 nm prefer tetrahedral coordination. The coordination environment of Zn^{2+} ions in ZnO is ideal for 0.069 nm sized Ni^{2+} ions. This can also result in the formation of Ni-ZnO solid solutions within the structure [388].

The dielectric properties of the fabricated Ni-ZnO samples are clearly portrayed in Figure 8.6. The capacitance of the fabricated Ni-ZnO sample was clearly shown to be greater than its counterpart ZnO present in the composite. Since the size difference between Ni and Zn ions are small, there is a chance that nickel ions will replace zinc ions resulting in the formation of Ni- doped ZnO structure. The increase in lattice distortion and ionized impurity scattering centers that arise because of the interstitial small Ni^{2+} ions can have an adverse effect on the carrier mobility. Replacement of bigger Zn^{2+} ions by comparatively smaller Ni^{2+} ions and the generation of oxygen vacancies in ZnO matrix can be accounted for the decrease in carrier mobility while increase in carrier concentration can be attributed

to the generation of defects. The superior electrical properties thus imparted to the Ni-ZnO hybrid structure arises because of the formation of metallic nickel as well as due to the generation of oxygen defects [389]. The latter analyses provide us with the chance of proper tuning of polyol-based Ni-ZnO composite to develop it as a good capacitor material.

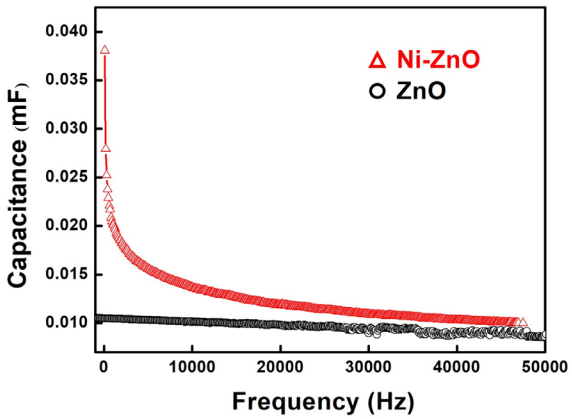

Figure 8.6 Dielectric behavior of Ni-ZnO and ZnO samples fabricated through the polyol method.

Figure 8.7(a) which is the PL study, illustrated the effect of optically active defects and relaxation pathways of excited states present in Ni-ZnO. Emission peaks were observed at around 380 nm. The UV emission peak positioned at around 3.3 eV corresponded to the free exciton emission, reaffirming the high crystal quality of fabricated Ni-ZnO. The PL spectra can be attributed to the formation of various hetero junctions that exists between semiconductor ZnO and Ni/NiO structure. Under different pH conditions, Ni-ZnO structures having multiple morphology (shape and size) can be formed, which indeed will affect the UV-Vis spectra.

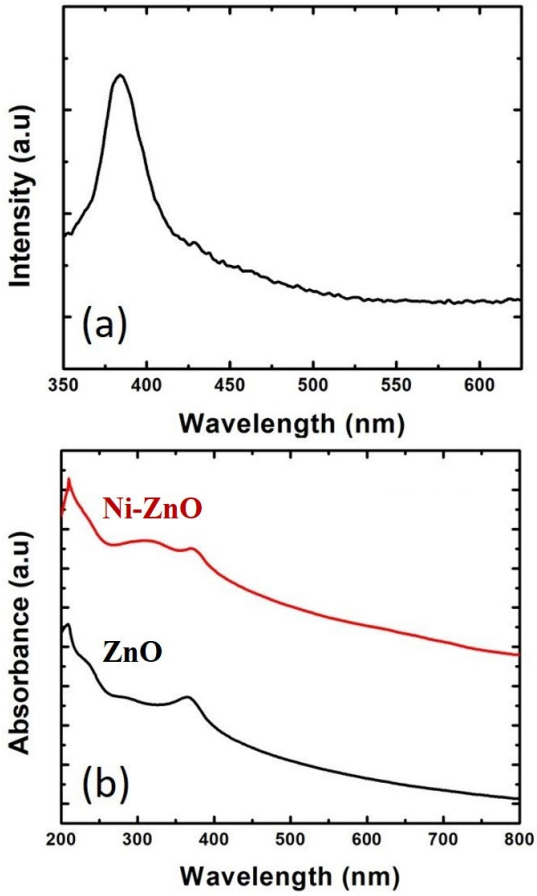

Figure 8.7 (a) Room temperature PL spectra of Ni-ZnO (b) optical absorption spectra of ZnO and Ni-ZnO.

Figure 8.7(b) represents the UV-Vis absorption spectra conducted across the profile of Ni-ZnO samples dispersed in ethanol. The excitonic absorption peaks of the prepared Ni-ZnO composite and ZnO samples was located at around 380 nm and 383 nm, respectively. Enhanced optical absorption/ reduced reflectance of Ni-ZnO composite and a slight blue shift in peak absorption wavelength with reference to ZnO were observed in other works[390]. The enhanced absorption in Ni-ZnO composite has been linked to the reduction in grain boundaries of composite structure [391] as well as to the scattering at the grain boundaries [361].

The optical absorption spectra of the transition metal-metal oxide composite has been also explained by researchers by the substitution of Zn^{2+} ions by Ni^{2+} ions occurring within a region of the meso-cellular composite [392]. All samples, which were subjected to optical studies, had their band edges in UV region. In doped zinc oxides, absorption band edges become less sharp with increasing nickel concentration, which can be attributed to the presence of crystallographic defects existing within nickel doped ZnO. The existence of crystallographic defects in the forbidden bands of Ni-ZnO composite structure might result in a less pronounced absorption band-edge.

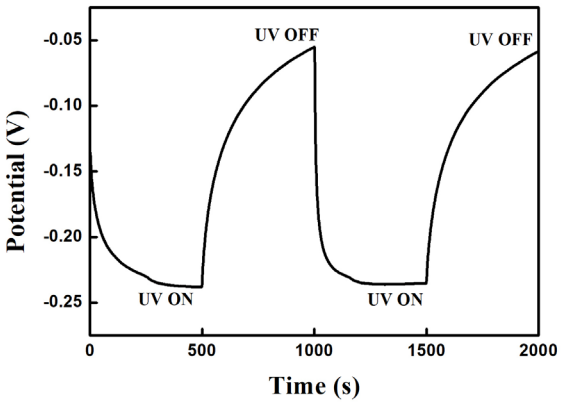

Figure 8.8 OCP variation of Ni-ZnO under UV irradiation.

Figure 8.8 represents the Open Cell Potential (OCP) variation conducted across samples under 365 nm UV light. The irradiation of UV light with an energy of 3.4 eV (more than the E_g of ZnO) on Ni-ZnO samples resulted in the formation of a large number of electron hole pairs, which accounted for the fluctuation in OCP. The high sensitivity of ZnO samples under UV light was imparted to Ni-ZnO sample. The drop in OCP upon the applied rectangular UV pulse can be attributed to the effective propagation of electrons within the structure contrary to the accumulation of electrons found in OCP drop structures.

Relaxing of OCP to normal value upon the removal of UV light implied the generation of electron hole pairs in ZnO composite.

The enhancement in photocurrent generation efficiency of Ni-ZnO electrode when compared to normal ZnO electrode prepared by the same method is clearly shown in Figure 8.9. By incorporating Ni into ZnO structures, we were able to observe significant increase in photocurrent due to the imparting high surface area and large current density as well as high photon to current conversion efficiency of Ni-ZnO DSSCs compared to ZnO counterparts. The enhanced surface area per unit volume of ZnO composites will contribute to maximum uptake of dye molecules and will have a larger electron diffusion coefficient, and a shorter electron transit time [302, 393].

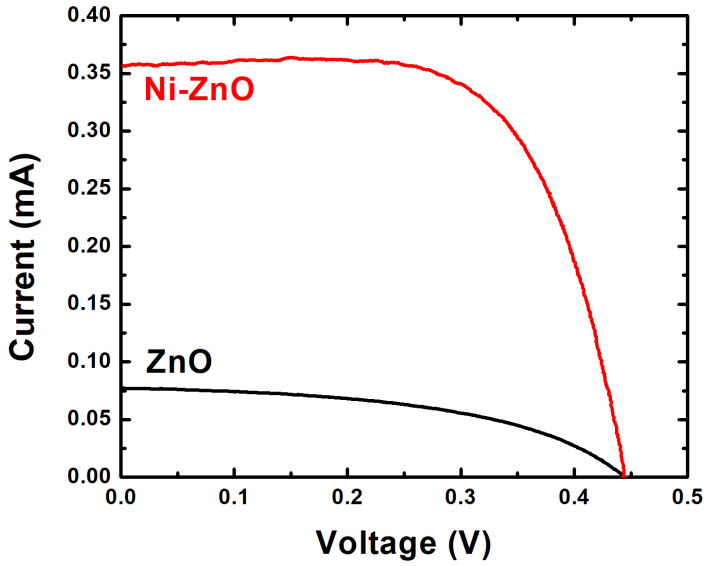

Figure 8.9 Current -voltage characteristics of DSSC electrode fabricated using Ni-ZnO material.

Table 8.1 Characteristics of Ni-ZnO Fabricated DSSC by Polyol Method

Material	J_{SC} (mA/cm^2)	V_{OC} (V)	Power Conversion Efficiency (η) (%)
ZnO	0.31	0.44	0.067
Ni-ZnO	1.42	0.44	0.416

The solar cell efficiency along with other parameters are shown in Table 8.1. The Ni-ZnO composites exhibited an enhanced Jsc value of 1.42 mA/cm2, around ~4 times higher than that of Jsc values of 0.31 mA/cm2 for bare ZnO sample fabricated by the same polyol route. The fill factor of Ni-ZnO composites also increased significantly from 0.165 in contrast to 0.121 for a counter bare ZnO sample. This in turn led to an enhanced efficiency that was 6 times higher for the Ni-ZnO DSSC compared to ZnO sample. The conversion efficiencies of Ni-ZnO and bare ZnO DSSCs were measured at 0.416% and 0.067%, respectively. Here we have synthesized Ni-ZnO crystallites with comparative photovoltaic conversion efficiency. AC conductivity which may be very useful for solar cell applications is known to increase six to eight orders of magnitude by the introduction of Ni^{2+} vacancies in nanostructured NiO [394].

8.4 Summary and Conclusion

In summary, we developed a facile, unique technique at moderate temperature to fabricate high crystalline mesocrystals of Ni-ZnO, by mixing undoped metal precursors- nickel nitrate hexahydrate and zinc nitrate hexahydrate along with ethylene glycol as the reducing agent. By controlling the composition, pH and processing temperature during the polyol

process route, we achieved highly porous Ni-ZnO hybrid composites. The fabrication route employed for the synthesis of Ni-ZnO composites is highly reproducible, facile and can be employed for large-scale industrial production with minimum production and operating costs. The Ni-ZnO composites displayed photovoltaic conversion efficiencies of 0.416% which was 6 times better than bare ZnO solar cell due to the increased optical absorption and enhanced photocurrent.

CHAPTER 9

SUMMARY AND FUTURE RESEARCH

9.1 Summary

This dissertation investigates the III-nitrides material system and the zinc oxide composite material systems which are the two main wide bandgap semiconductor classes existing within the market. III-nitride semiconductor material system can be utilized for developing LEDs and LD light sources within the broad wavelength range of near infrared to deep ultraviolet, by tuning the bandgap *viz.* In/Ga flux ratio. This can also be accomplished by careful design and controlling the growth parameters *viz.* temperature and flux ratio, thus consequently impacting the effective bandgap and thereby the wavelength of light source fabricated. In our studies, we have characterized several nanowire LED structures, grown by molecular beam epitaxy (MBE) using techniques like electroluminescence (EL), photoluminescence (PL), current-voltage (I-V) etc. Finite Difference Time Domain (FDTD) Lumericals software was used throughout the study for the design and simulation studies of the nanowire LEDs. In summary, we have investigated the molecular beam epitaxial growth and characterization of III-Nitride based nanowire heterostructures, including InGaN and AlGaN nanowires on Si (111) substrates.

We have further studied and demonstrated high performance zinc-oxide graphene and zinc oxide-nickel composite material systems by polyol method for dye sensitized solar cell (DSSC) applications. Main findings of this dissertation are briefly described below. We have also investigated several methods such as nanowire-based LEDs and approaches like flip chip nanowire-based LEDs to enhance the EQE of GaN based LEDs. We also

reported high performance flip chip nanowire LEDs on flexible metallic substrates like copper. Such claims have been supported by simulation and experimental results. We have further reported on the demonstration of full color tuning by controlling the *In* and *Ga* flux ratio in the quantum wells. Further, we reported phosphor-free white nanowire LEDs with improved LEE. Moreover, we have shown that the LEE of GaN LEDs can be significantly enhanced by integrating with nanowire arrays. The light extraction involves two successive steps, including the coupling from the light source to the tube and the subsequent emission from the tube to the air. We have enhanced the light extraction efficiency of deep UV LEDs using periodic array of nanowires. The emission of the guided modes could be inhibited and redirected into radiated modes utilizing nanowire structures. By polyol method we developed ZnO- Ni and ZnO-G composites within our research.

In overall, chapter 1 of dissertation covers the mechanisms involved in the nanowires, advantages of GaN based structures and presents a compilation on the current status of the III-nitride based device structures while Chapter 2 presents an overview of the MBE growth, device fabrication and characterization methods utilized for the GaN based LEDs. Chapter 3 encompasses the color tuning and thereby the controlling of color emission in nanowire LEDs. We also have investigated the topic of nearly defect-free III-nitride nanowire LEDs on account of the InGaN/GaN quantum well LEDs which are often plagued by presence of large densities of dislocations. This was made feasible by controlling the growth parameters such as In/Ga flux ratio in active region or by altering nanowire packing density, temperature, growth duration, deposition rate etc. This in turn results in a range of optoelectronic devices emitting light in a broad range spanning from deep UV to near IR. We have demonstrated highly stable, phosphor-free white light emission. Chapter 4 listed the budding future of GaN based nanowire LEDs for VLC on

account of their reduced QCSE resulting from strain relaxation. Nanowire LEDs on flexible metal substrates such as copper with high performance attributes were demonstrated in Chapter 5. Chapter 6 introduces the MBE growth and simulation studies based on ultraviolet based AlGaN nanowire LEDs. Specifically, UV-B LEDs having immense potential in the biomedical industry have been demonstrated. Chapter 6 also illustrates the effect of optical absorption and the need for new alternate designs w.r.t AlGaN based UV LED. Chapters 7 and 8 introduces polyol based ZnO-G and Ni-ZnO composites, respectively and their potential for dye sensitized solar cell on account of the enhanced absorption w.r.t bare ZnO. The highly porous ZnO based composites displayed a higher efficiency than the bare ZnO counterpart.

9.2 Future Research

The following section lists some of the potential future research directions following the research outcomes presented in this dissertation:

9.2.1 Micro Light-Emitting Diodes for Camera Flash and Micro-Display Applications:

Our technology with phosphor-free InGaN/AlGaN Nanowire Light-Emitting Diodes (LEDs) grown by Molecular Beam Epitaxy (MBE) creates LEDs with good characteristics including nearly zero efficiency droop at the current ~1000 A/cm^2; color rendering index > 95; and internal quantum efficiency (~ 60%), leading to high efficiency and bright, so they become a promising candidate for cutting edge technology for micro-display in and camera flash. with high energy efficiency and color quality, suitable for micro-display and camera flash. Since the micro-LED technology market has been driving a new wave of display standard on over the world in many sectors; LED markers, chip makers,

manufacturing equipment suppliers, and wafer suppliers the potential is immense. Overall, higher resolution for screens, energy saving, and flexibility to morph into any shape attributes are huge benefits for the latter approach.

9.2.2 III-nitride nanowire LEDs and LDs for VLC:

We are planning to explore further on the topic of VLC and InGaN/ AlGaN nanowire based visible LEDs and LDs on account of their reduced QCSE arising from the strain relaxation happening within the III-nitride structure. VLC using III-nitride nanowire system provides a higher 3 dB bandwidth than the thin film counterpart.

9.2.3 Zinc Oxide nanowires using hydrothermal growth:

The solution phase growth method which is a simple, low temperature approach is employed to grow a vertically aligned ZnO nanowire array. This method uses the hydrolysis of zinc salt in water.

1. The batch solution is usually prepared in quantities of 500 mL, consisting of 3.719 g 0.025M Zinc Nitrate Hexahydrate [$Zn(NO_3)_2 \cdot 6H_2O$], 1.753 g Hexamethylenetetramine (HMTA) [$C_6H_{12}N_4$], and 2 g 0.001M Polyethylenimine (PEI) and enough filtered deionized water so that it reaches the 500 mL mark.
2. The aforeknown solution mixture will be heated to 100^{o}C by keeping it on a hot plate. The proper mixing of the chemical reagents was ensured by using a magnetic stir bar. This is followed by the change in the solution color from milky white to pale yellow. A filter paper was used to ensure that all initial particulates formed thus were removed. The left over solution after cleaning can be stored for around 2 weeks for ZnO nanowire synthesis. This can be separated into different 100 mL beakers for each nanowire growth episode.

3. The cleaned substrates that went through acetone, isopropanol, methanol and HF treatments were then taped by double sided carbon tape onto holders in such a manner that they are suspended at an angle around 45^{o} in the solution. This ensures that any particulates that were formed in the solution during growth process would not fall onto the substrate and interfere with nanowire growth but also any bubbles in the solution would not rise and get stuck on the surface of the substrates.
4. The growth solution for ZnO nanowire was heated to 95^{o}C and once the solution temperature reaches around 85^{o}C, the substrate holder will be placed into the solution beaker. 2 hours growth time for the precursors in the solution ensures all reactants were completely used up and as a result we can obtain ~2um tall ZnO nanowires on the substrate. Precaution must be taken during each growth episode, as in confirm the formed bubbles aren't sticking anywhere on the substrate surface. If the bubbles stuck up on surface of substrate, voids can form on the substrate. Also, to get longer nanowires of ZnO that will improve LED operation and characteristics, repeat the growth procedure steps two more times. This can result in nanowire lengths of around 5-6 μm.

Such ZnO nanowires which emits along the wavelength regime of 360 nm has potential to be either integrated by itself or with III-nitride material system for high performance UV light sources.

REFERENCES

[1] F. Fichter, "Über aluminiumnitrid," *Zei. Für. Ano. Chem.,* vol. 54, no. 1, p. 322, 1907.

[2] F. Fischer and F. Schröter, "Über neue metall-stickstoff-verbindungen und ihre stabilität an der hand des periodischen systems," *Ber. Dtsch. Chem. Ges.,* vol. 43, no. 2, p. 1465, 1910.

[3] W. C. Johnson, J. B. Parson, and M. C. Crew, "Nitrogen compounds of gallium," *J. Phys. Chem.,* vol. 36, no. 10, p. 2651, 1931.

[4] H. P. Maruska and J. J. Tietjen, "The preparation and properties of vapor-deposited single-crystal-line GaN," *Appl. Phys. Lett.,* vol. 15, no. 10, p. 327, 1969.

[5] J. I. Pankove and J. A. Hutchby, "Photoluminescence of ion-implanted GaN," *J. Appl. Phys.,* vol. 47, no. 12, p. 5387, 1976.

[6] R. Dingle, K. L. Shaklee, R. F. Leheny, and R. B. Zetterstrom, "Stimulated emission and laser action in gallium nitride," *Appl. Phys. Lett.,* vol. 19, no. 1, p. 5, 1971.

[7] H. M. Manasevit, F. M. Erdmann, and W. I. Simpson, "The use of metalorganics in the preparation of semiconductor materials: iv . the nitrides of aluminum and gallium," *J. Electrochem. Soc.,* vol. 118, no. 11, p. 1864, 1971.

[8] I. H. Isamu Akasaki, "Research on blue emitting devices," *Ind. Sci. Tech.,* vol. 17, p. 48, 1976.

[9] S. Yoshida, S. Misawa, and S. Gonda, "Epitaxial growth of GaN/AlN heterostructures," *J. Vac. Sci. Technol. B.,* vol. 1, no. 2, p. 250, 1983.

[10] H. Amano, N. Sawaki, I. Akasaki, and Y. Toyoda, "Metalorganic vapor phase epitaxial growth of a high quality GaN film using an AlN buffer layer," *Appl. Phys. Lett.,* vol. 48, no. 5, p. 353, 1986.

[11] A. Isamu, A. Hiroshi, K. Masahiro, and H. Kazumasa, "Photoluminescence of Mg-doped p-type GaN and electroluminescence of GaN p-n junction LED," *J. Lum.,* vol. 48-49, p. 666, 1991.

[12] H. Amano, M. Kito, K. Hiramatsu, and I. Akasaki, "P-type conduction in Mg-doped GaN treated with low-energy electron beam irradiation (LEEBI)," *Jpn. J. Appl. Phys.,* vol. 28, no. 12, p. L2112, 1989.

[13] N. Shuji, M. Takashi, S. Masayuki, and I. Naruhito, "Thermal annealing effects on p-type Mg-doped GaN films," *Jpn. J. Appl. Phys.,* vol. 31, no. 2B, p. L139, 1992.

[14] T. Matsuoka, N. Yoshimoto, T. Sasaki, and A. Katsui, "Wide-gap semiconductor InGaN and InGaAln grown by MOVPE," *J. Electron. Mater.,* vol. 21, no. 2, p. 157, 1992.

[15] S. Nakamura, M. Senoh, and T. Mukai, "High-power InGaN/GaN double-heterostructure violet light emitting diodes," *Appl. Phys. Lett.,* vol. 62, no. 19, p. 2390, 1993.

[16] M. A. Khan, R. A. Skogman, J. M. Van Hove, S. Krishnankutty, and R. M. Kolbas, "Photoluminescence characteristics of AlGaN-GaN-AlGaN quantum wells," *Appl. Phys. Lett.,* vol. 56, no. 13, p. 1257, 1990.

[17] K. Itoh, T. Kawamoto, H. Amano, K. Hiramatsu, and I. Akasaki, "Metalorganic vapor phase epitaxial growth and properties of $GaN/Al_{0.1}Ga_{0.9}N$ layered structures," *Jpn. J. Appl. Phys.,* vol. 30, no. 9A, p. 1924, 1991.

[18] H. Hirayama, N. Maeda, S. Fujikawa, S. Toyoda, and N. Kamata, "Recent progress and future prospects of AlGaN-based high-efficiency deep-ultraviolet light-emitting diodes," *Jpn. J. Appl. Phys.,* vol. 53, no. 10, p. 100209, 2014.

[19] T. Takano, T. Mino, J. Sakai, N. Noguchi, K. Tsubaki, and H. Hirayama, "Deep-ultraviolet light-emitting diodes with external quantum efficiency higher than 20% at 275 nm achieved by improving light-extraction efficiency," *Appl. Phys. Express.,* vol. 10, no. 3, p. 031002, 2017.

[20] K. Nagamatsu *et al.*, "High-efficiency AlGaN-based UV light-emitting diode on laterally overgrown AlN," *J. Cryst. Growth.,* vol. 310, no. 7, p. 2326, 2008.

[21] S. Zhao *et al.*, "Aluminum nitride nanowire light emitting diodes: Breaking the fundamental bottleneck of deep ultraviolet light sources," *Sci. Rep.,* vol. 5, p. 8332, 2015.

[22] N. Abramova, M. Schöning and A. Poghossian, *Label-free biosensing*. Heidelberg: Springer, 2018.

[23] F. Glas, "Critical dimensions for the plastic relaxation of strained axial heterostructures in free-standing nanowires," *Phys. Rev. B.,* vol. 74, no. 12, p. 121302, 2006.

[24] M. R. Philip *et al.*, "Controlling color emission of InGaN/AlGaN nanowire light-emitting diodes grown by molecular beam epitaxy," *J. Vac. Sci. Technol. B.,* vol. 35, no. 2, p. 02B108, 2017.

[25] P. Renwick, H. Tang, J. Bai, and T. Wang, "Reduced longitudinal optical phonon-exciton interaction in InGaN/GaN nanorod structures," *Appl. Phys. Lett.,* vol. 100, no. 18, p. 182105, 2012.

[26] D. J. Eaglesham and M. Cerullo, "Dislocation-free Stranski-Krastanow growth of Ge on Si(100)," *Phys. Rev. Lett.,* vol. 64, no. 16, p. 1943, 1990.

[27] J. Ibáñez *et al.*, "High-pressure lattice dynamics in wurtzite and rocksalt indium nitride investigated by means of Raman spectroscopy," *Phys. Rev. B.,* vol. 88, no. 11, p. 115202, 2013.

[28] H. Xia, Q. Xia, and A. L. Ruoff, "High-pressure structure of gallium nitride: wurtzite-to-rocksalt phase transition," *Phys. Rev. B.,* vol. 47, no. 19, p. 12925, 1993.

[29] T. Zhu and R. A. Oliver, "Unintentional doping in GaN," *Phys. Chem. Chem. Phys.,* vol. 14, no. 27, p. 9558, 2012.

[30] J. Kim, "Growth and Characterization of III-nitride semiconductors for high-effcient light-emitting diodes by metalorganic chemical vapor deposition," PhD dissertation, School of Electrical and Computer Engineering, Georgia Institute of Technology, 2014.

[31] R. Collazo, S. Mita, A. Aleksov, R. Schlesser, and Z. Sitar, "Growth of Ga- and N- polar gallium nitride layers by metalorganic vapor phase epitaxy on sapphire wafers," *J. Cryst. Growth.,* vol. 287, no. 2, p. 586, 2006.

[32] K. Stacia *et al.*, " Recent progress in metal-organic chemical vapor deposition of \left(000\bar{1} \right) N-polar group-III nitrides," *Semicond. Sci. Technol.,* vol. 29, no. 11, p. 113001, 2014.

[33] J. Wu, "When group-III nitrides go infrared: new properties and perspectives," *J. Appl. Phys.,* vol. 106, no. 1, p. 011101, 2009.

[34] J. Wu and W. Walukiewicz, "Band gaps of InN and group III nitride alloys," *Superlatt. Microstruct.,* vol. 34, no. 1, p. 63, 2003.

[35] J. Huang, H. C.Kuo and S. C. Shen, *Nitride semiconductor light-emitting diodes (LEDs)*. Dublin, Ireland: Woodhead Publishing, 2018.

[36] D. A. Steigerwald *et al.*, "Illumination with solid state lighting technology," *IEEE. J. Sel. Area. Comm.,* vol. 8, no. 2, p. 310, 2002.

[37] S. Nakamura, "Current status of GaN-based solid-state lighting," *MRS. Bull.,* vol. 34, no. 2, p. 101, 2009.

[38] C. C. Sun, I. Moreno, S. H. Chung, W. T. Chien, C.T. Hsieh, and T. H. Yang, "Direct led backlight for large area lcd tvs: brightness analysis," *Proc. SPIE.,* vol. 6669, p. 10, 2017.

[39] M. S. S. Artūras Žukauskas, Remis Gaska, *Introduction to Solid-State Lighting.* New York, New York: Wiley-Interscience, 2002.

[40] D. A. Kirkpatrick, "Is solid state the future of lighting?," *Proc. SPIE.,* vol. 5187, p. 12, 2004.

[41] N. G. Yeh, C. H. Wu, and T. C. Cheng, "Light-emitting diodes—their potential in biomedical applications," *Renew. Sust. Energ. Rev.,* vol. 14, no. 8, p. 2161, 2010.

[42] M. Belz, F. A. Klein, and H. Habhegger, "UV LED fiber optic detection system for DNA and protein," *Proc. SPIE.,* vol. 6433, p. 8, 2007.

[43] F. R. A. Pereira *et al.*, "UVA system for human cornea irradiation," *Proc. SPIE.,* vol. 7163, p. 7, 2009.

[44] R. Magjarevic and J. H. Nagel, *World congress on medical physics and biomedical engineering.* Berlin, Germany: Springer, 2007.

[45] J. Close, J. Ip, and K. H. Lam, "Water recycling with PV-powered UV-LED disinfection," *Renew. Energy.,* vol. 31, no. 11, p. 1657, 2006.

[46] M. A. Würtele *et al.*, "Application of GaN-based ultraviolet-C light emitting diodes – UV LEDs – for water disinfection," *Water. Res.,* vol. 45, no. 3, p. 1481, 2011.

[47] M. Mori *et al.*, "Development of a new water sterilization device with a 365 nm UV-LED," *Med. Biol. Eng. Comput.,* vol. 45, no. 12, p. 1237, 2007.

[48] A. Hamamoto *et al.*, "New water disinfection system using UVA light-emitting diodes," *J. Appl. Microbiol.,* vol. 103, no. 6, p. 2291, 2007.

[49] Y. C. Shen, G. O. Mueller, S. Watanabe, N. F. Gardner, A. Munkholm, and M. R. Krames, "Auger recombination in InGaN measured by photoluminescence," *Appl. Phys. Lett.,* vol. 91, no. 14, p. 141101, 2007.

[50] M. Zhang, P. Bhattacharya, J. Singh, and J. Hinckley, "Direct measurement of auger recombination in $In_{0.1}Ga_{0.9}N$/GaN quantum wells and its impact on the efficiency of $In_{0.1}Ga_{0.9}N$/GaN multiple quantum well light emitting diodes," *Appl. Phys. Lett.,* vol. 95, no. 20, p. 201108, 2009.

[51] M. H. Kim *et al.*, "Origin of efficiency droop in GaN-based light-emitting diodes," *Appl. Phys. Lett.,* vol. 91, no. 18, p. 183507, 2007.

[52] B. C. Lin *et al.*, "Hole injection and electron overflow improvement in InGaN/GaN light-emitting diodes by a tapered AlGaN electron blocking layer," *Opt. Express.,* vol. 22, no. 1, p. 463, 2014.

[53] T. Wei *et al.*, "Investigation of efficiency and droop behavior comparison for InGaN/GaN super wide-well light emitting diodes grown on different substrates," *IEEE. Photonic. Tech. L.,* vol. 6, no. 6, p. 1, 2014.

[54] R. Haitz, F. Kish, J. Tsao and J. Nelson, "The case for a national research program on semiconductor lighting", Sandia National Laboratories, Albuquerque, New Mexico, 2000.

[55] J. L. Liu *et al.*, "Status of GaN-based green light-emitting diodes," *Chin. Phys. B.,* vol. 24, no. 6, p. 067804, 2015

[56] N. Shuji, S. Masayuki, I. Naruhito, and N. Shin-ichi, "High-brightness InGaN blue, green and yellow light-emitting diodes with quantum well structures," *Jpn. J. Appl. Phys.,* vol. 34, no. 7A, p. L797, 1995.

[57] M. R. Krames *et al.*, "Status and future of high-power light-emitting diodes for solid-state lighting," *J. Disp. Technol.,* vol. 3, no. 2, p. 160, 2007.

[58] M. H. Crawford, "LEDs for solid-state lighting: performance challenges and recent advances," *IEEE. J. Sel. Top. Quantum Electron.,* vol. 15, no. 4, p. 1028, 2009.

[59] N. Tansu *et al.*, "III-nitride photonics," *IEEE. Photon. J.,* vol. 2, no. 2, p. 241, 2010.

[60] H. P. T. Nguyen *et al.*, "Breaking the carrier injection bottleneck of phosphor-free nanowire white light-emitting diodes," *Nano. Lett.,* vol. 13, no. 11, p. 5437, 2013.

[61] H. P. T. Nguyen *et al.*, "Full-color InGaN/GaN dot-in-a-wire light emitting diodes on silicon," *Nanotec.,* vol. 22, no. 44, p. 445202, 2011.

[62] K. Akihiko, K. Mizue, T. Makoto, and K. Katsumi, "InGaN/GaN multiple quantum disk nanocolumn light-emitting diodes grown on (111) Si substrate," *Jpn. J. Appl. Phys.,* vol. 43, no. 12A, p. L1524, 2004.

[63] S. D. Hersee, X. Sun, and X. Wang, "The controlled growth of GaN nanowires," *Nano. Lett.,* vol. 6, no. 8, p. 1808, 2006.

[64] K. Kishino, H. Sekiguchi, and A. Kikuchi, "Improved Ti-mask selective-area growth (SAG) by rf-plasma-assisted molecular beam epitaxy demonstrating extremely uniform GaN nanocolumn arrays," *J. Cryst. Growth.,* vol. 311, no. 7, p. 2063, 2009.

[65] H. P. T. Nguyen *et al.*, "p-Type modulation doped InGaN/GaN dot-in-a-wire white-light-emitting diodes monolithically grown on Si(111)," *Nano. Lett.,* vol. 11, no. 5, p. 1919, 2011.

[66] Y. J. Hong *et al.*, "Visible-color-tunable light-emitting diodes," *Adv. Mater.,* vol. 23, no. 29, p. 3284, 2011.

[67] H. W. Lin, Y. J. Lu, H. Y. Chen, H. M. Lee, and S. Gwo, "InGaN/GaN nanorod array white light-emitting diode," *Appl. Phys. Lett.,* vol. 97, no. 7, p. 073101, 2010.

[68] C. Chang, L. Chen, L. Huang, Y. Wang, T. Lu, and J. J. Huang, "Effects of strains and defects on the internal quantum efficiency of InGaN/GaN nanorod light emitting diodes," *IEEE. J. Quantum. Elect.,* vol. 48, no. 4, p. 551, 2012.

[69] H. P. T. Nguyen *et al.*, "Engineering the carrier dynamics of InGaN nanowire white light-emitting diodes by distributed p-AlGaN electron blocking layers," *Sci. Rep.,* vol. 5, p. 7744, 2015.

[70] M. Auf der Maur, A. Pecchia, G. Penazzi, W. Rodrigues, and A. Di Carlo, "Efficiency drop in green InGaN/GaN light emitting diodes: the role of random alloy fluctuations," *Phys. Rev. Lett.,* vol. 116, no. 2, p. 027401, 2016.

[71] G. Stringfellow and M. Craford, *Semiconductors and semimetals*. Cambridge, Massachusetts: Elsevier Science, 1997.

[72] F. Bernardini, V. Fiorentini, and D. Vanderbilt, "Spontaneous polarization and piezoelectric constants of III-V nitrides," *Phys. Rev. B.,* vol. 56, no. 16, p. R10024, 1997.

[73] Q. Dai *et al.*, "Carrier recombination mechanisms and efficiency droop in GaInN/GaN light-emitting diodes," *Appl. Phys. Lett.,* vol. 97, no. 13, p. 133507, 2010.

[74] H. Y. Ryu, H. S. Kim, and J. I. Shim, "Rate equation analysis of efficiency droop in InGaN light-emitting diodes," *Appl. Phys. Lett.,* vol. 95, no. 8, p. 081114, 2009.

[75] M. Y. Ryu *et al*., "Photoluminescence study of InGaN/GaN double quantum wells with varying barrier widths," *J. Korean. Phys. Soc.,* vol. 37, no. 4, p. 387, 2000.

[76] S. De *et al.*, "Quantum-confined stark effect in localized luminescent centers within InGaN/GaN quantum-well based light emitting diodes," *Appl. Phys. Lett.,* vol. 101, no. 12, p. 121919, 2012.

[77] C. D. Lee *et al.*, "Properties of GaN epitaxial layers grown on 6H-SiC(0001) by plasma-assisted molecular beam epitaxy," *J. Electron. Mater.,* vol. 30, no. 3, p. 162, 2001.

[78] M. Haeberlen, D. Zhu, C. McAleese, M. J. Kappers, and C. J. Humphreys, "Dislocation reduction in MOVPE grown GaN layers on (111)Si using SiN_x and AlGaN layers," *J. Phys. Conf. Ser.,* vol. 209, no. 1, p. 012017, 2010.

[79] H. Y. Shin, S. K. Kwon, Y. I. Chang, M. J. Cho, and K. H. Park, "Reducing dislocation density in GaN films using a cone-shaped patterned sapphire substrate," *J. Cryst. Growth.,* vol. 311, no. 17, p. 4167, 2009.

[80] S. Chichibu, T. Azuhata, T. Sota, and S. Nakamura, "Luminescences from localized states in InGaN epilayers," *Appl. Phys. Lett.,* vol. 70, no. 21, p. 2822, 1997.

[81] L. Yen-Lin *et al.*, "Origins of efficient green light emission in phase-separated InGaN quantum wells," *Nanotec.,* vol. 17, no. 15, p. 3734, 2006.

[82] B. Monemar and B. E. Sernelius, "Defect related issues in the “current roll-off” in InGaN based light emitting diodes," *Appl. Phys. Lett.,* vol. 91, no. 18, p. 181103, 2007.

[83] H. P. T. Nguyen *et al*., "Temperature-dependent nonradiative recombination processes in GaN-based nanowire white-light-emitting diodes on silicon," *Nanotec.,* vol. 23, no. 19, p. 194012, 2012.

[84] C. K. Li *et al.*, "3D numerical modeling of the carrier transport and radiative efficiency for InGaN/GaN light emitting diodes with V-shaped pits," *AIP. Adv.,* vol. 6, no. 5, p. 055208, 2016.

[85] O. Ü, H. Liu, X. Li, X. Ni, and H. Morkoc, "GaN-Based light-emitting diodes: efficiency at high injection levels," *Proc. IEEE.,* vol. 98, no. 7, p. 1180, 2010.

[86] K. Emmanouil, Y. Qimin, S. Daniel, and G. V. d. W. Chris, "Temperature and carrier-density dependence of Auger and radiative recombination in nitride optoelectronic devices," *New. J. Phys.,* vol. 15, no. 12, p. 125006, 2013.

[87] E. Kioupakis, P. Rinke, K. T. Delaney, and C. G. Van de Walle, "Indirect Auger recombination as a cause of efficiency droop in nitride light-emitting diodes," *Appl. Phys. Lett.,* vol. 98, no. 16, p. 161107, 2011.

[88] J. Iveland, L. Martinelli, J. Peretti, J. S. Speck, and C. Weisbuch, "Direct measurement of auger electrons emitted from a semiconductor light-emitting diode under electrical injection: identification of the dominant mechanism for efficiency droop," *Phys. Rev. Lett.,* vol. 110, no. 17, p. 177406, 2013.

[89] W. Guo, M. Zhang, P. Bhattacharya, and J. Heo, "Auger recombination in III-nitride nanowires and its effect on nanowire light-emitting diode characteristics," *Nano. Lett.,* vol. 11, no. 4, p. 1434, 2011.

[90] E. Kioupakis, P. Rinke, A. Schleife, F. Bechstedt, and C. G. Van de Walle, "Free-carrier absorption in nitrides from first principles," *Phys. Rev. B.,* vol. 81, no. 24, p. 241201, 2010.

[91] A. Laubsch, M. Sabathil, J. Baur, M. Peter, and B. Hahn, "High-power and high-efficiency InGaN-based light emitters," *IEEE. T. Electron. Dev.,* vol. 57, no. 1, p. 79, 2010.

[92] M. Meneghini, N. Trivellin, G. Meneghesso, E. Zanoni, U. Zehnder, and B. Hahn, "A combined electro-optical method for the determination of the recombination parameters in InGaN-based light-emitting diodes," *J. Appl. Phys.,* vol. 106, no. 11, p. 114508, 2009.

[93] X. Ni, Q. Fan, R. Shimada, Ü. Özgür, and H. Morkoç, "Reduction of efficiency droop in InGaN light emitting diodes by coupled quantum wells," *Appl. Phys. Lett.,* vol. 93, no. 17, p. 171113, 2008.

[94] M. Tsai, S. Yen, Y. Lu, and Y. Kuo, "Numerical study of blue InGaN light-emitting diodes with varied barrier thicknesses," *IEEE. Photonics. J.,* vol. 23, no. 2, p. 76, 2011.

[95] J. Piprek and S. Li, "Electron leakage effects on GaN-based light-emitting diodes," *Opt. Quant. electron.,* vol. 42, no. 2, p. 89, 2010.

[96] H. P. T. Nguyen *et al.*, "Controlling electron overflow in phosphor-free InGaN/GaN nanowire white light-emitting diodes," *Nano. Lett.,* vol. 12, no. 3, p. 1317, 2012.

[97] A. Taflove and M. E. Brodwin, "Numerical solution of steady-state electromagnetic scattering problems using the time-dependent maxwell's equations," *IEEE. Trans. Microw. Theory. Tech.,* vol. 23, no. 8, p. 623, 1975.

[98] Y. Kane, "Numerical solution of initial boundary value problems involving maxwell's equations in isotropic media," *IEEE. Trans. Antennas. Propag.,* vol. 14, no. 3, p. 302, 1966.

[99] I. M. Tiginyanu *et al.*, "Luminescence of GaN nanocolumns obtained by photon-assisted anodic etching," *Appl. Phys. Lett.,* vol. 83, no. 8, p. 1551, 2003.

[100] E. Makoto, J. Zhi, K. Seiya, and H. Hideki, "Reactive ion beam etching of GaN and AlGaN/GaN for nanostructure fabrication using methane-based gas mixtures," *Jpn. J. Appl. Phys.,* vol. 41, no. 4S, p. 2689, 2002.

[101] S. Y. Park, S. J. Di Giacomo, R. Anisha, P. R. Berger, P. E. Thompson, and I. Adesida, "Fabrication of nanowires with high aspect ratios utilized by dry etching with SF_6:C_4F_8 and self-limiting thermal oxidation on Si substrate," *J. Vac. Sci. Technol. B.,* vol. 28, no. 4, p. 763, 2010.

[102] M. He *et al.*, "Growth of large-scale GaN nanowires and tubes by direct reaction of Ga with NH_3," *Appl. Phys. Lett.,* vol. 77, no. 23, p. 3731, 2000.

[103] J. Zhang, X. S. Peng, X. F. Wang, Y. W. Wang, and L. D. Zhang, "Micro-Raman investigation of GaN nanowires prepared by direct reaction Ga with NH_3," *Chem. Phys. Lett.,* vol. 345, no. 5, p. 372, 2001.

[104] E. Calleja *et al.*, "Luminescence properties and defects in GaN nanocolumns grown by molecular beam epitaxy," *Phys. Rev. B.,* vol. 62, no. 24, p. 16826, 2000.

[105] C. Yi-Lu, L. Feng, F. Arya, and M. Zetian, "Molecular beam epitaxial growth and characterization of non-tapered InN nanowires on Si(111)," *Nanotec.,* vol. 20, no. 34, p. 345203, 2009.

[106] R. K. Debnath, R. Meijers, T. Richter, T. Stoica, R. Calarco, and H. Lüth, "Mechanism of molecular beam epitaxy growth of GaN nanowires on Si(111)," *Appl. Phys. Lett.,* vol. 90, no. 12, p. 123117, 2007.

[107] H. Y. Peng *et al.*, "Bulk-quantity GaN nanowires synthesized from hot filament chemical vapor deposition," *Chem. Phys. Lett.,* vol. 327, no. 5, p. 263, 2000.

[108] T. Kuykendall, P. Ulrich, S. Aloni, and P. Yang, "Complete composition tunability of InGaN nanowires using a combinatorial approach," *Nat. Mat.,* vol. 6, p. 951, 2007.

[109] P. K. Mohseni, C. Maunders, G. A. Botton, and R. R. LaPierre, "GaP/GaAsP/GaP core–multishell nanowire heterostructures on (111) silicon," *Nanotec.,* vol. 18, no. 44, p. 445304, 2007.

[110] R. S. Wagner and W. C. Ellis, "Vapor-liquid-solid mechanism of single crystal growth," *Appl. Phys. Lett.,* vol. 4, no. 5, p. 89, 1964.

[111] J. C. Harmand, G. Patriarche, N. Péré-Laperne, M. N. Mérat-Combes, L. Travers, and F. Glas, "Analysis of vapor-liquid-solid mechanism in Au-assisted GaAs nanowire growth," *Appl. Phys. Lett.,* vol. 87, no. 20, p. 203101, 2005.

[112] W. I. Park, G. Zheng, X. Jiang, B. Tian, and C. M. Lieber, "Controlled synthesis of millimeter-long silicon nanowires with uniform electronic properties," *Nano. Lett.,* vol. 8, no. 9, p. 3004, 2008.

[113] W. Braun *et al.*, "Diffusion and incorporation: shape evolution during overgrowth on structured substrates," *J. Cryst. Growth.,* vol. 227-228, p. 51, 2001.

[114] S. G. Ihn, J. I. Song, Y. H. Kim, and J. Y. Lee, "GaAs nanowires on Si substrates grown by a solid source molecular beam epitaxy," *Appl. Phys. Lett.,* vol. 89, no. 5, p. 053106, 2006.

[115] V. Gottschalch, G. Wagner, J. Bauer, H. Paetzelt, and M. Shirnow, "VLS growth of GaN nanowires on various substrates," *J. Cryst. Growth.,* vol. 310, no. 23, p. 5123, 2008

.

[116] Z. Cai, S. Garzon, M. V. S. Chandrashekhar, R. A. Webb, and G. Koley, "Synthesis and properties of high-quality InN nanowires and nanonetworks," *J. Electron. Mater.,* vol. 37, no. 5, p. 585, 2008.

[117] E. Stern *et al.*, "Electrical characterization of single GaN nanowires," *Nanotec.,* vol. 16, no. 12, p. 2941, 2005.

[118] S. M. Kang, B. K. Kang, and D. H. Yoon, "Growth and properties of vertically well-aligned GaN nanowires by thermal chemical vapor deposition process," *Mater. Lett.,* vol. 65, no. 4, p. 763, 2011.

[119] L. J. Lauhon, M. S. Gudiksen, and C. M. Lieber, "Semiconductor nanowire heterostructures," *Philos. Trans. A. Math. Phys. Eng. Sci.,* vol. 362, no. 1819, p. 1247, 2004.

[120] L. J. Lauhon, M. S. Gudiksen, D. Wang, and C. M. Lieber, "Epitaxial core–shell and core–multishell nanowire heterostructures," *Nature.,* vol. 420, p. 57, 2002

[121] B. Tian *et al.*, "Coaxial silicon nanowires as solar cells and nanoelectronic power sources," *Nature.,* vol. 449, p. 885, 2007.

[122] E. Durgun, N. Akman, C. Ataca, and S. Ciraci, "Atomic and electronic structures of doped silicon nanowires: A first-principles study," *Phys. Rev. B.,* vol. 76, no. 24, p. 245323, 2007.

[123] J. Ristić *et al.*, "On the mechanisms of spontaneous growth of III-nitride nanocolumns by plasma-assisted molecular beam epitaxy," *J. Cryst. Growth.,* vol. 310, no. 18, p. 4035, 2008.

[124] A. P. Vajpeyi *et al.*, "Spontaneous growth of III-nitride nanowires on Si by molecular beam epitaxy," *Microelectron. Eng.,* vol. 86, no. 4, p. 812, 2009.

[125] K. A. Bertness, A. Roshko, L. M. Mansfield, T. E. Harvey, and N. A. Sanford, "Mechanism for spontaneous growth of GaN nanowires with molecular beam epitaxy," *J. Cryst. Growth.,* vol. 310, no. 13, p. 3154, 2008.

[126] M. A. Sanchez-Garcia *et al.*, "The effect of the III/V ratio and substrate temperature on the morphology and properties of GaN- and AlN-layers grown by molecular beam epitaxy on Si(111)," *J. Cryst. Growth.,* vol. 183, no. 1, p. 23, 1998.

[127] K. A. Bertness, A. Roshko, N. A. Sanford, J. M. Barker, and A. V. Davydov, "Spontaneously grown GaN and AlGaN nanowires," *J. Cryst. Growth.,* vol. 287, no. 2, p. 522, 2006.

[128] J. Gao *et al.*, "UV light emitting transparent conducting tin-doped indium oxide (ITO) nanowires," *Nanotec.,* vol. 22, no. 19, p. 195706, 2011.

[129] T. Schumann, T. Gotschke, F. Limbach, T. Stoica, and R. Calarco, "Selective-area catalyst-free MBE growth of GaN nanowires using a patterned oxide layer," *Nanotec.,* vol. 22, no. 9, p. 095603, 2011.

[130] S. Hiroto, K. Katsumi, and K. Akihiko, "Ti-mask selective-area growth of GaN by RF-plasma-assisted molecular-beam epitaxy for fabricating regularly arranged InGaN/GaN nanocolumns," *Appl. Phys. Express.,* vol. 1, no. 12, p. 124002, 2008.

[131] B. H. Le, S. Zhao, X. Liu, S. Y. Woo, G. A. Botton, and Z. Mi, "Controlled coalescence of AlGaN nanowire arrays: an architecture for nearly dislocation-free planar ultraviolet photonic device applications," *Adv. Mater.,* vol. 28, no. 38, p. 8446, 2016.

[132] T. Stoica, R. Meijers, R. Calarco, T. Richter, and H. Lüth, "MBE growth optimization of InN nanowires," *J. Cryst. Growth.,* vol. 290, no. 1, p. 241, 2006.

[133] M. Ralph Joseph, "Growth and Characterisation of Group-III Nitride-based Nanowires for Devices," PhD dissertation, Physics Department, Research Centre Jülich, Julich, 2007.

[134] T. K. Zywietz, J. Neugebauer, and M. Scheffler, "The adsorption of oxygen at GaN surfaces," *Appl. Phys. Lett.,* vol. 74, no. 12, p. 1695, 1999.

[135] P. Van Mieghem, "Theory of band tails in heavily doped semiconductors," *Rev. Mod. Phys.,* vol. 64, no. 3, p. 755, 1992.

[136] L. Zhang, K. Cheng, S. Degroote, M. Leys, M. Germain, and G. Borghs, "Strain effects in GaN epilayers grown on different substrates by metal organic vapor phase epitaxy," *J. Appl. Phys.,* vol. 108, no. 7, p. 073522, 2010.

[137] M. Boroditsky, R. Vrijen, R. Coccioli, R. Bhat, and E. Yablonovitch, "Spontaneous emission extraction and purcell enhancement from thin-film 2-d photonic crystals," *J. Light. Technol.,* vol. 17, no. 11, p. 2096, 1999.

[138] C. Netzel *et al.*, "Temperature and excitation power dependent photoluminescence intensity of GaInN quantum wells with varying charge carrier wave function overlap," *J. Appl. Phys.,* vol. 107, no. 3, p. 033510, 2010.

[139] S. Watanabe *et al.*, "Internal quantum efficiency of highly-efficient $In_xGa_{1-x}N$-based near-ultraviolet light-emitting diodes," *Appl. Phys. Lett.,* vol. 83, no. 24, p. 4906, 2003.

[140] Y. Lee *et al.*, "Study of the Excitation Power Dependent Internal Quantum Efficiency in InGaN/GaN LEDs Grown on Patterned Sapphire Substrate," *IEEE. J. Sel. Area. Comm.,* vol. 15, no. 4, p. 1137, 2009.

[141] W. Davis, "Color Rendering of Light Sources | DigiKey", Digikey.com, 2011. https://www.digikey.com/en/articles/techzone/2011/feb/color-rendering-of-light-sources (accessed on March 1,2019).

[142] M. Rajan Philip, D. D. Choudhary, M. Djavid, K. Q. Le, J. Piao, and H. P. T. Nguyen, "High efficiency green/yellow and red InGaN/AlGaN nanowire light-emitting diodes grown by molecular beam epitaxy," *J. Sci: Adv. Mat. Dev.,* vol. 2, no. 2, p. 150, 2017.

[143] Y. Narukawa *et al.*, "Recent progress of high efficiency white LEDs," *Phys. Status. Solidi. A.,* vol. 204, no. 6, p. 2087, 2007.

[144] J. Xie, X. Ni, Q. Fan, R. Shimada, Ü. Özgür, and H. Morkoç, "On the efficiency droop in InGaN multiple quantum well blue light emitting diodes and its reduction with p-doped quantum well barriers," *Appl. Phys. Lett.,* vol. 93, no. 12, p. 121107, 2008.

[145] V. Rozhansky and D. A. Zakheim, "Analysis of the causes of the decrease in the electroluminescence efficiency of AlGaInN light-emitting-diode heterostructures at high pumping density," *Semicond.,* vol. 40, no. 7, p. 839, 2006.

[146] L. Cerutti *et al.*, "Wurtzite GaN nanocolumns grown on Si(001) by molecular beam epitaxy," *Appl. Phys. Lett.,* vol. 88, no. 21, p. 213114, 2006.

[147] R. Calarco, R. J. Meijers, R. K. Debnath, T. Stoica, E. Sutter, and H. Lüth, "Nucleation and growth of GaN nanowires on Si(111) performed by molecular beam epitaxy," *Nano. Lett.,* vol. 7, no. 8, p. 2248, 2007.

[148] W. Guo, M. Zhang, A. Banerjee, and P. Bhattacharya, "Catalyst-Free InGaN/GaN nanowire light emitting diodes grown on (001) silicon by molecular beam epitaxy," *Nano. Lett.,* vol. 10, no. 9, p. 3355, 2010.

[149] C. Hahn *et al.*, "Epitaxial growth of InGaN nanowire arrays for light emitting diodes," *ACS. Nano.,* vol. 5, no. 5, p. 3970, 2011.

[150] Y.-H. Ra, R. Navamathavan, H.-I. Yoo, and C.-R. Lee, "Single nanowire light-emitting diodes using uniaxial and coaxial InGaN/GaN multiple quantum wells synthesized by metalorganic chemical vapor deposition," *Nano. Lett.,* vol. 14, no. 3, p. 1537, 2014.

[151] M. Tchernycheva *et al.*, "InGaN/GaN core–shell single nanowire light emitting diodes with graphene-based p-contact," *Nano. Lett.,* vol. 14, no. 5, p. 2456, 2014.

[152] S. Jahangir, M. Mandl, M. Strassburg, and P. Bhattacharya, "Molecular beam epitaxial growth and optical properties of red-emitting ($\lambda = 650$ nm) InGaN/GaN disks-in-nanowires on silicon," *Appl. Phys. Lett.,* vol. 102, no. 7, p. 071101, 2013.

[153] H. P. T. Nguyen, M. Djavid, and Z. Mi, "Nonradiative recombination mechanism in phosphor-free GaN-based nanowire white light emitting diodes and the effect of ammonium sulfide surface passivation," *ECS. Trans.,* vol. 53, no. 2, p. 93, 2013.

[154] H. Eisele, S. Borisova, L. Ivanova, M. Dähne, and P. Ebert, "Cross-sectional scanning tunneling microscopy and spectroscopy of nonpolar GaN(11 bar 0 0) surfaces," *J. Vac. Sci. Technol. B.,* vol. 28, no. 4, p. C5G11, 2010.

[155] C. G. Van de Walle and D. Segev, "Microscopic origins of surface states on nitride surfaces," *J. Appl. Phys.,* vol. 101, no. 8, p. 081704, 2007.

[156] H. Sekiguchi, K. Kishino, and A. Kikuchi, "Emission color control from blue to red with nanocolumn diameter of InGaN/GaN nanocolumn arrays grown on same substrate," *Appl. Phys. Lett.,* vol. 96, no. 23, p. 231104, 2010.

[157] K. A. Bertness *et al.*, "Controlled nucleation of GaN nanowires grown with molecular beam epitaxy," *Adv. Funct. Mater.,* vol. 20, no. 17, p. 2911, 2010.

[158] W. Guo, A. Banerjee, P. Bhattacharya, and B. S. Ooi, "InGaN/GaN disk-in-nanowire white light emitting diodes on (001) silicon," *Appl. Phys. Lett.,* vol. 98, no. 19, p. 193102, 2011.

[159] J. Piprek, "Efficiency droop in nitride-based light-emitting diodes," *Phys. Status. Solidi. A.,* vol. 207, no. 10, p. 2217, 2010.

[160] C. C. Hong, H. Ahn, C. Y. Wu, and S. Gwo, "Strong green photoluminescence from $In_xGa_{1-x}N$/GaN nanorod arrays," *Opt. Express.,* vol. 17, no. 20, p. 17227, 2009.

[161] C. Zhao *et al.*, "Droop-free, reliable, and high-power InGaN/GaN nanowire light-emitting diodes for monolithic metal-optoelectronics," *Nano. Lett.,* vol. 16, no. 7, p. 4616, 2016.

[162] B. Janjua *et al.*, "True yellow light-emitting diodes as phosphor for tunable color-rendering index laser-based white light," *ACS. Photo.,* vol. 3, no. 11, p. 2089, 2016.

[163] M. Rajan Philip et al., “Phosphor-free III-nitride nanowire white-light-emitting diodes for visible light communication,” *Proc. SPIE.,* vol. 10595, p. 7, 2018.

[164] G. Heliotis, G. Itskos, R. Murray, M. D. Dawson, I. M. Watson, and D. D. C. Bradley, "Hybrid inorganic/organic semiconductor heterostructures with efficient non-radiative energy transfer," *Adv. Mater.,* vol. 18, no. 3, p. 334, 2006.

[165] E. F. Schubert, K. Jong Kyu, L. Hong, and J. Q. Xi, "Solid-state lighting—a benevolent technology," *Rep. Prog. Phys.,* vol. 69, no. 12, p. 3069, 2006.

[166] F. Zhang *et al.*, "Multimodal fast optical interrogation of neural circuitry," *Nature.,* vol. 446, p. 633, 2007.

[167] J. J. D. McKendry *et al.*, "Visible-light communications using a CMOS-controlled micro-light- emitting-diode array," *J. Light. Technol.,* vol. 30, no. 1, p. 61, 2012.

[168] L. Zeng *et al.*, "High data rate multiple input multiple output (MIMO) optical wireless communications using white led lighting," *IEEE. J. Sel. Areas. Commun.,* vol. 27, no. 9, p. 1654, 2009.

[169] H. L. Minh *et al.*, "100-Mb/s NRZ visible light communications using a postequalized white LED," *IEEE. Photonic. Tech. L.,* vol. 21, no. 15, p. 1063, 2009.

[170] T. Komine and M. Nakagawa, "Integrated system of white LED visible-light communication and power-line communication," *IEEE. Trans. Consum. Electron.,* vol. 49, no. 1, p. 71, 2003.

[171] D. Giustiniano, N. O. Tippenhauer, and S. Mangold, "Low-complexity visible light networking with LED-to-LED communication," *Proc. IFIP. Wireless. Days.*, p. 1, 2012.

[172] H. Le Minh *et al.*, "High-Speed Visible Light Communications Using Multiple-Resonant Equalization," *IEEE. Photonics. Technol. Lett.,* vol. 20, no. 14, p. 1243, 2008.

[173] J. Grubor, et al., "Wireless high-speed data transmission with phosphorescent white-light LEDs," *Proc. ECOC.,* p. 1, 2007.

[174] C. Du *et al.*, "Tuning carrier lifetime in InGaN/GaN LEDs via strain compensation for high-speed visible light communication," *Sci. Rep.,* vol. 6, p. 37132, 2016.

[175] Z. Jiang *et al.*, "Monolithic integration of nitride light emitting diodes and photodetectors for bi-directional optical communication," *Opt. Lett.,* vol. 39, no. 19, p. 5657, 2014.

[176] P. Deng, M. Kavehrad, and M. A. Kashani, "Nonlinear modulation characteristics of white LEDs in visible light communications," in *Opt. Fib.Comm. Conf.,* p. 1, 2015.

[177] S. Rajagopal, R. D. Roberts, and S. K. Lim, "IEEE 802.15.7 visible light communication: modulation schemes and dimming support," *IEEE. Commun. Mag.,* vol. 50, no. 3, p. 72, 2012.

[178] M. Rajan Philip *et al.*, "Fabrication of phosphor-free iii-nitride nanowire light-emitting diodes on metal substrates for flexible photonics," *ACS. Omega.,* vol. 2, no. 9, p. 5708, 2017.

[179] S. Z. Y. Pei, H. Yang, L. Zhao, X. Yi, J. Junxi Wang and J. Li, "LED modulation characteristics in a visible-light communication system," *Opt. Photon. J.,* vol. 3, no. 2B, p. 139, 2013.

[180] B. Janjua *et al.*, "Ultrabroad linewidth orange-emitting nanowires LED for high CRI laser-based white lighting and gigahertz communications," *Opt. Express.,* vol. 24, no. 17, p. 19228, 2016.

[181] J. D. Albrecht, R. P. Wang, P. P. Ruden, M. Farahmand, and K. F. Brennan, "Electron transport characteristics of GaN for high temperature device modeling," *J. Appl. Phys.,* vol. 83, no. 9, p. 4777, 1998.

[182] I. Vurgaftman, J. R. Meyer, and L. R. Ram-Mohan, "Band parameters for III–V compound semiconductors and their alloys," *J. Appl. Phys.,* vol. 89, no. 11, p. 5815, 2001.

[183] V. G. Dubrovskii and N. V. Sibirev, "Growth thermodynamics of nanowires and its application to polytypism of zinc blende III-V nanowires," *Phys. Rev. B.,* vol. 77, no. 3, p. 035414, 2008.

[184] Y. L. Chang, J. L. Wang, F. Li, and Z. Mi, "High efficiency green, yellow, and amber emission from InGaN/GaN dot-in-a-wire heterostructures on Si(111)," *Appl. Phys. Lett.,* vol. 96, no. 1, p. 013106, 2010.

[185] Q. Li and G. T. Wang, "Improvement in aligned GaN nanowire growth using submonolayer Ni catalyst films," *Appl. Phys. Lett.,* vol. 93, no. 4, p. 043119, 2008.

[186] Y. Cui and C. M. Lieber, "Functional nanoscale electronic devices assembled using silicon nanowire building blocks," *Science.,* vol. 291, no. 5505, p. 851, 2001.

[187] Y. Li, F. Qian, J. Xiang, and C. M. Lieber, "Nanowire electronic and optoelectronic devices," *Mater. Today.,* vol. 9, no. 10, p. 18, 2006.

[188] X. Duan, Y. Huang, Y. Cui, J. Wang, and C. M. Lieber, "Indium phosphide nanowires as building blocks for nanoscale electronic and optoelectronic devices," *Nature.,* vol. 409, no. 6816, p. 66, 2001.

[189] A. M. Ionescu, "Electronic devices: nanowire transistors made easy," *Nat. Nano.,* vol. 5, no. 3, p. 178, 2010.

[190] O. Ambacher, "Growth and applications of group iii-nitrides," *J. Phys. D.,* vol. 31, no. 20, p. 2653, 1998.

[191] P. Feng, J. Y. Zhang, Q. H. Li, and T. H. Wang, "Individual β-Ga_2O_3 nanowires as solar-blind photodetectors," *Appl. Phys. Lett.,* vol. 88, no. 15, p. 153107, 2006.

[192] L. Yanbo, V. Florent Della, S. Mathieu, Y. Ichiro, and D. Jean-Jacques, "High-performance UV detector made of ultra-long ZnO bridging nanowires," *Nanotec.,* vol. 20, no. 4, p. 045501, 2009.

[193] P. Dong *et al.*, "282-nm AlGaN-based deep ultraviolet light-emitting diodes with improved performance on nano-patterned sapphire substrates," *Appl. Phys. Lett.,* vol. 102, no. 24, p. 241113, 2013.

[194] X. Wei and Y. Joshi, "Stacked microchannel heat sinks for liquid cooling of microelectronic components," *J. Electron. Packaging.,* vol. 126, no. 1, p. 60, 2004.

[195] D. H. Lee *et al.*, "Temperature and thermal characteristics of InGaN/GaN vertical light-emitting diodes on electroplated copper," *Semicond. Sci. Technol.,* vol. 26, no. 5, p. 055014, 2011.

[196] T. Zyung *et al.*, "Flexible organic led and organic thin-film transistor," *Proc. IEEE.,* vol. 93, no. 7, p. 1265, 2005.

[197] G. S. Buller and R. J. Collins, "Single-photon generation and detection," *Meas. Sci. Technol.,* vol. 21, no. 1, p. 012002, 2010.

[198] Ł. Dusanowski *et al.*, "Single photon emission at 1.55 μm from charged and neutral exciton confined in a single quantum dash," *Appl. Phys. Lett.,* vol. 105, no. 2, p. 021909, 2014.

[199] M. Mikulics and H. Hardtdegen, "Nano-LED array fabrication suitable for future single photon lithography," *Nanotec.,* vol. 26, no. 18, p. 185302, 2015.

[200] M. Mikulics *et al.*, "Direct electro-optical pumping for hybrid CdSe nanocrystal/III-nitride based nano-light-emitting diodes," *Appl. Phys. Lett.,* vol. 108, no. 6, p. 061107, 2016.

[201] V. C. Sundar *et al.*, "Elastomeric transistor stamps: reversible probing of charge transport in organic crystals," *Science.,* vol. 303, no. 5664, p. 1644, 2004.

[202] A. L. Briseno *et al.*, "High-performance organic single-crystal transistors on flexible substrates," *Adv. Mater.,* vol. 18, no. 17, p. 2320, 2006.

[203] J. Petroski, "Spacing of high-brightness LEDs on metal substrate PCB's for proper thermal performance," *Proc. ITHERM.*, vol. 2, p. 507, 2004.

[204] X. Zou, X. Zhang, W. C. Chong, C. W. Tang, and K. M. Lau, "Vertical LEDs on rigid and flexible substrates using GaN-on-Si epilayers and au-free bonding," *IEEE. Trans. Electron. Devices.,* vol. 63, no. 4, p. 1587, 2016.

[205] L. Zhang, N. G. Alexopoulos, D. Sievenpiper, and E. Yablonovitch, "An efficient finite-element method for the analysis of photonic band-gap materials," *Proc. IEEE. Int. Microwave. Symp. Dig.,* vol. 4, p. 1703, 1999.

[206] C. Zhao *et al.*, "An enhanced surface passivation effect in InGaN/GaN disk-in-nanowire light emitting diodes for mitigating Shockley-Read-Hall recombination," *Nanoscale.,* vol. 7, no. 40, p. 16658, 2015.

[207] A. L. Bavencove *et al.*, "Submicrometre resolved optical characterization of green nanowire-based light emitting diodes," *Nanotec.,* vol. 22, no. 34, p. 345705, 2011.

[208] M. Oh and H. Kim, "High-efficiency GaN-based light-emitting diodes fabricated with identical Ag contact formed on both n- and p-layers," *Opt. Express.,* vol. 21, no. 18, p. 20857, 2013.

[209] J. O. Song, J. S. Ha, and T. Y. Seong, "Ohmic-contact Technology for GaN-based light-emitting diodes: role of p-type contact," *IEEE. Trans. Electron. Devices.,* vol. 57, no. 1, p. 42, 2010.

[210] M. A. Green and M. J. Keevers, "Optical properties of intrinsic silicon at 300 K," *Prog. Photovoltaics.,* vol. 3, no. 3, p. 189, 1995.

[211] M. A. Green, "Self-consistent optical parameters of intrinsic silicon at 300 K including temperature coefficients," *Sol. Energy. Mater. Sol. Cells.,* vol. 92, no. 11, p. 1305, 2008.

[212] W. C. Chong and K. M. Lau, "Performance enhancements of flip-chip light-emitting diodes with high-density n-type point-contacts," *IEEE. Electr. Device. L.,* vol. 35, no. 10, p. 1049, 2014.

[213] M. Nami and D. F. Feezell, "Optical properties of plasmonic light-emitting diodes based on flip-chip III-nitride core-shell nanowires," *Opt. Express.,* vol. 22, no. 24, p. 29445, 2014.

[214] H. P. T. Nguyen, Q. Wang, and Z. Mi, "Phosphor-free InGaN/GaN dot-in-a-wire white light-emitting diodes on copper substrates," *J. Electron. Mater.,* vol. 43, no. 4, p. 868, 2014.

[215] S. Zhao, M. G. Kibria, Q. Wang, H. P. T. Nguyen, and Z. Mi, "Growth of large-scale vertically aligned GaN nanowires and their heterostructures with high uniformity on SiO_x by catalyst-free molecular beam epitaxy," *Nanoscale.,* vol. 5, no. 12, p. 5283, 2013.

[216] Q. Wang, J. Bai, Y. P. Gong, and T. Wang, "Influence of strain relaxation on the optical properties of InGaN/GaN multiple quantum well nanorods," *J. Phys. D.,* vol. 44, no. 39, p. 395102, 2011.

[217] C. Chen-Fu *et al.*, "High Brightness GaN Vertical Light-Emitting Diodes on Metal Alloy for General Lighting Application," *Proc. IEEE.,* vol. 98, no. 7, p. 1197, 2010.

[218] W. Y. Lin *et al.*, "High-power GaN-mirror-Cu light-emitting diodes for vertical current injection using laser liftoff and electroplating techniques," *IEEE. Photonics. Technol. Lett.,* vol. 17, no. 9, p. 1809, 2005.

[219] M. Hisashi, S. Junichi, P. Nathan, K. Ingrid, N. Shuji, and P. D. Steven, "Quantum-confined Stark effect on photoluminescence and electroluminescence characteristics of InGaN-based light-emitting diodes," *J. Phys. D.,* vol. 41, no. 16, p. 165105, 2008.

[220] H. Hirayama *et al.*, "222-282 nm AlGaN and InAlGaN based deep-UV LEDs fabricated on high-quality AlN template," *Proc. SPIE.,* vol. 7216, p. 14, 2009.

[221] A. Bhattacharyya, T. D. Moustakas, L. Zhou, D. J. Smith, and W. Hug, "Deep ultraviolet emitting AlGaN quantum wells with high internal quantum efficiency," *Appl. Phys. Lett.,* vol. 94, no. 18, p. 181907, 2009.

[222] C. Himwas *et al.*, "AlGaN/AlN quantum dots for UV light emitters," *Phys. Status. Solidi. C.,* vol. 10, no. 3, p. 285, 2013.

[223] Y. Taniyasu, M. Kasu, and T. Makimoto, "An aluminium nitride light-emitting diode with a wavelength of 210 nanometres," *Nature.,* vol. 441, p. 325, 2006.

[224] A. Khan, K. Balakrishnan, and T. Katona, "Ultraviolet light-emitting diodes based on group three nitrides," *Nat. Photonics.,* vol. 2, no. 2, p. 77, 2008.

[225] M. S. Shur and R. Gaska, "Deep-ultraviolet light-emitting diodes," *IEEE Trans. Electron. Devices.,* vol. 57, no. 1, p. 12, 2010.

[226] H. Hirayama *et al.*, "222–282 nm AlGaN and InAlGaN-based deep-UV LEDs fabricated on high-quality AlN on sapphire," *Phys. Status. Solidi. A.,* vol. 206, no. 6, p. 1176, 2009.

[227] E. Takashi and S. Bin Abu Bakar Ahmad, "High performance InGaN LEDs on Si (1 1 1) substrates grown by MOCVD," *J. Phys. D.,* vol. 43, no. 35, p. 354008, 2010.

[228] S. Strite and H. Morkoç, "GaN, AlN, and InN: A review," *J. Vac. Sci. Technol. B. Microelectron. Nanometer. Struct. Process. Meas. Phenom.,* vol. 10, no. 4, p. 1237, 1992.

[229] D. Zhu, D. J. Wallis, and C. J. Humphreys, "Prospects of III-nitride optoelectronics grown on Si," *Rep. Prog. Phys.,* vol. 76, no. 10, p. 106501, 2013.

[230] M. A. Khan, M. Shatalov, H. P. Maruska, H. M. Wang, and E. Kuokstis, "III–nitride UV Devices," *Jpn. J. Appl. Phys.,* vol. 44, no. 10R, p. 7191, 2005.

[231] S. Kamiyama *et al.*, "Low-temperature-deposited AlGaN interlayer for improvement of AlGaN/GaN heterostructure," *J. Cryst. Growth.,* vol. 223, no. 1, p. 83, 2001.

[232] J. Han *et al.*, "Control and elimination of cracking of AlGaN using low-temperature AlGaN interlayers," *Appl. Phys. Lett.,* vol. 78, no. 1, p. 67, 2000.

[233] H. Kazumasa, "Epitaxial lateral overgrowth techniques used in group III nitride epitaxy," *J. Phys. Condens. Matter.,* vol. 13, no. 32, p. 6961, 2001.

[234] Z. R. Zytkiewicz, "Laterally overgrown structures as substrates for lattice mismatched epitaxy," *Thin. Solid. Films.,* vol. 412, no. 1, p. 64, 2002.

[235] O.-H. Nam, M. D. Bremser, T. S. Zheleva, and R. F. Davis, "Lateral epitaxy of low defect density GaN layers via organometallic vapor phase epitaxy," *Appl. Phys. Lett.,* vol. 71, no. 18, p. 2638, 1997.

[236] M. Asif Khan, J. N. Kuznia, D. T. Olson, T. George, and W. T. Pike, "GaN/AlN digital alloy short-period superlattices by switched atomic layer metalorganic chemical vapor deposition," *Appl. Phys. Lett.,* vol. 63, no. 25, p. 3470, 1993.

[237] M. Asif Khan, J. N. Kuznia, R. A. Skogman, D. T. Olson, M. Mac Millan, and W. J. Choyke, "Low pressure metalorganic chemical vapor deposition of AIN over sapphire substrates," *Appl. Phys. Lett.,* vol. 61, no. 21, p. 2539, 1992.

[238] M. Asif Khan, R. A. Skogman, J. M. Van Hove, D. T. Olson, and J. N. Kuznia, "Atomic layer epitaxy of GaN over sapphire using switched metalorganic chemical vapor deposition," *Appl. Phys. Lett.,* vol. 60, no. 11, p. 1366, 1992.

[239] V. Kueller *et al.*, "Modulated Epitaxial Lateral Overgrowth of AlN for Efficient UV LEDs," *IEEE. Photonics. Technol. Lett.,* vol. 24, no. 18, p. 1603, 2012.

[240] H. X. Jiang and J. Y. Lin, "Hexagonal boron nitride for deep ultraviolet photonic devices," *Semicond. Sci. Technol.,* vol. 29, no. 8, p. 084003, 2014.

[241] M. L. Nakarmi, N. Nepal, J. Y. Lin, and H. X. Jiang, "Photoluminescence studies of impurity transitions in Mg-doped AlGaN alloys," *Appl. Phys. Lett.,* vol. 94, no. 9, p. 091903, 2009.

[242] S. Krishnamoorthy, F. Akyol, P. S. Park, and S. Rajan, "Low resistance GaN/InGaN/GaN tunnel junctions," *Appl. Phys. Lett.,* vol. 102, no. 11, p. 113503, 2013.

[243] S. Krishnamoorthy, D. N. Nath, F. Akyol, P. S. Park, M. Esposto, and S. Rajan, "Polarization-engineered GaN/InGaN/GaN tunnel diodes," *Appl. Phys. Lett.,* vol. 97, no. 20, p. 203502, 2010.

[244] J. Simon, V. Protasenko, C. Lian, H. Xing, and D. Jena, "Polarization-induced hole doping in wide–band-gap uniaxial semiconductor heterostructures," *Science., v*ol. 327, no. 5961, p. 60, 2010.

[245] L. Zhang *et al.*, "Theoretical study of polarization-doped GaN-based light-emitting diodes," *Appl. Phys. Lett.,* vol. 98, no. 10, p. 101110, 2011.

[246] M. L. Nakarmi, K. H. Kim, J. Li, J. Y. Lin, and H. X. Jiang, "Enhanced p-type conduction in GaN and AlGaN by Mg-δ-doping," *Appl. Phys. Lett.,* vol. 82, no. 18, p. 3041, 2003.

[247] K. B. Nam, J. Li, M. L. Nakarmi, J. Y. Lin, and H. X. Jiang, "Unique optical properties of AlGaN alloys and related ultraviolet emitters," *Appl. Phys. Lett.,* vol. 84, no. 25, p. 5264, 2004.

[248] R. G. Banal, M. Funato, and Y. Kawakami, "Optical anisotropy in [0001]-oriented $Al_xGa_{1-x}N$/AlN quantum wells (x>0.69)," *Phys. Rev. B.,* vol. 79, no. 12, p. 121308, 2009.

[249] H. Kawanishi, M. Senuma, and T. Nukui, "Anisotropic polarization characteristics of lasing and spontaneous surface and edge emissions from deep-ultraviolet (λ≈240nm) AlGaN multiple-quantum-well lasers," *Appl. Phys. Lett.,* vol. 89, no. 4, p. 041126, 2006.

[250] H. Kawanishi, M. Senuma, M. Yamamoto, E. Niikura, and T. Nukui, "Extremely weak surface emission from (0001) c-plane AlGaN multiple quantum well structure in deep-ultraviolet spectral region," *Appl. Phys. Lett.,* vol. 89, no. 8, p. 081121, 2006.

[251] T. Kolbe *et al.*, "Optical polarization characteristics of ultraviolet (In)(Al)GaN multiple quantum well light emitting diodes," *Appl. Phys. Lett.,* vol. 97, no. 17, p. 171105, 2010.

[252] J. E. Northrup *et al.*, "Effect of strain and barrier composition on the polarization of light emission from AlGaN/AlN quantum wells," *Appl. Phys. Lett.,* vol. 100, no. 2, p. 021101, 2012.

[253] N. Narendran and Y. Gu, "Life of LED-based white light sources," *J Disp Technol.,* vol. 1, no. 1, p. 167, 2005.

[254] S. T. Tan, X. W. Sun, H. V. Demir, and S. P. DenBaars, "Advances in the led materials and architectures for energy-saving solid-state lighting toward "lighting revolution"," *IEEE. Photon. J.,* vol. 4, no. 2, p. 613, 2012.

[255] S. Nakamura, T. Mukai, and M. Senoh, "High-brightness InGaN/AlGaN double-heterostructure blue-green-light-emitting diodes," *J. Appl. Phys.,* vol. 76, no. 12, p. 8189, 1994.

[256] K. Davitt *et al.*, "Spectroscopic sorting of aerosols by a compact sensor employing UV LEDs," *Aerosol. Sci. Technol.,* vol. 40, no. 12, p. 1047, 2006.

[257] S. Ek, B. Anderson, and S. Svanberg, "Compact fiber-optic fluorosensor employing light-emitting ultraviolet diodes as excitation sources," *Spectrochim. Acta. B.,* vol. 63, no. 2, p. 349, 2008.

[258] I. Akasaki, "Nitride semiconductors-impact on the future world," *J. Cryst. Growth.,* vol. 237–239, p. 905, 2002.

[259] O. P. Lupan, Thierry ; Bahers, Tangui Le; Viana, Bruno; Ciofini, Ilaria "Wavelength-emission tuning of ZnO nanowire-based light-emitting diodes by Cu doping: experimental and computational insights," *Adv. Funct. Mater.,* vol. 21, no. 18, p. 3564, 2011.

[260] O. Lupan, T. Pauporté, and B. Viana, "Low-voltage UV-electroluminescence from ZnO-nanowire array/p-GaN light-emitting diodes," *Adv. Mater.,* vol. 22, no. 30, p. 3298, 2010.

[261] J. Heikenfeld, M. Garter, D. S. Lee, R. Birkhahn, and A. J. Steckl, "Red light emission by photoluminescence and electroluminescence from Eu-doped GaN," *Appl. Phys. Lett.,* vol. 75, no. 9, p. 1189, 1999.

[262] M. Takashi, Y. Motokazu, and N. Shuji, "Characteristics of InGaN-Based UV/blue/green/amber/red light-emitting diodes," *J. Appl. Phys.,* vol. 38, no. 7R, p. 3976, 1999.

[263] N. F. Gardner *et al.*, "Blue-emitting InGaN–GaN double-heterostructure light-emitting diodes reaching maximum quantum efficiency above 200A/cm^2," *Appl. Phys. Lett.,* vol. 91, no. 24, p. 243506, 2007.

[264] T. Mukai, D. Morita, and S. Nakamura, "High-power UV InGaN/AlGaN double-heterostructure LEDs," *J. Cryst. Growth.,* vol. 189–190, p. 778, 1998.

[265] M. Takashi and N. Shuji, "Ultraviolet InGaN and GaN single-quantum-well-structure light-emitting diodes grown on epitaxially laterally overgrown GaN substrates," *J. Appl. Phys.,* vol. 38, no. 10R, p. 5735, 1999.

[266] T. Nishida, H. Saito, and N. Kobayashi, "Efficient and high-power AlGaN-based ultraviolet light-emitting diode grown on bulk GaN," *Appl. Phys. Lett.,* vol. 79, no. 6, p. 711, 2001.

[267] Y. Motokazu *et al.*, "InGaN-based near-ultraviolet and blue-light-emitting diodes with high external quantum efficiency using a patterned sapphire substrate and a mesh electrode," *J. Appl. Phys.,* vol. 41, no. 12B, p. L1431, 2002.

[268] J. Shakya, K. Knabe, K. H. Kim, J. Li, J. Y. Lin, and H. X. Jiang, "Polarization of III-nitride blue and ultraviolet light-emitting diodes," *Appl. Phys. Lett.,* vol. 86, no. 9, p. 091107, 2005.

[269] S. Max *et al.*, "AlGaN deep-ultraviolet light-emitting diodes with external quantum efficiency above 10%," *Appl. Phys. Express.,* vol. 5, no. 8, p. 082101, 2012.

[270] M. Djavid and Z. Mi, "Enhancing the light extraction efficiency of AlGaN deep ultraviolet light emitting diodes by using nanowire structures," *Appl. Phys. Lett.,* vol. 108, no. 5, p. 051102, 2016.

[271] J. Shakya, K. H. Kim, J. Y. Lin, and H. X. Jiang, "Enhanced light extraction in III-nitride ultraviolet photonic crystal light-emitting diodes," *Appl. Phys. Lett.,* vol. 85, no. 1, p. 142, 2004.

[272] E. F. Schubert, *Light-Emitting Diodes.* Cambridge, Massachusetts: Cambridge University Press, 2006.

[273] W. S. Choi, J. Kim, Y. Neumeier, and J. Jagoda, "Preliminary Study of a Low Power Plasma Radical Jet Generator for Combustion Systems," *Turbo Expo: Power for Land, Sea, and Air.*, vol. 1, no. 42363, p. 877, 2006.

[274] D. M. Sullivan, *Electromagnetic simulation using the FDTD method.* Hoboken, New Jersey: John Wiley & Sons, 2013.

[275] X. Duanyi, *Multi-dimensional Optical Storage*. Singapore, Singapore: Springer, 2016.

[276] H. Hideki, A. Katsushi, K. Takashi, N. Takao, and I. Koji, "High-Efficiency 352 nm quaternary InAlGaN-based ultraviolet light-emitting diodes grown on GaN substrates," *J. Appl. Phys.,* vol. 43, no. 10A, p. L1241, 2004

[277] T. A. Kalajian, A. Aldoukhi, A. J. Veronikis, K. Persons, and M. F. Holick, "Ultraviolet B light emitting diodes (leds) are more efficient and effective in producing vitamin D(3) in human skin compared to natural sunlight," *Sci. Rep.,* vol. 7, no. 1, p. 11489, 2017.

[278] P. Chandra *et al.*, "Treatment of vitamin D deficiency with UV light in patients with malabsorption syndromes: a case series," *Photodermatol. Photoimmunol. Photomed.,* vol. 23, no. 5, p. 179, 2007.

[279] A. Reich and K. Mędrek, "Effects of narrow band UVB (311 nm) irradiation on epidermal cells," *Int. J. Mol. Sci.,* vol. 14, no. 4, p. 8456, 2013.

[280] G. D. Bandow and J. Y. M. Koo, "Narrow-band ultraviolet B radiation: a review of the current literature," *Int. J. Dermatol.,* vol. 43, no. 8, p. 555, 2004.

[281] A. Kawada, "UVB-induced erythema, delayed tanning, and UVA-induced immediate tanning in Japanese skin," *Photo-dermatology.,* vol. 3, no. 6, p. 327, 1986.

[282] A. Yasan *et al.*, "Characteristics of high-quality p-type $Al_xGa_{1-x}N$/GaN superlattices," *Appl. Phys. Lett.,* vol. 80, no. 12, p. 2108, 2002.

[283] M. Djavid, X. Liu, and Z. Mi, "Improvement of the light extraction efficiency of GaN-based LEDs using rolled-up nanotube arrays," *Opt. Express.,* vol. 22, no. S7, p. A1680, 2014.

[284] C. E. Lee, B. S. Cheng, Y. C. Lee, H. C. Kuo, T. C. Lu, and S. C. Wang, "Output power enhancement of vertical-injection ultraviolet light-emitting diodes by GaN-free and surface roughness structures," *Electrochem. Solid. State. Lett.,* vol. 12, no. 2, p. H44, 2009.

[285] N. Shuji, S. Masayuki, I. Naruhito, N. Shin-ichi, Y. Takao, and M. Takashi, "Superbright green InGaN single-quantum-well-structure light-emitting diodes," *J. Appl. Phys.,* vol. 34, no. 10B, p. L1332, 1995.

[286] S. Fischer, C. Wetzel, E. E. Haller, and B. K. Meyer, "On p-type doping in GaN-acceptor binding energies," *Appl. Phys. Lett.,* vol. 67, no. 9, p. 1298, 1995.

[287] T. K. John E. Ayers, Paul Rago, and Johanna Raphael, *Heteroepitaxy of semiconductors: theory, growth, and characterization.* Boca Raton, Florida: CRC Press, 2016.

[288] X. Tang, G. Li, and S. Zhou, "ultraviolet electroluminescence of light-emitting diodes based on single n-ZnO/p-AlGaN heterojunction nanowires," *Nano. Lett.,* vol. 13, no. 11, p. 5046, 2013.

[289] J. P. Berenger, "Perfectly matched layer for the FDTD solution of wave-structure interaction problems," *IEEE. Trans. Antennas. Propag.,* vol. 44, no. 1, p. 110, 1996.

[290] J. P. Berenger, "Evanescent waves in PML's: origin of the numerical reflection in wave-structure interaction problems," *IEEE. Trans. Antennas. Propag.,* vol. 47, no. 10, p. 1497, 1999.

[291] L. Yaxun and C. D. Sarris, "AMR-FDTD: a dynamically adaptive mesh refinement scheme for the finite-difference time-domain technique," *Proc. IEEE. Antennas. and Propagat. Soc. Int. Symp.,* vol. 1A, p. 134, 2005.

[292] M. Djavid *et al.*, "Effects of optical absorption in deep ultraviolet nanowire light-emitting diodes," *Photo. Nanostruct: Fundam. Appl.,* vol. 28, p. 106, 2018.

[293] Q. Wang, H. P. T. Nguyen, K. Cui, and Z. Mi, "High efficiency ultraviolet emission from $Al_xGa_{1-x}N$ core-shell nanowire heterostructures grown on Si (111) by molecular beam epitaxy," *Appl. Phys. Lett.,* vol. 101, no. 4, p. 043115, 2012.

[294] Q. Wang *et al.*, "Highly efficient, spectrally pure 340 nm ultraviolet emission from $Al_xGa_{1-x}N$ nanowire based light emitting diodes," *Nanotec.,* vol. 24, no. 34, p. 345201, 2013.

[295] B. Janjua *et al.*, "Droop-free $Al_xGa_{1-x}N/Al_yGa_{1-y}N$ quantum-disks-in-nanowires ultraviolet LED emitting at 337 nm on metal/silicon substrates," *Opt. Express.,* vol. 25, no. 2, p. 1381, 2017.

[296] K. Kishino, T. Hoshino, S. Ishizawa, and A. Kikuchi, "Selective-area growth of GaN nanocolumns on titanium-mask-patterned silicon (111) substrates by RF-plasma-assisted molecular-beam epitaxy," *Electron. Lett.,* vol. 44, no. 13, p. 819, 2008.

[297] K. Tomioka, T. Tanaka, S. Hara, K. Hiruma, and T. Fukui, "III–V nanowires on Si substrate: selective-area growth and device applications," *IEEE. J. Sel. Top. Quantum. Electron.,* vol. 17, no. 4, p. 1112, 2011

[298] C. D. Sarris, "Adaptive mesh refinement for time-domain numerical electromagnetics," *Synth. Lect. Comput. Electromagn.,* vol. 11, p. 1, 2007 .

[299] F. Akleman and L. Sevgi, "A novel implementation of Berenger's PML for FDTD applications," *IEEE. Microw. Wirel. Compon. Lett.,* vol. 8, no. 10, p. 324, 1998

[300] R. Eberhart, P. Simpson, and R. Dobbins, *Computational intelligence PC tools*. San Diego, California: Academic Press Professional, 1996.

[301] J. Zhang *et al.*, "AlGaN multiple-quantum-well-based, deep ultraviolet light-emitting diodes with significantly reduced long-wave emission," *Appl. Phys. Lett.,* vol. 83, no. 17, p. 3456, 2003.

[302] K. X. Chen *et al.*, "Recombination dynamics in ultraviolet light-emitting diodes with Si-doped $Al_xGa_{1-x}N/Al_yGa_{1-y}N$ multiple quantum well active regions," *J. Appl. Phys.,* vol. 101, no. 11, p. 113102, 2007.

[303] J. Bai, Q. Wang, and T. Wang, "Characterization of InGaN-based nanorod light emitting diodes with different indium compositions," *J. Appl. Phys.,* vol. 111, no. 11, p. 113103, 2012.

[304] M. Rajan Philip et al., "Polyol synthesis of zinc oxide-graphene composites: enhanced dye- sensitized solar cell efficiency," *Curr. Nanomat.,* vol. 3, p. 1, 2018.

[305] A. Kołodziejczak-Radzimska and T. Jesionowski, "Zinc Oxide-from synthesis to application: a review," *Materials.,* vol. 7, no. 4, p. 2833, 2014.

[306] M. Jacobs, S. Muthukumar, A. Panneer Selvam, J. Engel Craven, and S. Prasad, "Ultra-sensitive electrical immunoassay biosensors using nanotextured zinc oxide thin films on printed circuit board platforms," *Biosens. Bioelectron.,* vol. 55, p. 7, 2014.

[307] J. I. Hoffman, "The use of zinc oxide in determinations of cobalt and manganese," *J. Res. Natl. Bur. Stand.,* vol. 7, no. 5, p. 883, 1931

[308] H. P. Kim, A. R. b. Mohd Yusoff, M. S. Ryu, and J. Jang, "Stable photovoltaic cells based on graphene oxide/indium zinc oxide bilayer anode buffer," *Org. Electron.,* vol. 13, no. 12, p. 3195, 2012.

[309] Z. L. Wang and J. Song, "Piezoelectric nanogenerators based on zinc oxide nanowire arrays," *Science.,* vol. 312, no. 5771, p. 242, 2006.

[310] W. Han *et al.*, "Strain-gated piezotronic transistors based on vertical zinc oxide nanowires," *ACS. Nano.,* vol. 6, no. 5, p. 3760, 2012.

[311] B. Sun and H. Sirringhaus, "Solution-processed zinc oxide field-effect transistors based on self-assembly of colloidal nanorods," *Nano. Lett.,* vol. 5, no. 12, p. 2408, 2005.

[312] M. Bitenc and Z. Crnjak Orel, "Synthesis and characterization of crystalline hexagonal bipods of zinc oxide," *Mater. Res. Bull.,* vol. 44, no. 2, p. 381, 2009.

[313] C. Pholnak, C. Sirisathitkul, and D. J. Harding, "Characterizations of octahedral zinc oxide synthesized by sonochemical method," *J. Phys. Chem. Solids.,* vol. 72, no. 6, p. 817, 2011.

[314] S. C. Lyu *et al.*, "Low temperature growth and photoluminescence of well-aligned zinc oxide nanowires," *Chem. Phys. Lett.,* vol. 363, no. 1–2, p. 134, 2002.

[315] Y. Peng, A.-W. Xu, B. Deng, M. Antonietti, and H. Cölfen, "Polymer-controlled crystallization of zinc oxide hexagonal nanorings and disks," *J. Phys. Chem. B.,* vol. 110, no. 7, p. 2988, 2006.

[316] A. Anžlovar, Z. Crnjak Orel, K. Kogej and M. Zigon, "Polyol-mediated synthesis of zinc oxide nanorods and nanocomposites with poly(methyl methacrylate)," *J. Nanomater.,* vol. 2012, p. 9, 2012.

[317] S. H. Basri, M. A. Mohd Sarjidan, and W. H. A. Abd Majid, "Structural and optical properties of nickel-doped and undoped zinc oxide thin films deposited by sol-gel method," *Adv. Mater. Res.,* vol. 895, p. 250, 2014.

[318] C. Wu, F. Li, Y. Zhang, and T. Guo, "Improving the field emission of graphene by depositing zinc oxide nanorods on its surface," *Carbon.,* vol. 50, no. 10, p. 3622, 2012.

[319] I. Y. Y. Bu, "Highly conductive and transparent reduced graphene oxide/aluminium doped zinc oxide nanocomposite for the next generation solar cell applications," *Opt. Mater.,* vol. 36, no. 2, p. 299, 2013.

[320] R. C. Pawar, D. Cho, and C. S. Lee, "Fabrication of nanocomposite photocatalysts from zinc oxide nanostructures and reduced graphene oxide," *Curr. Appl. Phys.,* vol. 13, p. S50, 2013.

[321] M. Rajan Philip, T. N. Narayanan, M. Praveen Kumar, S. B. Arya, and D. K. Pattanayak, "Self-protected nickel-graphene hybrid low density 3D scaffolds," *J. Mater. Chem. A,* vol. 2, no. 45, p. 19488, 2014.

[322] K. Q. Le, H. P. T. Nguyen, Q. M. Ngo, A. Canimoglu, and N. Can, "Experimental and numerical optical characterization of plasmonic copper nanoparticles embedded in ZnO fabricated by ion implantation and annealing," *J. Alloys. Compd.,* vol. 669, p. 246, 2016.

[323] Y. Wang *et al.*, "Plasmon resonances of highly doped two-dimensional MoS_2," *Nano. Lett.,* vol. 15, no. 2, p. 883, 2015.

[324] Y. Wang *et al.*, "Electrochemical control of photoluminescence in two-dimensional MoS_2 nanoflakes," *ACS. Nano.,* vol. 7, no. 11, p. 10083, 2013.

[325] Y. Wang *et al.*, "Intercalated 2D MoS_2 utilizing a simulated sun assisted process: reducing the HER overpotential," *J. Phys. Chem. C.,* vol. 120, no. 4, p. 2447, 2016.

[326] S. Niyogi, E. Bekyarova, M. E. Itkis, J. L. McWilliams, M. A. Hamon, and R. C. Haddon, "Solution properties of graphite and graphene," *J. Am. Chem. Soc. ,* vol. 128, no. 24, p. 7720, 2006.

[327] K. N. Kudin, B. Ozbas, H. C. Schniepp, R. K. Prud'homme, I. A. Aksay, and R. Car, "Raman spectra of graphite oxide and functionalized graphene sheets," *Nano. Lett.,* vol. 8, no. 1, p. 36, 2008.

[328] A. C. Ferrari, "Raman spectroscopy of graphene and graphite: disorder, electron–phonon coupling, doping and nonadiabatic effects," *Solid. State. Commun.,* vol. 143, no. 1–2, p. 47, 2007.

[329] A. C. Ferrari *et al.*, "Raman spectrum of graphene and graphene layers," *Phys. Rev. Lett.,* vol. 97, no. 18, p. 187401, 2006.

[330] H. N. Tien *et al.*, "One-pot synthesis of a reduced graphene oxide–zinc oxide sphere composite and its use as a visible light photocatalyst," *Chem. Eng. J.,* vol. 229, p. 126, 2013.

[331] S. Larach and J. Turkevich, "Characterization of red zinc oxide by electron paramagnetic resonance," *J. Phys. Chem. Solids.,* vol. 29, no. 9, p. 1519, 1968.

[332] M. J. Zheng, L. D. Zhang, G. H. Li, and W. Z. Shen, "Fabrication and optical properties of large-scale uniform zinc oxide nanowire arrays by one-step electrochemical deposition technique," *Chem. Phys. Lett.,* vol. 363, no. 1–2, p. 123, 2002.

[333] R. Laiho, D. S. Poloskin, Y. P. Stepanov, M. P. Vlasenko, L. S. Vlasenko, and V. S. Zakhvalinskii, "Persistent photoconductivity and electron paramagnetic resonance in zinc oxide ceramics," *J. Appl. Phys.,* vol. 106, no. 1, p. 013712, 2009.

[334] P. A. Rodnyi and I. V. Khodyuk, "Optical and luminescence properties of zinc oxide (Review)," *Opt. Spectrosc.,* vol. 111, no. 5, p. 776, 2011.

[335] T. Xu, L. Zhang, H. Cheng, and Y. Zhu, "Significantly enhanced photocatalytic performance of ZnO via graphene hybridization and the mechanism study," *Appl. Catal. B.,* vol. 101, no. 3, p. 382, 2011.

[336] F. S. Omar, H. Nay Ming, S. M. Hafiz, and L. H. Ngee, "Microwave synthesis of zinc oxide/reduced graphene oxide hybrid for adsorption-photocatalysis application," *Int. J. Photoenergy.,* vol. 2014, p. 8, 2014.

[337] S. Vijay Kumar, N. M. Huang, N. Yusoff, and H. N. Lim, "High performance magnetically separable graphene/zinc oxide nanocomposite," *Mater. Lett.,* vol. 93, p. 411, 2013.

[338] M. S. Kim *et al.*, "Photoluminescence studies of ZnO thin films on R-plane sapphire substrates grown by sol–gel method," *J. Lumin.,* vol. 132, no. 10, p. 2581, 2012.

[339] R. F. Haglund, B. J. Lawrie, and R. Mu, "Coupling of photoluminescent centers in ZnO to localized and propagating surface plasmons," *Thin. Solid. Films.,* vol. 518, no. 16, p. 4637, 2010.

[340] D. J. Gargas, H. Gao, H. Wang, and P. Yang, "High quantum efficiency of band-edge emission from ZnO nanowires," *Nano. Lett.,* vol. 11, no. 9, p. 3792, 2011.

[341] A. Du Pasquier, H. Chen, and Y. Lu, "Dye sensitized solar cells using well-aligned zinc oxide nanotip arrays," *Appl. Phys. Lett.,* vol. 89, no. 25, p. 253513, 2006.

[342] L. Ke, S. C. Lai, J. D. Ye, V. L. Kaixin, and S. J. Chua, "Point defects analysis of zinc oxide thin films annealed at different temperatures with photoluminescence, Hall mobility, and low frequency noise," *J. Appl. Phys.,* vol. 108, no. 8, p. 084502, 2010.

[343] G. L. Eda, Yun-Yue ; Mattevi,Cecilia; Yamaguchi,Hisato; Chen,Hsin-An; Chen,I-Sheng; Chen,Chun-Wei; Chhowalla,Manish, "Blue photoluminescence from chemically derived graphene oxide," *Adv. Mater.,* vol. 22, no. 4, p. 505, 2009.

[344] E. M. Likovich, R. Jaramillo, K. J. Russell, S. Ramanathan, and V. Narayanamurti, "Narrow band defect luminescence from Al-doped ZnO probed by scanning tunneling cathodoluminescence," *Appl. Phys. Lett.,* vol. 99, no. 15, p. 151910, 2011.

[345] D. Li *et al.*, "Different origins of visible luminescence in ZnO nanostructures fabricated by the chemical and evaporation methods," *Appl. Phys. Lett.,* vol. 85, no. 9, p. 1601, 2004.

[346] L. E. Greene *et al.*, "Low-Temperature Wafer-Scale Production of ZnO Nanowire Arrays," *Angew. Chem. Int. Ed.,* vol. 42, no. 26, p. 3031, 2003.

[347] F. Han *et al.*, "Surface plasmon enhanced photoluminescence of ZnO nanorods by capping reduced graphene oxide sheets," *Opt. Express.,* vol. 22, no. 10, p. 11436, 2014.

[348] K. Kim, S. Min Lee, Y. Seon Do, S. Il Ahn, and K. Cheol Choi, "Enhanced photoluminescence from zinc oxide by plasmonic resonance of reduced graphene oxide," *J. Appl. Phys.,* vol. 114, no. 7, p. 074903, 2013.

[349] S. W. Hwang *et al.*, "Plasmon-enhanced ultraviolet photoluminescence from hybrid structures of graphene/ZnO films," *Phys. Rev. Lett.,* vol. 105, no. 12, p. 127403, 2010.

[350] G. Khurana, S. Sahoo, S. K. Barik, and R. S. Katiyar, "Improved photovoltaic performance of dye sensitized solar cell using ZnO–graphene nano-composites," *J. Alloys. Compd.,* vol. 578, p. 257, 2013.

[351] L. Zhang, H. Cheng, R. Zong, and Y. Zhu, "Photocorrosion suppression of ZnO nanoparticles via hybridization with graphite-like carbon and enhanced photocatalytic activity," *J. Phys. Chem. C.,* vol. 113, no. 6, p. 2368, 2009.

[352] H. Zhang, X. Lv, Y. Li, Y. Wang, and J. Li, "P25-graphene composite as a high performance photocatalyst," *ACS. Nano.,* vol. 4, no. 1, p. 380, 2010.

[353] Y. Zhang, Z.-R. Tang, X. Fu, and Y.-J. Xu, "TiO_2-graphene nanocomposites for gas-phase photocatalytic degradation of volatile aromatic pollutant: is TiO_2−graphene truly different from other TiO_2−carbon composite materials?," *ACS. Nano.,* vol. 4, no. 12, p. 7303, 2010.

[354] X. Liu *et al.*, "Microwave-assisted synthesis of ZnO–graphene composite for photocatalytic reduction of Cr(vi)," *Catal. Sci. Technol.,* vol. 1, no. 7, p. 1189, 2011.

[355] Q. Zhang, C. S. Dandeneau, X. Zhou, and G. Cao, "ZnO nanostructures for dye-sensitized solar cells," *Adv. Mater.,* vol. 21, no. 41, p. 4087, 2009.

[356] S. Kundu and U. Nithiyanantham, "DNA-mediated fast synthesis of shape-selective ZnO nanostructures and their potential applications in catalysis and dye-sensitized solar cells," *Ind. Eng. Chem. Res.,* vol. 53, no. 35, p. 13667, 2014.

[357] U. Nithiyanantham, A. Ramadoss, and S. Kundu, "Supercapacitor and dye-sensitized solar cell (DSSC) applications of shape-selective TiO_2 nanostructures," *RSC. Adv.,* vol. 4, no. 67, p. 35659, 2014.

[358] U. Nithiyanantham, A. Ramadoss, S. R. Ede, and S. Kundu, "DNA mediated wire-like clusters of self-assembled TiO_2 nanomaterials: supercapacitor and dye sensitized solar cell applications," *Nanoscale.,* vol. 6, no. 14, p. 8010, 2014.

[359] M. Rajan Philip, R. Babu, K. Vasudevan, and H. P. T. Nguyen, "Enhanced efficiency of dye-sensitized solar cells based on polyol-synthesized nickel–zinc oxide composites," *J. Electron. Mater.,* vol. 48, no. 1, p. 252, 2019.

[360] D. G. Thomas, "The exciton spectrum of zinc oxide," *J. Phys. Chem. Solids.,* vol. 15, no. 1, p. 86, 1960.

[361] E. Bacaksiz, M. Parlak, M. Tomakin, A. Özçelik, M. Karakız, and M. Altunbaş, "The effects of zinc nitrate, zinc acetate and zinc chloride precursors on investigation of structural and optical properties of ZnO thin films," *J. Alloys. Compd.,* vol. 466, no. 1, p. 447, 2008.

[362] J. Wang, J. Cao, B. Fang, P. Lu, S. Deng, and H. Wang, "Synthesis and characterization of multipod, flower-like, and shuttle-like ZnO frameworks in ionic liquids," *Mater. Lett.,* vol. 59, no. 11, p. 1405, 2005.

[363] R. Wahab, S. G. Ansari, Y.-S. Kim, H.-K. Seo, and H.-S. Shin, "Room temperature synthesis of needle-shaped ZnO nanorods via sonochemical method," *Appl. Surf. Sci.,* vol. 253, no. 18, p. 7622, 2007.

[364] Q. Xie, Z. Dai, J. Liang, L. Xu, W. Yu, and Y. Qian, "Synthesis of ZnO three-dimensional architectures and their optical properties," *Solid. State. Commun.,* vol. 136, no. 5, p. 304, 2005.

[365] Q. Zhong and E. Matijevic, "Preparation of uniform zinc oxide colloids by controlled double-jet precipitation," *J. Mater. Chem.,* vol. 6, no. 3, p. 443, 1996.

[366] L. Wang and M. Muhammed, "Synthesis of zinc oxide nanoparticles with controlled morphology," *J. Mater. Chem.,* vol. 9, no. 11, p. 2871, 1999.

[367] J. Zhang, Sun, Yin, Su, Liao, and Yan, "Control of ZnO Morphology via a Simple Solution Route," *Chem. Mater.,* vol. 14, no. 10, p. 4172, 2002.

[368] O. A. Fouad, A. A. Ismail, Z. I. Zaki, and R. M. Mohamed, "Zinc oxide thin films prepared by thermal evaporation deposition and its photocatalytic activity," *Appl. Catal. B.,* vol. 62, no. 1, p. 144, 2006.

[369] M. J. Alam and D. C. Cameron, "Preparation and properties of transparent conductive aluminum-doped zinc oxide thin films by sol–gel process," *J. Vac. Sci. Technol. A. ,* vol. 19, no. 4, p. 1642, 2001.

[370] C. R. Gorla *et al.*, "Structural, optical, and surface acoustic wave properties of epitaxial ZnO films grown on (01$\bar{1}$2) sapphire by metalorganic chemical vapor deposition," *J. Appl. Phys.,* vol. 85, no. 5, p. 2595, 1999.

[371] J. A. Anta, E. Guillén, and R. Tena-Zaera, "ZnO-Based Dye-Sensitized Solar Cells," *J. Phys. Chem. C.,* vol. 116, no. 21, p. 11413, 2012.

[372] M. Rajan Philip *et al*., "Polyol synthesis of zinc oxide-graphene composites: enhanced dye- sensitized solar cell efficiency," *Curr. Nanomat.,* vol. 3, p. 1, 2018.

[373] P. Nunes, E. Fortunato, P. Tonello, F. Braz Fernandes, P. Vilarinho, and R. Martins, "Effect of different dopant elements on the properties of ZnO thin films," *Vacuum.,* vol. 64, no. 3, p. 281, 2002.

[374] S. B. Majumder, M. Jain, P. S. Dobal, and R. S. Katiyar, "Investigations on solution derived aluminium doped zinc oxide thin films," *Mater. Sci. Eng. B.,* vol. 103, no. 1, p. 16, 2003.

[375] T. I. Yang, R. N. C. Brown, L. C. Kempel, and P. Kofinas, "Surfactant-modified nickel zinc iron oxide/polymer nanocomposites for radio frequency applications," *J. Nanoparticle. Res.,* vol. 12, no. 8, p. 2967, 2010.

[376] A. F. Lotus *et al.*, "Electrospinning route for the fabrication of p-n junction using nanofiber yarns," *J. Appl. Phys.,* vol. 106, no. 1, p. 014303, 2009.

[377] M. Kurian and D. S. Nair, "Effect of preparation conditions on Nickel Zinc Ferrite nanoparticles: A comparison between sol–gel auto combustion and co-precipitation methods," *J. Saudi. Chem. Soc.,* vol. 20, p. S517, 2016.

[378] M. Veith, M. Haas, and V. Huch, "Single source precursor approach for the sol−gel synthesis of nanocrystalline $ZnFe_2O_4$ and zinc−iron oxide composites," *Chem. Mater.,* vol. 17, no. 1, p. 95, 2005.

[379] L. Poul, S. Ammar, N. Jouini, F. Fievet, and F. Villain, "Synthesis of inorganic compounds (metal, oxide and hydroxide) in polyol medium: a versatile route related to the sol-gel process," *J. Sol-Gel. Sci. Technol.,* vol. 26, no. 1, p. 261, 2003.

[380] A. A. Tanveer, A. Dar, and P. Sen, "Pulsed laser deposited nickel doped zinc oxide thin films: structural and optical investigations," *J. Nano-Electron. Phys.,* vol. 5, no. 2, p. 02024, 2013.

[381] D. Devadathan, and R. Raveendran, "Polyindole Based Nickel-Zinc Oxide Nanocomposite – Characterization and Antifungal Studies," *Int. J. Chem. Eng. Appl.,* vol. 5, no. 3, p. 240, 2014

[382] G. Chandrashekaran and R. Elilarassi, "Synthesis, structural and magnetic characterization of Ni-Doped ZnO diluted magnetic semiconductor," *American. J. Mater. Sci.,* vol. 2, no. 1, p. 46, 2012.

[383] S. Husain, F. Rahman, N. Ali, and P. A. Alvi, "Nickel sub-lattice effects on the optical properties of ZnO nanocrystals," *J. Opto. Eng.,* vol. 1, no. 1, p. 28, 2013.

[384] S. Ramachandran, J. Narayan, and J. T. Prater, "Effect of oxygen annealing on Mn doped ZnO diluted magnetic semiconductors," *Appl. Phys. Lett.,* vol. 88, no. 24, p. 242503, 2006.

[385] Z. Xiong, X.-C. Liu, S.-Y. Zhuo, J.-H. Yang, E.-W. Shi, and W.-S. Yan, "Oxygen enhanced ferromagnetism in Cr-doped ZnO films," *Appl. Phys. Lett.,* vol. 99, no. 5, p. 052513, 2011.

[386] X. Liu, F. Lin, L. Sun, W. Cheng, X. Ma, and W. Shi, "Doping concentration dependence of room-temperature ferromagnetism for Ni-doped ZnO thin films prepared by pulsed-laser deposition," *Appl. Phys. Lett.,* vol. 88, no. 6, p. 062508, 2006.

[387] X. F. Liu and R. H. Yu, "Mediation of room temperature ferromagnetism in Co-doped SnO_2 nanocrystalline films by structural defects," *J. Appl. Phys.,* vol. 102, no. 8, p. 083917, 2007.

[388] B. B. Li *et al.*, "Study of structure and magnetic properties of Ni-doped ZnO-based DMSs," *Mater. Sci. Semicond. Process.,* vol. 9, no. 1, p. 141, 2006.

[389] H. Liu, F. Zeng, Y. Lin, G. Wang, and F. Pan, "Correlation of oxygen vacancy variations to band gap changes in epitaxial ZnO thin films," *Appl. Phys. Lett.,* vol. 102, no. 18, p. 181908, 2013.

[390] M. Y. Ghotbi, "Nickel doped zinc oxide nanoparticles produced by hydrothermal decomposition of nickel-doped zinc hydroxide nitrate," *Particuology.,* vol. 10, no. 4, p. 492, 2012.

[391] M. Karunakaran, R. Chandramohan, S. Balamurali, S. Gomathi, K. Kabila and T. Mahalingam, "Structural and Optical Properities of Nickel Doped Zinc Oxide Thin Films Grown by Low Cost Modified SILAR Method " *Inter. J. Thin. Fil. Sci. Tech.,* vol. 3, no. 2, p. 61, 2014.

[392] P. K. Sharma, R. K. Dutta, and A. C. Pandey, "Effect of nickel doping concentration on structural and magnetic properties of ultrafine diluted magnetic semiconductor ZnO nanoparticles," *J. Magn. Magn. Mater.,* vol. 321, no. 20, p. 3457, 2009.

[393] G. K. Mor, K. Shankar, M. Paulose, O. K. Varghese, and C. A. Grimes, "Use of highly-ordered TiO_2 nanotube arrays in dye-sensitized solar cells," *Nano. Lett.,* vol. 6, no. 2, p. 215, 2006.

[394] V. Biju and M. Abdul Khadar, "AC conductivity of nanostructured nickel oxide," *J. Mater. Sci.,* vol. 36, no. 24, p. 5779, 2001.